Investigation of GDNF loaded electrospun fibres to enhance peripheral nerve regeneration

PhD candidate: Rebecca Lomax

A thesis submitted in partial fulfilment of the requirements for the degree of

Doctor of Philosophy

The University of Sheffield

Faculty of Engineering

Department of Materials Science and Engineering

June 2024

Abstract

Research indicates that peripheral nerve regeneration is a complex cellular and molecular process. The current gold standard for peripheral nerve repair is the autologous nerve graft (autograft) used for injury gaps ≥ 5 mm. Nonetheless, the autograft comes with limitations such as donor site morbidity, neuropathic pain in addition to poor physical and functional recovery outcomes. Consequently, research into an alternative repair method using nerve guide conduits (NGC) has increased over the past several decades. Presently, preclinical outcomes of NGCs and cell-based therapies do not compare with autografts. First and foremost, studies have shown that without the formation of a migrating substrate, regenerating axons are unable to grow across the injury gap. The natural structure that develops post injury is a fibrin/fibronectin matrix which provides a migrating substrate to highly important Schwann cells[1, 2]. In large gaps this structure does not form fully hindering the migration of Schwann cells which provide contact guidance for regenerating axons *via* the bands of Büngner. These studies highlight the requirement of a guidance structure that is biodegradable and biocompatible removing the need for surgical removal of the device and reducing the possibility of inflammation and fibrotic reaction. Advances in nerve guide design such as intraluminal structures or polymer surface modification, have led to improved regeneration outcomes compared to empty NGCs however, further development of design and manufacturing methods is needed. Herein, the development of a surface modification method has been evaluated showing successful immobilisation of glial cell-derived neurotrophic factor (GDNF) *via* XPS, ATR-FTIR and SEM-EDX analysis. To the author's knowledge, the use of air plasma in combination with chemical linkage of aminosilane, N^1-(3-trimethoxysilylpropyl)diethylenetriamine, has not been utilized to bind growth factors to polymer surfaces. Polycaprolactone (PCL) aligned microfibre scaffolds were successfully fabricated

through electrospinning and surface modified to assess the effects of topographical and neurotrophic cues on neurite length of NG108-15 neuronal cells and embryonic chick dorsal root ganglia (DRG) explants. GDNF immobilised PCL scaffolds promoted greater neurite growth of NG108-15 neuronal cells compared to functionalized PCL films. Moreover, primary Schwann cells isolated from mice trigeminal ganglia were shown to attach and differentiate on functionalized PCL scaffolds, exhibiting characteristic bipolar spindle shape morphologies. 10 ng/mL GDNF immobilised PCL scaffolds promoted significantly greater neurite extension from embryonic chick DRG compared to heparin sulfate immobilised PCL scaffolds and tissue culture plastic (TCP), highlighting 10 ng/mL GDNF as a potential concentration for evaluation *in vivo* nerve injury studies.

Acknowledgements

"*People go through life regretting what they could not achieve rather than making the most of what lies before them.*"

– Thomas Hardy, Jude the Obscure

Firstly, I would like to thank my supervisors, Professors John Haycock, Frederik Claeyssens and Fiona Boissonade for your continuous support and guidance. I would like to thank Prof. John Hayock for seeing my potential as a scientist and giving me the opportunity to develop as a person through the experience of academic research. To Prof. Frederik Claeyssens, thank you for giving me the space to work independently but always being there to provide advice and support when needed. This allowed me to develop into a skilled and knowledgeable researcher. Thank you to Dr. Caroline Taylor, Ana Sandoval-Castellanos, Sara Memarpour-Hobbi and Victoria Workman for providing mentorship and guidance throughout my PhD. I owe thanks to my colleagues and friends in Professor Claeyssens' group and the Kroto Research Institute. The collaborative environment and kind people, making me feel welcome and supported aided my progress throughout my PhD. Great thanks goes to Battelle who's financial support was received most gratefully.

On a personal note, to my friends, Mina Aleemardani, Rachel Furmidge, Aimée Van Domburg and Elliot Amadi, thank you for the joy and laughter you brought during difficult times. To my siblings, Sarah, David and Fritz and my parents, Gillian and Allistair, thank you for your unconditional love, support and believing in me when times were difficult. To Santiago, thank you for all your kindness and love. Finally to Andrea, thank you for pushing me to be the best version of myself and showing me I can achieve anything when I put my mind to it.

Academic outputs

Conferences

1. White Rose Biomaterials and Tissue Engineering Group (**BiTEG**) 2019, York, UK, ***Delegate.***
2. Tissue and Cell Engineering Society (**TCES**) 2020, Online, ***Delegate.***
3. Tissue Engineering and Regenerative Medicine International Society (**TERMIS**) 2023, Manchester, UK, ***Delegate.***
4. Lomax R, Claeyssens F, Boissonade F, **"Investigating the effects of local delivery of glial cell-derived neurotrophic factor on neurite growth *in vitro*",** European Society for Biomaterials (**ESB**) 2023, Davos, Switzerland, ***Poster presentation.***

Oral presentations

1. **"Bioactive nerve guides"**, Materials Science and Engineering PGR conference, University of Sheffield, 2021, Sheffield, UK.
2. **"The design, manufacture and testing of advanced nerve guide conduits"**, SUNY Polytechnic Institute seminar, 2021, Online, joint presentation with Prof. J Hayock.
3. **"Bioactive nerve guides"**, Battelle scholarship meeting with former Batelle CEO Jeff Wadsworth, 2021, Online.

Activities

Graduate Teaching Assistant - Bioengineering labs, MEE, 2020/2021.

Doctoral development module - HAR6042 Introduction to Statistics, 2021/2022.

Student Support

MSc project student (2020/21) and PhD student (2021/22) – Dila Hatun Sal

PhD student (2021/22) – Louis Johnson

Abbreviations

2D	Two-dimensional
3D	Three-dimensional
AC	Autoclave bag
ADSC	Adipose-derived stem cell
AEO	2-(2-aminoethoxy)ethanol
AFM	Atomic force microscopy
APTES	3-aminopropyltriethoxysilane
Ar	Argon
ATR-FTIR	Attenuated total reflectance - Fourier transform infrared
BCA	Bicinchoninic acid
BDNF	Brain-derived neurotrophic factor
BMSC	Bone marrow-derived stem cell
BSA	Bovine serum albumin
BSE	Back scattered electrons
C/O	Carbon to oxygen ratio
cDRG	Chick dorsal root ganglia

CIPN	Chemotherapy-induced peripheral neuropathy
CMAP	Compound muscle action potentials
CNS	Central nervous system
CS- C	Chondroitin sulfate-C
CS-A	Chondroitin sulfate-A
CTS	Carpal tunnel syndrome
CV	Conduction velocity
DAPI	40,6-diamidino-2-phenylindole dihydrochloride
DCM	Dichloromethane
DIL	Dialkylcarbo-cyanine
DMEM	Dulbecco’s modified eagle medium
dMSC	Differentiated MSC
DOA	Degree of acetylation
DPSC	Dental pulp stem cell
DRG	Dorsal root ganglion/ganglia
DTA	Diethylenetriamine
ECM	Extracellular matrix

EDC	1-(3-dimethylaminopropyl)-3-ethyl carbodiimide
EDD	Embryonic development day
EHD	Electrohydrodynamic
ELISA	Enzyme linked immunosorbent assay
EngNT	Engineered neural tissue
ET	Everhart-thornley
eV	Electron volts
FCS	Foetal calf serum
FDA	Food and drug administration
FG	Fluorogold
FGF	Fibroblast growth factor
FITC	Fluorescein isothiocyanate
FWHM	Full width at half maximum
GAG	Glycosaminoglycan
GBS	Guillain-Barré syndrome
GDNF	Glial cell-derived neurotrophic factor
GDNFR	GDNF receptor

GGF	Glial growth factor
GRDGS	Cell adhesion peptide
HBSS	Hank's balanced salt solution
HIV	Human immunodeficiency virus
HS	Heparan sulfate
IL	Interleukin
IR	Infrared radiation
LC-11	11-aminoundecyltriethoxysilane
LIF	Leukaemia inhibitory factor
MAG	Myelin-associated glycoprotein
MCP	Monocyte chemoattractant
MHC	Major histocompatibility complex
MPa	Megapascals
mRNA	Messenger ribonucleic acid
MSC	Mesenchymal stem cell
MW	Molecular weight
N3S	N^1-(3-trimethoxysilylpropyl)diethylenetriamine

NDS	Normal donkey serum
NG	Nerve guide
NGC	Nerve guide conduit
NGF	Nerve growth factor
NHS	N-hydroxysuccinimide
NT	Neurotrophin
NVC	Nerve conduction velocity
O/C	Oxygen to carbon ratio
PBS	Phosphate buffered saline
PCL	Polycaprolactone
PCL-PVP	PCL-poly(vinyl pyrrolidone)
PCM	Phase change material
PD	Petri dish
PDLLA	Poly(D,L-lactide)
PDMS	Polydimethylsiloxane
PEG	Polyethylene glycol
PFA	Paraformaldehyde

PGA	Polyglycolic acid
PGS	Poly(glycerol sebacate)
PHB	Poly(β -hydroxybutyrate)
PIL	Personal licence
PK	Proteinase K
PLA	Polylactic acid
PLA2	Phospholipase A_2
PLC	Poly(L-lactide-*co*-caprolactone)
PLGA	Poly(lactic-*co*-glycolic acid)
PLLA	Poly(L-lactic acid)
PMT	Photomultiplier tube
PNI	Peripheral nerve injury
PNS	Peripheral nervous system
PPL	Project licence
RF	Radiofrequency
RTK	Receptor tyrosine kinase
SC	Schwann cells

SE	Secondary electrons
SEM	Scanning electron microscopy
SFI	Sciatic function index
SHC	Short chain
SIS	Small intestine submucosa
SSI	Static sciatic index
TBI	Traumatic brain injury
TCP	Tissue culture plastic
TCR	T cell receptor
TEM	Transmission electron microscopy
TG	Trigeminal ganglia
TGF	Transforming growth factor
TLR	Toll-like receptor
TNF	Tumour necrosis factor
TSE	Tissue spongiform encephalopathies
UV	Ultra violet
VEGF	Vascular endothelial growth factor

W	Watt
WCA	Water contact angle
XPS	X-ray photoelectron spectrometry

Contents

List of figures

List of tables

Chapter 1. Introduction and Literature Review

1.1 Peripheral nerve anatomy and physiology

1.1.1 The peripheral nervous system

The nervous system is made up of the central nervous system (CNS) and the peripheral nervous system (PNS). The CNS is comprised of the brain and spinal cord whereas the PNS is comprised of nerves and ganglia [3]. It is one of the two organ systems of the body that maintains bodily functions and homeostasis[3]. Electrical signals are carried between neurons (nerve cells) to facilitate the function of the nervous system. Typical neuronal cells consist of a cell body (perikaryon – containing the nucleus and most of the major organelles), an axon and dendrite(s). The axon and dendrite are extensions of the neuronal cell membrane referred to as processes. The axon transmits action potentials away from the cell body. Neurons can have one or more dendrites which receive synaptic input from axon terminals of other neurons. Neuronal cells can be classified either by function or number of processes. There are three main neuronal types based on function: sensory, motor and interneuron. Sensory neurons (afferent neurons) function to transmit sensory information from peripheral extremities *e.g.* skin and limbs to the CNS. They detect changes in the external environment or internal body conditions. Motor neurons function to transmit signals from the CNS to muscles or glands. For example, motor neurons stimulate muscles to contract for movement. Interneurons transmit electrical impulses between sensory and motor neurons connecting the PNS and CNS. For example they connect spinal motor neurons to sensory neurons that coordinate reflexes. There are four types of neuronal cells when classified by number of process, (i) unipolar, (ii) bipolar, (iii) pseudo-unipolar and (vi) multipolar. Unipolar neurons have one axon extending from the cell body transmitting information with dendrites at the axon terminal receiving information. Unipolar neurons are primarily found in the PNS,

particularly in sensory ganglia associated with the cranial and spinal nerves. Bipolar neurons have two cell processes, one axon and one dendrite, extending from each pole of the neuronal cell body. Bipolar neurons are typically found in specialised sensory organs *e.g.* in the retina. Pseudo-unipolar neurons are sensory and develop from bipolar neurons. They have a single T-shaped process which forks, one part of the process goes to peripheral tissue and the other to the spinal cord. Pseudo-unipolar sensory neurons are found in dorsal root ganglia of the spinal chord. Neurons which have more than two process *i.e.* one axon and multiple dendrites are multipolar. Motor neurons and interneurons are examples of multipolar neurons.

1.1.1.1 Peripheral nervous system anatomy

In the PNS, there are twelve cranial nerves and thirty-one pairs of spinal nerves. The thirty-one pairs of spinal nerves can be found within the four regions of the vertebral column, the cervical region of the neck, the thoracic region, the lumbar region and inferior to the lumbar region, the sacral region (figure 1). The sacral region is superior to the coccyx. Spinal nerves branch into roots, anterior and posterior. The posterior nerve roots converge into a dorsal (posterior) root ganglion which hold the cell bodies of sensory neurons. Anterior root ganglia hold the cell bodies of motor neurons which receive signals from axons of upper motor neurons in the cerebral cortex or brain stem to control muscles[3].

Within the nerve trunk, axons are bundled in to a fascicle which is surrounded by connective tissue called the perineurium (figure 2a). The perineurium is comprised of alternating layers of perineurial cells (epithelioid myofibroblasts) and collagen type I and II [4, 5]. Each cell layer consists of basal lamina, fibronectin and heparan sulfate proteoglycan[6] . The inner smooth surface is made up of flattened mesothelial cells, collagen and fibroblasts and functions as the nerve-blood

diffusion barrier [6, 7]. In addition, the perineurium maintains pressure inside the fasciculi and is the main component that gives the nerve tensile strength and elasticity [8].

Each individual axon within a fascicle is in addition protected by the endoneurium. The endoneurium is composed mainly of tightly packed, fine, longitudinal collagen fibres[5], fibroblasts, macrophages and mast cells [9]. It is also referred to as the endoneurial tube. It can be divided into the inner and outer endonerium. The inner endoneurium is made up of fine reticulum and is sometimes referred to as the Schwann sheath or neurolemma/neurilemma[10]. The endoneurium is closely associated with a basement membrane that forms a continuous tube around axons across the nodes of Ranvier [11, 12].

The entire nerve trunk is surrounded by the epineurium, a layer of fibrous areolar connective tissue[3]. The epineurium is comprised of mainly longitudinal collagen in which fibroblasts are embedded [4, 5]. Adipose tissue may be found in the epineurium, especially in larger nerves. The epineurium holds fascicles within nerve and functions to loosely anchor the nerve to the nerve bed and protect fasciculi from compression[10]. The structure of a nerve is constantly changing along its length as fasciculi are repeatedly dividing and converging to form complex fascicular plexuses[8]. Fascicular plexus formations are responsible for ensuring no two sections of nerve structure have identical fascicular anatomy, due to repeated changes in size, number and arrangement of the fasciculi[8].

1.1.1.2 Neuroglia

Neuroglia or glial cells act as supporting cells to neurons[3]. In the PNS, the plasma membrane of Schwann cells wraps in a spiral fashion around individual segments of axon to form the myelin sheath [13]. Oligodendroglia cells myelinate the axons of the CNS. The segments of uncovered axon between the myelinating Schwann cells are the nodes of Ranvier [13, 14]. In the PNS, large axons over

1 micron are myelinated whereas smaller diameter axons under 1 micron remain unmyelinated (figure 2b). Generally, small axons (<1 µm) are bundled together and are ensheathed by Schwann cells forming a Remak bundle (figure 2b). Myelin is an electrical insulator which facilitates impulse conduction along axons [13]. The myelin sheath reduces the space and energy needed for conduction. To transmit signals between the CNS and PNS, neurotransmitters are released into synaptic clefts either between two neuronal cells or a neuronal cell and neuro-muscular/glandular junctions [15]. Neurotransmitters can either be excitatory or inhibitory. Action potentials transmitted along neurons due to excitatory neurotransmitters are facilitated by the uptake of sodium ions *via* sodium channels in the neuronal cell membrane. The uptake of sodium ions causes a change in the transmembrane potential from approximately -70 to +30 mV [16]. Sodium channels are concentrated at the Nodes of Ranvier causing a rapid saltatory ("jumping") conduction through the axon from node to node [17]. Conduction velocity correlates with nerve diameter, increasing with decreasing nerve diameter.

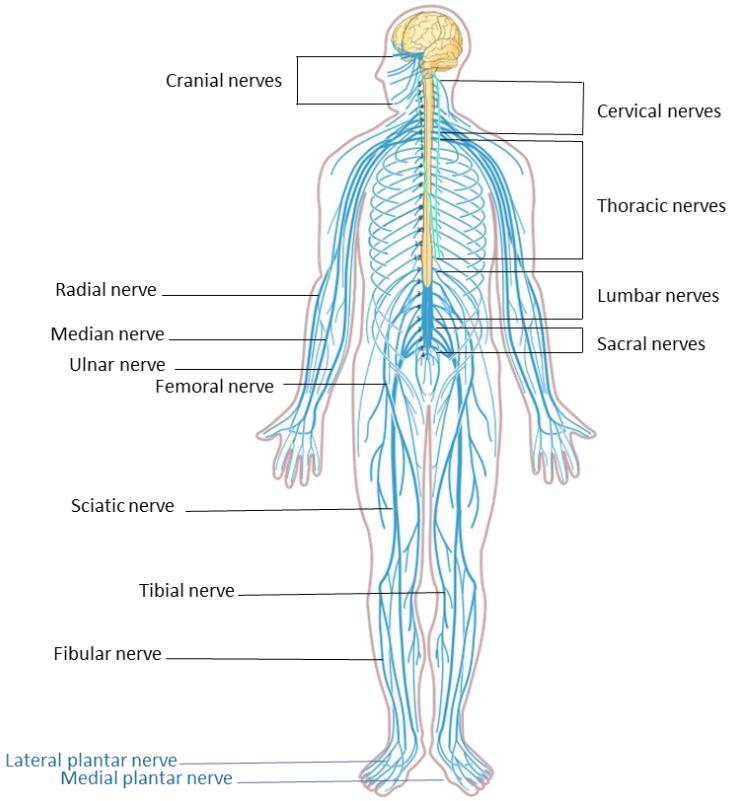

Figure 1. Diagram of select peripheral nerves of the human anatomy.

Spinal, cranial and autonomic nerves and their associated ganglia make up the PNS. The PNS is divided into somatic and autonomic parts. The somatic system receives sensory information from the skin, muscles and joints and provides motor innervation to skeletal muscle and the autonomic system innervates smooth and cardiac muscle and glands. The autonomic system is subdivided into an antagonistic system of sympathetic and parasympathetic parts. The twelve pairs of cranial nerves are olfactory, optic, oculomotor, trochlear, trigeminal, abducens, facial, vestibulocochlear, glossopharyngeal, vagus, accessory and hypoglossal. These nerves innervate structures in the head and neck but the vagus nerve also innervates the thoracic and abdominal region. Pairs of spinal nerves are attached to a specific segment of the spinal cord by anterior and posterior roots. There are eight cervical (C1-C8), twelve thoracic (T1-T12), five lumbar (L1-L5), five sacral (S1-S5) and one coccygeal pair(s) of spinal nerves. Axons from different spinal nerves converge into a systemic nerve. Limbs are innervated by several spinal nerves which form a plexus. There are four plexuses found in the human body for example, i) the cervical plexuses composed of axons from C1 to C5 spinal nerves which innervates structures in the posterior head and neck, ii) the branchial plexus consisting of spinal nerves C6 to T1 which differentially converge to innervate muscles of the arm, iii) the lumbar plexus consisting of L1 to L4 spinal nerves which innervate the pelvic region and anterior leg muscles and form the systemic femoral nerve, iv) the sacral plexus consisting of L4 to S4 spinal nerves which make up the tibial and fibular nerves that diverge from the major sciatic nerve (diagram sourced from creative commons and modified).

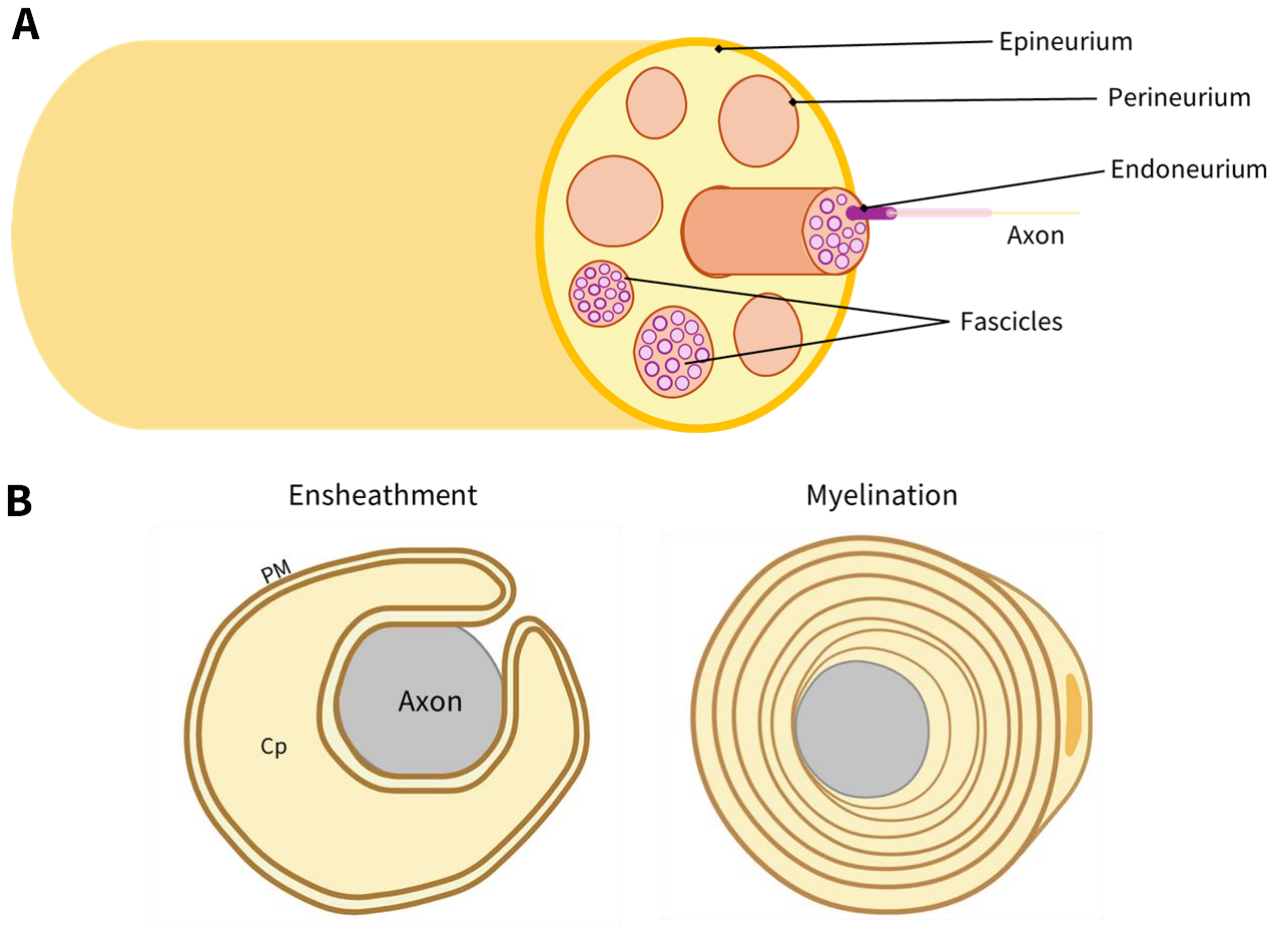

Figure 2. The structure of peripheral nerve (a) and Schwann cell myelination and ensheathment (b). Peripheral nerve is comprised of several fascicles containing axons and the three layers of connective tissue which have a protective function. Each axon is protected by the endoneurium and each fascicle is protected by the perineurium. The perineurium also acts as a diffusion barrier. The outer surface of a nerve is fibrous connective tissue called the epineurium, protecting the nerve from compression. Plasma membrane (PM), cytoplasm (Cp).

1.2 Peripheral nerve injury (PNI)

Peripheral nerve injuries were classified by Seddon in 1942 based on the effect of the nerve injury rather than the extent of the damage on the nerve[18]. PNIs were then further classified by Sunderland in 1951 based on the extent of damage to the nerve anatomy[19]. The Sunderland classification describes the severity of damage to nerve anatomy in ascending order (figure 3).

Statistics suggest that young males are most likely to suffer a peripheral nerve injury in a motor vehicle accident [20-22]. In a study by Noble *et al*. with 5777 patients, 83% of cases were male, comparably, 76.6% and 74% of cases in studies by Kouyoumdjian *et al*., were also male, with 1124 and 456 patients overall, respectively. The most common cause of PNI in the studies was motor vehicle accidents, a range of 44% to 46% of patients were involved in such accidents. Other common causes were car accidents involving pedestrians, falls, sports injuries and penetrating trauma *e.g.* from gunshot wounds, stab wounds or industrial accidents. Where sports injuries are the cause, the fibular nerves are the most commonly damaged. This is particularly the case for football injuries. Moreover, military personnel are highly likely to acquire PNIs during combat[23] for example, a case study in 2018 focused on combat related sciatic nerve injuries in soldiers fighting in the Iraq and Afghanistan wars[24]. The study found that the most common causes of combat-acquired sciatic nerve injury was *via* gunshot wounds followed by blast injury.

Stretch injuries have varying degrees of impairment on nerve function. Studies suggest that the speed of elongation decreases the elasticity of nerve. Haftek (1970) measured a mean elongation at break of rabbit tibial nerve at 73.3% when the nerve was stretched at a rate of 0.5 mm/min. The epineurium was observed to rupture at a mean elongation of 55.7% [25]. In contrast, Rydevik *et al.* (1990) found that when stretching rabbit tibial nerve at a rate of 1 cm/min the elongation at break was approximately half that measured by Haftek (1970) at 38.2% [26]. These studies indicate that if nerve is elongated at high speed or repeatedly over long periods it can cause rupture at different layers of the nerve fibre corresponding to injury grades of neurotmesis or higher. Stretch injuries commonly occur with bone fractures at the level of the brachial plexus, radial or peroneal nerves [27]. However, stretch injuries have a spontaneous recovery rate of 65 to 85% [27]. Patients for where the nerve does not spontaneously recover surgical exploration may be required.

In addition to nerve damage caused by traction, nerve compression can result in severe injury. One of the most common compression injuries is carpal tunnel syndrome (CTS) [28, 29]. CTS occurs when the median nerve in the wrist becomes compressed. The carpal tunnel is small passageway of ligament and bone that hold the nerves and tendons at the wrist [29, 30]. Current diagnostic tests for CTS are inaccurate making the syndrome difficult to diagnose [31]. Causes of CTS include genetic predisposition, injury to the wrist that may cause swelling such as fracture, obesity and rheumatoid arthritis [32]. Initial treatments include, neutral wrist splints, oral corticosteroids and local corticosteroid injection [29]. Surgical intervention may be required in severe cases.

Clinical research indicates that injection is the most common cause of serious sciatic nerve injury at the buttock-level [33, 34]. In a clinical study by Kline *et al*. (1998) injection injury was the cause of sciatic nerve damage in 36% of patients out of the 380 patients that were managed. Similarly, out of the 119 patients retrospectively researched by Topuz *et al*. (2011) 35% of sciatic nerve injuries at the buttock level were due to intramuscular injections. The mechanism of injury due to intramuscular injection includes, direct transection from impalement of the nerve, changes in the permeability of the nerve-blood barrier, swelling, pressure ischaemia and epinephrine-mediated vasoconstriction [34-36]. Studies show that injection directly into the nerve was the most destructive mechanism of nerve damage with damage ranging from mild to severe axonal and myelin degeneration depending on the agent and concentration used[33-37].

Besides physical injury due to transection, stretch and compression, disease-associated neuropathy can cause significant damage to peripheral nerve. Causes of peripheral neuropathy include chemotherapy, diseases such as diabetes and obesity and autoimmune disorders such as Guillain-Barré syndrome (GBS) and human immunodeficiency virus (HIV) .

Chemotherapy-induced peripheral neuropathy (CIPN) is caused by neurotoxic chemotherapeutic agents. The drugs most commonly associated with CIPN are taxanes, vinca alkaloids and platinums in addition to newer substances [38]. Approximately 30–40% of patients receiving neurotoxic chemotherapeutics will suffer from CIPN[39] which is characterised by loss of sensation in the hands and feet, burning or tingling in limbs, loss of hearing and blurred vision[40]. The occurrence and severity of CIPN in cancer patients is associated with the drug, dose and type of cancer[41, 42]. Currently, despite international guidelines there is a lack of effective diagnosis and treatment for CIPN. There is a need for in-depth research on pathology of CIPN to improve this. Many patients are unable to continue with treatment due to the development of CIPN. Although newer chemotherapeutics have been developed to reduce injury to normal tissue, damage to nerve tissue remains a clinical challenge[43]. Dorsal root ganglia are supplied by capillaries that allow the passage of molecules from the blood circulation into the extracellular fluid of the ganglia making neuronal cells contained within susceptible to damage or death by neurotoxic agents[43].

In addition to CIPN, diabetic peripheral neuropathy occurs in 30-50 % of prediabetic and type 2 diabetic patients[44, 45]. Autoimmune disorders can be particularly debilitating for example, 20-30 % of GBS cases lead to respiratory failure[46]. GBS is an acute inflammatory demyelinating polyneuropathy which mainly affects large diameter nerve fibres that control muscle movements, vibration and touch sensation[47]. It is the most common cause of acute paralysis with an incidence of 0.6 – 4 per 100 000 individuals per year[48]. GBS is typically caused by viral infections including Epstein-Barr virus, HIV, Zika virus, West Nile virus and most recently COVID-19[48]. Although, the syndrome can be caused by bacterial infections and immunizations. GBS may be treated with immunotherapy and supportive care however is often misdiagnosed as other pathologies which can severely impact patient outcomes[46, 48].

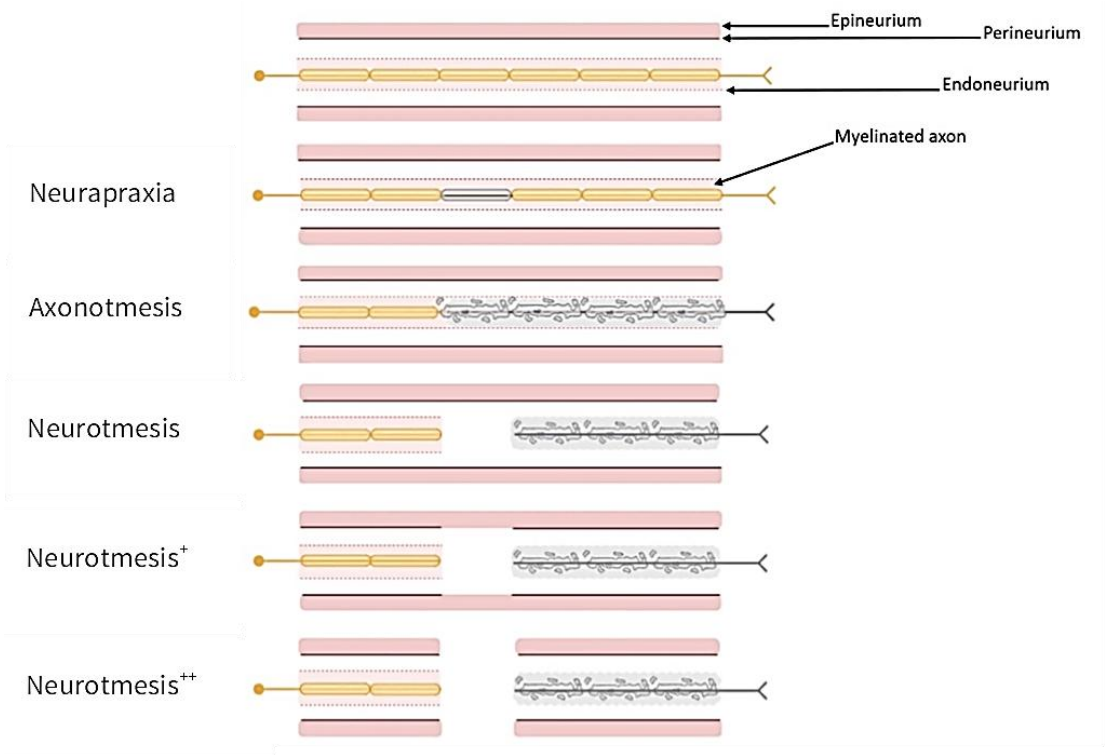

Figure 3. Sunderland classification of PNIs.

Illustration is developed based on diagrams by Sunderland 1990[8]. A first degree PNI inhibits conduction in the axon (neurapraxia) which could be due to compression for example. A second degree PNI severs the continuity of the axon (axonotmesis). A third degree PNI severs the endoneurium and the axon it surrounds (neurotmesis). A fourth degree PNI (neurotmesis+) injury severs the nerve fascicle and its contents and a fifth degree PNI (neurotmesis++) severs the entire nerve trunk.

1.2.1 Wallerian degeneration

Degeneration of the axon below the site of axotomy was first observed by physiologist Augustus Waller (1816-1870), hence Wallerian degeneration[49]. Axon degeneration proceeds in distal axons separated from the cell body due to a cascade of chemical and molecular signals (figure 4). Upon injury to the peripheral nerve, the axon takes several days to degenerate in primates[50, 51]. The roles of Schwann cells including molecular and cellular interactions are summarised in figure 5. The process begins with the swelling of axons followed by the breakdown of the neuronal cytoskeleton. The neuronal cytoskeleton and axon segment is degraded by the protease, calpain[52, 53], which is activated by an influx of calcium into the axoplasm[54, 55]. Phospholipase A_2 (PLA2; a

family of enzymes) activity is required for initiation of myelin degradation, its production is increased in Schwann cells and macrophages within hours of injury and remain at high levels for two weeks[56, 57]. Schwann cells begin to de-differentiate (this process is dependent on the ubiquitin-proteasome system)[58]. Myelinating Schwann cells that surround the severed axons alter their gene expression in which myelin gene expression decreases[59] and regeneration-associated gene expression increases *e.g.* neurotrophic factors and cytokines[60]. Schwann cells proliferate and align into Büngner bands which provide pathways for regenerating axons to reach the original target innervated[61, 62]. Mitosis is initiated in Schwann cells by the presence of invading leukocytes[63]. Furthermore, Schwann cells express a number of Toll-like receptors (TLRs) on their extracellular surface which recognise tissue damage by binding to ligands that are not typically extracellular for example, mRNA and degraded extracellular matrix (ECM) components[64-66]. Upon recognition of tissue damage ligands, pro-inflammatory factor expression such as Tumour necrosis factor (TNF)-α, interleukin (IL)-1α and IL-1β is upregulated in Schwann cells and are subsequently secreted[67]. Increased production and secretion of IL-6, increases expression of LIF (leukaemia inhibitory factor) mRNA and MCP-1 (monocyte chemoattractant-1) to attract monocytes from the blood to activate the immune response[68]. Monocytes differentiate into macrophages after migrating into tissues[69]. The activation of the immune response promotes increased clearing of dead cell material[70]. Delineating Schwann cells are the initial cells to breakdown myelin as they degrade their own and phagocytose dead cells[71, 72]. However, Schwann cell survival declines after 8 weeks of denervation thus, their ability to support axon growth also decreases[60, 73]. 2-9% of nucleated cells in uninjured nerve are endoneurial macrophages[74, 75]. Endoneurial macrophage proliferation and phagocytic activity increases within 2 days after injury[76]. Macrophages produce cytokines that activate Schwann cells (IL-1)[77] to produce neurotrophic factors such as nerve growth factor (NGF) to guide axon regeneration[78, 79]. In addition, macrophages re-model the ECM of distal nerves in

preparation for re-growing axons[80]. Within a week of PNI and towards the end of the Wallerian degeneration process, macrophages are the main immune cell type that phagocytose dead cells and produce growth factor. Schwann cells also secrete ECM molecules *e.g.* heparan sulfate, that aid axon growth in later Wallerian degeneration stages[81]. The last immune cells to arrive to the site of injury are T lymphocytes. Highest levels of T cells are reached around 14-28 days post injury[82]. Two types of T-helper cells secrete pro- or anti- inflammatory cytokines to modulate macrophage function to allow normal axon regeneration[83]. In summary, studies indicate that the process of Wallerian degeneration is a complex molecular and cellular pathway that requires communication between Schwann cells and immune cells such as macrophages to initiate and progress each stage. Clearing of dead tissue, ECM degradation followed by the gradual increase of neurotrophic factor and ECM component production by Schwann cells and macrophages creates an environment that guides and promotes the regeneration of axons.

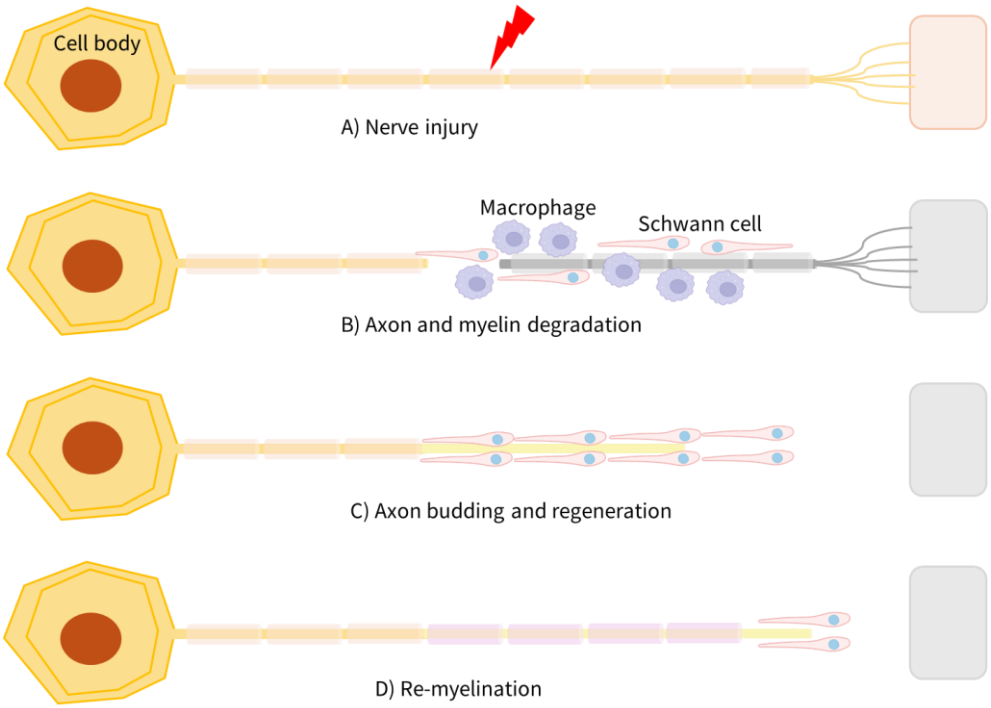

Figure 4. Wallerian degeneration and axon regeneration post PNI.

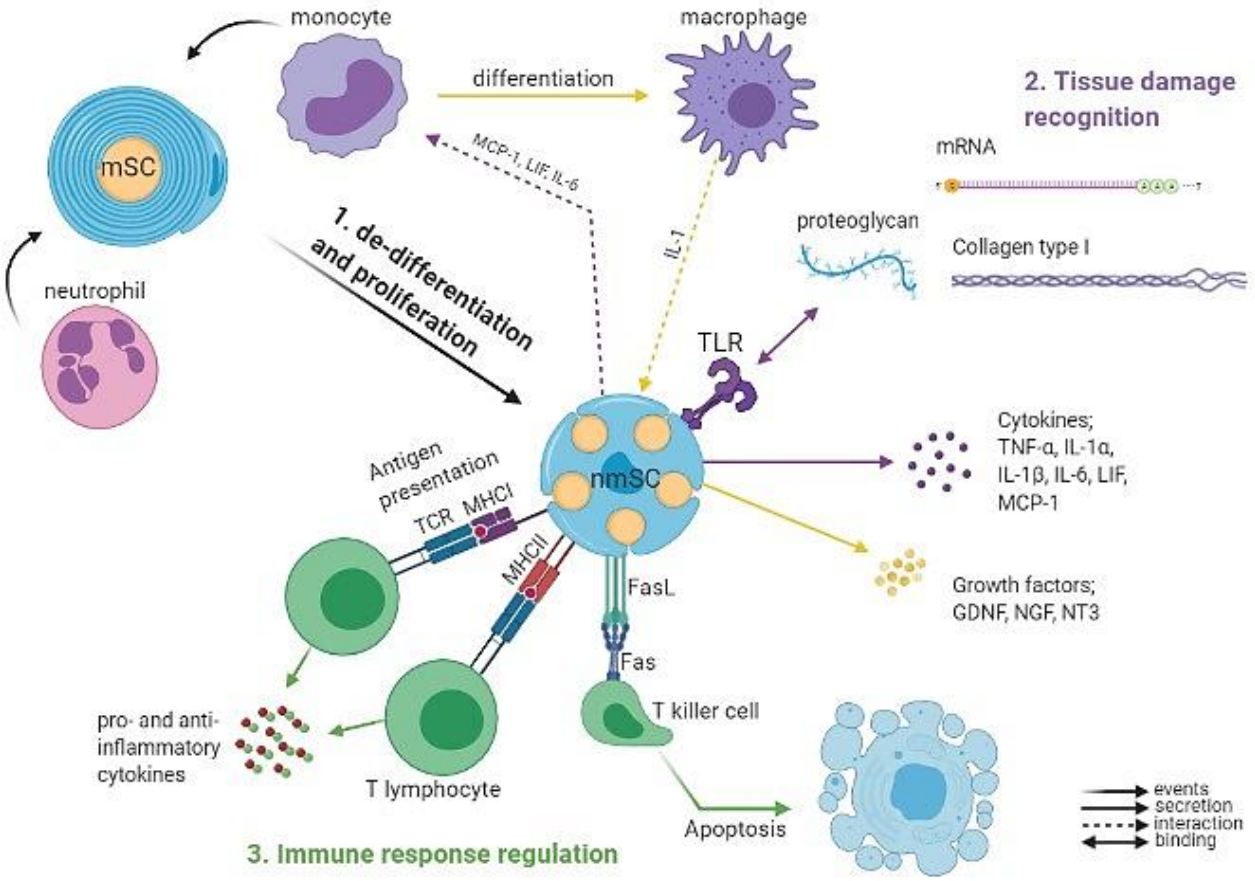

Figure 5. The roles of Schwann cells post PNI.

After the initiation of myelin degradation, Schwann cells begin to switch phenotype to non-myelinating. Subsequently, Schwann cell proliferation is initiated by invading leukocytes such as, neutrophils and monocytes from the blood. Schwann cells express Toll-like receptors to recognise tissue damage ligands such as extracellular matrix components and mRNA. This recognition causes upregulation of expression and subsequent secretion of cytokines that attract monocytes from the blood. Monocytes differentiate into macrophages in tissue. Recruited macrophages produce cytokines that act on Schwann cells leading to upregulation of expression, production and secretion of neurotrophic factors such as, GDNF and NGF. Schwann cells express MHCI and MHCII to present antigens (processed protein ligands) to regulate the immune response *via* recognition by T lymphocytes. Myelinating Schwann cell (mSC), non-myelinating Schwann cell (nmSC), Toll-like receptor (TLR), tumour necrosis factor (TNF), interleukin (IL), leukaemia inhibitory factor (LIF), monocyte chemoattractant protein (MCP), glial cell-derived growth factor (GDNF), nerve growth factor (NGF), neurotrophin (NT), messenger ribonucleic acid (mRNA), T cell receptor (TCR), major histocompatibility complex (MHC).

1.3 Peripheral nerve regeneration

Schwann cells play a crucial role providing contact guidance for axons regenerating from the proximal nerve segment post injury. For example, a study by Chen *et al*. (2019) showed that the average speed of axon growth on Büngner cords was faster than axons not associated with the cords [84]. Over the past few decades several studies have investigated a principal question; what do proliferating Schwann cells migrate upon in order to form the bands of Büngner? There are multiple studies which suggest Schwann cells use various substrates to migrate upon into the injury gap from the proximal and distal nerve segments. Williams (1987) and Schröder *et al*. (1993) present evidence that a fibrin matrix provides the substrate for migrating cells[1, 2]. Upon further investigation, Cattin *et al*. in 2015 showed that blood vessels provide a migrating substrate for proliferating Schwann cells into the nerve bridge. The study found that the formation of blood vessels is induced by VEGF-A secretion from macrophages which sense hypoxia at the site of transection[85]. In agreement with earlier studies[1, 2], analysis of the matrix components of the bridge showed the main component to be fibronectin associated with strands of elastin[85]. However, Chen at al. (2019) provide evidence that Schwann cells also use regenerating axons from the proximal end as a migrating substrate on day 4 post transection, passing the axons by day 6 [84]. Cattin *et al*. (2015) investigated the regeneration process in the sciatic nerve of mice and rats without a guidance structure whereas, Williams (1987) and Schröder *et al*. (1993) investigated a much larger gap of ~10 mm with silicone tubing also in rat sciatic nerve. Williams (1987) investigated the formation of the fibrin matrix in silicone tubes prefilled with PBS and dialysed plasma (which increased complete fibrin formation from ~5 days to 24 hours). These studies highlight the importance of stimulating the formation of fibrin/fibronectin matrices and blood vessels when repairing critical gap nerve injuries. Furthermore, if the nerve injury is severe *i.e.* neurotmesis to neurotmesis^{++} and a gap greater than 5 mm is formed, there are subsequent events that may

hinder successful reinnervation. Firstly, as the trunk or main part of the trunk is severed, the regenerating axons are no longer confined to the epineural space. Axons can grow out of the injury gap into the surrounding extracellular space or back along the proximal stump without contact guidance [84]. Second, scar tissue formation can impede axons regenerating across the injury gap which can cause multiple axonal sprouts to form a neuroma[86]. Lastly, if axon regeneration across the nerve bridge is hindered for a long period, the empty endoneurial tubes in the distal segment begin to shrink [87]. Once axons and myelin are degraded, the pressure inside the endoneurium falls causing the walls to contract. The reduction in size of the endoneurial tubes reduces tension in the perineurium causing the affected fascicle to reduce in area [10]. Regenerating axons are able to enter the contracted endoneurial tubes and reinnervate the target organ however, functional recovery is often reduced. If the gap is ≥ 5 mm the probability of successful regeneration is low without surgical intervention[84]. These studies highlight the importance of an internal guidance structure in critical gap injuries (>5 mm).

1.4 Peripheral nerve repair strategies in clinic

1.4.1 Nerve grafts and direct suturing

At present, for small nerve gap injuries (*e.g.* less than 5 mm) direct suturing of lacerated nerve ends is common practise[88]. However, direct suturing is not an option for larger gap injuries due to increased tension in the re-joined nerve which reduces blood flow to the injury site and thus affects nerve regeneration negatively. Autologous nerve grafts are the current "gold standard" used to repair nerve gap injuries larger than 5 mm. Generally, the sural nerve is harvested to be used as a donor nerve[89-91] however, other nerves can be used[92]. In a 2011 case study, a 7 cm median nerve injury was repaired with an 8 cm sciatic nerve harvested from the patient's (25-year-old soldier) above-the-knee-amputation[24]. Moreover, a 4 cm inferior alveolar nerve gap was repaired

using a 6 cm vascularised sural nerve [89]. The patient showed functional recovery of the lower lip and chin at a similar level to the normal side of the face after 10 months[89]. However, there are limitations to the use of nerve grafts such as a second surgical site, donor site morbidity, neuropathic pain and lowered motor function recovery in large nerve gaps and injuries in the upper extremities (a result of degeneration of neuromuscular junctions before regenerating nerve innervates target muscle)[90, 91, 93] and neuroma (axonal bud swellings) formation which can be due to iatrogenic injury[89]. Some studies have investigated the effect of placing a small nerve graft between the median and ulnar nerve above the wrist to prevent muscular atrophy in patients who have high median or ulnar nerve injuries. It is theorised that by placing the nerve graft lower in the arm between the ulnar and median nerve, it will decrease degeneration time of the affected nerve and allow the target muscle to be re-innervated[91, 93].

1.4.2 Nerve transfers

Further peripheral nerve repair techniques include nerve transfer (proximal or distal), this technique tends to be used when the injury is acquired in the upper extremities[94]. During a nerve transfer the proximal segment of an injured nerve is anastomosed to an adjacent nerve with redundant function, like that of the injured nerve. Moreover, nerve transfer and nerve grafts are typically used together depending on the injury in the upper extremity[90, 93]. For example, after a motor vehicle accident, a patient had a right brachial plexus injury that lead to neuroma formation in the proximal chord resulting in muscular atrophy in the muscles of the arm[95]. Three years after repair of the injury using a 9 cm nerve graft and distal nerve transfer, the patient showed recovery of motor function in the arm, wrist and fingers.

1.5 Nerve Guide Conduits

The limitations of autologous nerve grafts have led to the investigation of nerve guide conduits (NGCs) as a potential alternative for nerve repair. Case studies showed successful regeneration through hollow, non-biodegradable silicone guides, however, chronic nerve compression was reported in numerous cases thus, further surgery was required to remove the device[96, 97].

1.5.1 FDA approved NGCs

Several NGCs have been approved by the FDA for clinical use, composed of natural or synthetic polymers (table 1). In a study by Shin *et al*., Neurolac® gave the best results in a 10 mm rat sciatic nerve injury model as no difference was seen in percentage recovery compared to the autograft[98]. In this study, Neurolac® was also compared to NeuraGen® and Neurotube™. After Neurolac®, NeuraGen® seems to give better outcomes in terms of organisation and density of axonal sprouting and compound muscle action potentials (CMAP) compared to Neurotube™ [98, 99]. Neurotube™ overall gave poorest outcomes in repair and functional recovery, for example, the conduit collapsed by 12 weeks[98].

1.5.2 Neurolac®

Clinical studies on the use of Neurolac® in peripheral nerve repair have been controversial as different outcomes have been reported. Firstly, Bertleff *et al*. in 2005 published a randomised, multicentre study involving 34 patients[100]. Patients had nerve injuries distal to the wrist and the gap sizes were up to 2 cm. Patients in the control group nerves were repaired with end-to-end suturing. Patients were followed-up 3, 6, 9 and 12 months after surgery and to evaluate nerve recovery, 1- and 2-point discrimination tests were carried out. The results of moving and static 2-point discrimination tests were not significantly different between the experimental and control groups. Overall recovery of sensibility of the experimental group was comparable to the control group and the author concluded that nerve gaps up to 2 cm can be treated with synthetic nerve

guides and there is less tension in nerves treated with the tubes than direct end-to-end suturing. However, the removal of the Neurolac® guide was necessary in one patient and two patients required secondary surgery due to the rupture of a repaired tendon. In the study, it was reported that the Neurolac® device was difficult to handle due its stiffness, with the device needing to be placed in warm water to soften it prior to surgical implantation. The time needed to perform direct end-to end suturing is reported as being shorter than implanting the Neurolac® device. A similar issue was seen in clinical studies reported by Chiriac *et al*. and Costa Serrão de Araújo *et al*[101, 102]. Further issues with the Neurolac® device have been reported in experimental and clinical studies. Firstly, the resorption time of Neurolac® was inconsistent between studies, for example in rats resorption time was one year in a study by Ekholm *et al*. and two years in a study by Meek and Jansen[103, 104]. Severe inflammatory responses have been reported in patients by Hernández-Cortés *et al*., Chiriac *et al*. and Costa Serrão de Araújo *et al*., some leading to secondary surgery[102, 105]. Due to two fistulisations of the Neurolac® device in two patients and high rate of complications (8/23 patients) in the series by Chiriac *et al*., the authors concluded that Neurolac® had a low success rate for repairing hand nerves or nerves adjacent to joints. In fact, Chiriac *et al*. reported a clinical failure of 17 out of 28 transected nerve cases[102].

1.5.3 Neurotube™

Clinical studies investigating the efficacy of Neurotube™ in peripheral nerve repair demonstrate mainly excellent and good results in terms of functional recovery and are summarised in table 2. There were no complications reported in any of the case studies except for the study by Weber *et al*., here they reported three partial conduit extrusions which were due to severely damaged skin at the site of reconstruction. There were no complications with the PGA devices themselves.

Table 1. Commercially available NGCs composed of natural or synthetic materials.

Commercial name	**Material**	**Company**	**Degradation time**	**Length (mm)**	**Company website**
Neuroflex®/ NeuroMatrix® conduits and NeuroMend® wrap	Type I collagen	Collagen matrix inc.	4-8 months	25	www.collagenmatrix.com
NeuraGen®/Neur-aWrap™	Type I collagen	Integra	36-48 months	20-30	www.integralife.com
QiGel™	Chitosan	Medovent		26	www.medovent.com
RevolNerve®	Collagen type I and II from porcine skin	Orthomed			www.orthomed.fr
Surgisis®/Axoguard™	Porcine small intestinal submucosa	Axogen	3 months	10	www.axogeninc.com
Avance®	Decellularised nerve	Axogen		30	www.axogeninc.com
Neurotube™	Poly(glycolic acid) PGA	Synovis	3 months	20-40	www.synovismicro.com
Neurolac®	Poly-DL-lactide-*co*-Ɛ-caprolactone	Polyganics	16 months	30	www.polyganics.com
Salubridge™/ Salutunnel™	Polyvinyl alcohol hydrogen	Salumedica	Non-resorbable	63.5	www.salumedica.com

A summary of FDA-approved nerve guides and wraps, excluding Avance®, Qigel™ and RevolNerve®. Adapted from [106].

Table 2. Clinical case studies on the use of Neurotube™ devices to repair PNIs.

Clinical study	Cases	Nerve Location	Gap size (mm)	Repair methods	Evaluation Methods	Follow-up	Outcome
Mackinnon and Dellon [107]	15 subjects	Digital	5 – 30 Av: 17	Neurotube ™	Moving* and static** two-point discrimination	11 - 32 months Avg. 22 months	33% excellent functional sensation, 53% good functional sensation, one patient with poor sensory recovery, one patient with no sensory recovery.
+Weber, Breidenbach, Brown, Jabaley and Mass [108]	98 subjects 136 nerves	Digital	30	56 controls (end-to-end or graft) 46 Neurotube ™	Moving* and static** two-point discrimination	3, 6, 9 or 12 months. 75% of cases evaluated.	44% of Neurotube™ repairs gave excellent sensory recovery results, 43% of standard procedures gave excellent sensory recovery results, no excellent sensory recovery results were measured for nerve gap lengths > 8 mm repaired with standard procedures, 42% of Neurotube™ repairs of gap lengths >8 mm gave excellent results.
Donoghoe, Rosson and Dellon [109]	2 subjects	Median; forearm	30	Use of four conduits to repair resection of 30 mm neuromas.	Moving* and static** two-point and one-point discrimination	5 years	Recovered median motor and sensory function in their dominant hands, two-point discrimination recovered after two years.
++Rosson, Williams and Dellon [110]	6 subjects	Motor; spinal accessory, median, ulnar	15 - 40 Av: 28		Motor strength and electrodiagnostic testing	Avg. 39 months	Motor nerves regenerated through Neurotube™ and innervated target organs. All 6 patients recovered useful motor functions.

+ The study by Weber *et al*. was randomised and multicentre. ++The study by Rosson *et al*. was a retrospective study where injuries in the median and ulnar nerves were at different levels (*e.g.* proximal and distal to the wrist) so cannot be directly compared to other case series. *Excellent or good results for moving two-point discrimination are defined as 4 mm or less and 5 – 7 mm, respectively. ** Excellent or good results for static two-point discrimination are defined as 6 mm or less and 7 – 15 mm, respectively.

1.6 Tissue regeneration materials

1.6.1 Natural materials

Investigation into suitable materials for peripheral nerve repair has partly focused on the use of ECM components such as proteins, glycosaminoglycans or polysaccharides as they are known to play a role in neural and glial cell attachment and neurite outgrowth *via* interaction with receptors such as integrins expressed by neurons and glia[111]. For example, collagen (of which there are different types) is a major component of the ECM in humans and animals. Natural polymers such as, collagen and chitosan are theorised to be more biocompatible with nerve tissue as they have natural cell adhesion properties.

1.6.1.1 Collagen

Collagen NGCs have been used to successfully regenerate peripheral nerve over short gaps (4-5 mm) in primates and rats comparable to autologous nerve grafts[112, 113]. Studies have shown collagen is biodegradable with low toxicity and is non-immunogenic which are desirable qualities of a nerve guide[114-116]. Collagen has low antigenicity because of how purified collagen is obtained by digestion with pepsin. NeuraGen® (K011168, 2001), Neuroflex™ (K012814, 2001) and NeuroMatrix™ (K012814, 2001) are U.S. Food and Drug Administration (FDA)-approved NGCs composed of type I collagen sourced from Bovine tissue. There is limited clinical studies published on Neuroflex™ and NeuroMatrix™ however, there have been many clinical studies on NeuraGen® since it received FDA approval in 2001[117-120]. Overall, it has been reported that very good or good results were seen in treated patients with low numbers of poor or no improvement leading to the conclusion that NeuraGen® has comparable efficacy to nerve grafts in nerve injury gaps up to 2 cm. However, collagen has high water uptake which can contribute to faster degradation rates (unsuitable for long-term medical applications such as peripheral nerve repair). High water uptake

can lead to swelling *in vivo* potentially either hindering nerve regeneration or compressing the regenerating nerve[121]. To increase mechanical strength and control degradation rates studies have investigated the effect of crosslinking amine groups between collagen molecules[116]. The main disadvantage to using natural polymers sourced from animal tissues such as bovine is the risk of prion transmission[122]. Transmissible spongiform encephalopathies (TSE) also known as prion diseases are a group of neurodegenerative diseases that can be genetic or acquired[123]. The infectious agent is believed to be a small proteinaceous particle that is a misfolded form (PrPSc) of the host glycoprotein PrPC[123, 124]. PrPSc is resistant to proteinase K (PK) digestion as such diagnostic tests utilise the PK resistance of PrPSc to identify TSE[124]. There have been tissue processing methods created to inactivate prions and other infectious agents[125] however, the efficacy of the treatment methods have not been proven thus far[122].

1.6.1.2 Chitosan

Chitosan is a polymer obtained from alkaline deacetylation of chitin; it is the most abundant polysaccharide after cellulose. Chitosan has been considered for use in tissue engineering because of its biocompatibility and structural similarity to glycosaminoglycans. The structure of chitosan is hypothesised to play a role in Schwann cell and neural cell adhesion and survival seen in studies[126, 127]. Chitosan has low toxicity, is non-immunogenic, is low cost and highly available. Moreover, chitosan is biodegradable, data indicates degradation rates depend on the degree of acetylation (DOA)[128, 129]. Chitosan degrades *in vitro* enzymatically *via* hydrolysis of glycosidic bonds[128]. A disadvantage of chitosan is that it has low mechanical strength[127, 130]. However, it can be argued that an advantage of using chitosan is that various properties of chitosan (*e.g.* biocompatibility, mechanical strength and degradation rates) can be altered by changing the amine content[127-129].

1.6.1.3 Silk fibroin

There has been increased interest in the use of silk fibroin in tissue engineering as it has better mechanical properties compared to commonly investigated natural polymers such as collagen and chitosan[131]. Silk fibroin is easily processed, and the degradability can be modified. Silk is a natural protein polymer that is produced in specialised glands of several Lepidopteran larvae which they spin into fibres. The fibres are made of two components; a central protein, fibroin, surrounded by a coating of protein called sericin. Early studies reported bio-incompatibility however, sericin-free fibres have good biocompatibility *in vitro* and *in vitro*. Nearly 85 % of studies use silk fibroin from *Bombyx mori* (mulberry silk moth) although, investigation has begun on the use of other sources due to superior qualities. Utilization of silk fibroin in tissue engineering has been mostly investigated in *in vitro* bone and cartilage engineering[131].

1.6.1.4 Small intestine submucosa (SIS)

Small intestine submucosa (SIS) is commonly sourced from porcine small intestine segments. Certain layers of the segments are removed to leave the tunica submucosa (luminal) layer[132]. Decellularized SIS is an extracellular matrix comprised of crosslinked collagen I, II and VI and is the form generally applied *in vivo*[133]. Disadvantages of decellularized SIS include low porosity, low oxygen diffusion gradient and in terms of nerve repair near joints, insufficient strength in high-strain environments[134]. The mechanical strength is also donor age dependent thus, mechanical properties of devices are potentially unreliable[135]. SIS is highly populated with bacteria as it is derived from the gut thus, the material carries a risk of infection even after sterilisation methods which also can affect the structure of SIS[136]. However, decellularized SIS retain bioactive factors such as glycoproteins and glycosaminoglycans and growth factors demonstrated by western blotting and ELISA[137, 138]. In addition, research has demonstrated decellularized SIS has angiogenic

potential as SIS induced increased blood vessel density compared to controls which was confirmed by decreased angiogenesis when blocked with antibodies against VEGF (vascular endothelial growth factor) and FGF (fibroblast growth factor)-2[139]. Retainment of bioactive factors in SIS is hypothesised to play a role in promoting cell attachment, proliferation and migration *in vitro*[140]. Furthermore, xenogenic SIS is non-immunogenic *in vitro* when xenogenic cells and cell components are completely removed[141]. Presence of cell material can lead to inflammatory and immune reactions in primates[142].

1.6.1.5 Poly(β -hydroxybutyrate) PHB

PHB is a polyester synthesised by a wide variety of microorganisms[143]. It has low toxicity as PHB degrades to D-3-hydroxybutyric acid a normal component within human blood. PHB and its copolymers are commercially available and are named Biopol™. PHB is highly crystalline making it less flexible but can be fabricated as a co-polymer to increase the flexibility of the material[143].

1.6.2 Synthetic materials

In contrast, it is generally accepted that synthetic polymers do not come with the risk of disease transmission and have high reproducibility in terms of mechanical and chemical properties amongst other things, as such, may be preferred as alternative materials to natural polymers when being utilised for medical applications.

1.6.2.1 Polycaprolactone (PCL)

PCL is an aliphatic polyester than was first investigated amongst other synthetic polymers, to determine if it can be degraded by bacteria. PCL takes approximately 24 months to break down depending on its size, molecular weight (MW) and crystallinity. PCL degrades *in vivo via* hydrolysis of ester linkages and evidence supports the theory that low MW PCL is degraded by macrophages

and giant cells[144]. The degradation products of PCL are non-toxic which reduces the risk of tissue response. In addition to biodegradability and biocompatibility, PCL has a low glass transition temperature (T_g) of around -60 °C (in a rubbery state at room temperature) and melting point of around 60 °C. PCL has a Young's modulus (tensile modulus) of around 400 MPa which is higher than native nerve[143]. Moreover, PCL has hydrophobic surface properties which is theorised to decrease cell adhesion and protein adsorption.

1.6.2.2 Polylactic acid (PLA) and Polyglycolic acid (PGA)

PGA is a highly crystalline polyester with a high melting point and T_g between 35 and 40 °C, making it more suitable for clinical applications in hard tissue engineering[143]. It was used to make the first biodegradable suture named Dexon™. PGA has hydrophilic surface properties in contrast to PLA due to the extra methyl group in lactic acid. There are two stereoisomeric forms of lactic acid giving rise to D-PLA or L-PLA polymer forms. L-PLA is more commonly used as a biomaterial than D-PLA as hydrolysis of L-PLA produces L-lactic acid which is the naturally occurring form of lactic acid reducing the risk of toxicity. The fast degradation of PLA makes it unsuitable for peripheral nerve regeneration[145]. In addition, it has poor mechanical properties but may be used in a polymer blend to tune properties such as tensile strength, Young's modulus and rate of degradation for example in Neurolac® [98] and in sutures Vicryl™ and Polyglactin™ which are fabricated from a PLA and PGA co-polymer[143].

1.6.2.3 Polyethylene glycol (PEG)

Reports suggest PEG enables direct repair between severed axons by mediating axolemmal fusion[146-149]. PEG is a fusogen; it mediates cell fusion by cell aggregation and membrane modification[150]. Reports indicate PEG may also prevent Wallerian degeneration occurring post PNI[146, 151]. PEG is mainly applied in solution form in conjugation with end-to-end suturing as PEG

in the form of solution is more effective at promoting axolemmal fusion compared to PEG conduits. Paskal reviews seventeen papers; sixteen animal studies and one human study investigating the efficacy of PEG solution in accelerating nerve regeneration[152]. Moreover, there are a small number of publications on the use of PEG conduits to facilitate nerve regeneration[153-156]. Arcuate *et al*. (2011) reports the use of stereolithography as a rapid fabrication method that is potentially scalable. Their results indicated conduits that were multi-lumen showed higher resistance to compression (thus collapse) than to single-lumen designs.

1.6.2.4 Poly(glycerol sebacate) PGS

PGS is an elastomeric thermoset polyester making it suitable for soft tissue engineering applications such as cardiac, nerve or vascular tissue regeneration. PGS is commonly synthesised by polycondensation of the monomers glycerol and sebacic acid[157]. Glycerol and sebacic acid have been approved by the FDA as a humectant in foods and in medical applications *e.g.* drug delivery systems, respectively[157, 158]. The biocompatibility of PGS stems from the use of natural monomers as glycerol is the building block for lipids and sebacic acid is a metabolic intermediate of medium to long chain fatty acid production[157, 158]. Furthermore, no catalysts or additives are used in PGS synthesis avoiding potential toxic effects on biological tissues and cells. The hydrophobic nature and absence of cell recognition sites for cell adhesion make the use of polyesters such as PCL and PLLA in biomedical applications limited. In contrast, the PGS surface is hydrophilic in part due to hydroxyl groups attached to the carbon backbone of the polymer[158]. Another advantage of the use of PGS in soft tissue engineering is the mechanism of degradation. PGS undergoes surface degradation *via* the cleavage of ester linkages which has been linked to reduced fibrotic tissue formation and less swelling of PGS structures *in vivo* compared to polymers that degrade *via* bulk material degradation[158-160]. Studies have shown that the Young's modulus of PGS ranges from

approximately 25 kPa to 1.2 MPa and elongation at break being similar to that of arteries or veins (up to 260%)[158, 161]. However, the mechanical and degradation properties of PGS can be tailored by altering the processing parameters; curing time, curing temperature and molar ratio of the monomers. A disadvantage of PGS, in regards to nerve tissue engineering, is the difficulty of electrospinning pure PGS solutions[162]. Often PGS solutions require a polymer carrier in order to be electrospun which can lead to undesired mechanical, chemical and topographical properties of the electrospun fibres[162].

1.7 Nerve guide conduit advancements

1.7.1 Contact guidance

Contact guidance was observed by P. Weiss in 1929 in experiments where mechanical structures orientated the migration of fibroblasts and in 1934 where he reports the outgrowth of neurites from neuroblasts along orientated substratum[163, 164]. A study by Ebendal aimed to investigate the extent to which contact inhibition and contact guidance affects orientation of axon extension from chick dorsal root ganglion along collagen fibrils using time lapse cinemicrography and scanning electron microscopy (SEM)[165]. Ebendal's results indicate that axon outgrowth is influenced by contact guidance as axonal outgrowth occurred along the aligned fibres. This is because at lower axon densities contact guidance seemed to be the main factor that influenced axonal outgrowth orientation. Extending axons that form mutual contacts with other axons demonstrate contact inhibition characterised by radial orientation of axons extending from DRGs[165]. Supporting Ebendal's observations, Dunn reported increasing axon density correlated with a greater extent of radial orientation of axons from the DRG[166]. Ebendal provided further evidence of this positive correlation as higher doses of NGF resulted in higher densities of axons with radial orientation outgrowth on aligned collagen fibres[165]. However, lower doses of NGF resulted in lower densities

of axons that extended orientated to aligned collagen fibres. Overall, the experimental data from Ebendal's study suggests that axon outgrowth orientation along aligned fibres is influenced by numerous factors. Subsequently, attempts to achieve contact guidance influence on axonal outgrowth orientation include intraluminal design features such as i) fibre scaffolds, ii) channels (*e.g.* multi-lumen) and iii) grooves.

1.7.2 Electrospinning

The technique of electrospinning can be employed to create microfibre scaffolds for use as intraluminal guidance in NGCs. The history of electrospinning begins in 1600 with the publishing of William Gilbert's book "De Magnete, Magneticisque Corporibus, et de Magno Magnete Tellure". William Gilbert's published works describes his research on magnetic bodies and electrical attractions[167]. Following these works, Lord Rayleigh theoretically estimated the maximum amount of charge a droplet of liquid could carry (known as the Rayleigh limit) in 1882[168]. Five years later, Boys described a method for producing the "finest possible threads" using "electrical spinning"[169]. His experiment consisted of a small dish filled with a viscous material such as beeswax connected to an electrical supply. He observed the contents of the dish to be "shot out" onto surrounding paper and form fine threads as the material cooled. In 1902, an electrospinning process and apparatus was patented, invented by John F. Cooley[170]. His apparatus describes a tube with a small nozzle at one end through which a material dissolved in solvent can be ejected using an electric field. The patent describes two electrodes attached to the negative and positive pole of an electric generator and placed so that dispensed liquid falls inside the electric field. A rotating reel is placed adjacent to this, outside of the electric field, to collect the fibres produced. From 1902 onwards, electrospinning apparatus and processes were developed for a variety of applications[171-176].

In the current electrospinning process, typically a liquid polymer is dispensed at a constant rate from a syringe using a syringe pump. The polymer solution is held by its surface tension at the end of the needle. When the droplet is subjected to an electric field, charge is induced on the liquid surface leading to mutual charge repulsion which acts as an opposite force to the surface tension. As the voltage is increased the hemispherical droplet elongates to form a conical shape known as the Taylor Cone[177]. Eventually as the intensity of the electric field is increased it reaches a critical value where the repulsive forces overcome the surface tension resulting in the ejection of charged polymer solution. A grounded rotating or static collector of opposite polarity is used to control the trajectory and collect the fibre jet. Static collectors are often used to collect randomly aligned fibre mats whereas rotating mandrels can be used to collect aligned fibre mats. Over the past 100 years, research focus was on microscale fibre diameters *e.g.* >5 microns. However, from the early 1990s researchers began investigating nanoscale fibre diameters from the electrospinning process[178].

There are several parameters that affect electrospun fibre diameter these include solution properties (viscosity, conductivity and surface tension), controlled variables (flow rate, voltage, tip-to-collector distance and syringe diameter) and ambient parameters such as temperature and humidity[179]. Polymer solution concentration affects solution viscosity and surface tension. Generally, decreasing solution concentration will lower the viscosity of the solution leading to decreased fibre diameter however, only to a critical value will a low viscosity solution be able to form a stable jet and vice versa[179]. Higher flow rates are required as solution viscosity increases due to greater force required to overcome surface tension to eject the polymer solution. However, if the viscosity is too high the rate at which it is dispensed is not fast enough to form a stable jet leading to blockages in the needle or nozzle[179]. Unstable jets which result in bead formation occur as the polymer droplet charge becomes equal to or greater than the Rayleigh limit[180]. Bead

formation can occur when the voltage applied is too high or with low solution viscosities[180]. In contrast, polymer jets can also form unstable whipping motions due to higher charge-to-volume ratios of the polymer jet *i.e.* high voltages and low flow rates[180, 181]. Moreover, increasing applied voltage will typically result in decreased fibre diameters, with fibre diameter increasing as voltage is lowered due to less stretching and the lengthening of Taylor cone [180]. The distance between the needle tip and collector can also be adjusted to influence fibre diameter. Decreasing fibre diameters are observed with increasing tip-to-collector distances due to stretching of the polymer molecules and evaporation of the solvent causing the jet diameter to become smaller[178, 179]. Finally, by increasing flow rate, increased fibre diameters can be produced as higher volumes of polymer solution is dispensed and vice versa.

1.7.3 Key variables of electrospun fibre scaffolds

The development of electrospun fibre scaffolds for use in peripheral nerve tissue engineering has been increasingly researched since the early 2000s as an attempt to mimic the extracellular matrix architecture. Over the past 20 years, studies have shown that there are key factors which influence neuronal and glial cell growth on electrospun fibre scaffolds. These key factors are fibre diameter, fibre density, fibre alignment and surface topography.

1.7.3.1 Fibre diameter

The majority of earlier studies on the potential application of electrospun fibres for peripheral nerve regeneration were in the nanoscale range[182-186]. Although these studies investigating electrospun nanofibers show successful neuronal cell attachment, proliferation, alignment and differentiation, Wang *et al*. (2010) observed greatest Schwann cell migration matching neurite length from chick DRGs on 1.3 µm average diameter poly-L-lactic acid (PLLA) fibres compared to 759 nm and 293 nm[187]. A trend also seen by Gnavi *et al*. (2015) where the longest adult rat DRG

neurite lengths were measured on gelatin fibres of average diameters 1 and 1.3 µm compared to 300 and 600 nm[188]. As such, studies investigating the effect of fibre diameter in the micro range show promising outcomes for peripheral nerve repair[189-193].

Studies utilising polycaprolactone to produce electrospun fibres for peripheral nerve regeneration indicate optimal fibre diameters depending on the assessment model used. For example, Daud *et al*. (2012) found that 8 µm average PCL fibre diameter promoted greatest NG108-15 neuronal cell differentiation in monoculture[191]. However, in co-culture with rat Schwann cells the average maximum neurite length was greatest on 5 µm PCL fibres compared to 8 and 1 µm. Greatest average neurite length of NG108-15 neuronal cells on 8 µm fibre diameters has also been observed by other researchers using polycaprolactone and 50:50 P(3HO)/P(3HB) polymer blends[194, 195]. When utilising dorsal root ganglia explant models, different fibre diameters have shown to be optimal for neurite growth. Daud *et al*. (2012) saw decreasing neurite length from adult rat DRGs with increasing PCL fibre diameter from 8 to 1 µm with the longest neurite length and Schwann cell migration measured on 1 µm[191]. In contrast, M. Behbehani found that air plasma-modified PCL fibres with 10 µm average diameters supported the longest chick DRG outgrowth[195]. However, it should be noted that the PCL fibres used in this study were surface modified which may influence which size diameter is optimal. Although it is still unclear which fibre diameter is optimal for peripheral nerve regeneration, it can be inferred from current research that the value lies between 1 and 10 µm. As no one part of the fascicular anatomy of human nerve is the same and the ratio of large and small diameter axons changes throughout the nerve, it is highly probable that different average fibre diameters will be required depending on the architecture of the injured nerve segment.

1.7.3.2 Fibre alignment

Research evidences that the fibre alignment of electrospun scaffolds *i.e.* random or aligned can affect neuronal cell differentiation, Schwann cell maturation, proliferation and cell morphology [182, 183, 185, 190, 196]. Corey *et al*. (2007) found that highly aligned poly-L-lactide nanofibre scaffolds promoted 20% longer neurites from embryonic rat DRGs compared to randomly aligned scaffolds, a correlation also observed by Xie *et al*. (2009) on random and aligned PCL[183, 186]. Increased expression of early myelination marker, myelin-associated glycoprotein (MAG) and downregulation of the immature Schwann cell marker NCAM-1 of human Schwann cells cultured on aligned PCL fibres indicates that an aligned growth substrate promotes Schwann cell maturation[190]. Aligned microfibre scaffolds also effect the morphology of neuronal and Schwann cells promoting lower aspect ratios compared to random and flat surfaces[196]. Cirillo *et al*. (2014) found PC12 neuronal cells to have decreased aspect ratios *i.e.* elongation of the cell, when grown on aligned PCL microfibres compared to randomly aligned. In addition, Schwann cell morphology was seen to transition from flat fibroblastic-like to the characteristic bipolar elongated spindle shape when cultured on PCL films compared to PCL microfibres, respectively [190]. Highly aligned fibres appear to be a key aspect to nerve guide conduit design as they can act as a migrating substrate and provide contact guidance, leading the migration of Schwann cell and growth of axons into the injury gap and toward the distal nerve segment[156, 189, 191, 197, 198].

1.7.3.3 Fibre density

Following fibre alignment, although less studied, the density of electrospun fibre scaffolds has been shown to play an important role in neurite growth. Research suggests that decreasing fibre densities promote greater neurite growth from chick DRGs[187, 199]. A study by Xie *et al*. (2014) is of particular interest as they provide evidence building on a study by Nisbet *et al*. which challenges the view that neurites will extend parallel to aligned fibres[200, 201]. Xie *et al*. (2014) found that over

certain fibre densities neurites from chick DRGs grow perpendicular rather than parallel to the PCL fibre direction. However, when high density fibre scaffolds were coated with laminin, the neurites extended once again parallel to fibre orientation. This suggests that trophic cues my override the effect of fibre density on neurite growth and orientation.

1.7.3.4 Surface topography

Recent studies analysing the effect of anisotropic/isotropic architecture and surface roughness on neuronal and glial cell response provide evidence that these factors can affect cell morphological features and phenotype[202-206]. D'Amato *et al*. investigated the effect of three PLLA fibre surface topographies (smooth, shallow and deep pits) on rat DRG neurite length[204]. The group observed greater neurite extension on smooth uncoated fibres compared to pitted fibres. However, neurite length and branching was greatest on fibres with shallow pits compared to smooth fibres when coated with laminin, providing insight to the effects of univariate and multivariate environments on neuronal cell features. A similar trend was observed in a study assessing the effects of four different groove widths and ridge thicknesses (distance between adjacent grooves) on neurite extension compared to smooth PCL and poly(vinyl pyrrolidone) blend (PCL-PVP) fibres coated with laminin[205]. The group measured greatest neurite length and Schwann cell migration distance from chick DRG explants on PCL-PVP fibres with 238 and 301 nm groove width and ridge thickness, respectively. Furthermore, Nelson *et al*. used multivariate analysis to study the effect fibrous and flat topographies have on rat DRG neurite morphological features such as average and maximum neurite length, branching density and number of primary neurites[206]. Univariate analysis revealed greater maximum neurite length and lowest branching density on fibre scaffolds compared to PLLA films. Multivariate analysis indicated that neurite branching is dependent on other neurite features when neurons are cultured on fibres but is more

independent on films. The study provides evidence that aligned fibre topographies affect the relationship between neurite morphological features. Increasing understanding of the effects of fibre diameter, alignment, density and topography on neuronal and glial cell morphological features will aid the development of fibre scaffolds for peripheral nerve repair by eliciting desired neuronal and glial cell responses optimum for regeneration.

1.7.4 Surface modification

Although natural polymers often have the benefits of similar mechanical, physical and chemical properties to biological tissues of interest, using synthetic polymers in tissue engineering is generally more cost-effective. Moreover, the mechanical and chemical properties of synthetic polymers can be tailored to specific tissue engineering applications. The majority of synthetic polyesters such as PCL are hydrophobic, a disadvantage which leads to poor cell attachment. A multitude of surface modification techniques can be used to increase hydrophilicity and roughness, for example, plasma modification, wet chemical methods, protein-polymer blends and direct adsorption of proteins to the polymer surface[207-216].

France and Short (1994) investigated methods that modify the surface chemistry of materials without affecting their bulk properties[217]. This is a disadvantage for chemical treatment methods as they can penetrate through the material further, potentially changing the bulk properties of the material. Plasma treatment was investigated as the resulting modification depth is between one to three nanometers and potential effects were hypothesized to be adhesive properties and biocompatibility. Researchers are searching for treatment methods that give desired changes in surface properties without reducing the surface molecular weight (*e.g.* as a result of erosion processes) and decreasing the surface stability to washing and ageing. During plasma treatment, microwave or radio-frequency electromagnetic radiation is directed at gas in a glass reaction

chamber to form charged molecules or atoms (*e.g.* ions, free radicals), neutral molecules and metastable products. The radiofrequency waves excite electrons in the gas vapour detaching them from their parent atom or molecule. These reactive plasma species from the excitation process can attack the polymer chain at the surface and form interactions. Different reactions take place depending on what gas is being used for example inert gases such as argon or reactive gases such as oxygen[218]. The main aim of a study by France and Short was to determine the effects of argon plasma treatment on the surface chemistry of polystyrene[217]. They examined the effects of treatment time on the maximum level of oxygen incorporation on to the surface (saturation) and the stability of the surface material using X-ray photoelectron spectrometry (XPS). In addition, the researchers investigated the effects of storage time and storage conditions post treatment. Using oxygen to carbon (O/C) ratios to indicate surface reactivity they found that up to a certain length of time, the level of oxygen incorporation lead to stable surfaces which were not removed by washing in polymer non-solvent (methanol) or ageing (defined as over 48 hours in this study). In addition, above certain treatment times, unstable surfaces were indicated by a reduction in the O/C ratio post washing. After a 20-day period no changes in contact angle were observed on samples with stable surfaces indicating ageing did not affect the stability of the modified surfaces. They observed that storage conditions affect surface reactivity when treatment times were below a certain value. For example, storage in argon post treatment increased surface reactivity whereas storage in the laboratory did not. In 1997, France and Short published a further study in which they determined the argon plasma treatment time that gives a stable level of oxygen incorporation on to four different polymers[218]. From these studies it can be concluded that most materials have an optimum treatment time before saturation (no more reactive species can be incorporated on to the surface) of the surface leads to a measurable amount of modified material removed by

washing in a polymer non-solvent. In addition, it is important to consider the effects of factors such as storage time and conditions on the surface chemistry post plasma treatment.

Koh *et al*. (2008) investigated the efficacy of different surface modification techniques for immobilising laminin onto PLLA nanofibers[207]. The group tested three different methods which were air plasma treatment and subsequent reaction with imides, physical adsorption of laminin post air plasma treatment and creation of a PLLA-laminin blend which was electrospun directly. Higher percentages of laminin bound to the PLLA surface when modified with air plasma and covalently bound imides compared to other surface modification methods. However, neurite length of PC12 cells was higher on laminin-PLLA blend fibres followed by covalently bound laminin PLLA surfaces. Yet, cell viability was higher on covalently bound laminin PLLA.

Factors to be taken into consideration when developing manufacturing methods for NGCs include scalability, cost and simplicity. Recent research by Taylor *et al*. (2021) demonstrates a potential simple and cost-effective method for increasing hydrophilicity and roughness of polymer surfaces for nerve tissue engineering using oxygen plasma treatment and silanization with long chain aminosilane 11-aminoundecyltriethoxysilane (LC-11)[219]. Taylor *et al*. investigated the effects of -NH_2 monolayer surfaces on neuronal cell differentiation and Schwann cell viability. LC-11 enriched glass surfaces were shown to promote greater neuronal differentiation compared to short-chain (SHC) 3-aminopropyl triethoxysilane (APTES) and fibronectin-bound glass. In addition, the chain length of bound aminosilane was shown to affect primary Schwann cell morphology. The aspect ratio of primary Schwann cells cultured on LC-11 bound surfaces was significantly lower compared to APTES-bound surfaces, exhibiting characteristic bipolar spindle shape morphology. Furthermore, a later study investigating the previously described method on PCL microfibre scaffolds showed increased protein adsorption from foetal bovine serum on LC-

11 bound surfaces compared to oxygen plasma treated PCL[215]. Similar trends were observed to Taylor *et al*. (2021) on neurite length and Schwann cell morphology from embryonic chick DRG explants. Nonetheless, research suggests that increasing surface hydrophilicity and roughness alone does not lead to optimum neurite differentiation and Schwann cell response[210, 213, 215, 219]. Therefore, based on the findings of these studies, it can be inferred that bioactive molecules such ECM proteins or growth factors incorporated into polymeric scaffolds may improve neuronal and Schwann cell responses.

1.8 Biofunctionalized NGCs

Following PNI, it is theorised neurotrophic factor levels can become insufficient to maintain neuronal cells and to maintain Schwann cell proliferation at the site of damage due to the loss of retrograde transport of some neurotrophic factors from innervated target organs[220-222]. Post PNI, neuronal cell death occurs (up to 40%) in the DRG[223-226]. Axon regeneration depends on interaction between the regenerating axons from the proximal stump (growth cone) and proliferating Schwann cells migrating from the distal stump. Schwann cells from the distal stump mediate outgrowth of the axonal buds *via* secretion of neurotrophic factors[227]. Contact with the regenerating axons facilitates further Schwann cell proliferation mediated by neuronally-derived glial growth factor (GGF) specific for Schwann cells[228]. Studies indicate GGF is required for Schwann cell survival during neuromuscular junction development[229] and in adults, increases Schwann cell motility and proliferation[230]. If regeneration from the proximal stump is prevented or delayed, Schwann cell death occurs at the distal stump[231, 232]. Decrease in Schwann cell survival after 2 months limits axonal regeneration in large nerve gap injuries. Therefore, one may hypothesise that the delivery of neurotrophic factors *via* NGCs may maintain axon regeneration

from the proximal stump and potentially increase the rate of regeneration to reduce neuronal cell death in DRGs post PNI.

There are three families of neurotrophic factors; 1. neurotrophin, 2. The GDNF family and 3. neuropoietic cytokines. Neurotrophic factors are classified into families based on sequence homology, structural similarities and the type of receptors they bind[233, 234]. Neurotrophic factors have overlapping and complex interactions with neuronal, glia and target cells during embryonic and neonatal development, maturity and after injury. They interact with receptors expressed on the outer surface of cells to transduce a signal to the nucleus to alter the expression patterns of specific genes *i.e.* to upregulate or downregulate gene expression in response to PNI.

1.8.1 Glial cell-derived neurotrophic factor (GDNF)

GDNF is a glycosylated, disulphide bonded homodimer and a member of the transforming growth factor (TGF)-β superfamily[235]. In 1993, Lin *et al.* first isolated GDNF from rat glial cell line B49 and showed that GDNF promoted survival and differentiation of rat embryonic midbrain dopaminergic neurons. Early studies suggest GDNF plays a role in preventing axonal death in the distal end of nerve post injury. In 1994, Henderson *et al.* found GDNF to be 75-fold more potent than members of the neurotrophin family in supporting the survival of embryonic rat motor neurons *in vitro*[236]. Henderson *et al*. also investigated the trophic ability of GDNF *in vivo*. GDNF (20 µg) was supplied to injured rat facial nerve *via* gel foam application to the proximal nerve stump. Post axotomy, brain-derived neurotrophic factor (BDNF) and neurotrophin (NT)-4/5 promoted similar levels of facial motor neuron survival to GDNF (almost 100%). However, neither neurotrophic factor prevented atrophy of facial motor neurons to the same level as GDNF. Moreover, a further study reported that the effects of axotomy of lumbar motor neurons (~50% cell loss and atrophy) in neonatal mice were reversed by exogenously supplied GDNF[237]. In 1996,

it was first demonstrated that GDNF may signal through the Ret receptor tyrosine kinase (RTK) using explant cultures from wild-type and Ret-deficient mouse embryos[238]. Moreover, the mechanism of GDNF signalling was further elucidated when Jing *et al*. and Treanor *et al*. published the first characterization of a cell surface receptor denoted as GDNF receptor (GDNFR)-α[239, 240]. It was hypothesized that Ret RTK acts as a signalling component and GDNFR-α acts as the ligand binding component of a multi-subunit receptor complex for GDNF signalling. Expression patterns of GDNF, GDNFR-α and Ret mRNA post injury support the concept that GDNF plays a role in preventing neuronal cell and axonal death (at the distal end) post injury. Naveilhan *et al.* investigated expression patterns in sciatic nerve lesions of adult mice using RNase protection assay and in situ hybridization[241]. They observed an increase in expression of GDNF and GDNFR-α mRNA in the distal end of lesioned nerves. In addition, Hammarberg *et al.* reported an in increase in GDNF mRNA expression in DRG satellite cells and in SCs at the distal and proximal end of sciatic nerve lesion in adult rats[242]. Furthermore, there is evidence that GDNF acts to stimulate axonal growth from the proximal end post injury. For example, spinal cord motor neurons of neonatal rats were shown to be able to bind and retrogradely transport GDNF[243]. Naveilhan *et al.* found that GDNFRα mRNA was not upregulated in proximal nerve or spinal cord. However, an increase in Ret mRNA expression in spinal cord motor neurons and DRG neurons was observed[241].

Multiple studies report the ability of GDNF to promote neurite growth *in vitro* and *in vivo*. For example, in a study by Trupp *et al.*, GDNF promoted the survival and growth of fasciculated neurites from chick sympathetic ganglion explants[244]. GDNF also promoted survival of half of the neurons in embryonic chick nodose ganglion and a small subpopulation of sensory neurons in chick dorsal root and rat trigeminal ganglia[244]. In addition, Naveilhan *et al.* investigated the effects of exogenously supplied GDNF on regeneration distance of lesioned nerve[241]. The sciatic nerve of

adult mice was crushed using iris forceps and GDNF was exogenously supplied by positioning a gel foam soaked in GDNF solution (0.5 µg) at the site of lesion. The site of lesion was marked using Indian ink and a fine insect pin needle. Three days post-lesion, the nerve regeneration was examined *via* a sensory nerve pinch test. The nerve was pinched from the distal to proximal end marking where the animal first responded. The site of lesion marked by ink and the area where the animal first responded gave the regeneration distance. GDNF administration significantly increased regeneration distance compared with saline treated mice. Additionally, Munson and McMahon investigated the effects of GDNF administration on conduction velocity (CV) of rat transected tibial nerves[245]. 10 days post-axotomy of left tibial nerve, GDNF was supplied directly to cut nerve using mini-osmotic pumps for 2 or 4 weeks or intrathecally to the spinal cord for 2 weeks. CV declined during the 10 days post-lesion. Treatment with GDNF improved sensory axon CV but not significantly compared to control groups. However, GDNF treatment significantly improved CV of motor neurons in a time- and dose-dependent way.

Overall, early studies suggest GDNF may function to maintain or regulate growth of motor and sensory neurons from the proximal end post injury as well as preventing axon death in the distal end of nerve lesions. Thus, these studies support the hypothesis that GDNF could be therapeutically useful to improve regeneration distance, reduce muscular atrophy and retain sensory and motor function of affected denervated targets.

1.8.2 Protein delivery systems

Electrohydrodynamic (EHD) techniques surrounding electrospinning allows the fabrication of nano- and micro-fibres with high surface area-to-volume ratios, varied topographies and controllable release profiles. EHD methods include blend, emulsion and co-/multi-axial electrospinning and electrospraying for the development of peptide and protein delivery

systems. A key issue faced with protein delivery systems is burst release, an undesired property when developing polymeric fibre scaffolds for tissue engineering applications such as peripheral nerve repair. Peripheral nerve repair is a process that occurs over several weeks meaning delivery systems require properties that lead to sustained release of growth factor(s) over long periods of time. Varying degrees of success have been reported using protein carrier blends, emulsion, co-axial electrospinning and microspheres to reduce initial burst release of neurotrophic factors [246-252] . For example, a study by Xu *et al.* using polyphosphoester microspheres as carriers for the delivery of NGF to cultured PC12 neuronal cell line reported lower initial burst release compared to poly(lactic-*co*-glycolic acid) (PLGA) microspheres and sustained release over 10 weeks. *In vivo* assessment using filled NGCs resulted in 67 % of NGF microsphere treated groups showing regenerated nerve fibres at the distal stump compared to 50 % of NGF saline treated group and 0 % of the saline control group[246]. Moreover, over the past decade researchers have begun assessing the use of electrospraying neurotrophic factor encapsulated micro- and nano-particles onto electrospun scaffolds. Multiple studies have shown increased neurite extension in various models such as neuronal cell lines and chick DRG explants compared to unmodified polymer scaffolds[253-255]. In 2018, Xie *et al.* reported on the fabrication of a tri-layer construct comprising of NGF encapsulated in a phase-change material (PCM) sandwiched between two layers of electrospun fibres. As the microparticles are made using a PCM the release of NGF can be controlled by temperature, the NGF being released when the temperature rises above the melting point of the PCM[254].

Another important factor to consider when developing electrospun protein delivery systems is the retainment of protein activity. Proteins can become denatured depending on the fabrication process resulting in loss of activity. Emulsion and co-axial electrospinning are methods which

have been utilised in an attempt to protect proteins during the fabrication process as well as reduce burst release. Studies utilizing emulsion electrospinning *i.e.* using water phase-in-oil phase solutions, indicate the method can still lead to burst release within the first 24 hours, however still exhibit sustained release up to 28 days[247, 256-259]. A similar result is seen when using co-axial electrospinning to create fibres comprised of an outer polymer sheath containing an inner core of protein solution (*e.g.* NGF)[249, 250, 260]. A study by Yan *et al*. showed burst release of NGF from coaxially electrospun fibres using a core solution of bovine serum albumin in distilled water and poly(L-lactide-*co*-ε-caprolactone) sheath solution. The burst release of NGF suggested that the proteins were distributed throughout the nanofibre surface rather than contained within the core of the polymer fibre[249].

An alternative to EHD techniques is the use of chemical linkage. Chemically linking the protein to the electrospun fibres can reduce burst release as the protein is physically bound to the fibre rather than simply encapsulated. Proteins can be immobilised either covalently or *via* electrostatic interactions. Cho *et al*. reported sustained release of NGF with no burst release when NGF was chemically immobilised to electrospun fibres comprised of amine-terminated poly(ethylene glycol) (PEG) and PCL. Chemically immobilised NGF nanofibres were shown to promote significantly greater levels of neuronal cell differentiation of rat mesenchymal stem cells compared to physically adsorbed NGF nanofibre scaffolds[261].

1.8.3 Delivery of GDNF *via* electrospun fibre scaffolds *in vitro* and in *vivo* studies

The majority of studies examining the effects of neurotrophic factor delivery focus on NGF as it has been shown to be upregulated primarily in Schwann cells following peripheral nerve injury and plays a prominent role in sensory neuron regeneration[78, 79]. However, *in vitro* and *in vivo* studies have shown greater neurotrophic effects of GDNF on sensory and motor neurons when

compared to NGF[189, 258, 262]. In 2002, Fine *et al*. reported on the regenerative capability of NGF or GDNF releasing ethylene vinyl acetate nerve guide conduits in a 15 mm rat sciatic nerve injury gap[262]. They found that GDNF lead to greater overall regeneration in the sciatic nerve compared to NGF. The average number of myelinated axons at the midpoint of regenerated nerves was significantly greater in the GDNF group compared to the NGF NGC group. Moreover, five days before explantation, FluoroGold solution was injected into the sciatic nerve 3–5 mm distal to the implant. A significantly greater number of neuronal cells in the GDNF group retrogradely transported FluoroGold compared to the NGF group. In the dorsal root ganglia, 22.7 % versus 3.2 % of sensory neurons were labelled retrogradely in the GDNF and NGF treatment groups, respectively. Although, this study did not compare the NGCs to autografts giving limited insight into how GDNF releasing systems compare to the gold standard. Liu *et al*. observed a similar outcome *in vitro* with GDNF encapsulated PLGA scaffolds promoting longer neurite extension of PC12 neuronal cells compared to NGF encapsulated PDLLA scaffolds[258].

As the process of regeneration is a complex molecular and cellular pathway involving the release of a multitude of growth factors from non-neuronal cells, theory suggests delivery of multiple neurotrophic factors may have a synergistic effect on axonal growth across the injury gap. This effect was demonstrated by Liu *et al.* using bi-component core-sheath scaffolds comprised of GDNF encapsulated PLGA fibres and NGF encapsulated PDLLA fibres[248]. Although the scaffolds exhibited initial low burst release within 24 hours, they observed a synergistic effect on neuronal cell differentiation compared to unmodified fibres and mono-component growth factor scaffolds. On culture day seven longest neurite outgrowth was measured on bicomponent scaffolds with 1:2 fibre component ratios of GDNF PLGA fibres to NGF PDLLA fibres.

1.8.4 Heparin sulfate

Considering the cost of utilising neurotrophic factors in intraluminal guidance scaffolds, extracellular matrix components are an alternative, low-cost option for providing cell recognition sites and binding substrates for endogenous neurotrophic factors. The extracellular matrix molecule heparan sulfate (HS) binds many proteins such as growth factors and can mediate association between growth factors and their receptors[263]. Researchers were interested in utilising heparin (a molecular mimic of HS) to emulate the environment in which proteins interact with HS to mediate biological processes such as cellular proliferation, differentiation, migration, tissue homeostasis and viral pathogenesis. However, heparin does not bind to polymer surfaces in its biologically active state thus limiting its use in biological assays. In addition, chemical modification of heparin to link it to surfaces generally affects its functionality thus potentially its protein-binding property[263]. Mahoney *et al.* reported that the method of plasma polymerisation allows the binding of heparin to surfaces without affecting its functionality[263]. The group confirmed this by determining if the heparin immobilised on allylamine plasma surface films were able to bind four heparin binding proteins, TSG-6, chemokines IL-8 and KC and complement factor H. Furthermore, in 2016, the aim of Robinson *et al.* was to create a method that was fast, simple and reproducible in order to improve cell attachment, proliferation, migration and organisation[264]. The group utilised allylamine plasma polymerisation to immobilise heparin onto an electrospun PCL scaffold and subsequently FGF-2. They reported enhanced cell ingress (primary fibroblasts and keratinocytes) on plasma polymerised PCL scaffolds with heparin and FGF-2 compared to other controls (unmodified PCL, allylamine plasma coated PCL scaffold) after three weeks. In addition, two distinct layers were observed forming; a keratinocyte-rich epidermal layer and a fibroblast-rich dermal layer. Their developed protocol of utilising plasma

polymerisation and passive adsorption of biomolecules is demonstrated as effective for enhanced cell attachment, migration, proliferation and organisation as their data indicated greater cell ingress, proliferation and better cell organisation in modified PCL scaffolds over a five-week period[264].

Studies report mixed outcomes of glycosaminoglycan (GAG) and GAG mimetic functionalized surfaces on neuronal cell differentiation[265-268]. For example, extensive neurite outgrowth of chick DRGs was observed on heparan sulfate-bound type I collagen-coated culture dishes however, neurites avoided dermatan sulfate coated surfaces[265]. Furthermore, Ikehami *et al*. found that cell viability and neurite length of PC12 neuronal cells on heparin-conjugated PCL-gelatine nanofibres treated with 100 ng/mL of NGF solution was significantly greater when compared to unmodified scaffolds[268]. Of particular interest is a study by Menezes *et al*. which indicates the degree and position of sulfation of GAG mimetics effects neurotrophic ability[266]. NGF binding and neurite extension of rat DRG on cellulose sulfate-gelatine electrospun scaffolds was greater than on native GAGs, chondroitin sulfate-A (CS-A) and chondroitin sulfate-C (CS-C) scaffolds. Overall, the literature suggests that functionalising surfaces with GAGs and/or neurotrophic factors may improve the regenerative capability of intraluminal guidance scaffolds for applications in peripheral nerve repair. Nevertheless, the concentration, density of bioactive components and method of functionalisation are important factors that require exploration for optimising intraluminal scaffold designs.

1.9 Conclusion and research challenges

This chapter has provided an overview of the advancements and continuing challenges in peripheral nerve tissue engineering, specifically in protein delivery systems *via* surface modified polymeric scaffolds.

The current gold standard for peripheral nerve repair is the autologous nerve graft (autograft) used for injury gaps ≥ 5 mm. Nonetheless, the autograft comes with limitations such as donor site morbidity, neuropathic pain in addition to poor physical and functional recovery outcomes, especially as the gap size increases. Consequently, research into an alternative repair method using nerve guide conduits (NGC) has increased over the past several decades. Initial designs included non-degradable silicone tubes. Lundborg *et al.* reported successful growth of macroscopically normal nerve across a 3 mm gap in the ulnar nerve of an adult male after a 3-year follow-up period[269]. The same group reported successful regeneration through silicone guides across 5 mm gaps of the median nerve of two male patients in 1994[96]. However, complications with the use of silicone tubes include, chronic nerve compression, discomfort at the site of operation requiring surgical intervention, inflammation and fibrotic reaction leading to inhibited nerve regeneration and impermeability to oxygen and other nutrients[96, 270]. Deeper understanding of the cellular and molecular mechanisms of peripheral nerve repair lead to the development of nerve guide designs that attempted to address the core issues that occur during nerve regeneration over large gaps. First and foremost, studies have shown that without the formation of a migrating substrate regenerating axons are unable to grow across the injury gap. The natural structure that develops post injury is a fibrin/fibronectin matrix which provides a migrating substrate to highly important Schwann cells[1, 2]. In increasing nerve gaps this structure does not form successfully hindering the migration of Schwann cells which provide contact guidance for

regenerating axons *via* the bands of Büngner. These studies highlight the requirement of a guidance structure that is biodegradable and biocompatible removing the need for surgical removal of the device and reducing the possibility of inflammation and fibrotic reaction. One such method that can be employed for fabricating biodegradable polymer scaffolds is electrospinning. Aligned fibres are critical for orienting neurite growth across the injury gap. Fibre characteristics such as diameter, topography and density are key variables to optimise in order to improve glial cell attachment, migration and differentiation in addition to axon growth. Various natural and synthetic materials have been investigated for application in peripheral nerve regeneration, including but not limited to type I collagen, chitosan, poly(glycolic acid) (PGA), polycaprolactone (PCL), polyethylene glycol (PEG) and poly(lactic-*co*-glycolic acid) (PLGA)[118, 119, 156, 247, 259, 271]It is also evident that surface modification can improve cell attachment to synthetic polymers such as PCL, by increasing surface hydrophilicity thereby providing cell recognition sites. However, research suggests that increasing surface hydrophilicity and roughness alone does not lead to optimum neurite growth and Schwann cell response. The incorporation of bioactive molecules such as ECM proteins or neurotrophic factors such as NGF and GDNF have shown great promise for improving axonal growth and Schwann cell response.

Despite the promising results of protein delivery systems for peripheral nerve tissue regeneration, several challenges remain to be addressed to translate advanced NGCs to clinic. These challenges include simple and cost effective manufacturing methods, optimisation of fibre characteristics *e.g.* diameter, density, topography, further research into the effects of locally delivered bioactive molecule such as GDNF and heparin and the optimisation of sustained protein release from scaffolds in alignment with the time scale of peripheral nerve regeneration in large injury gaps (>5mm).

In order to address the identified research challenges two methods of surface modification have been explored in this study to immobilise bioactive factors heparin and GDNF. The first method explored was adsorption of heparin onto allylamine plasma surface modified polycaprolactone (PCL) films as research indicates that the immobilisation of heparin onto plasma modified surfaces does not affect heparin functionality thus it's ability to bind GDNF. The second method explored was the adsorption of heparin onto chemically linked N^1-(3-trimethoxysilylpropyl)diethylenetriamine (N3S) on PCL surfaces. The reproducibility and efficacy of the two methods were explored principally *via* XPS analysis and neuronal cell (NG108-15 cell line) differentiation assays *in vitro* on PCL films. Furthermore, the effects of GDNF concentration on neurite growth *in vitro* (NG108-15) and *ex vivo* (embryonic chick dorsal root ganglion explants) on PCL electrospun scaffolds were investigated.

1.10 Project aims and objectives

The overall aim of this project was to develop bioactive electrospun scaffolds to investigate the main research question: can local delivery of GDNF improve neurite growth *in vitro*? Within this aim, a set of objectives have been identified for each experimental chapter to be achieved upon completion of the PhD.

In chapter two, the research question addressed is: can surface modification of PCL *via* allylamine plasma or chemical linkage of aminosilane be used to successfully immobilise heparin sulfate and GDNF? The main objectives of chapter two are as follows:

- To assess the efficacy of the two surface modification techniques *via* x-ray photoelectron spectroscopy (XPS), attenuated total reflectance Fourier-transform infrared spectroscopy

(ATR-FTIR) and scanning electron microscopy with energy dispersive X-ray (SEM-EDX) to characterise elemental composition of functionalized PCL films and electrospun fibres.

- To assess the release of GDNF from surface modified PCL *via* enzyme-linked immunosorbent assay (ELISA).

In chapter three, the research question addressed is: does local delivery of GDNF significantly improve neurite growth *in vitro* compared to non-bioactive PCL surfaces? The main objectives of chapter three include:

- To assess the efficacy of both surface modification methods *via* NG108-15 neuronal cell differentiation.
- To compare the effects of control surfaces: TCP, NH2+ monolayer PCL, heparin-bound PCL and exogenous GDNF delivery to immobilised GDNF concentrations ranging from 100 ng/mL to 1pg/mL on neurite length of NG108-15 neuronal cells.
- To assess the cytotoxicity of the modified PCL surfaces on NG108-15 neuronal cells.

In chapter four, the research question addressed is: does providing cell recognition sites and neurotrophic cues lead to greater neurite growth *in vitro* and *ex vivo*? The main objectives of chapter four are as follows:

- To assess the effects of GDNF immobilised aligned PCL microfibre scaffolds on NG108-15 neuronal cell differentiation compared to GDNF immobilised PCL films.
- To assess the effects of GDNF immobilised PCL aligned microfibres on embryonic chick dorsal root ganglion explant neurite outgrowth compared to 2D TCP surfaces and heparin-immobilised PCL microfibres.

Chapter 2. Production and characterisation of surface modified PCL films and fibres

2.1 Introduction and chapter aims

In this chapter, surface modification of PCL using patented technology developed by our research group[272] is explored as a method to bind glial cell-derived neurotrophic factor (GDNF). Upon discovery of low reproducibility of the patented technology, a second surface modification method was developed using air plasma and subsequent treatment of PCL surfaces with two long chain amino-silanes. The Ninhydrin assay, and XPS was utilised to assess which plasma gas (air or argon) was to be used as prior treatment for covalent bonding of long chain aminosilane *N*[1]-(3-trimethoxysilylpropyl)diethylenetriamine (N3S). XPS and ATR-FTIR was used to confirm the reproducibility of the surface modification method and characterise the N3S, heparin and GDNF functionalized PCL surfaces. Furthermore, electrospinning parameters were assessed in order to manufacture different size diameters of PCL electrospun microfibres for *in vitro* and *in vivo* assays. The fibre diameter, alignment and topography was analysed using SEM imaging. The distribution of coatings at each step of the surface modification *i.e.* N3S, heparin and GDNF, was explored using SEM-EDX. Finally, the release profile of two GDNF concentrations, 10 ng/mL and 100 pg/mL were assessed *via* ELISA to understand the potential release kinetics of GDNF immobilised PCL at storage temperature (4 °C) and mammalian body temperature (37 °C). The chapter aims are as follows:

- Assess the method of allylamine monomer plasma polymerisation to immobilise GDNF onto PCL surfaces.

- Assess the method of air plasma polymerisation and amino-silane modification to immobilise GDNF onto PCL surfaces.

- Determine the electrospinning processing parameters for highly aligned 5 and 8 µm average diameter PCL fibre scaffolds.

- Characterise surface topography and elemental composition of functionalized PCL films and fibres using x-ray photoelectron spectroscopy (XPS), attenuated total reflectance Fourier-transform infrared spectroscopy (ATR-FTIR) and scanning electron microscopy (SEM).

2.2 Materials and Methods

2.2.1 Fabrication of PCL films by spin coating

Polycaprolactone polymer (PCL; Sigma Aldrich) of M_n 80,000 g/mol was dissolved in dichloromethane (DCM, Fisher Scientific) at 10% or 15% (w/v). Various diameters of PCL films were fabricated using 10, 13 or 22 mm coverslips on a spin coater (Laurell WS-400B-6NPP/Lite, US), vacuum pump and compressed air supply. PCL solution was dispensed onto the coverslip using a 1 mL plastic syringe (Becton Dickinson, BD UK). The parameters used to fabricate 100 µm thick PCL films were 30 second spin time and 3000 rpm.

2.2.2 Fabrication of aligned PCL microfibres by electrospinning

PCL polymer of M_n 80,000 g/mol was dissolved in DCM at 15 % wt. Average PCL fibre diameters of 5, 6 and 8 µm were fabricated using parameters which were developed based on conditions described by Daud *et al.,* 2012. Aligned microfibres where spun using Fluidnatek-LE10® (Bioinicia, Spain) which briefly comprises of a single syringe pump, a high-voltage power supply and a rotating cylindrical collector (figure 6). A 1 mL plastic luer-lock syringe (Henke-Ject®, Denmark)

was attached to the syringe pump. The FLUIDNATEK single-phase nozzle was connected to the power supply and fibres were collected on a sheet of aluminium foil wrapped around the rotating collector which was electrically grounded. A summary of the parameters used to generate 5, 6 and 8 µm PCL fibres are shown in table 3.

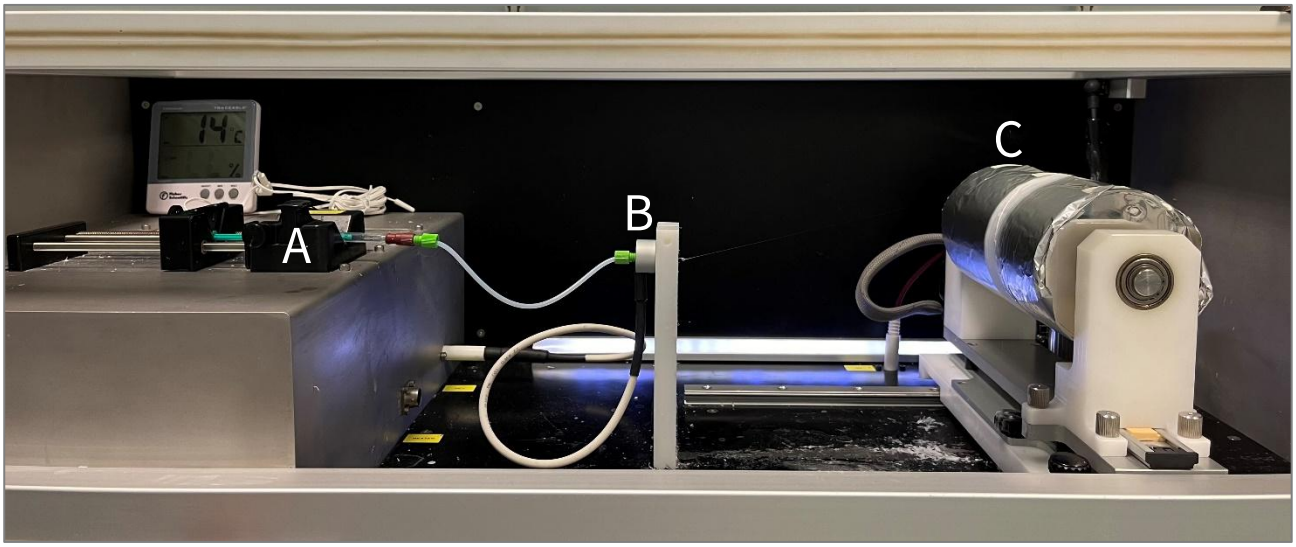

Figure 6. Fluidnatek-LE10® electrospinning set up.

A) Syringe pump, B) FLUIDNATEK single-phase nozzle and C) Rotating mandrel.

Table 3. Electrospinning parameters to generate aligned microfibre scaffolds.

Average fibre diameter (µm)	Flow rate (mL/hr)	Needle-to-collector distance (cm)	Voltage (kV)	Collector speed (rpm)
5	4	20	18	800
6				600
8				500

2.2.3 Surface modification of PCL films by allylamine plasma polymerisation

The reaction chamber for the plasma polymerisation process consists of a cylindrical glass tube enclosed by a pair of earthed metal flanges and encircled by a coil of copper wire (figure 7). The coils of copper wire emit tuneable radiofrequency. The monomer inlet is attached at one end of the vacuum line. On the opposite side of the reactor there is a radiofrequency generator (Coaxial Power Systems, UK) vacuum gauge followed by cold trap which is attached to the vacuum pump (Edwards, UK). Samples were placed inside the "in-coil" region of the reactor. The reaction chamber was evacuated to a base pressure of 8 x 10^{-3} mbar using the vacuum pump and liquid nitrogen cold trap. The monomer inlet is opened, and the vacuum pump draws in liquid monomer through the reactor. Allylamine monomer is drawn through the reaction chamber to give a chamber pressure of 2 x 10^{-2}. A 13.56 MHz radiofrequency (RF) at a continuous wave power of 10 W with 0 reflected, was used to excite the plasma within the reaction chamber for 10 minutes. After the RF power was switched off, monomer was allowed to flow over the sample for 5 minutes to react with any ionised species still on the surface.

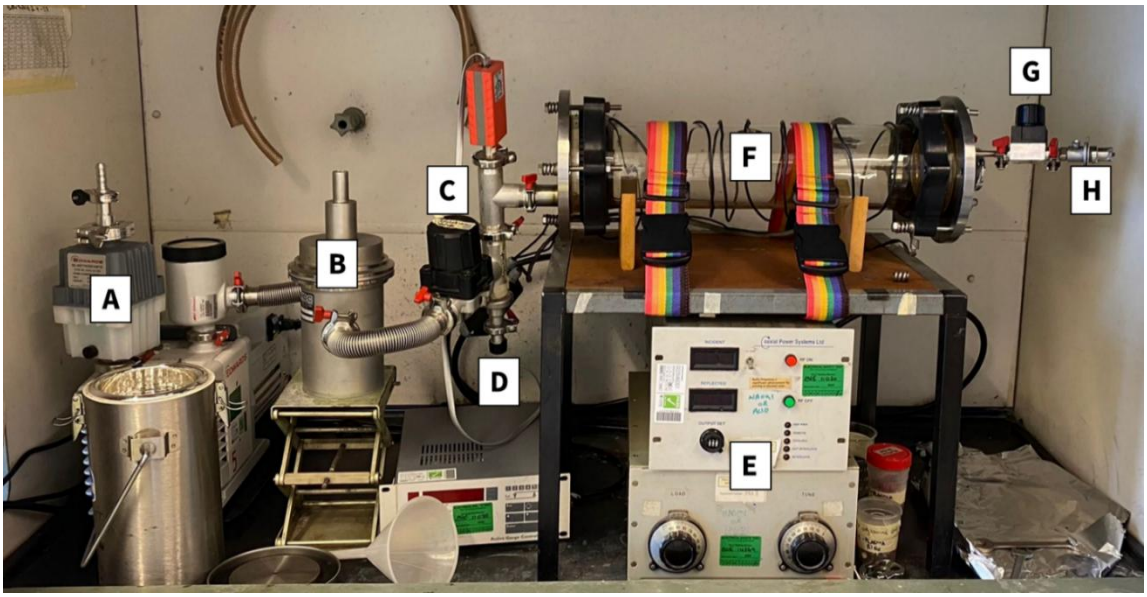

Figure 7. Allylamine plasma rig set up.

The components are A) vacuum pump, B) N2 cold trap, C) isolation valve, D) equaliser valve, E) radio frequency generator, F) glass reaction chamber, G) monomer inlet valve and H) monomer inlet.

2.2.4 PCL surface modification by argon or air plasma treatment

PCL samples were exposed to low-pressure argon gas or air in a Diener Electronic Zepto plasma cleaner at 40 kHz, 10, 25 or 50 W and 0.3 mbar for 60 or 120 seconds. A total of six PCL films or fibres were placed in a 6-well plate within a sealed autoclave/ethylene oxide gas permeable sterilisation bag.

2.2.5 Silane modification of PCL films and scaffolds

Samples were plasma treated using the method described in 2.2.4. Samples were then modified using 0.1 M *N*[1]-(3-trimethoxysilylpropyl)diethylenetriamine (N3S; Sigma, UK) or 11-aminoundecyl -triethoxysilane (11AS; Fluorochem, UK) in 95% (v/v) propan-2-ol (Fisher Scientific, UK) in deionised water for 2 h. Samples were washed in 100% propan-2-ol for 5 minutes once and then three times with either sterile, deionised water for characterisation studies or sterile PBS for *in vitro* studies.

2.2.6 Heparin incubation

Amine- or silane- coated samples were incubated in an assay dependent volume of 100 µg/mL heparin sodium (Merck, UK) in PBS in a class II biosafety cabinet for 18 hours at room temperature. The supernatant was removed and samples were rinsed three times in sterile dH_2O for XPS analysis or sterile PBS for cell culture. Samples were left to dry overnight in a class II biosafety cabinet.

2.2.7 GDNF incubation

Heparin-immobilised samples were incubated in one of the following GDNF (Universal Biologicals Ltd) in PBS concentrations; 100, 10, 1 ng/mL, 100 or 1 pg/mL. Samples were incubated in a class II biosafety cabinet for 5 hours at room temperature. The supernatant was discarded and the

samples were rinsed three times in sterile dH_2O for XPS analysis or sterile PBS for cell culture. Samples were then left to dry overnight in a class II biosafety cabinet.

2.2.8 Ninhydrin assay (Ruhemann's purple)

A Ninhydrin colorimetric assay was used to indirectly measure the presence of bound *N*[1]-(3-trimethoxysilylpropyl)diethylenetriamine or 11-aminoundecyltriethoxysilane to PCL samples. Ninhydrin oxidises ammonia, primary/secondary amines or amino acids. This reaction is then followed by the condensation of reduced Ninhydrin with free ammonia and a second molecule of Ninhydrin to form a deep blue or purple product which absorbs light at a wavelength of 562 nm. Silane modified PCL samples were incubated in 0.35% (wt/v) of Ninhydrin salt (Sigma Aldrich, UK) in 100% ethanol (Fisher Scientific, UK) for 10 minutes at 90 °C using unmodified PCL as a control. Incubated solutions were aspirated three times before being added to a 96 well plate. Absorbance of the solution was read at 562 nm using an ELx800 (Bio-Tek, US) spectrophotometer. The absorbance value of the unmodified PCL blank was subtracted from experimental sample values. A total of two repeats were carried out to quantitatively assess the reproducibility of the formation of $-NH_2$ functional groups on the surface.

2.2.9 Characterisation of silane modified PCL films by Attenuated Total Reflectance Fourier-Transform Infrared Spectroscopy (ATR-FTIR).

PCL films were used to investigate the functional groups and chemical structure of unmodified and functionalized PCL ATR-FTIR. Samples of 22 mm diameter and 100 micrometre thickness were placed onto a Perkin Elmer Frontier FTIR Spectrometer and analysed at room temperature using a spectral range of 4000 to 400 cm^{-1}, 16 scans, resolution of 4 cm^{-1} and temperature-stabilised coated FR-DTGS detector. Unmodified and surface modified PCL films were analysed from three independent experiments with triplicate used within experiments.

2.2.10 Characterisation of surface modified samples by X-ray Photoelectron Spectroscopy (XPS)

X-ray photoelectron spectroscopy (XPS) surface analysis was performed by the Sheffield Surface Analysis Centre at the University of Sheffield. Analysis was performed on PCL and surface functionalized PCL films. Films were mounted onto the sample holder with double sided carbon tape and charge neutralisation was used throughout the data collection to prevent differential charging. The analysis was carried out using a Kratos Supra instrument with a monochromated aluminium source and two analysis points per sample of 700 µm by 300 µm. Survey scans were collected between 1200 to 0 eV binding energy, at 160 eV pass energy, 1 eV intervals, and 300 seconds/sweep with one sweep being collected. High-resolution O 1s, C 1s, N 1s, S 2p, and Si 2p were also collected at 40 eV pass energy and 0.1 eV intervals for each analysis point over an appropriate energy range, with one 300 second sweep for all spectra except the N 1s and S 2p for which two sweeps were collected. The data collected was analysed in CasaXPS and calibrated in intensity using a transmission function characteristic of the instrument to make the values instrument independent. The data can then be quantified using theoretical Schofield relative sensitivity factors modified to account for instrument geometry, variation in penetration depth with energy and the angular distribution of the photoelectrons. Full width at half maximum (FWHM) were between 1.1 and 2.0 eV depending on the samples. The high-resolution spectra were all calibrated in eV by fixing the main C 1s peak to be 285.0 eV. Samples were analysed in triplicate from three independent experiments.

2.2.11 Characterisation of aligned PCL microfibres by scanning electron microscopy (SEM)/SEM-EDX

12 mm Leit adhesive conductive carbon stickers (Agar Scientific) were adhered to 12.5 mm SEM pin metal stubs (Agar Scientific). Samples for SEM were mounted to the carbon stickers and coated with a layer of gold (approx. 5 nm) using a Quorum gold splutter coater. Mounted samples for SEM-EDX are coated with a layer of carbon using a Quorum carbon coater. Gold coated samples were imaged using an Inspect F field emission gun scanning electron microscope (FEI company, US) operating at 5 kV with a spot size of 3.5. Carbon coated SEM-EDX samples were imaged using an Inspect F50 field emission gun scanning electron microscope (FEI company, US) operating 15 kV with a spot size of 4.5. Unmodified and surface modified PCL films were analysed from three independent experiments with triplicate used within experiments.

2.2.12 Water contact angle (WCA)

Unmodified PCL and PCL surface functionalized with N3S, heparin (100 µg/mL) and GDNF (10 ng/mL) films were used for water contact angle (WCA) measurement. The films were placed on the measurement stage in a DSA100S Drop Shape Analyzer (KRÜSS GmbH, Germany). A droplet of 5µl was placed on the surface of the samples with an automatic user-independent dosing system and the contact angle was determined by the camera and Sessile Drop Fitting Algorithm integrated into the device software. Unmodified and surface modified PCL films were analysed from three independent experiments with triplicate used within experiments.

2.2.13 Enzyme linked immunosorbent assay (ELISA)

Clear 96-well assay plates were coated with 2.5 µg/mL capture antibody in PBS (anti-human GDNF; R&D systems, UK) at 4°C for 12-18 hours. The contents were aspirated one time and washed with 1X wash buffer (Thermo Fischer, UK). Following each wash step, the plates were inverted and tapped onto absorbent paper to remove excess liquid. The coated plates were blocked with blocking buffer (Thermo Fischer, UK) for one hour at room temperature. The blocking buffer was

aspirated and then discarded. Experimental samples and standards in PBS were added to designated wells and were incubated for 90 minutes at room temperature. The contents were aspirated and the wells were washed thrice with 1X washing buffer. Biotinylated anti-GDNF (R&D systems, UK) in PBS at a concentration of 0.4 µg/mL was added to wells and incubated for two hours at room temperature. Contents were aspirated and then washed thrice with wash buffer before adding Streptavidin-HRP (Thermo Fischer, UK) at a dilution of 1:5000. Well plates were incubated for one hour at room temperature. The contents were aspirated and the wells washed thrice. 100 µl TMB substrate was added to wells and incubated for 20 minutes at room temperature. Stop solution (0.16 M sulfuric acid) was added and absorbance was read at 450 nm within 30 minutes of adding the Stop solution. Absorbance was also measured at 540 nm for wavelength correction. Samples were analysed from two independent experiments with triplicate used within experiments.

2.2.14 Statistical analysis

Statistical comparisons between groups were made using GraphPad Prism (version 10.0 for Windows; GraphPad Software, San Diego, CA). Significance was analysed using either a one-way ANOVA Tukey's multiple comparisons test, Kruskal-Wallis Dunn's multiple comparisons test or for comparison of two groups an unpaired parametric t-test was used and differences were considered significant when $p<0.05$.

2.3 Results

2.3.1 X-ray photoelectron spectroscopy (XPS) of allylamine plasma coated PCL films

XPS was performed to evaluate the elemental composition of the nano-surface layer of PCL films post allylamine plasma deposition and incubation in heparin sodium (50 µg/mL) and GDNF (100

ng/mL). Two areas (700 µm by 300 µm) were analysed for each sample. CASA XPS software was used to quantify peak intensities and positions on XPS spectra. For all PCL samples, expected elements are carbon and oxygen (unmodified PCL should include only these elements). For all surface modified PCL samples additional nitrogen is expected. Heparin and GDNF contain sulfur and are identified as such. Survey scans show all elements that are detected in the sample area however, high resolution scans include only elements which have been selected. Silicon contamination was seen in all samples analysed. It is possible this contamination comes from a silicon lubricant (polydimethylsiloxane; PDMS) present in the plastic syringes used to dispense the PCL solution onto glass coverslips for spin coating or PDMS contamination in the vacuum chamber. Figure 8 shows survey scans identified carbon and oxygen in all PCL samples at approximate peak positions 285 eV and 532 eV, respectively. In allylamine, heparin and GDNF coated PCL samples, survey scans also identified nitrogen presence at peak position ~400 eV. However, the peak position (168 – 169.9 eV) for sulfur was not present. The surface concentration of sulfur is around 0.2%, this is low and therefore not possible to detect as a peak on the survey scan spectra[273]. The silicone contamination is also likely to obscure the detection of the S 2p peak.

Table 4 shows the elemental surface composition of each PCL sample. Carbon to oxygen ratios (C/O) were calculated after carbon and oxygen percentages were adjusted for assumed silicon contamination. The expected C/O for pure PCL is 3. The calculated ratio for unmodified PCL was 3.6 suggesting that there is additional carbon contamination. In theory, if a homogenous layer of amine groups is deposited onto PCL *via* the carboxyl groups, the C/O should decrease as carbon is obscured from detection. The C/O of PCL post allylamine plasma modification decreased to 2.6 this may be due to amine groups obscuring the carbon chain of PCL however, the increased oxygen concentration in the plasma modified samples indicating oxygen contamination.

Heparin sodium has an expected C/O of 0.6. If there is a homogenous layer of amine groups deposited onto the PCL sample, successful heparin deposition should give rise to a homogenous layer of heparin. PCL samples coated with heparin were expected to have a slight decrease in C/O due to the higher number of oxygen atoms compared to carbon in heparin sodium. The calculated ratio was 2.9 which suggests that heparin is present but as a thin layer and/or non-homogenous. The nitrogen concentration decreases after heparin deposition compared to plasma modified PCL also indicating the presence of heparin due to the molecule binding *via* the amine groups and obscuring detection. After GDNF deposition all elements decrease in concentration and the C/O was calculated as 2.7 which is similar to the heparin functionalized PCL thus, it is not clear if GDNF was deposited. There was a very low concentration of sulfur detected for heparin and GDNF functionalized PCL samples which further suggests that a thin/non-homogenous layer of heparin was deposited.

High resolution scans of the C 1s region further supports evidence that oxygen contamination was introduced during the allylamine plasma deposition process. Figure 9 shows a representative high resolution C 1s spectra of unmodified PCL, allylamine plasma, heparin and GDNF functionalized PCL films. It is observed in literature that the oxygen-to-carbon ratio (O/C) should decrease and the nitrogen concentration increase post allylamine plasma treatment[274]. Allylamine plasma functionalized PCL had an O/C of 0.39 which is higher than that of pure PCL (0.28) this is indicative of oxygen contamination (table 4). Theoretically, if the deposition of amine groups was non-uniform or at a low concentration, the O/C should be similar to that of pure PCL. Further evidence of oxygen contamination is the high atomic percentage (19 %) of carbonyl groups introduced post allylamine plasma modification (table 5). Research suggests the process introduces carbonyl groups but at a low concentration. It is observed in previous research that typically a low

concentration of oxygen is introduced during allylamine plasma deposition as it is likely that there is a small amount of water vapour in the plasma chamber. In addition, when removing samples from the chamber it is likely that any reactive species left on the surface will react with the air[274, 275]. In the literature, the peak corresponding to the ester bond (binding energy approx. 289 eV) typically present in pure PCL is observed to disappear post allylamine plasma treatment[275]. However, high resolution scans of the C 1s spectra for allylamine plasma treated samples show the peak for the ester bond and was calculated as 15.6% of the atomic percentage (figure 9 and table 5) similar to that of pure PCL (16%). This is indicative of either oxygen contamination and/or a thin/non-homogenous layer of amine groups upon the surface.

To confirm the successful deposition of amine groups, high resolution scans of the N 1s region was performed. Figure 11 shows a representative high resolution N 1s spectra of PCL films exposed to allylamine plasma. In the N1s spectra two peaks were identified at approx. 400 and 402 eV corresponding to unprotonated amine and protonated amine, respectively[276, 277]. The peak at 402 eV is not present in PCL films functionalized with heparin sodium and GDNF solution, suggesting that heparin and GDNF are bound to the sample *via* the positively charged amine groups. The nitrogen concentration decreases from 9.6% for allylamine plasma exposed PCL films to 4.1% for GDNF functionalized PCL films similar to effects seen in a study by Sandoval-Castellanos *et al.*[198] (table 4). Figure 12 shows the representative high resolution S 2p spectra of PCL films functionalized with heparin sodium and GDNF solution whilst table 8 gives the atomic percentage of S 2p orbitals present in the samples. The spectra indicates a low concentration of sulfur in samples as the peaks are not clear in addition to a weak and noisy signal[273]. Thus, it is unlikely that heparin and GDNF have been deposited at a high concentration.

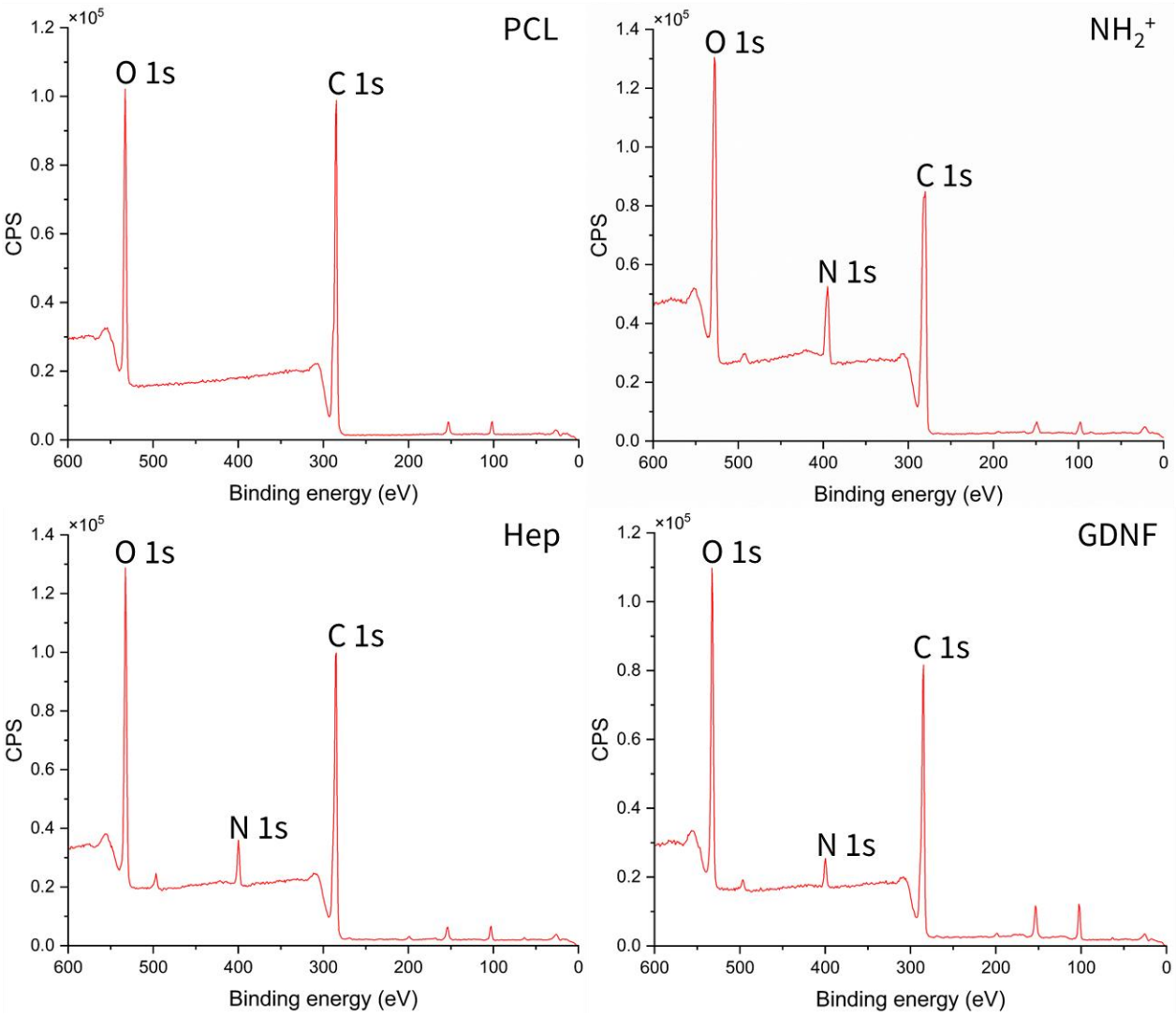

Figure 8. Wide survey scans of unmodified and allylamine plasma functionalized PCL films. Unmodified PCL (PCL), allylamine plasma polymerised (NH_2^+), plasma modified plus 50 µg/mL heparin (heparin) and plasma modified plus heparin and 100 ng/ml GDNF (GDNF).

Table 4. Surface composition of unmodified PCL and surface modified PCL films using allylamine plasma deposition determined from survey scans.

Sample	Surface composition (at%)					
	C	O	N	S	C/O	O/C
PCL	72.3	20.3	>0.1	>0.1	3.6	0.28
PCL-NH_2^+	58.7	22.6	9.6	>0.1	2.6	0.39
PCL-Heparin	61.6	21.1	5.7	0.2	2.9	0.34
PCL-GDNF	48.3	17.8	4.1	0.1	2.7	0.37

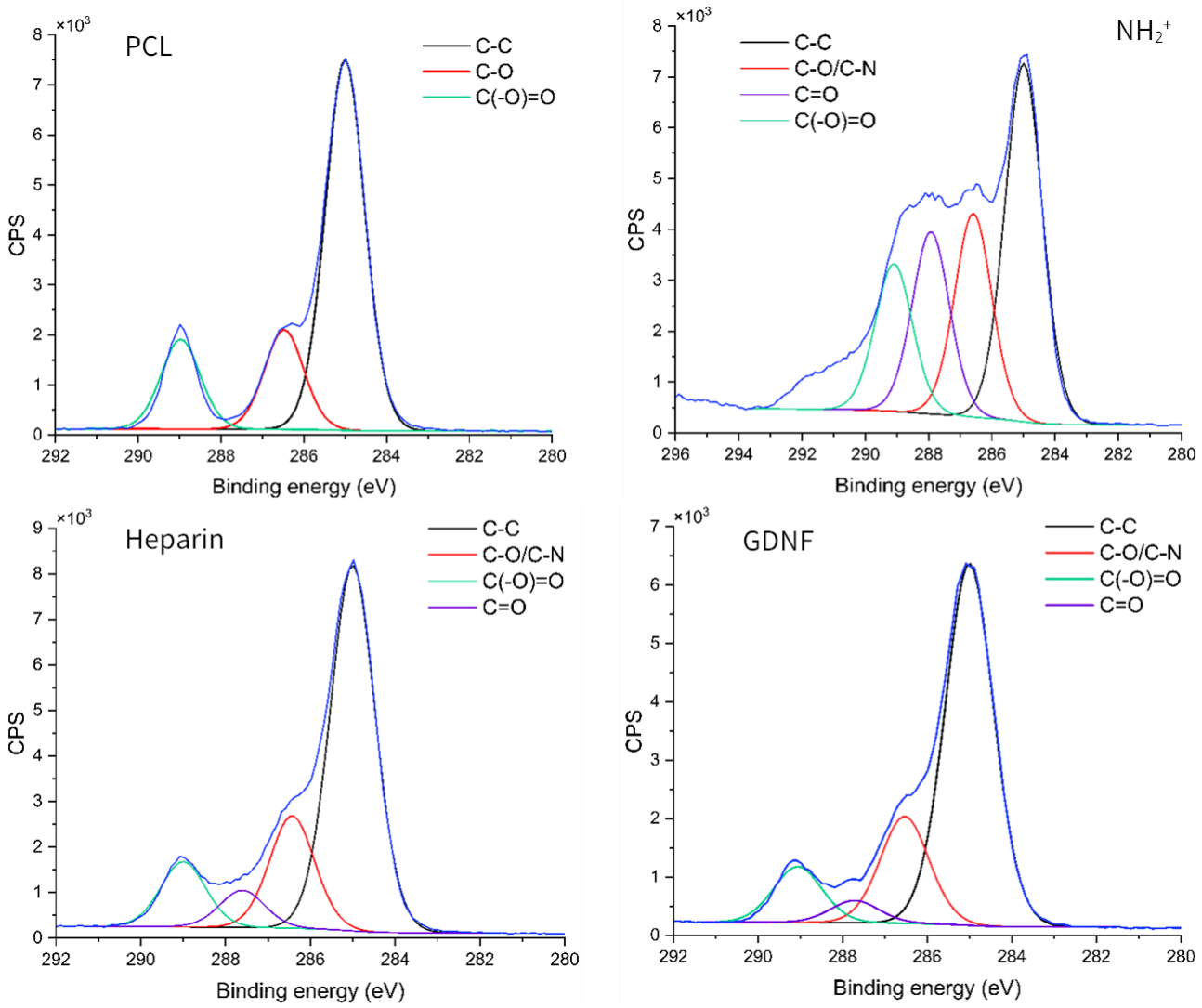

Figure 9. Representative C 1s spectra determined by high resolution scans of allylamine plasma modified PCL films and PCL control.

Table 5. Atomic percentage (At %) of carbon species determined by high resolution scans of the C 1s region of unmodified and allylamine plasma surface modified PCL films.

Sample	C-C		C-O/C-N		C=O		O-C=O	
	BE (eV)	At %	BE (eV)	At %	BE (eV)	At %	BE (eV)	At %
PCL	285	66.2	286.5	17.8	-	-	289	16
PCL-NH_2^+	285	37.8	286.6	21.5	287.9	19.3	289.1	15.6
PCL-Heparin	285	63	286.4	19.4	287.6	6.4	289	11.3
PCL-GDNF	285	66.1	285.5	19.6	287.7	4.1	289.1	10.2

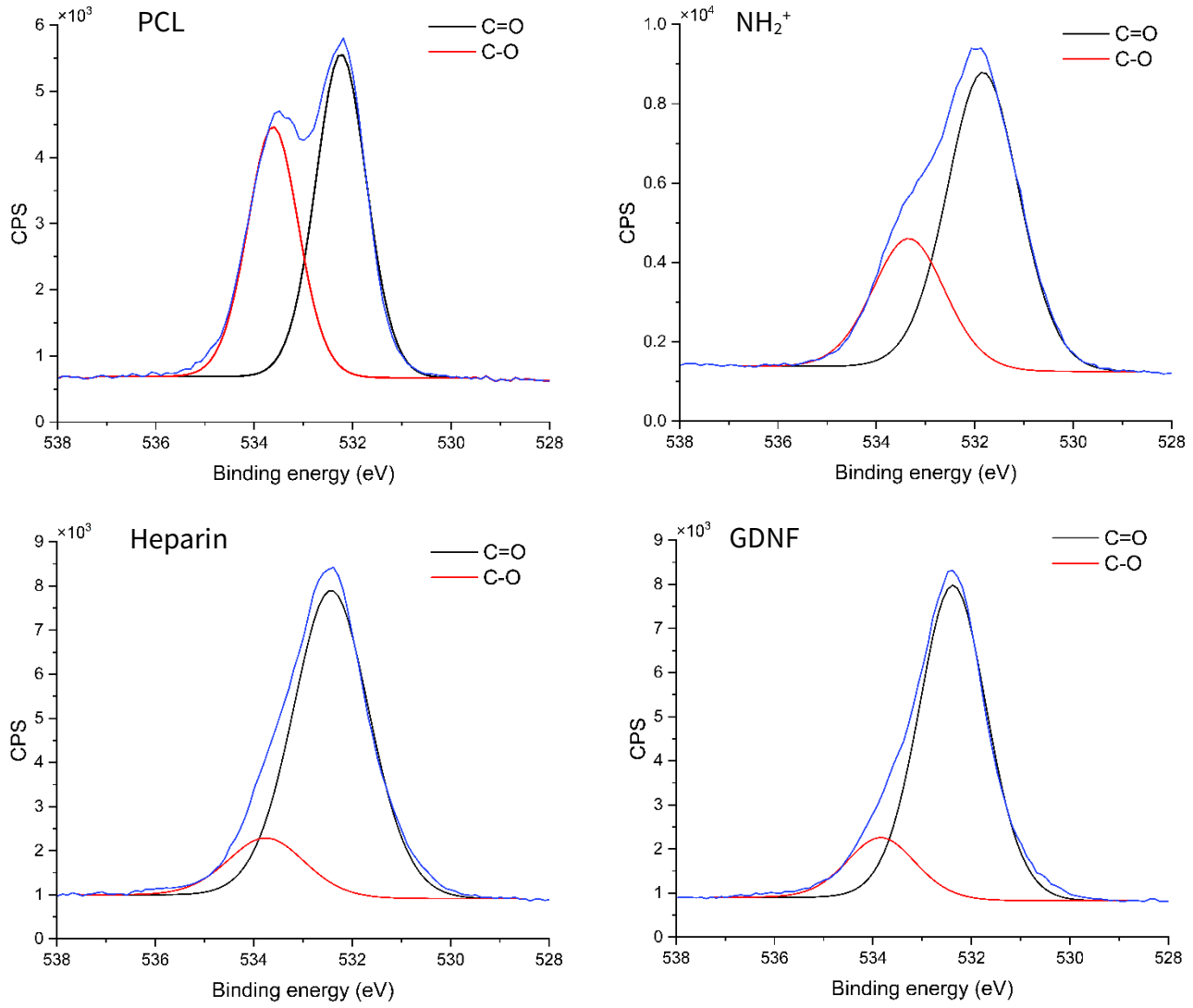

Figure 10. O 1s spectra determined by high resolution scans of allylamine plasma modified PCL films versus PCL control.

Table 6. Atomic percentage of oxygen species determined by high resolution scans of the O 1s region of unmodified and allylamine plasma surface modified PCL films.

Sample	**C=O**		**C(O)-O**	
	Binding energy (eV)	at%	Binding energy (eV)	at%
PCL	532.2	56	533.6	44.1
PCL-NH_2^+	532.2	52.2	533.7	31.8
PCL-Heparin	532.4	84.2	533.8	15.8
PCL-GDNF	532.4	84	533.8	16.1

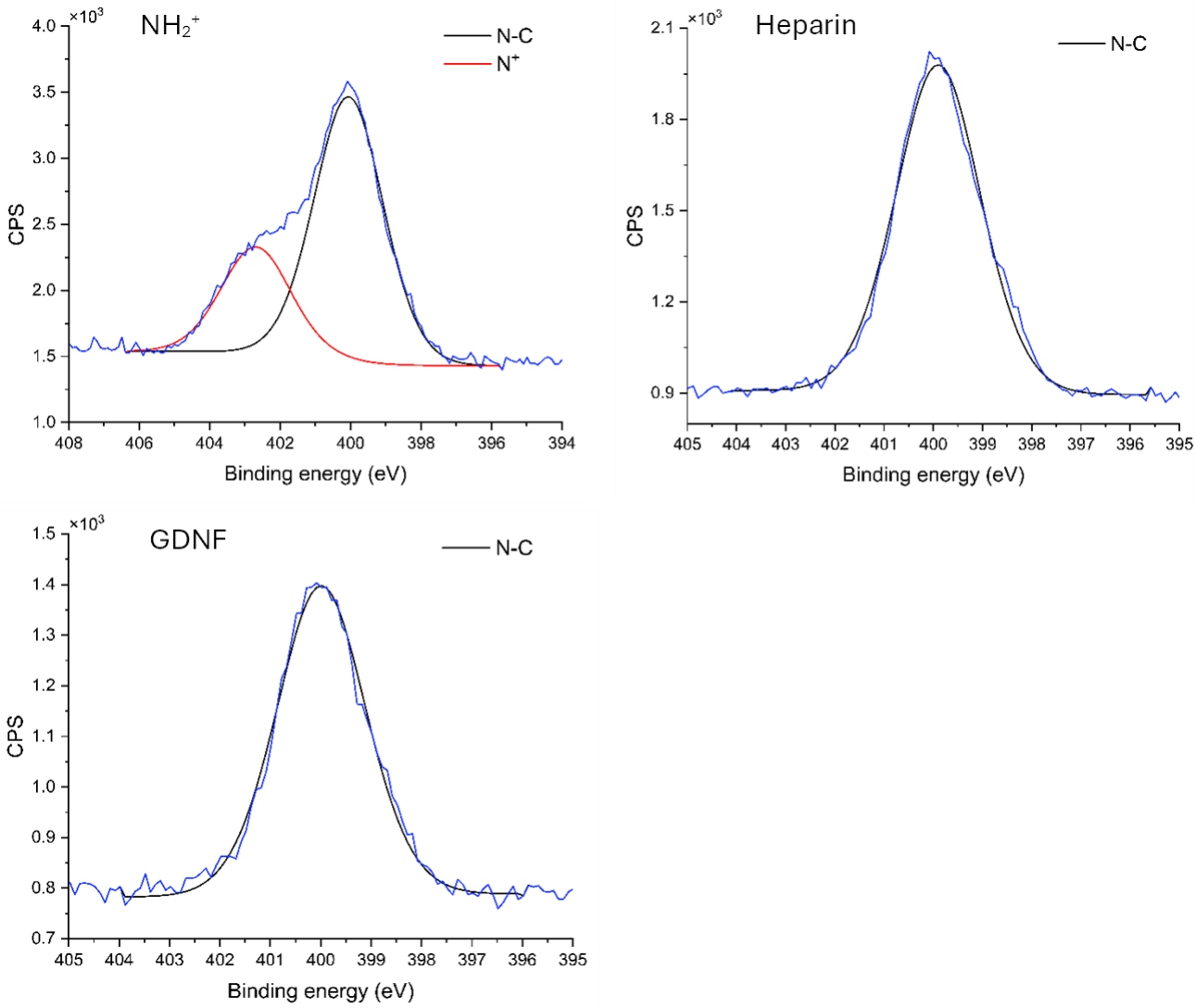

Figure 11. N 1s spectra determined by high resolution scans of allylamine plasma surface modified PCL films.

Table 7. Atomic percentage of nitrogen species determined from high resolution scans of the N 1s region of unmodified and allylamine plasma surface modified PCL films.

Sample	**N-C/N-C=O**		**N^+**	
	Binding energy (eV)	at%	Binding energy (eV)	at%
PCL	-	-	-	-
PCL-NH_2^+	400.1	71.3	402.7	28.7
PCL-Heparin	399.9	100	-	-
PCL-GDNF	400	100	-	-

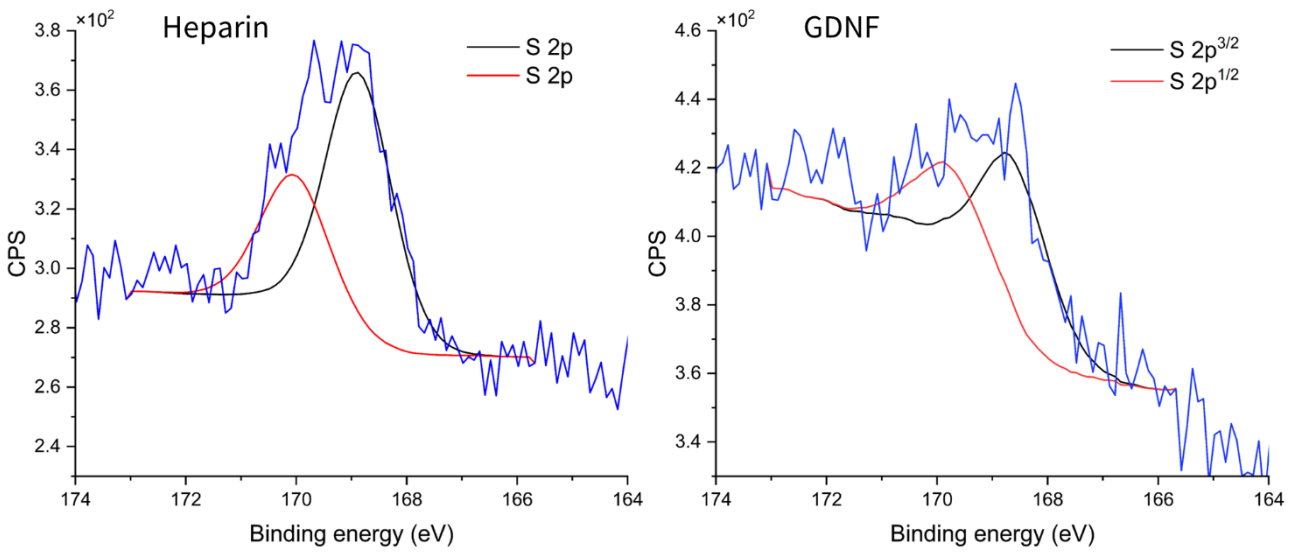

Figure 12. S 2p spectra determined by high resolution scans of allylamine plasma modified PCL films treated with heparin (50 µg/ml) and GDNF (100 ng/ml).

Table 8. Atomic percentage of S 2p orbitals determined by high resolution scans of heparin and GDNF functionalized PCL films.

Sample	**S 2p$^{3/2}$**		**S 2p$^{1/2}$**	
	Binding energy (eV)	at%	Binding energy (eV)	at%
PCL	-	-	-	-
PCL-NH_2^+	-	-	-	-
PCL-Heparin	168.9	66.7	170	33.3
PCL-GDNF	168.6	66.7	169.8	33.3

2.3.2 XPS of allylamine plasma modified TCP

To investigate the oxygen contamination of previous PCL film samples, allylamine plasma deposition on 35 mm diameter tissue culture petri dishes was performed to determine if there was a leak in the plasma deposition reaction chamber. A study by Girardeaux and Pireaux describes what is typically expected for a C 1s spectrum of pure polystyrene[278]. They observed peaks at approximate positions, 284.7 and 285.0 eV corresponding to carbons in different hybridisation states, sp^2 (aromatic carbon in benzene ring) and sp^3 (aliphatic carbon), respectively. In addition, they also observed a peak at position 291.3 eV corresponding to a shake-up feature which is due

to the π-π* transition expected with sp^2 hybridised carbon. These positions were observed in TCP samples analysed in addition to extra peaks at positions approximately 286, 287 and 289 eV which correspond to oxygen functionalized carbon indicating the TCP has been air plasma treated during manufacture. The sp^2 to sp^3 ratio of TCP samples (0.99) showed that the TCP is polystyrene. It was also observed that the sp^2 (graphitic) carbon reduced after allylamine plasma.

Battiston *et al.* describes what is typically expected for a C 1s spectrum of commercially available TCP from manufacturers such as Sarstedt, BD and Wisent[279]. Battiston *et al.* shows that the concentrations of functional groups present in commercially available TCP differ slightly between manufacturers. For this study, well bottoms were removed from CELLSTAR® 48-well plates manufactured by Greiner BIO-ONE. The concentration of groups identified in Battiston *et al.* were similar to those in TCP samples analysed (table 10 and 11). However, one additional peak was observed at 287 eV corresponding to carbonyl or imine. This is possibly due to different plasma modification methods manufacturers use to treat the TCP.

Figure 14 shows the deconvoluted C 1s spectra determined from high resolution scans of TCP and allylamine plasma modified TCP. Post allylamine plasma treatment, the concentration of ester groups seems to increase as the identifying peak at 289.0 eV increases. This is indicative of oxygen contamination present in allylamine plasma modified TCP samples and samples have not been deposited with a uniform layer of amine groups. Figure 16 shows the deconvoluted N 1s spectrum determined from the high resolution scans of allylamine plasma modified TCP. The N 1s peaks further indicate oxygen contamination as although non-protonated amine was detected (approx. 400 eV), a second peak was observed for the N 1s region at peak position 406 eV which is assigned to nitrate. Table 13 shows the atomic concentration of nitrogen species calculated using high resolution scans of TCP and allylamine plasma modified TCP. The O/C calculated for allylamine

plasma modified TCP samples was 0.14 which is higher than the O/C for unmodified TCP (0.12). As mentioned in section 2.3.1, the oxygen concentration is not expected to increase post allylamine plasma treatment[274]. The oxygen concentration is expected to decrease as amine groups that are deposited obscure detection of the polymer chain. The chemical formula for allylamine is C_3H_7N, thus if the reaction chamber is filled with 100% allylamine plasma there should be no oxygen present. This oxygen increase suggests contamination from possible sources such as air getting into the reaction chamber, water vapour present in the chamber and/or reactive species remaining on the surface and reacting with the water vapour in the air upon removal from the reaction chamber. Based on these results, it was decided that the method of using allylamine plasma to deposit protonated amine groups on the surface of PCL was not reliable nor reproducible for binding heparin and GDNF.

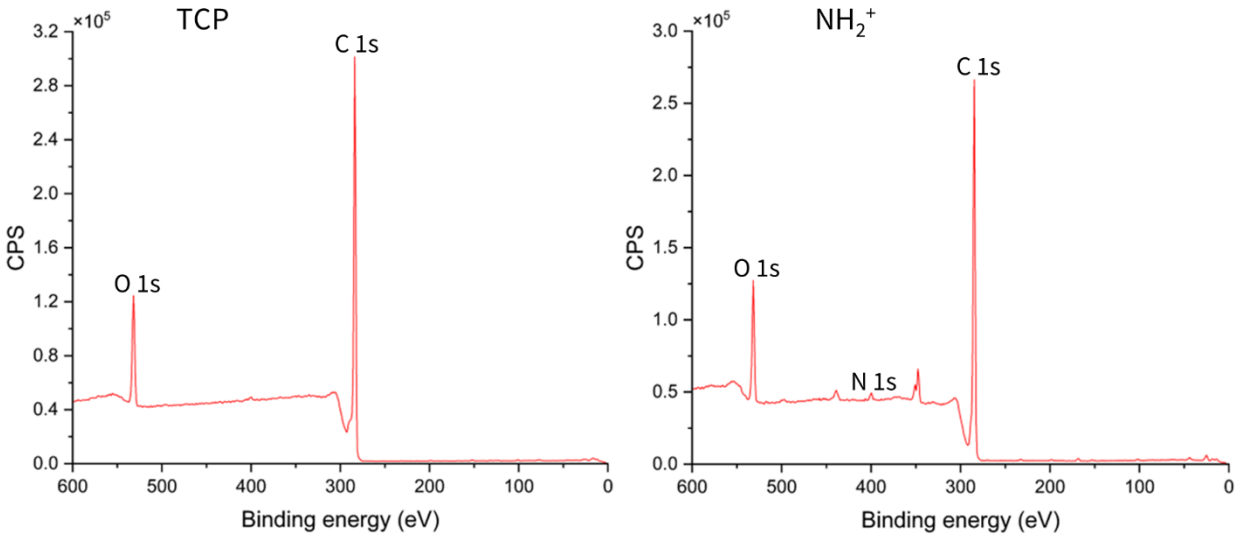

Figure 13.Wide survey scans of unmodified TCP and TCP-NH_2^+.

Table 9. Surface composition of TCP and allylamine plasma modified TCP determined from survey scans.

	Surface composition (at%)			
Sample	C	O	N	O/C
TCP	89.2	10.8	<0.1	0.12
TCP-NH_2^+	86.5	11.9	1.7	0.14

Table 10. Atomic percentage of carbon species in TCP from different manufactures determined from C 1s spectra. Modified from Battiston et al., 2012[279].

Manufacturer	C-C	C-O	C(-O)=O	π-π satellite
Sarstedt	60.3 ± 0.2	21.2 ±0.1	16.8 ± 0.1	1.8 ± 0.2
BD	87.7 ± 0.5	7.2 ± 0.8	2.1 ± 0.9	3.0 ± 0.2
Wisent	86.0 ± 0.5	6.7 ± 0.4	5.2 ± 0.5	2.1 ± 0.2

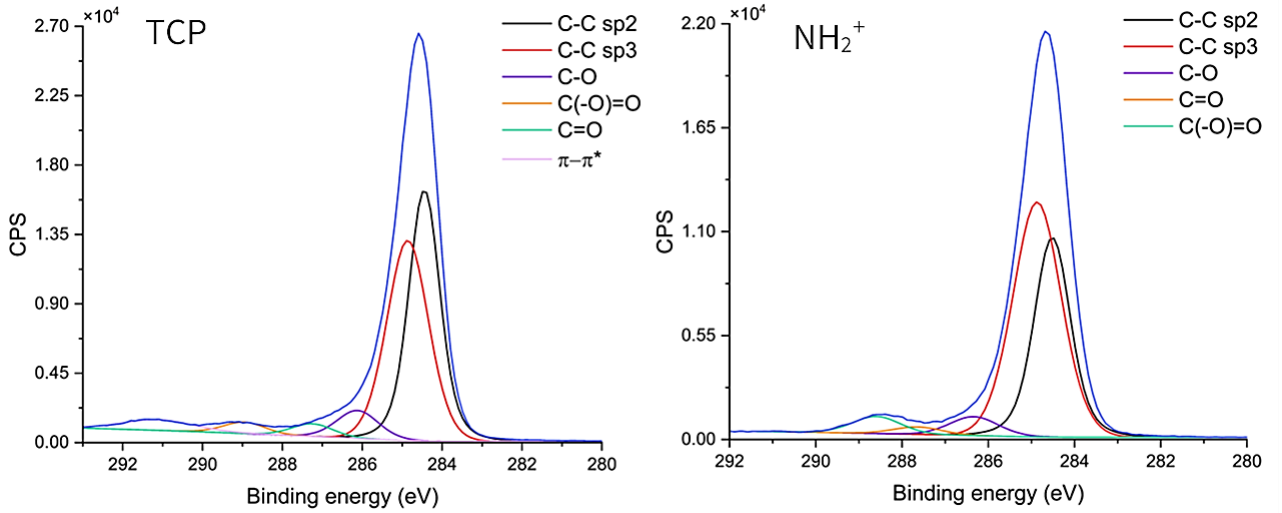

Figure 14. Representative C 1s spectra determined by high resolution scans of unmodified TCP and allylamine plasma modified TCP (NH_2^+).

Table 11. Atomic percentage of carbon species present on the surface of TCP and allylamine plasma modified TCP.

	C-C sp^2		C-C sp^3		C-O/N		C=O/C=N		C(-O/N)=O		π-π satellite	
Sample	**BE (eV)**	**at%**	**BE (eV)**	**at%**	**BE (eV)**	**at%**	**BE (eV)**	**at%**	**BE (eV)**	**at%**	**BE (eV)**	**at%**
TCP	284.5	42.3	284.9	42.7	286.1	6	287.3	2.7	289	2.4	291.1	3.9
TCP-NH_2^+	284.5	36.2	284.9	53.9	286.3	4.4	287.6	1.7	288.6	3.9		

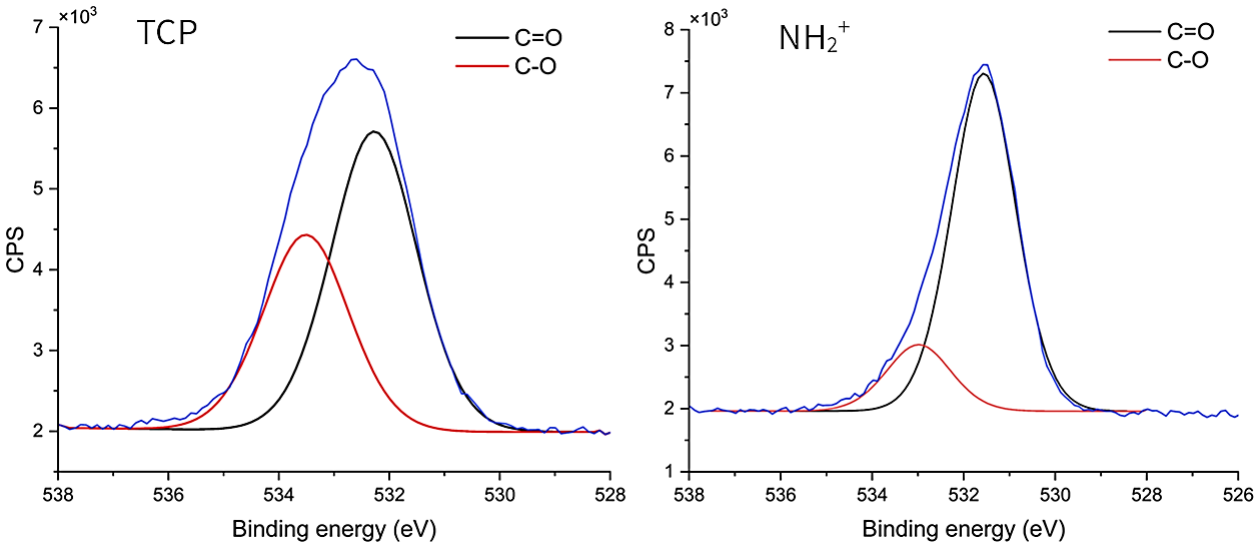

Figure 15. Representative O 1s spectra determined by high resolution scans of TCP and allylamine plasma modified TCP (NH_2^+).

Table 12. Atomic percentage of oxygen species determined from high resolution scans of the O 1s region of TCP and allylamine plasma modified TCP.

	C=O		C-O	
Sample	**BE (eV)**	**at%**	**BE (eV)**	**at%**
TCP	532.3	60.5	533.2	39.5
TCP-NH_2^+	531.6	83.6	533	16.5

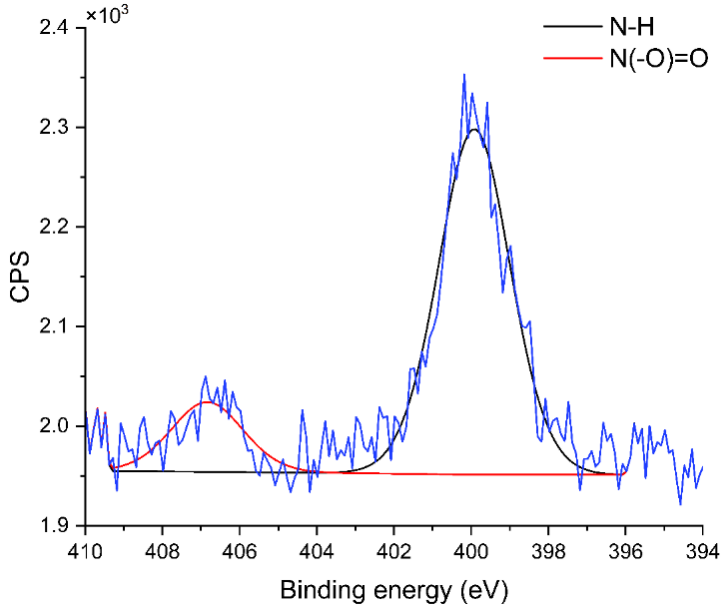

Figure 16. Representative N 1s spectra determined by high resolution scans of allylamine plasma modified TCP.

Table 13. Atomic percentage of nitrogen species determined from high resolution scans of the N 1s region of TCP and allylamine plasma modified TCP.

	N-C/N-C=O		NO_3	
Sample	**BE (eV)**	**at%**	**BE (eV)**	**at%**
TCP	400.2	100		
TCP-NH_2^+	399.9	83.2	406.8	16.8

2.3.3 XPS of air and argon plasma treated PCL films

Four groups of plasma modified PCL films were analysed by XPS to determine which parameters lead to the highest concentration of hydroxyl groups on the PCL surface. The four groups analysed were PCL films modified with air or argon plasma at 10 or 50 W discharge power. Silicon contamination was detected post air plasma modification, indicating that the process introduces the contaminant as silicone was not present in untreated PCL samples analysed. The deconvolution of the C 1s spectra (figure 18) of untreated PCL gave peaks at approx. 285, 286 and 289 eV correlating with the literature[280, 281]. For both air and argon plasma modified PCL an additional peak at ~287 eV is identified corresponding to the carbonyl group (C=O) conforming with the literature[280, 281]. Carbon to oxygen (C/O) and oxygen to carbon (O/C) ratios were calculated after carbon and oxygen percentages were adjusted for silicon contamination. PCL films modified with air plasma at 50 W had the highest O/C, followed by PCL modified with argon plasma at 10 W which correlates with the surface composition determined from wide survey scans of the modified PCL samples (figure 17). PCL modified with air at 50 W had the highest atomic percentage of oxygen, followed by PCL modified with argon plasma at 10 W. However, as the aim was to determine the optimal parameters for incorporating hydroxyl groups, the O/C is not necessarily indicative of the optimal parameters. An increase in single carbon-to-oxygen bonds is the most useful indication of parameters which give rise to higher concentrations of hydroxyl groups incorporated at the surface of PCL chain. High resolution scans of the C 1s region (figure 18)

showed that the carbon-to-carbon bond decreases, whilst the carbon-to-oxygen bond increases for PCL modified with air or argon plasma at 10 W. In contrast, the atomic percentage of carbon-to-oxygen bonds decreased for PCL films modified with air or argon plasma at 50 W (figure 17, table 14). This correlates with the higher intensity of the peak at 533.7 eV (assigned to the carbon-to-oxygen bond) deconvoluted from the high resolution scans of the O 1s region of PCL films modified with air plasma or argon plasma at 10 W (figure 19, table 16). Furthermore, the atomic percentage of the carbonyl bond seemed to increase with the increase in discharge power (10 to 50 W) (table 16). The atomic percentage of the ester group decreased with the increase in discharge power (table 16) further indicating that the higher discharge powers lead to less incorporation of hydroxyl groups.

A small amount of nitrogen was detected on plasma modified PCL compared to untreated PCL. This is expected in films exposed to air plasma however, it isn't expected to be present in samples exposed to argon plasma[280-282]. The atomic percentage of nitrogen detected was low, approximately 0.3% for all plasma modified samples. High resolution scans of the N 1s region of films modified with air or argon plasma at 50 W show protonated nitrogen species (peak position ~ 402 eV) present on the surface whereas this peak was not detected in films modified at a lower discharge power (figure 20).

The surface composition of air or argon plasma modified PCL determined from XPS is only indicative of potential optimal parameters for incorporation of long chain amino-silanes used in this study (*i.e.* N^1-(3-trimethoxysilylpropyl)diethylenetriamine and 11-aminoundecyltriethoxysilane), onto the PCL surface. Further analysis was required to determine which plasma treatments lead to the highest incorporation of N^1-(3-

trimethoxysilylpropyl)diethylenetriamine *via* a Ninhydrin assay which indirectly measures the concentration bound to PCL.

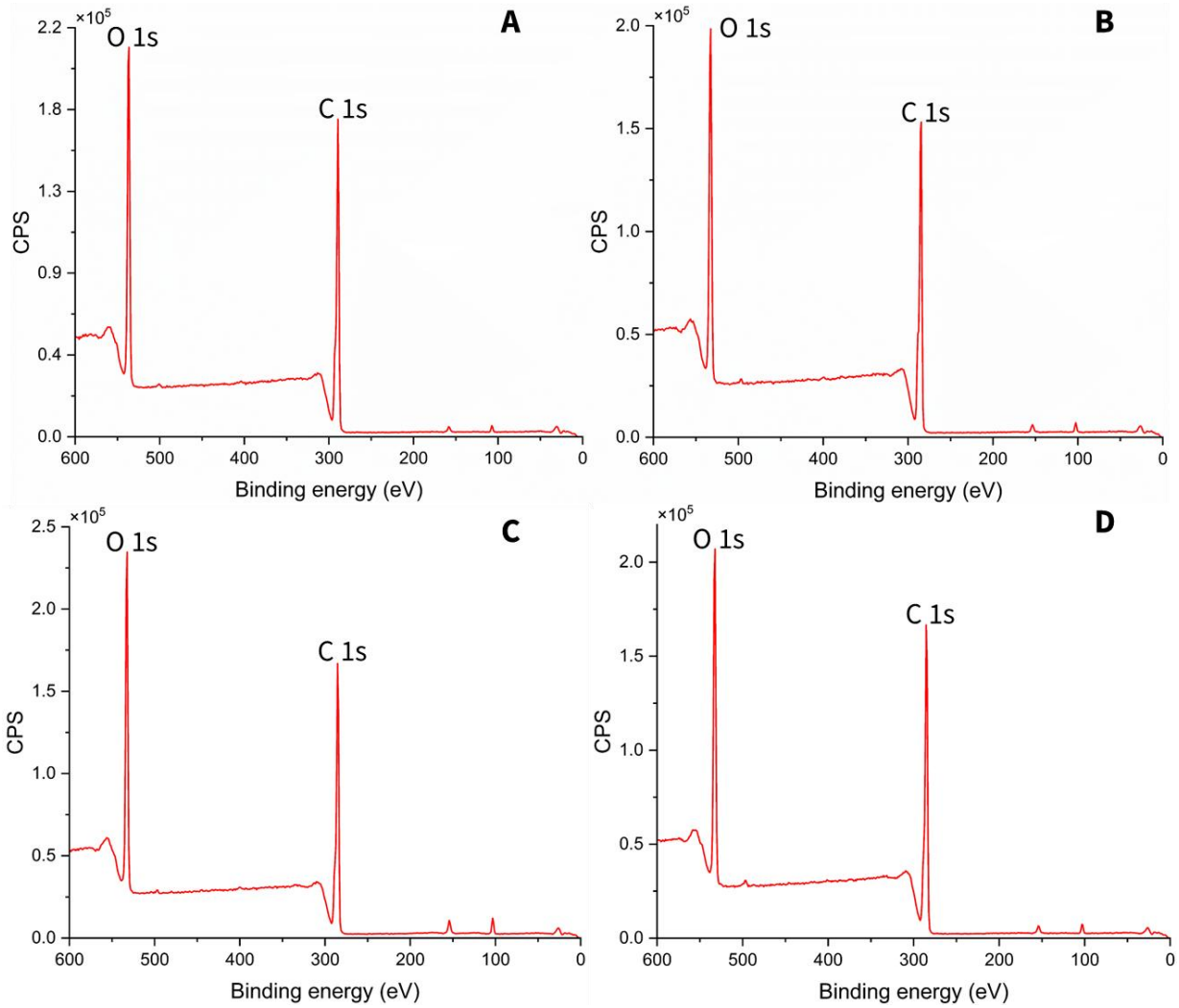

Figure 17. Surface composition of surface modified PCL determined from wide survey scans. Air plasma 10 W (a) , argon plasma 10 W (b), air plasma 50 W (c) and argon plasma 50 W (d).

Table 14. Surface composition, oxygen-to-carbon and carbon-to-oxygen ratios of PCL and PCL modified with air or argon (Ar) plasma at 10 or 50 W.

	Surface composition (at %)				
Sample	**C**	**O**	**N**	**O/C**	**C/O**
PCL	75.5 ± 0.1	24.6 ± 0.1	-	0.33	3.10
PCL Air 10W	70.5 ± 0.4	29.2 ± 0.4	0.30	0.42	2.40
PCL Air 50W	69.3 ± 0.1	30.4 ± 0.1	0.4 ± 0.1	0.46	2.20
PCL Ar 10W	69.7 ± 1.3	30.1 ± 1.4	0.3 ± 0.1	0.44	2.30
PCL Ar 50W	71.1 ± 1.0	28.5 ± 1.0	0.4 ± 0.1	0.41	2.50

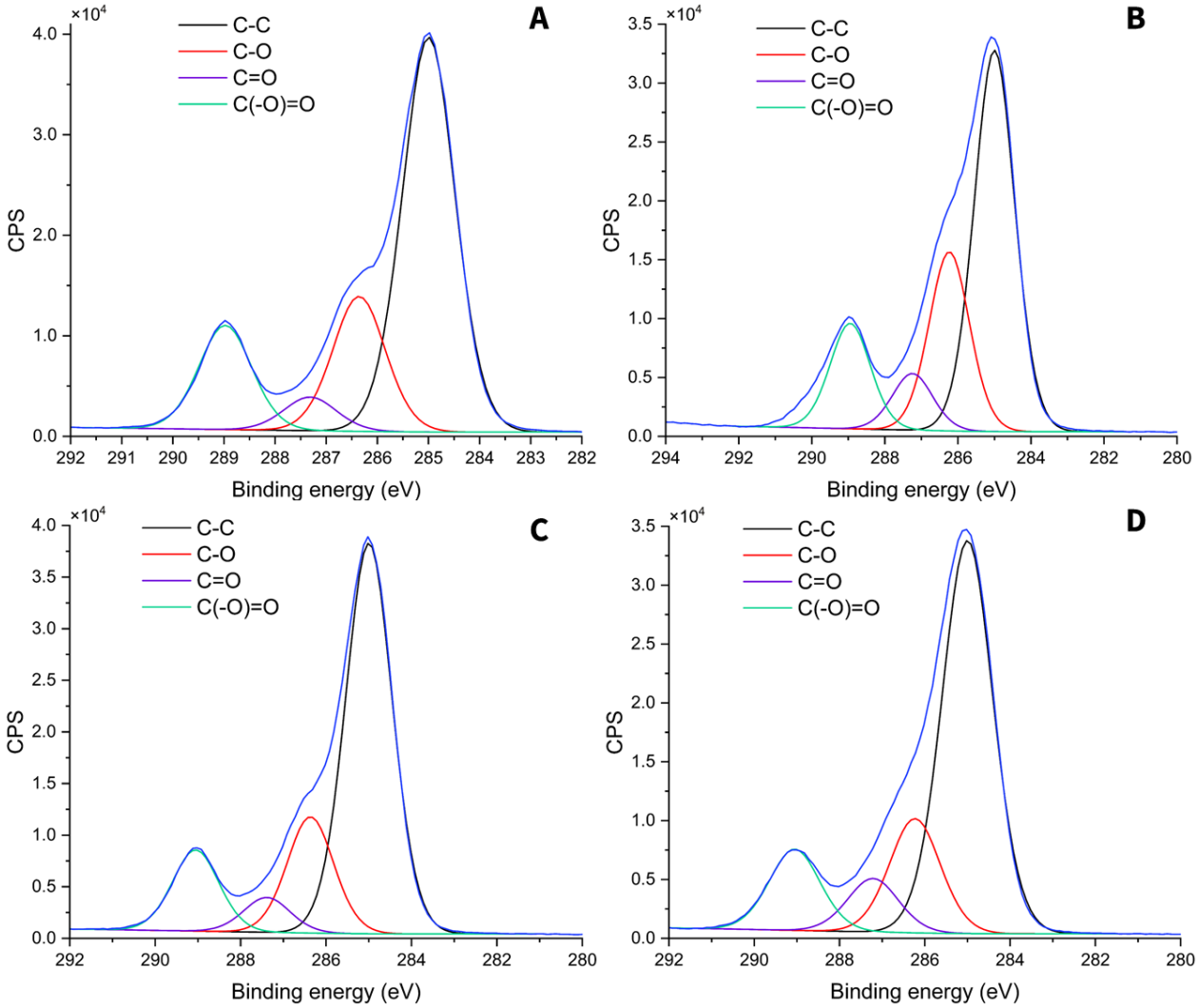

Figure 18. Deconvolution of C 1s region of plasma modified PCL films determined from high resolution scans. Air plasma 10 W (a) , argon plasma 10 W (b), air plasma 50 W (c) and argon plasma 50 W (d).

Table 15. Atomic concentration (% At) of carbon species determined from high resolution scans of the C 1s region of PCL and PCL modified with air or argon (Ar) plasma at 10 or 50 W.

	C-C		**C-O**		**C=O**		**C(-O)=O**	
Sample	B.E (eV)	% At	B.E (eV)	% At	B.E (eV)	% At	B.E (eV)	% At
PCL	285	63.6	286.4	19.7	-	-	289	16.7
PCL Air 10 W	285	59.6 ± 0.7	286.4	20.2 ± 0.1	287.3	4.8 ± 0.4	289	15.5 ± 0.2
PCL Air 50 W	285	63.2 ± 0.7	286.4	17.5 ± 1.8	287.3	6.4 ± 1.1	289	13.0
PCL Ar 10 W	285	55.2 ± 5.6	286.4	22.1 ± 2.8	287.3	6.0 ± 2.3	289	15.3 ± 1.5
PCL Ar 50 w	285	61.5 ± 0.4	286.4	18.6 ± 1.1	287.3	7.4 ± 1.5	289	12.7 ± 0.1

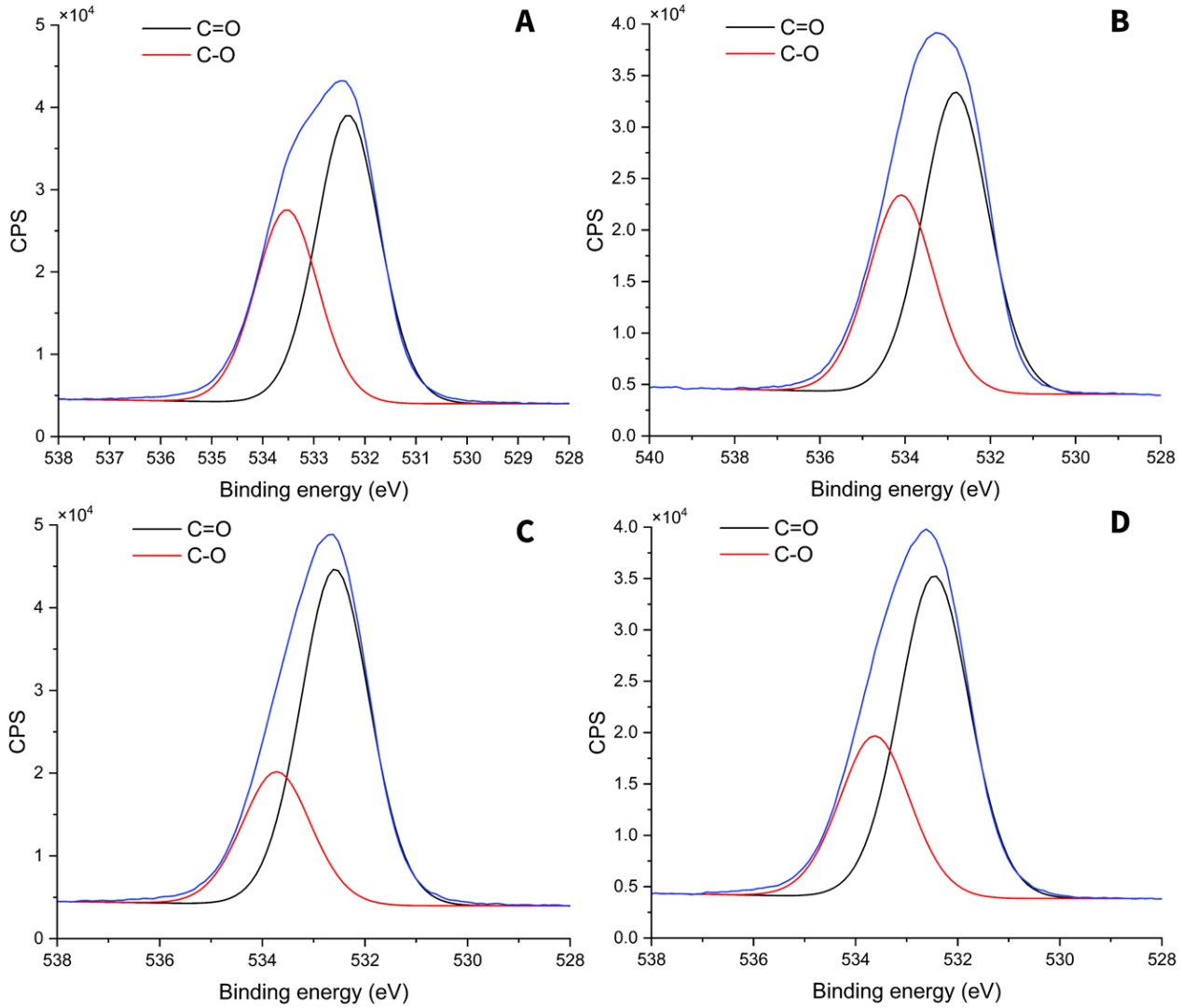

Figure 19. Deconvolution of O 1s region of plasma modified PCL films determined from high resolution scans. Air plasma 10 W (a) , argon plasma 10 W (b), air plasma 50 W (c) and argon plasma 50 W (d).

Table 16. Atomic concentration (% At) of oxygen species determined from high resolution scans of the O 1s region of PCL and PCL exposed to air or argon (Ar) plasma at 10 or 50 W.

	C=O		**C-O**	
Sample	B.E. (eV)	% At	B.E. (eV)	% At
PCL	532.5	50.0 ± 0.1	533.7	50.0 ± 0.1
PCL Air 10 W	532.5	61.1 ± 1.6	533.7	39.0 ± 1.6
PCL Air 50 W	532.5	72.5 ± 1.1	533.7	27.6 ± 1.2
PCL Ar 10 W	532.5	61.1 ± 0.9	533.7	39.0 ± 0.9
PCL Ar 50 W	532.5	68.1 ± 2.1	533.7	31.9 ± 2.1

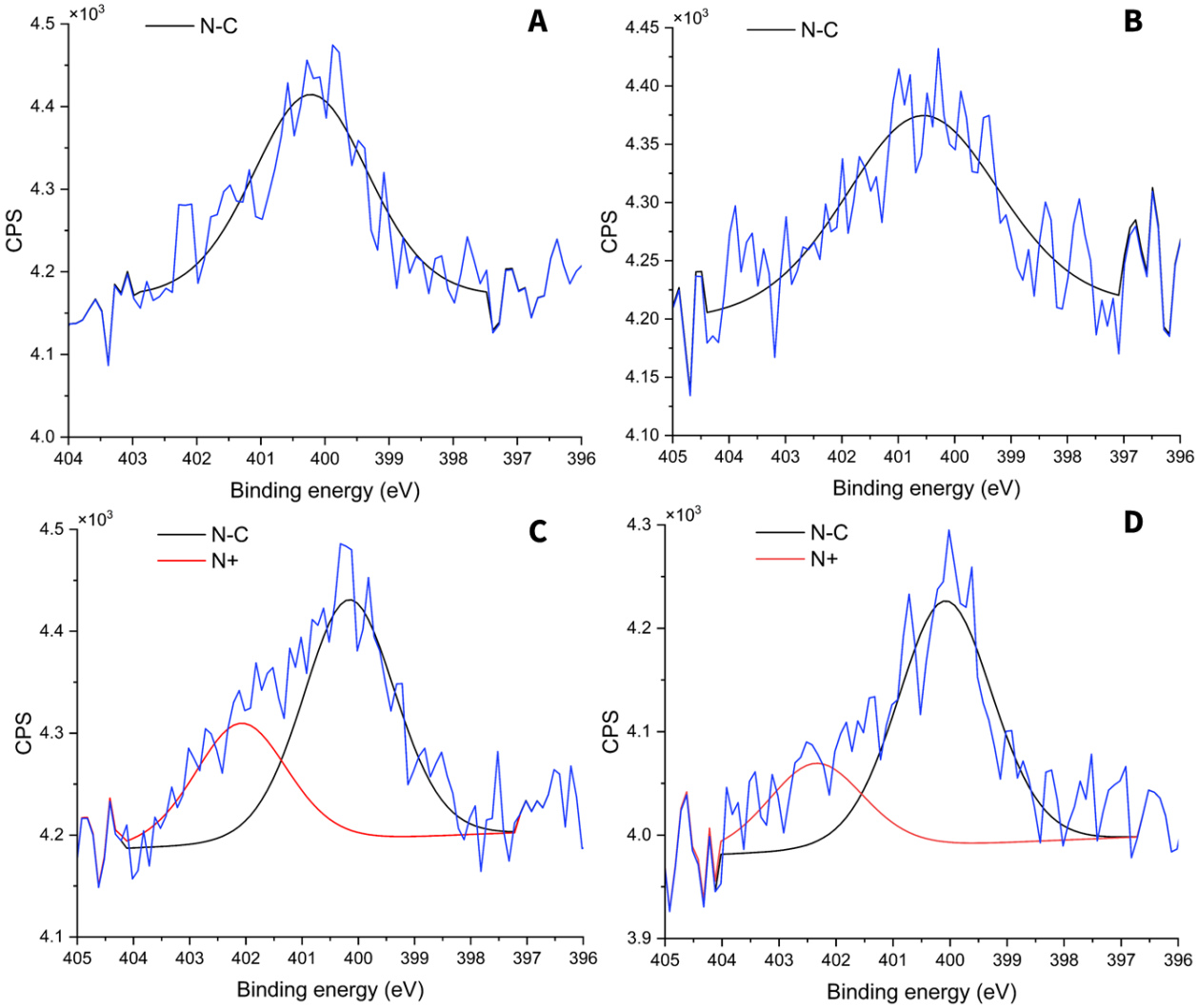

Figure 20. Deconvolution of N 1s region of plasma modified PCL determined from high resolution scans. Air plasma 10 W (a) , argon plasma 10 W (b), air plasma 50 W (c) and argon plasma 50 W (d).

Table 17. Atomic concentration (% At) of nitrogen species determined from high resolution scans of the N 1s region of PCL and PCL exposed to air or argon (Ar) plasma at 10 or 50 W.

	N-C		**N^+**	
Sample	B.E. (eV)	% At	B.E. (eV)	% At
PCL Air 10 W	400.0	100.0	402.0	-
PCL Air 50 W	400.0	64.8 ± 2.5	402.0	35.2 ± 2.5
PCL Ar 10 W	400.0	100.0	402.0	-
PCL Ar 50 W	400.0	75.2 ± 2.1	402.0	24.8 ± 2.1

2.3.4 Optimising plasma treatment for silane surface modification of PCL

Based on the XPS results of allylamine modified PCL films and TCP (see 2.3.1-2), a different method of surface functionalizing PCL was investigated. The oxygen contamination could not be reduced and lead to the formation of undesired nitrogen species on the surface layer. This in turn affects the success of heparin and GDNF deposition.

Air and argon plasma was evaluated as a method of exposing hydroxyl groups of the PCL chain for silane surface modification. A colorimetric Ninhydrin assay was utilised to determine the optimal power and gas for binding 11-aminoundecyltriethoxysilane. PCL films were exposed to air or argon plasma at 10, 25 and 50 W discharge power in a Zepto plasma chamber. Samples were then incubated in 11-aminoundecyltriethoxysilane in 95 % propan-2-ol for two hours at room temperature on a rocker. Samples were incubated in 0.35 % (wt/v) Ninhydrin salt in 100 % ethanol for 10 minutes at 90 °C. As the Ninhydrin salt reduces amine groups an observable colour transition occurs from clear to blue/purple which absorbs light at a wavelength of 562 nm allowing an indirect measure of aminosilane bound to the sample. The intensity of the colour is proportional to the concentration of amine groups present in the sample. Figure 21 shows the absorbance values of PCL films exposed to air or argon plasma at 10, 25 and 50 W prior to incubation in 11-aminoundecyltriethoxysilane. PCL exposed to air plasma at 10 W for two minutes prior to silane incubation gave significantly higher absorbance values compared to all other groups tested. Samples exposed to air plasma at 50W gave the lowest absorbance compared to all other groups tested. There were no significant differences between absorbance values of samples exposed to air at 25 and 50 W compared to argon plasma at 10, 25 and 50 W power.

To improve the cost effectiveness of the modification method, the use of another long chain aminosilane N^1-(3-trimethoxysilylpropyl)diethylenetriamine was explored as a potential cheaper alternative to 11-aminoundecyltriethoxysilane. Figure 22 shows absorbance values of PCL films exposed to air plasma at 10 W and 25 W discharge power prior to incubation in N^1-(3-trimethoxysilylpropyl)diethylenetriamine. Higher absorbance values were measured for PCL samples exposed to air at 10 W plasma prior to incubation compared to samples exposed to air at 25 W indicative of a higher concentration of N^1-(3-trimethoxysilylpropyl)diethylenetriamine. However, there was no significant difference between absorbance values of PCL films exposed to air at 10 or 25 W.

The use of autoclave/ethylene oxide sterilisation bags to hold PCL fibres during air plasma modification was explored as a potential method of maintaining sample sterility for cell culture. These bags were utilised as they are gas permeable. As plasma modification is under vacuum it sterilises the sample during the process, thus whilst in sealed sterilisation bags, samples retain sterile during transport to culture cabinets. PCL fibres were surface modified with N^1-(3-trimethoxysilylpropyl)-diethylenetriamine as described in methods section 2.2.4-5. Before air plasma deposition PCL fibres were sealed in sterilisation bags used for autoclaving/ethylene oxide sterilisation. PCL fibres were also put in an open petri dish as a control. A colorimetric Ninhydrin assay was used to indirectly measure the concentration of bound N^1-(3-trimethoxysilylpropyl)diethylenetriamine *via* absorbance at 562nm. Figure 23 shows the absorbance values of PCL fibres exposed to air plasma at 10 W either in a sealed autoclave bag or open petri dish. There was no significant difference found between PCL fibres exposed to air plasma in sterilisation bags and the open petri dish control. The absorbance measured for PCL treated in autoclave bags was slightly lower than that of fibres treated using the control method.

As there was no significant difference between groups, the absorbance values indicate that PCL fibres can be treated in a sterilisation bag, maintaining sterility and also successful enrichment of surfaces with -NH_2^+ silane monolayers.

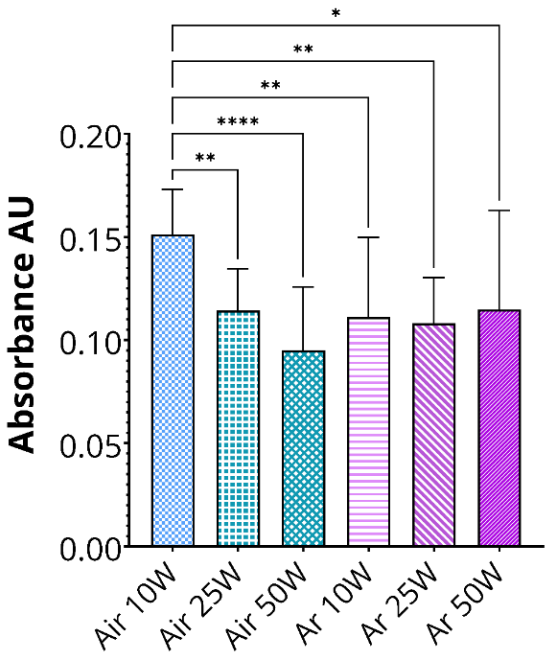

Figure 21. Absorbance values of PCL films modified using 11-aminoundecyltriethoxysilane post plasma polymerisation using air or argon plasma at 10, 25 or 50 W. A Ninhydrin assay was used to indirectly measure bound 11-aminoundecyltriethoxysilane *via* reduction of the NH_2^+ functional groups. The column graph displays measurements from two independent experiments with triplicate used within experiments. Error bars = standard deviation. Significance analysed by one-way ANOVA Tukey's multiple comparisons test and displayed as * $p<0.05$, ** $p<0.002$ and **** $p< 0.0001$.

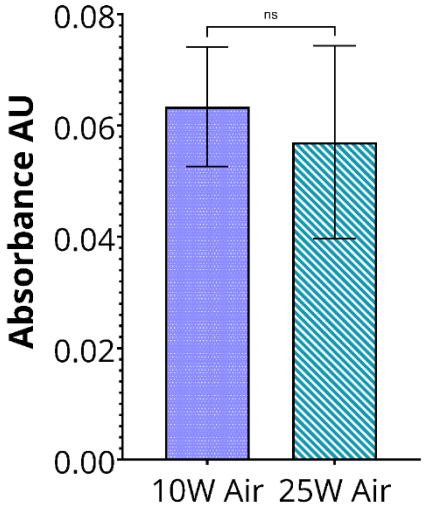

Figure 22. Absorbance values of PCL films modified using N^1-(3-trimethoxysilylpropyl)diethylenetriamine post exposure to air plasma at 10 or 25 W power. The column graph displays measurements from two independent experiments with triplicate used within experiments. Error bars = standard deviation. Significance analysed by unpaired parametric t test and displayed as ns p>0.01.

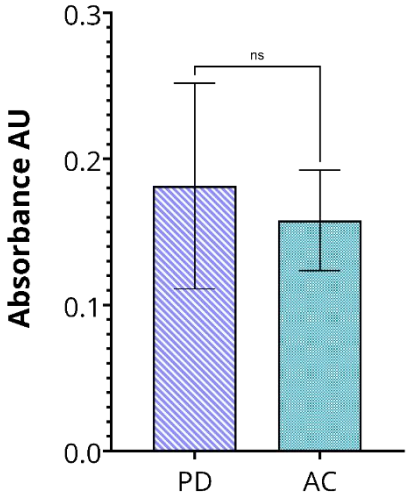

Figure 23. Absorbance values of PCL fibres modified using N^1-(3-trimethoxysilylpropyl)diethylenetriamine post exposure to air plasma at 10 W. PCL fibres were placed in the plasma chamber either in an autoclave bag (AC) or open petri dish (PD, control). The column graph displays measurements from two independent experiments with triplicate used within experiments. Error bars = standard deviation. Significance analysed by unpaired parametric t test and displayed as ns p>0.01.

2.3.5 XPS of silane modified PCL films

XPS was performed to evaluate the elemental composition of the PCL film surface layer produced at each step of surface functionalisation using *N*[1]-(3-trimethoxysilylpropyl)diethylenetriamine (N3S) and confirm the efficacy of the method. The wide scan and the deconvoluted high resolution scans of the C and O 1s region for PCL are not presented in figures 24-26, however, representative spectra can be found in section 2.3.1.

Table 18 shows the surface composition of all samples analysed which includes PCL and PCL modified with air plasma at 10 W. There was a low concentration of silicon contamination in PCL samples analysed which increased after exposure to air plasma consistent with XPS data described in section 2.3.3. The silane surface modification step seemed to remove silicon contamination introduced during film fabrication and exposure to air plasma as the silicon atomic percentage decreases from 5.9 to 1.7 % in N3S modified samples.

O/C ratios for PCL and PCL exposed to air plasma were calculated after the carbon and oxygen percentages were adjusted for the silicon contamination and are displayed in table 18. The O/C increases from 0.29 for PCL to 0.33 for air plasma modified PCL suggesting oxidation of the PCL surface by the plasma correlating with results described in section 2.3.3 and the literature[283]. Table 20 shows the atomic percentages of oxygen species determined from the high resolution O 1s scans. Consistent with results described in section 2.3.3, the atomic percentage of carbonyl groups detected in air plasma modified PCL is approximately 10 % higher than unmodified PCL.

Figure 24 shows the wide scans of PCL treated with air plasma and surface functionalized with N3S, heparin (100 µg/mL) and GDNF (10 ng/mL). PCL exposed to air plasma gave peak positions at approximately, 285, 532 and 102 eV assigned to carbon, oxygen and silicon, respectively. The

detection of nitrogen in the samples is evidence of the presence of N3S, heparin and GDNF on the surface of the PCL film as pure PCL is composed only of carbon and oxygen.

An additional peak at 400 eV was detected for PCL films functionalized with N3S, heparin and GDNF which corresponds to nitrogen. The peaks in the spectra generated for N3S coated PCL correlate with a study by Yi et *al.* in which they coat polycarbonate with *N*[1]-(3-Trimethoxy-silylpropyl)diethylenetriamine[284].

Figure 27 shows the deconvoluted N 1s spectra determined from the high resolution scans of PCL surface functionalized with N3S, heparin and GDNF. The envelope of the N 1s peak of PCL surface functionalized with N3S can be deconvoluted into two components; a peak at ~399 eV attributed to C-N bonds and a peak at 400.9 eV corresponding to amines[285, 286]. The N 1s spectra produced from PCL functionalized with heparin and GDNF can be deconvoluted into three components, two of which are the aforementioned peaks at ~399 and ~401 eV and an additional peak at ~402 eV assigned to the sulfamate functional group ($R_2NSO_3^-$)[287] present in heparin sulfate. After surface functionalisation with N3S the atomic percentage of nitrogen decreases from 3% to 2.5% for PCL samples functionalized with heparin and GDNF which correlates with the decrease in nitrogen atoms per heparin molecule compared to N3S which contains three per molecule.

Figure 28 shows the deconvoluted Si 2p spectra determined from high resolution scans of PCL functionalized with N3S, heparin and GDNF. The envelope of the Si 2p peak for each surface functionalized PCL sample can be deconvoluted into two peaks at ~102 and 103 eV corresponding to the two spin orbits of Si 2p electrons and is indicative of N3S present within the surface layer of PCL functionalized with heparin and GDNF.

The detection of sulfur in the samples is an indication of the presence of heparin and GDNF on the surface of the PCL film[198, 288]. An extra peak at ~169 eV on the wide scan spectra for heparin and GDNF immobilised PCL is attributed to sulfur[289, 290]. The atomic percentage of sulfur detected by the wide scans was calculated as an average of 0.7 % for PCL films functionalized with heparin and GDNF (table 18). Figure 29 shows the deconvolution of the S 2p spectra determined from the high resolution scans of PCL films functionalized with heparin and GDNF. The envelope of the S 2p peak can be deconvoluted into two components; one peak at ~168 eV and one at ~169 eV corresponding to the spin orbitals of the S 2p electrons.

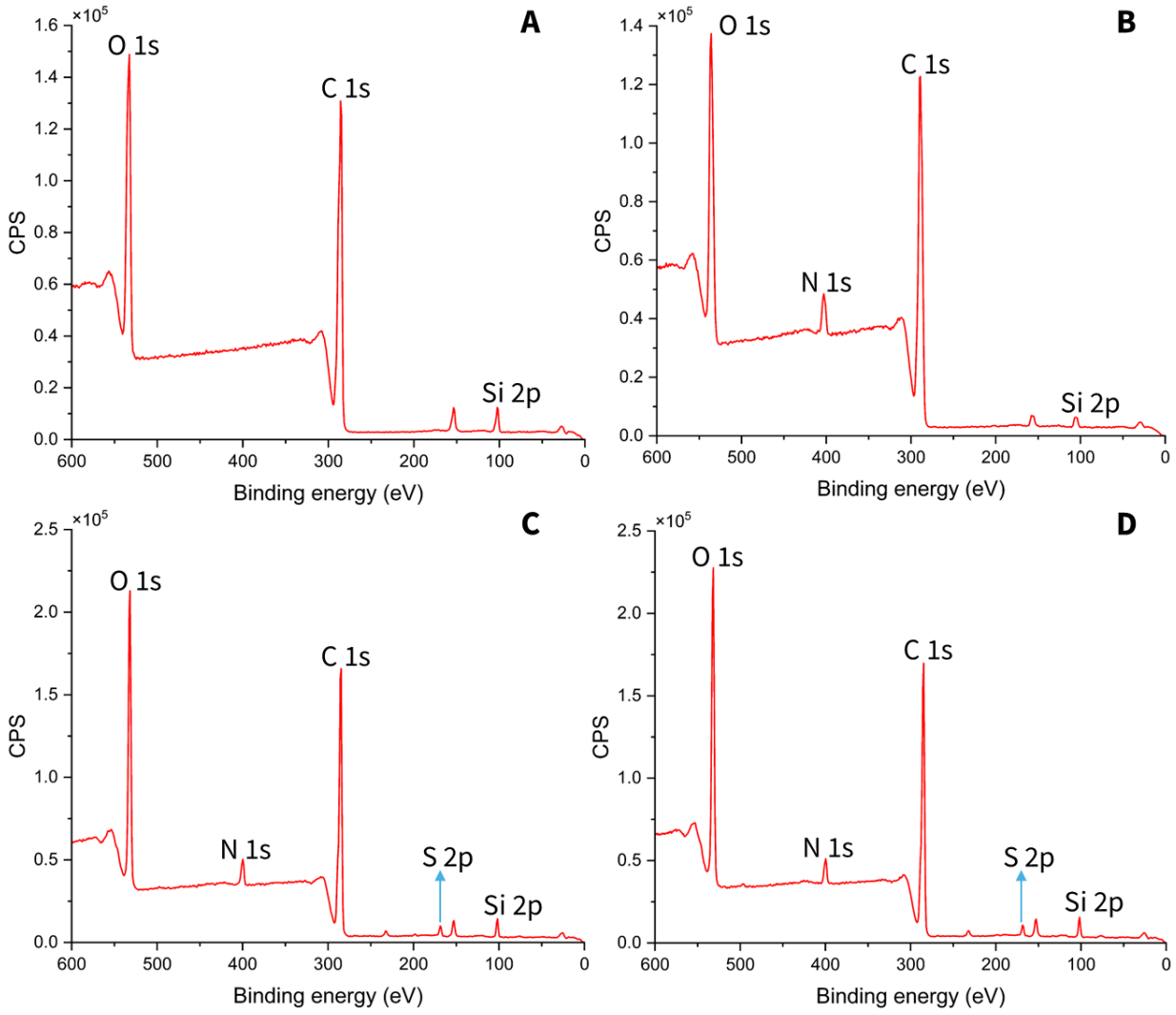

Figure 24. Surface composition of PCL treated with air plasma 10 W (a), N3S (b), 100 µg/mL heparin sodium (c) and 10 ng/mL GDNF (d) determined from wide survey scans.

Table 18. Surface composition, carbon-to-oxygen and oxygen-to-carbon ratios of PCL and PCL treated with air plasma 10 W, N3S, heparin sodium (100 µg/mL) and GDNF (10 ng/mL).

Sample	Surface composition (% At)						
	C	O	N	Si	S	C/O	O/C
PCL	77.1 ± 0.4	22.8 ± 0.4	-	0.2 ± 0.1	-	3.4	0.29
PCL Air 10W	69.4 ± 1.7	24.7 ± 0.3	-	5.9 ± 2.0	-	3.1	0.33
PCL-N3S	72.5 ± 0.2	22.9 ± 0.8	3.0 ± 0.4	1.7 ± 0.1	-	3.2	0.32
PCL-Hep	66.7 ± 1.3	25.0 ± 0.5	2.7 ± 0.1	4.9 ± 2.1	0.7 ± 0.1	2.7	0.37
PCL-GDNF	64.8 ± 2.3	25.6 ± 1.1	2.5 ± 0.2	6.4 ± 3.9	0.7 ± 0.1	2.5	0.40

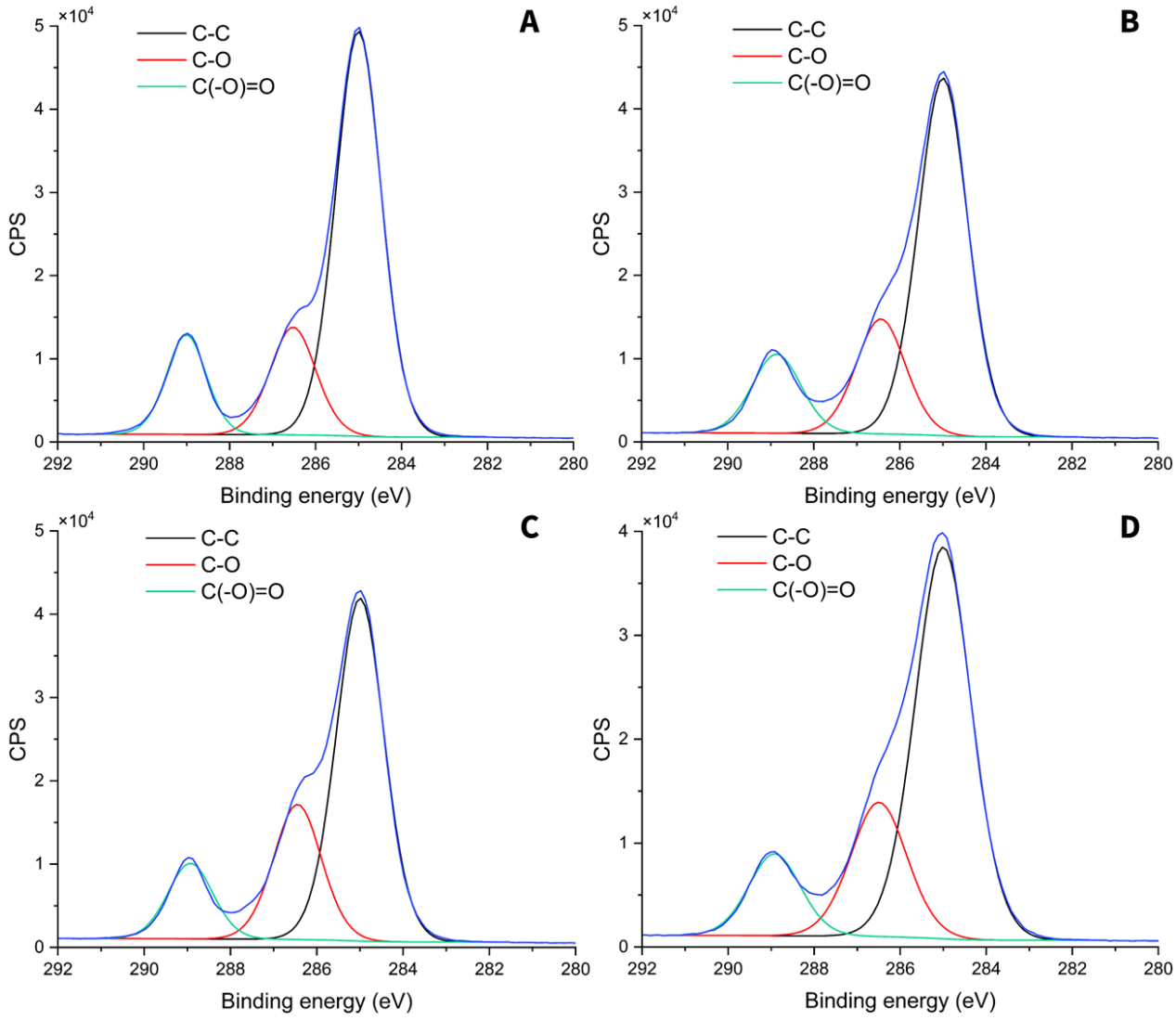

Figure 25. Deconvolution of C 1s region of PCL films treated with a) air plasma 10 W, b) N3S, c) heparin sodium (100 µg/mL) and d) GDNF (10 ng/mL) determined from high resolution scans.

Table 19. Atomic concentration (% At) of carbon species determined from high resolution scans of the C 1s region of the surface layer of PCL and PCL treated with air plasma 10 W, N3S, heparin sodium (Hep; 100 µg/mL) and GDNF (10 ng/mL).

Sample	C-C		C-O		C(-O)=O	
	B.E. (eV)	% At	B.E. (eV)	% At	B.E. (eV)	% At
PCL	285	65.1 ± 0.1	287	19.4	289	15.6 ± 0.1
PCL Air 10W	285	67.6	287	18	289	14.4
PCL-N3S	285	65.5 ± 0.8	287	20.4 ± 0.8	289	14.3 ± 0.1
PCL-Hep	285	64.1 ± 2.4	287	23.6 ± 1.4	289	12.3 ± 1.0
PCL-GDNF	285	65.8 ± 0.9	287	22.4 ± 0.1	289	12.0 ± 0.9

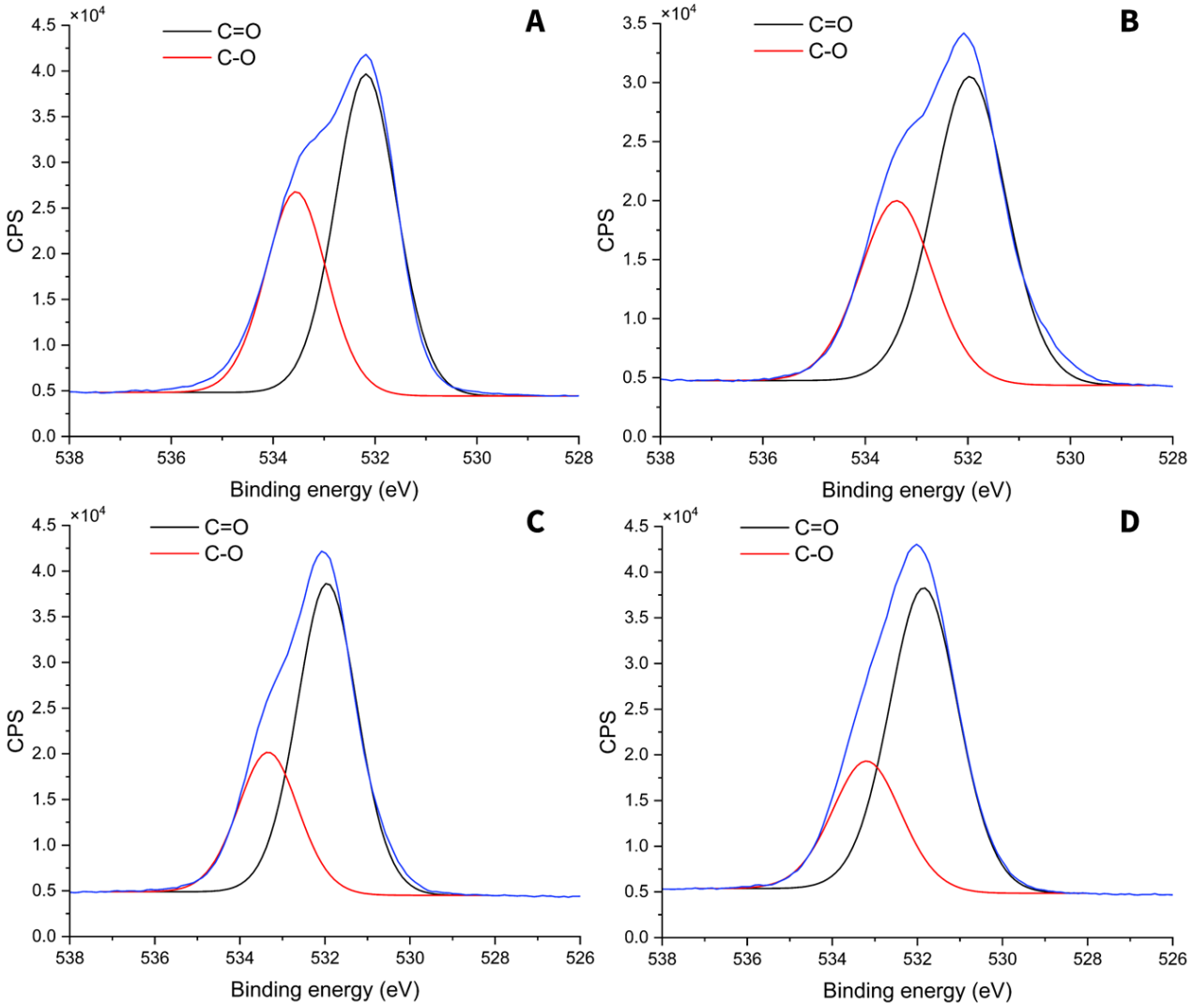

Figure 26. Deconvolution of O 1s region of PCL films treated with a) air plasma 10 W, b) N3S, c) heparin sodium (100 µg/mL) and d) GDNF (10 ng/mL) determined from high resolution scans.

Table 20. Atomic concentration (% At) of oxygen species determined from high resolution scans of the O 1s region of the surface layer of PCL and PCL treated with air plasma 10 W, N3S, heparin sodium (Hep; 100 µg/mL) and GDNF (10 ng/mL).

Sample	C=O		C-O	
	B.E. (eV)	% At	B.E. (eV)	% At
PCL	532.0	50.6	533.0	49.4
PCL Air 10W	532.0	60.6 ± 1.1	533.0	39.4 ± 1.1
PCL-N3S	532.0	61.9 ± 1.6	533.0	38.2 ± 1.5
PCL-Hep	532.0	71.1 ± 3.0	533.0	29.0 ± 3.0
PCL-GDNF	532.0	73.8 ± 4.9	533.0	26.2 ± 4.9

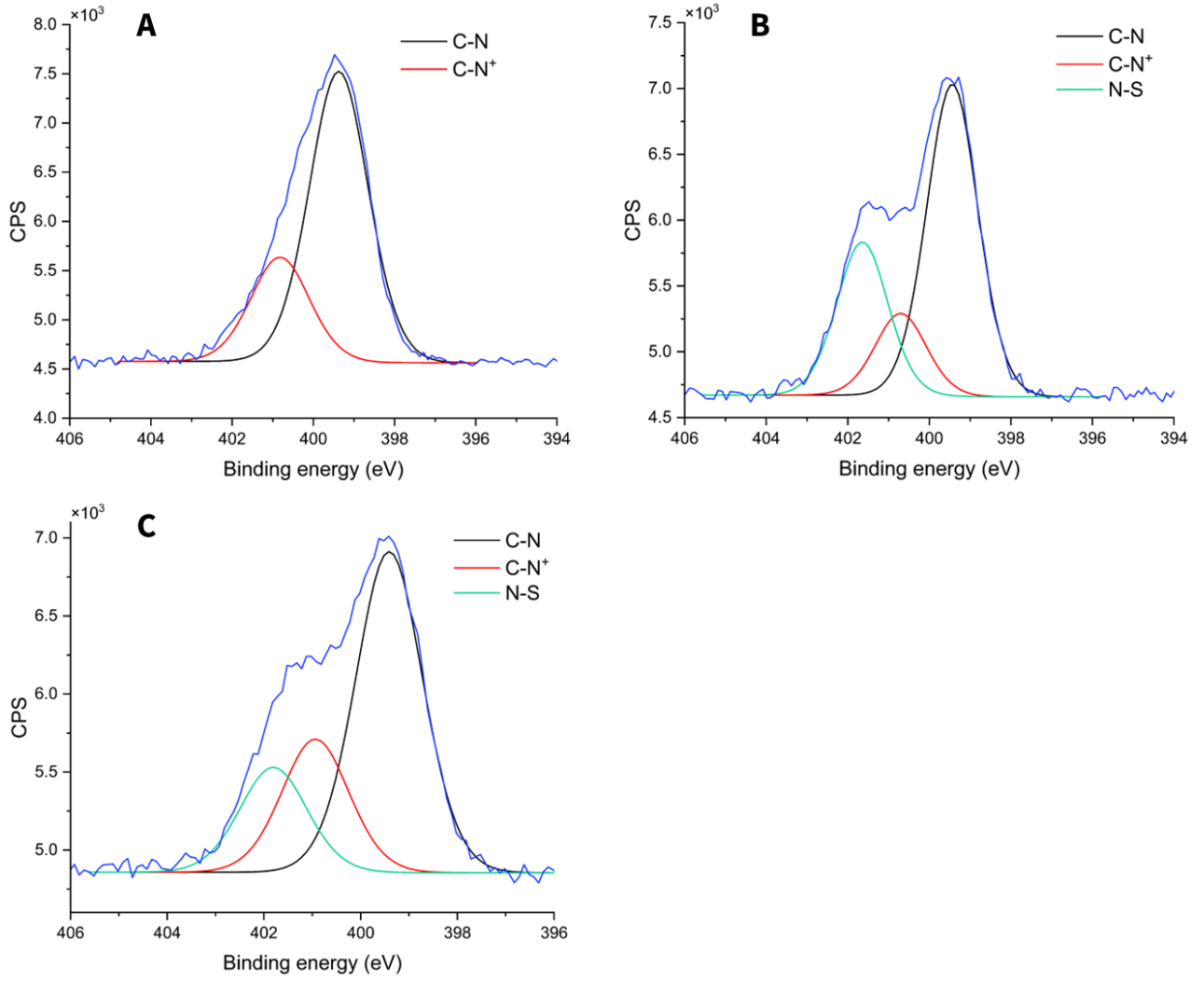

Figure 27. Deconvolution of N 1s region of PCL films functionalized with a) N3S, b) heparin sodium (100 µg/mL) and c) GDNF (10 ng/mL) determined from high resolution scans.

Table 21. Atomic concentration (% At) of nitrogen species determined from high resolution scans of the N 1s region of the surface layer of PCL functionalized with N3S, heparin sodium (Hep; 100 µg/mL) and GDNF (10 ng/mL).

Sample	C-N		$C\text{-}N^{+}$		N-S	
	B.E. (eV)	% At	B.E. (eV)	% At	B.E. (eV)	% At
PCL-N3S	399.4	73.4 ± 0.3	400.9	26.7 ± 0.4	401.9	-
PCL-Hep	399.4	59.0 ± 2.8	400.9	18.0 ± 4.2	401.9	23.0 ± 7.1
PCL-GDNF	399.4	59.0 ± 2.1	400.9	23.3 ± 1.5	401.9	17.8 ± 0.6

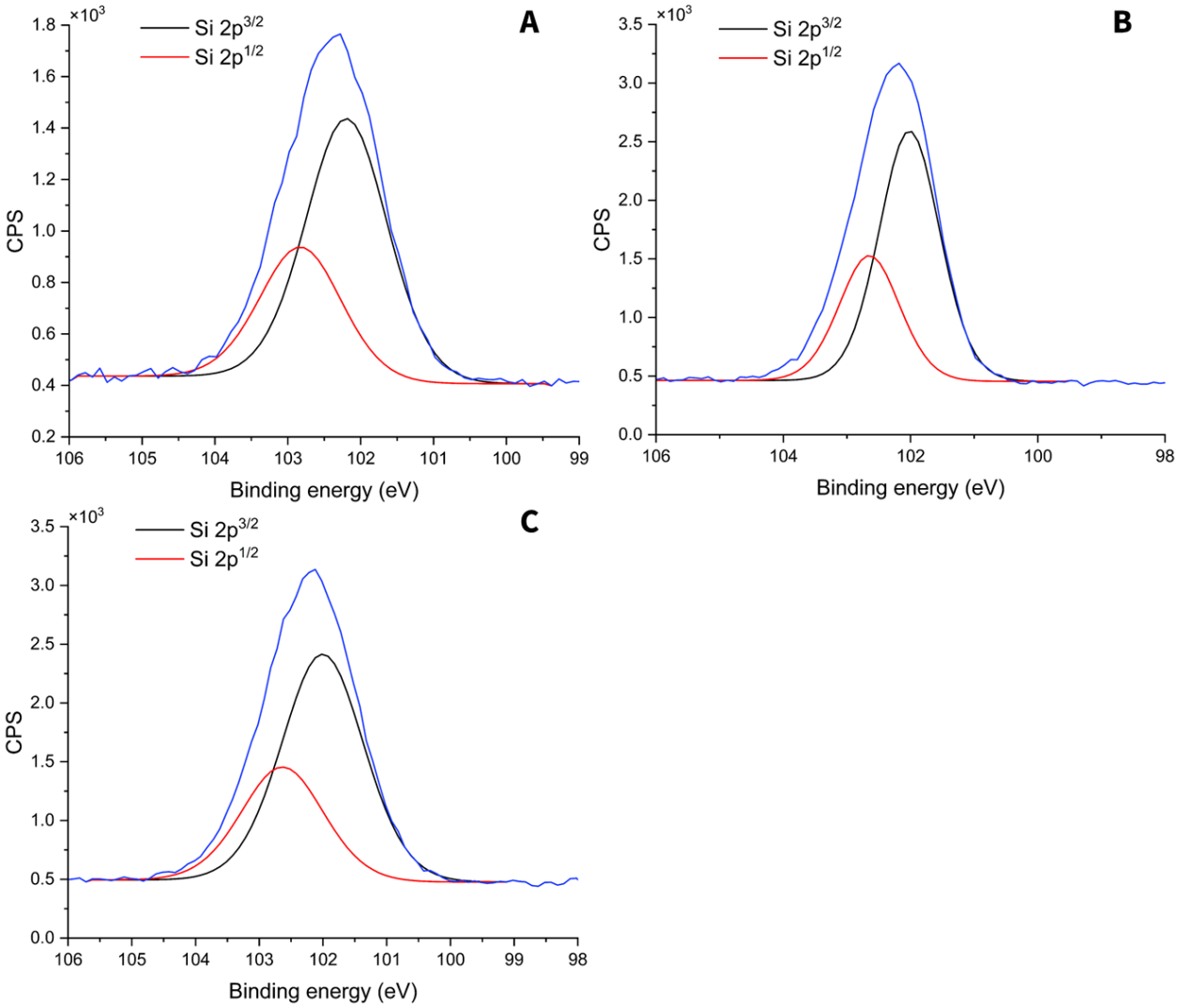

Figure 28. Deconvolution of Si 2p region of PCL films functionalized with a) N3S, b) heparin sodium (100 µg/mL) and c) GDNF (10 ng/mL) determined from high resolution scans.

Table 22. Atomic concentration (% At) of silicon 2p orbitals determined from high resolution scans of the Si 2p region of PCL functionalized with N3S, heparin sodium (Hep; 100 µg/mL) and GDNF (10 ng/mL).

Sample	Si $2p^{3/2}$		Si $2p^{1/2}$	
	B.E. (eV)	% At	B.E. (eV)	% At
PCL	102.1	100	102.7	-
PCL Air 10 W	102.1	66.7	102.7	33.3
PCL-N3S	102.1	66.7	102.7	33.3
PCL-Hep	102.1	66.7	102.7	33.3
PCL-GDNF	102.1	66.7	102.7	33.3

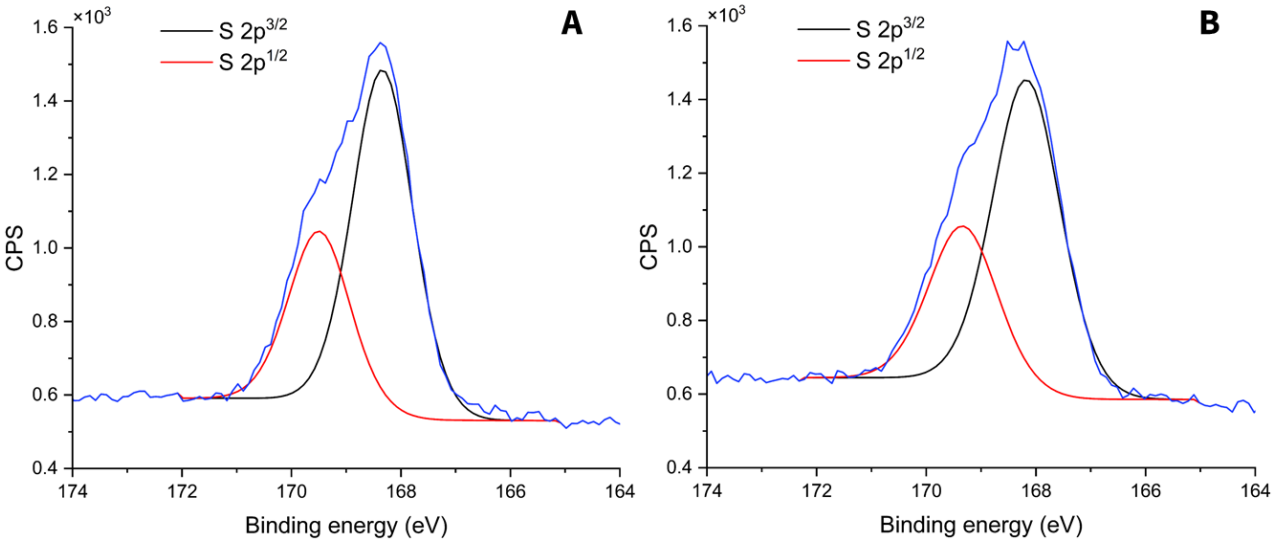

Figure 29. Deconvolution of S 2p region of PCL films functionalized with a) heparin sodium (100 µg/mL) and b) GDNF (10 ng/mL) determined from high resolution scans.

Table 23. Atomic concentration (% At) of sulfur 2p orbitals determined from high resolution scans of the S 2p region of the surface layer of PCL functionalized with heparin sodium (Hep; 100 µg/mL) and GDNF (10 ng/mL).

Sample	S $2p^{3/2}$		S $2p^{1/2}$	
	B.E. (eV)	% At	B.E. (eV)	% At
PCL-Hep	168.4	66.7	169.5	33.3
PCL-GDNF	168.4	66.7	169.5	33.3

2.3.6 Attenuated Total Reflectance Fourier-Transform Infrared Spectroscopy (ATR-FTIR) of surface functionalized PCL films

ATR-FTIR was utilised for additional characterisation of the chemical properties of silane modified PCL films. Elzein *et al.* and Can-Herrera *et al.* describe the characteristic infrared bands of the PCL as shown in table 24[282, 291]. The ATR-FTIR spectrum of air plasma treated PCL is expected to be similar to the spectrum of unmodified PCL samples as the air plasma process exposes hydroxyl groups on the surface. Thus, higher absorption at approximately 3000 - 3500 cm^{-1} assigned to the -OH functional group was expected[274]. However, figure 30 indicates absorption at this band for air plasma treated PCL is similar to unmodified PCL.

Mello *et al.* describe absorption bands that characterise different functional groups present in *N*[1]-(3-trimethoxysilylpropyl)diethylenetriamine (N3S)[292]. Mello *et al.* identify absorption bands at 1134 and 1045 cm^{-1} attributed to Si-O-Si asymmetric stretching. Figure 31b shows absorption wavelengths between 1000 and 1250 cm^{-1}. At approx. 1134 cm^{-1} a difference in gradient can be seen for the spectrum of N3S functionalized PCL compared to the other groups this could be indicative of Si-O-Si asymmetric stretching. PCL characteristically absorbs at ~1170 cm^{-1} attributed to symmetric C-O-C stretching, potentially affecting the differentiation of the band at 1134 cm^{-1} as these wavelengths are close on the spectrum. Figure 31a displays the ATR-FTIR spectra between wavelengths 680 and 840 cm^{-1}, a small infrared radiation band at ~800 cm^{-1} can be attributed to the Si-O bond[293] and is seen for N3S functionalized PCL only. It is unclear why bands for silicon-oxygen environments are not identifiable in PCL functionalized with heparin and GDNF as these samples are prior functionalized with N3S.

PCL films coated with heparin sodium (PCL-Hep) are expected to show characteristic absorptions at 1230 and 1040 cm^{-1} assigned to SO_3^- asymmetric and symmetric stretching, respectively[294].

Absorption at 1240 cm^{-1} assigned to asymmetric C-O-C stretching is a characteristic of PCL meaning that it is difficult to distinguish between this infrared radiation band and the band at 1230 cm^{-1} assigned to the SO_3^- asymmetric stretching seen in figure 31a. In addition, in the Elzein *et al.* FTIR study a characteristic band at 1044 cm^{-1} for unmodified PCL was identified also making the band at 1040 cm^{-1} assigned to SO_3^- symmetric stretching difficult to distinguish[291]. Absorption at 1550 cm^{-1} assigned to amide II group N-H bending is expected based on the literature[295]. Figure 30 and 31c show the presence of this infrared radiation band ~1550 cm^{-1}, most notably in PCL samples functionalized with N3S. This is likely due to N3S having a higher ratio of N-H environments compared to heparin sodium. Figure 31c displays wavelengths between 1300 to 1800 cm^{-1}, for heparin and GDNF functionalized PCL, a band is present at approximately 1637 cm^{-1} and is assigned to NH_2 scissoring (symmetric in plane bending) which is likely amide functionality (amide I band)[289, 292, 295]. ATR FTIR spectra of PCL films functionalized with N3S, heparin and GDNF all display absorption at approximately 3000-3500 cm^{-1}. This band is assigned to NH_x and -OH functional groups[274, 289]. A small band is present in PCL and air plasma functionalized PCL however a gradient which progressively increases from N3S- to heparin- to GDNF- functionalized PCL is indicative of increasing numbers of NH_x and -OH groups in these samples (figure 30 and 31d).

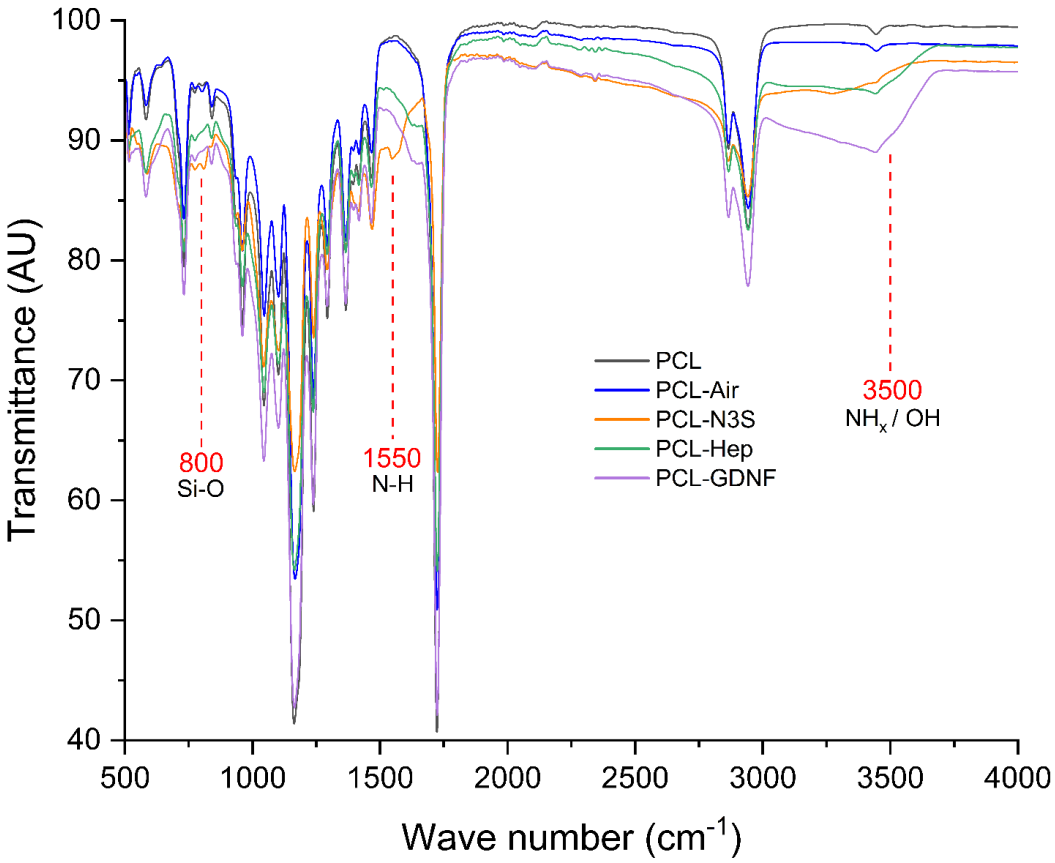

Figure 30. FTIR-ATR spectrum of unmodified PCL, air plasma 10 W, N3S, heparin sodium (100 µg/mL) and GDNF (10 ng/mL) treated PCL films.

Table 24. Characteristic infrared bands of PCL. Modified from Elzein et al., 2004, Can-Herrera et al., 2016[282, 291].

Position (cm^{-1})	**Assignment**
2949	Asymmetric CH_2 stretching
2865	Symmetric CH_2 stretching
1727	Carbonyl stretching
1293	C-O and C-C stretching in the crystalline phase
1240	Asymmetric COC stretching
1190	OC-O stretching
1170	Symmetric COC stretching
1157	C-O and C-C stretching in the amorphous phase

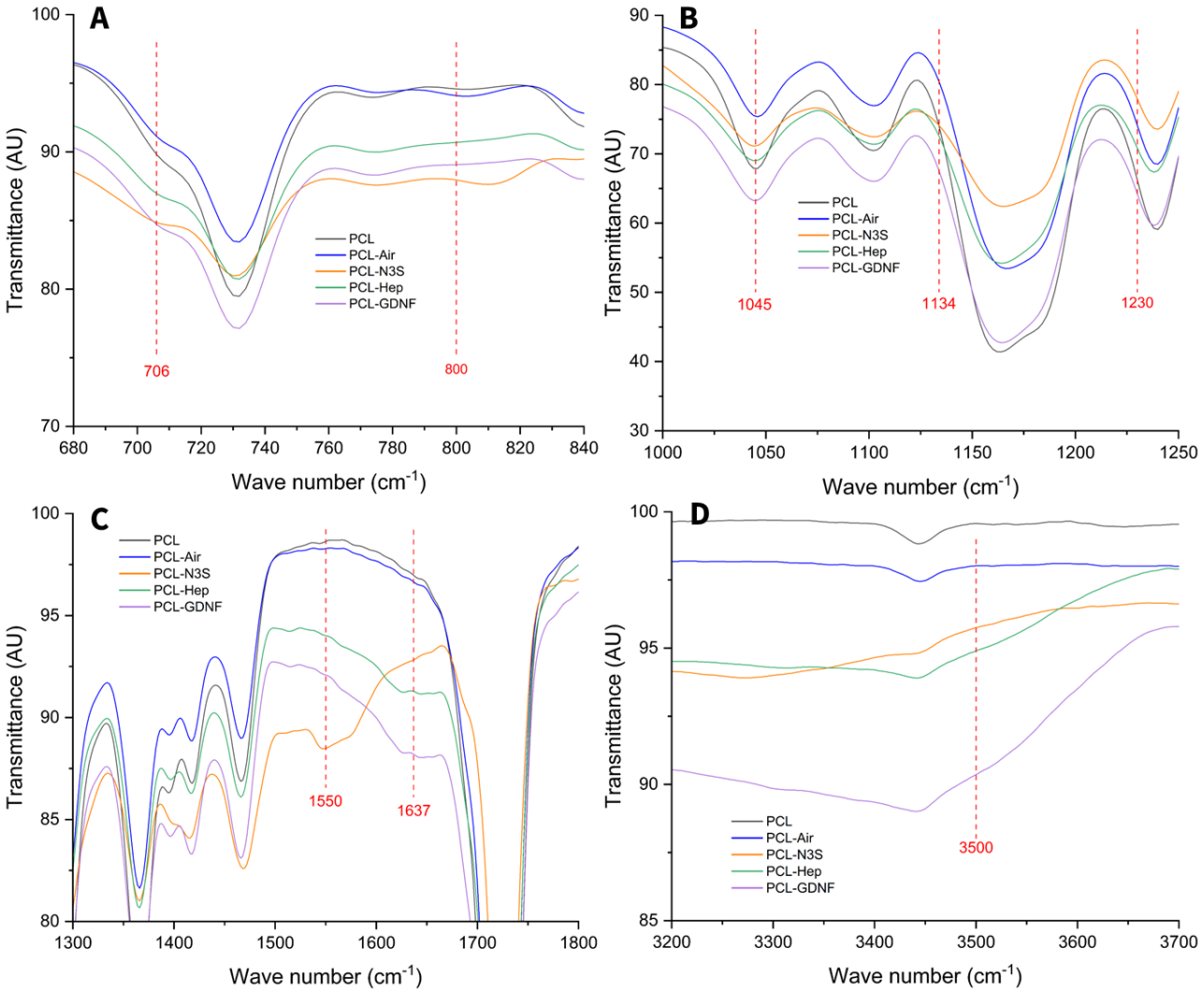

Figure 31. FTIR-ATR spectra of unmodified PCL, air plasma 10 W, N3S, heparin sodium (100 µg/mL) and GDNF (10 ng/mL) treated PCL films. Infrared radiation between a) 680 – 840 cm^{-1}, b) 1000 – 1250 cm^{-1}, c) 1300 – 1800 cm^{-1}, d) 3200 – 3700 cm^{-1}.

2.3.7 Scanning electron microscopy (SEM) images of PCL fibres

2.3.7.1 Fibre diameter and alignment

To determine the optimal parameters for spinning PCL fibres with 5 and 8 µm diameter, parameters described by Daud et *al.*, 2012 were used as a starting point[191]. Fibres were manufactured by electrospinning using constant parameters of 15 %wt PCL:DCM, 4 ml/hr flow rate, 18 kV and 20 cm needle-to-collector distance. The variable parameter assessed was collector speed in which three speeds were evaluated; 500, 600 and 800 rpm.

To analyse the collector speed effect on fibre diameter and alignment, PCL microfibres were imaged by SEM. For each collector speed assessed, fibre diameter and fibre angles were measured using 0.8 x 0.8 mm samples taken from four independent experiments with three areas imaged per sample (N=4, n=12). Figure 32 shows representative images of PCL microfibres spun using collector speeds 600 and 800 rpm from four independent experiments. Figure 34a demonstrates that the fibre diameter decreased as the collector speed increased from 500 to 800 rpm. The average diameter of PCL fibres span using a collector speed of 500 rpm was 8 µm +/- 4 whereas when using 600 and 800 rpm the average diameter was 6 µm +/- 4 and 5 µm +/- 4, respectively, (figure 34a). Figure 34b shows the percentage distribution of the angular differences between fibres. The angular difference was measured by using the mode angle and setting it as the reference angle which was subtracted from all other angles measured. When using a collector speed of 800 rpm, 78 % of fibres measured showed an angular difference of 0 to 2 degrees with a maximum variation of 7 degrees. In comparison, 68 and 48 % of fibres measured showed an angular difference of 0 to 2 degrees when using a collector speed of 600 rpm and 500 rpm, respectively. The percentage distribution of the angular difference from the reference fibre suggested increasing alignment as the collector speed increased from 500 to 800 rpm, with the highest alignment seen using a collector speed of 800 rpm.

Furthermore, the microfibre morphology was assessed. Figure 33 shows SEM images taken at 3000x and 10000x magnification of microfibres span using 600 or 800 rpm, respectively. Both groups show surface topographies of elliptic shape showing elongated grooves in the fibre direction. This is in alignment with previous studies by Daud *et al.*, 2012[191]. These results indicate that using the constant parameters shown in table 3 and collector speed of 800 rpm allow the manufacture of highly aligned fibres with an average fibre diameter of 5 µm for the culture of Thy1-

YFP mice trigeminal ganglion neuronal and glial cells (Chapter 4). In addition, using constant parameters shown in table 3 and 500 rpm collector speed allowed the manufacture of aligned fibres with an average diameter of 8 µm for neuronal differentiation assays using NG108-15 neuronal cells and for use in chick DRG *ex vivo* injury models (Chapter 4).

2.3.7.2 Energy dispersive X-ray spectroscopy (SEM-EDX) images of PCL fibres

PCL fibres with an average diameter of 5 microns were functionalized using the methods described in section 2.2.4-7. The distribution of N3S, heparin and GDNF was qualitatively analysed using SEM-EDX imaging. Figure 35 shows SEM-EDX images of PCL fibres functionalized with N3S, heparin (100 µg/mL) and GDNF (10 ng/mL). The spectra for the functionalized scaffolds shows the detection of carbon, oxygen and silicone for each surface analysed. Additional sulfur was detected on heparin and GDNF treated PCL microfibres indicting successful immobilisation of heparin and GDNF (figure 35b and c). Moreover, the map reconstruction for individual elements demonstrated homogenous distribution of N3S, heparin and GDNF throughout the sample surface.

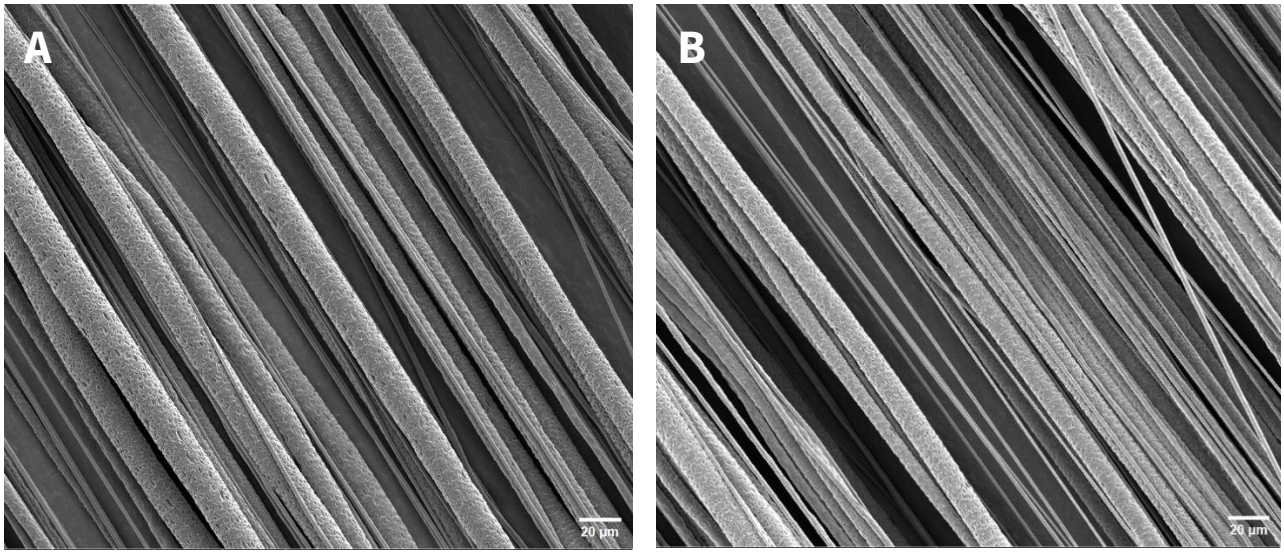

Figure 32. Scanning electron microscopy images of aligned PCL fibres spun using different collector speeds. 15 %wt PCL:DCM spun using a collector speed of 600 rpm (a) and 800 rpm (b). Images are representatives of 4 independent experiments.

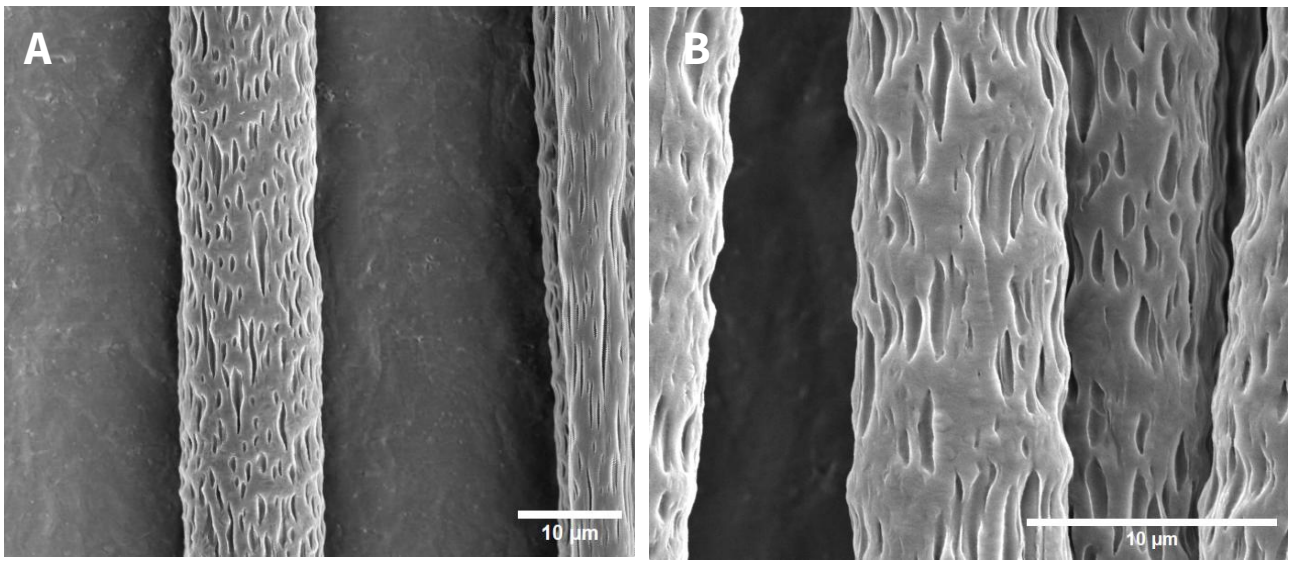

Figure 33. Topographies of PCL microfibre surface. SEM images showing the topography of PCL microfibres spun using collector speed 600 (a) or 800 rpm (b). Representative images of 4 independent experiments shown.

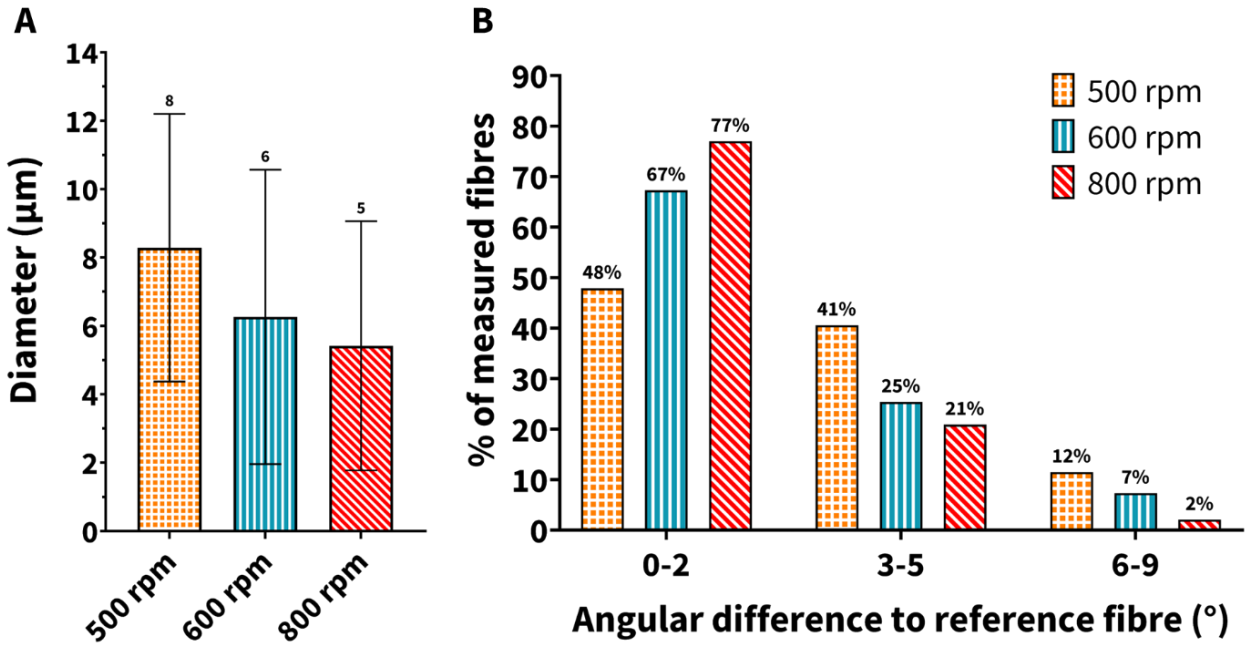

Figure 34. Fibre diameter and alignment evaluation of PCL microfibres. Average fibre diameter (a) and fibre alignment (b). PCL fibres were spun using collector speeds of 500, 600 or 800 rpm. Microfibres were imaged by SEM and measurements were taken using Fiji.

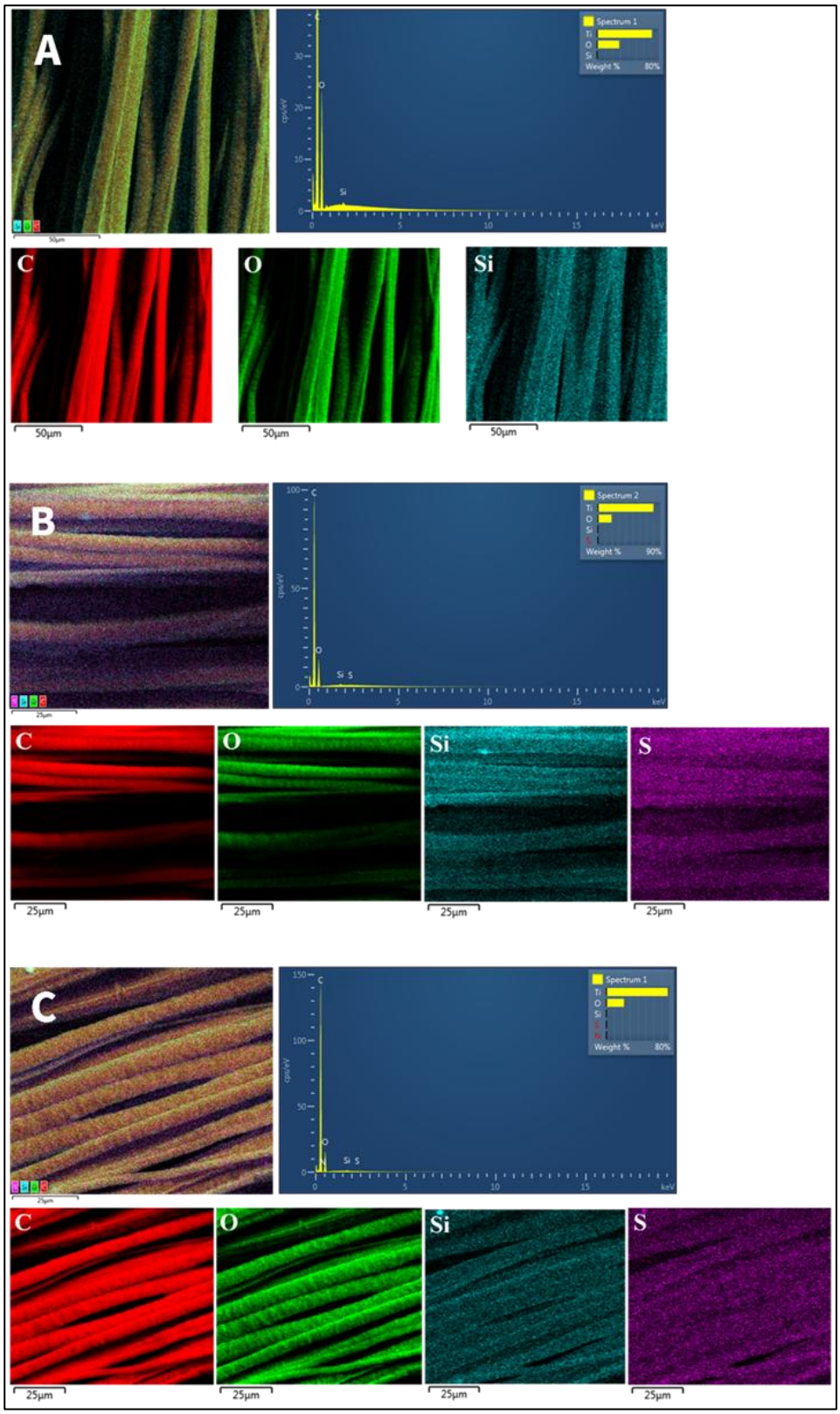

Figure 35. SEM-EDX images of N3S, heparin sulfate and GDNF functionalized PCL microfibres.

N3S bound PCL (a), heparin sulfate bound PCL (b) and GDNF (c) bound PCL. The original SEM image with merged elemental distribution is shown in the top left corner. The elemental spectra is shown in the top right corner. The images for corresponding elements detected on PCL microfibres are shown at the bottom. C carbon; O, oxygen; Si, silicone and S, sulfur.

2.3.8 Water contact angle of silane modified PCL films

PCL films were prepared using the methods described in 2.2.1 and subsequently coated with heparin sodium and GDNF using the methods described in 2.2.4-7. Four groups of PCL films were analysed by water contact angle (WCA) to assess the hydrophilicity of the PCL surface after each step of surface functionalisation. The groups analysed were unmodified PCL and PCL surface modified with *N*[1]-(3-trimethoxysilylpropyl)diethylenetriamine, heparin sodium (100 µg/mL) and GDNF (10 ng/mL). Figure 36 displays the average WCA as a bar chart and images taken during the WCA analysis representing three independent experiments. The average WCA decreased after each step of surface functionalisation with GDNF having an average WCA of 35° showing an increase in hydrophilicity. The average WCA of unmodified PCL was 84° compared to an average of 64° for N3S surface functionalized PCL showing a slight increase in hydrophilicity. Significant differences were found between the average WCA for PCL and PCL surfaces functionalized with heparin sodium and GDNF using the Kruskal-Wallis Dunn's multiple comparisons test. Furthermore, there was a significant difference between the average WCA of N3S surface functionalized PCL and GDNF functionalized PCL.

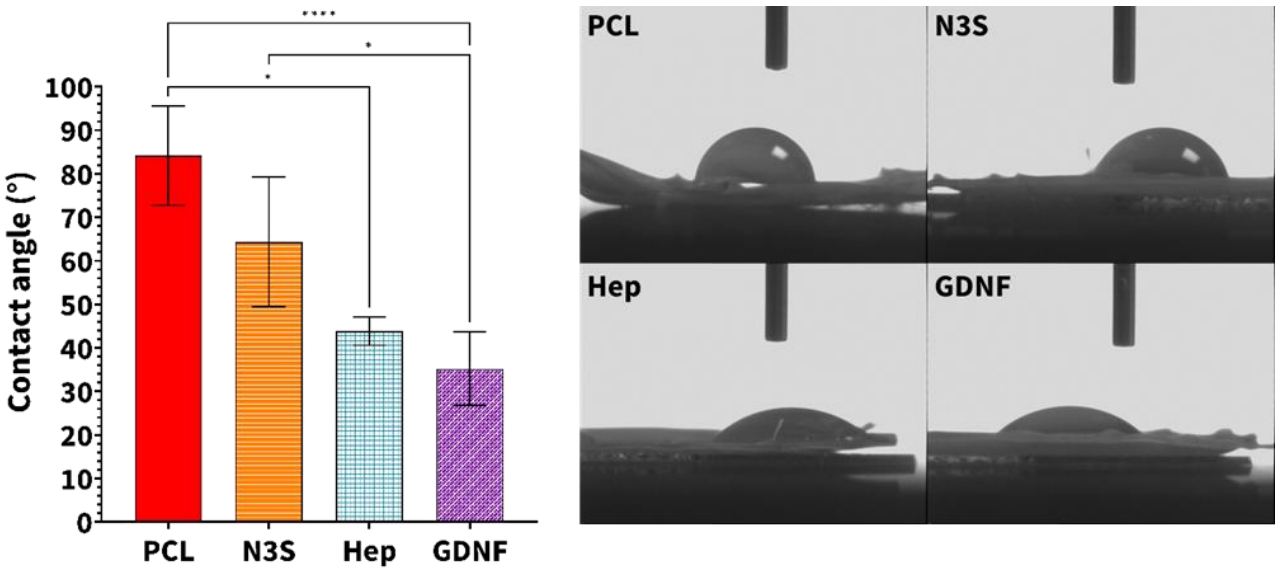

Figure 36. Water contact angle of silane functionalized PCL films. The bar graph displays the average water contact angle measured of unmodified PCL, N3S, heparin sodium (100 µg/mL) and GDNF (10 ng/mL) surface functionalized PCL films. Statistical significance was measured using a non-parametric Kruskal-Wallis Dunn's multiple comparisons test, groups were considered significantly different if $p<0.05$ and displayed as * $p<0.05$ and **** $p< 0.0001$. The right hand side shows images taken during the WCA analysis and are representative of three independent experiments. Error bars represent standard deviation.

2.3.9 Release profile of GDNF from PCL films at 4° and 37° C

An enzyme-linked immunosorbent assay (ELISA) was utilized to assess the release of 10 ng/mL and 100 pg/mL GDNF immobilised on PCL films when stored at 4 °C or 37 °C over 7 days. These temperatures were chosen as they correspond to a potential storage temperature (4 °C) of the nerve guide devices and the mammalian body temperature (37 °C). 10 ng/mL and 100 pg/mL GDNF in PBS were immobilised onto PCL films using the method described section 2.2.4-7 in triplicate over two independent experiments. The supernatant after GDNF incubation on PCL films was kept in order to quantify the percentage of GDNF bound to the surface before profiling PCL films. Figure 37 displays a bar graph of the percentage of 10ng/mL and 100 pg/mL bound to PCL surfaces after a 5 hour incubation period. An average of 99.8 % of 10 ng/mL bound to the PCL surface compared to an average of 99.5 % of 100 pg/mL GDNF indicating successful immobilization of both concentrations. Figure 38 shows the release profile of 10 ng/mL and 100 pg/mL GDNF

immobilised on PCL films incubated in PBS at 4 °C and 37 °C. No release of GDNF (0 pg/mL) was detected for both concentrations over 7 days when incubated at 4 °C suggesting that immobilised surfaces can be stored at 4 °C for at least 7 days without release. Highest concentrations of both GDNF concentrations were detected after 1 hour of incubation indicating a burst release mechanism from the PCL surface. Decreasing concentrations were detected at the 24 to 48 hour time points from 10 ng/mL immobilised GDNF PCL films followed by a slight increase at the 168 hour time point. No release of GDNF was detected on 100 pg/mL for the 24 to 48 hour period followed by a detection of approximately 30 pg/mL GDNF at the 168 hour time point. Overall, the release profiles of 10 ng/mL and 100 pg/mL GDNF immobilised PCL films incubated at 37 °C suggests a burst release mechanism followed by sustained release for at least 24 to 168 hours.

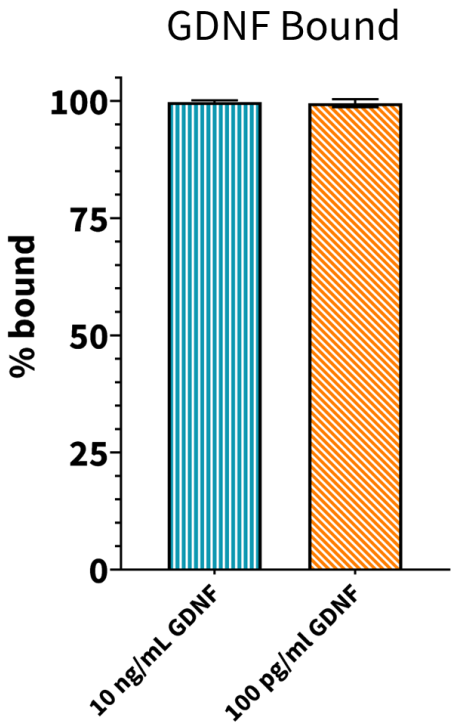

Figure 37. Percentage of GDNF bound to PCL films before incubation at 4 or 37 °C. PCL films were surfaced modified as described in 2.2.4-7 in triplicate over two independent experiments. Significance analysed using a unpaired parametric t-test revealed no significant difference between groups. Error bars = standard deviation.

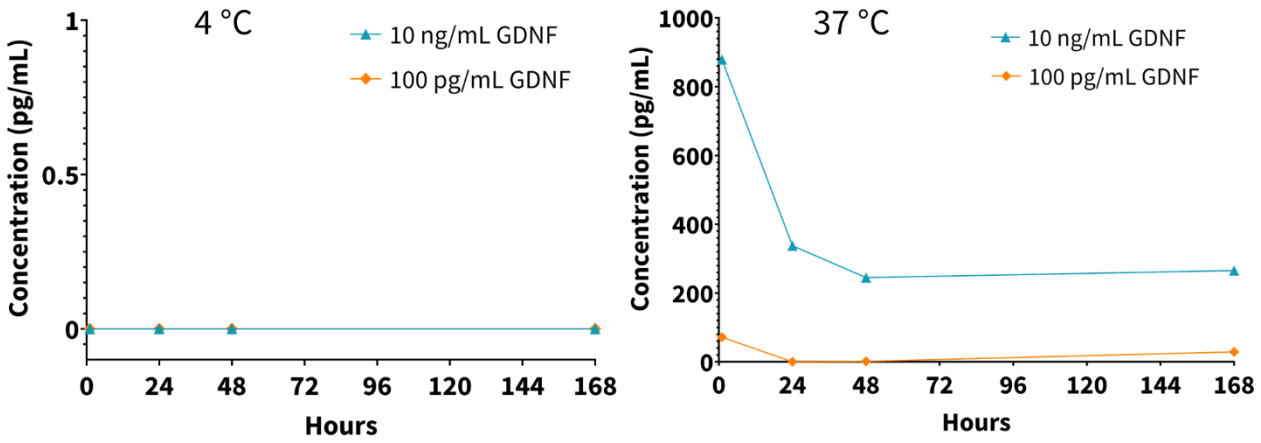

Figure 38. Release profile of 10 ng/mL and 100 pg/mL GDNF immobilised on PCL films stored at 4 or 37 °C over 168h. PCL films were surfaced modified as described in 2.2.4-7 in triplicate over two independent experiments. Samples were added to assay plates in duplicate and absorbance was read at a wavelength of 450 nm.

2.4 Discussion

2.4.1 Development of surface modification methods

A main objective of this research project was to investigate polymer surface modification methods to achieve reproducible immobilisation of bioactive factors such as heparin sulfate and GDNF.

The first method of surface modification analysed was the use of allylamine plasma to functionalise the PCL surface with a $-NH^{2+}$ monolayer to passively adsorb heparin sulfate. XPS analysis revealed oxygen contamination on allylamine plasma modified PCL samples as shown in table 4 by the increase of O/C ratio from 0.28 for pure PCL to 0.39 for modified PCL films. This unexpected result was re-investigated using 35 mm diameter tissue culture petri dishes to elucidate the source of the contamination *e.g.* user error or equipment failure. XPS analysis of allylamine plasma modified TCP provided further evidence of oxygen contamination into the plasma chamber shown by an increase in ester groups and an unexpected peak at 406 eV assigned to nitrate. These results are in disagreement with the literature as oxygen concentration is not expected to increase post allylamine plasma treatment[274]. Possible sources of contamination

include water vapor present in the reaction chamber or a air leak into the reaction chamber. Furthermore as shown in table 4, low atomic concentrations of sulfur were detected for heparin and GDNF treated PCL films post allylamine plasma modification at 0.2% and 0.1%, respectively, indicating low or non-homogenous binding of the bioactive factors. Thus, it was concluded that allylamine plasma deposition was an unreliable method for binding heparin and GDNF. A similar outcome was observed by Sandoval *et al.* (2021) for heparin and GDNF incubated PCL films post allylamine modification[198]. This study reported 0.2% sulfur detected on heparin treated allylamine plasma modified PCL films[198].

A second surface modification method was therefore developed and analysed for the immobilisation of bioactive compounds using air plasma treatment and chemical linkage of long chain aminosilanes. Air and argon plasma were assessed at different discharge powers to determine which parameters introduced the highest concentration of hydroxyl groups onto the PCL surface in order to covalently bind long chain aminosilanes. Treatment time was kept constant at 120 seconds. As shown in tables 15 and 16, highest atomic percentages of single carbon to oxygen bonds were detected on PCL films modified with air or argon plasma at a discharge power of 10 W indicating higher concentrations of hydroxyl groups were incorporated onto the surface.

A Ninhydrin assay was utilised to further assess the optimal gas and discharge power for binding 11-aminoundecyltriethoxysilane as the assay provides an indirect measure of aminosilane bound to PCL. To improve cost effectiveness the aminosilane *N*[1]-(3-trimethoxysilylpropyl)-diethylenetriamine (N3S) was also assessed. A Ninhydrin assay can be used to obtain qualitative or quantitative data as the reduction of Ninhydrin salt is observable as a colour change from clear to blue/purple indicating the presence of amine groups on the sample. In addition, the reduced

product absorbs light at a wavelength of 562 nm thus can give an indirect measure of the amine groups bound to the surface. PCL films treated using air plasma at 10 W discharge power resulted in significantly higher absorbance values compared to air plasma at 25 and 50W or argon at 10, 25 and 50 W discharge power indicating a significantly higher concentration of 11-aminoundecyltriethoxysilane bound to the PCL surface. The assay was repeated using PCL films modified incubated in *N*[1]-(3-trimethoxysilylpropyl)diethylenetriamine (N3S) post air plasma at 10 and 25 W discharge powers. Although, no significant difference in absorbance was found between conditions, the average absorbance value measured was higher on PCL samples modified with air plasma at 10 W compared to 25 W discharge power. Conclusions drawn from the data maybe somewhat limited due to the high temperature used in the Ninhydrin assay. PCL samples were incubated at 90 °C which is above the melting point of PCL at 60 °C which led to partial melting of the PCL samples. However, the boiling point of in *N*[1]-(3-trimethoxysilylpropyl)-diethylenetriamine is 118 °C thus still present in the assay medium if released from the PCL surface upon melting of the polymer. This is in agreement with the literature as Cao *et al.* 2017 and Hanuman *et al.* 2021 report methods in which aminated PCL scaffolds were heated in 1M ninhydrin solution up to 75 °C in a water bath and subsequently dissolved in solvent either THF or chloroform to read the reduced ninhydrin salt solution at ~562 nm[296, 297].

Air plasma at a discharge power of 10 W were chosen as processing parameters for binding *N*[1]-(3-trimethoxysilylpropyl)-diethylenetriamine based on XPS and ATR-FTIR analysis and Ninhydrin assay results. As such final XPS analysis was performed on heparin sulfate (100 µg/mL) and GDNF (10 ng/mL) treated PCL films surface modified using air plasma at 10 W discharge power and subsequent covalent binding of *N*[1]-(3-trimethoxysilylpropyl)-diethylenetriamine to determine the reproducibility of the functionalisation method. In contrast to heparin and GDNF immobilised PCL

films using allylamine plasma functionalisation, wide survey scans identified a peak at ~169 eV for heparin and GDNF immobilised PCL modified with air plasma and N3S which is attributed to sulphur[289, 290] (figure 24). Furthermore, as shown in table 18, the atomic percentage of sulfur was calculated at an average of 0.7% for heparin and GDNF immobilised PCL films using air plasma and N3S linkage compared to 0.2% for allylamine plasma functionalized PCL films. The presence of the sulphur peak at 169 eV on wide survey scans and 0.5% increase in atomic concentration indicated that the alternative surface modification method could be used successfully immobilise bioactive factors heparin and GDNF compared to allylamine plasma modification. In fact, various studies using alternative methods to immobilise heparin to polymer surfaces reported low atomic concentrations of sulfur[289, 290] detected *via* XPS analysis compared to the present research. For example, Edlund *et al.* reported a sulfur concentration of 0.4 % when coupling heparin to PCL films using vapor-phase to graft acrylamide, followed by reduction of the amide groups[289]. A study by Wan *et al*. reported a 0.3 % increase of sulfur concentration when immobilising heparin onto PCL-keratin nanofibres using 1-(3-dimethylaminopropyl)-3-ethyl carbodiimide (EDC) and N-hydroxysuccinimide (NHS)[290].

In agreement with XPS results in section 2.3.5, ATR-FTIR and SEM-EDX analysis of N3S, heparin and GDNF treated PCL films detected nitrogen, silicon and sulfur surface functionalities providing supporting evidence of the reproducibility of the developed functionalisation method to immobilise bioactive factors. ATR-FTIR analysis revealed nitrogen and silicon functionalities on PCL films surface modified using air plasma and N3S. However, as seen in figure 31b, absorption at 1240 cm^{-1} assigned to asymmetric C-O-C stretching is a characteristic of PCL meaning that it is difficult to distinguish between this infrared radiation band and the band at 1230 cm^{-1} assigned to the SO_3^- asymmetric stretching[294] used to identify heparin. Shown in figure 35, SEM-EDX imaging

analysis revealed homogenous distribution of silicon and sulfur on N3S, heparin and GDNF treated PCL fibres indicating successful functionalisation at each step in the surface modification method in addition to homogenous distribution of the bioactive molecules on PCL microfibres.

An additional objective of this project was to decrease the hydrophobic surface properties of PCL. The hydrophobic surface properties of PCL lead to poor cell attachment and growth. Numerous studies report improved neuronal and Schwann cell attachment on PCL surfaces post surface modification utilising plasma modification or wet chemical methods[208, 209, 214-216, 267, 283]. In section 2.3.8, water contact angle analysis of air plasma and N3S bound PCL films showed increasing surface hydrophilicity after each step of surface functionalisation as the water contact angle decreased from an average of 84° for PCL to 35° for GDNF immobilised PCL.

Moreover, a further objective of the surface modification method developed was to provide sustained release of GDNF for at least 28 days corresponding to a key time period during peripheral nerve regeneration[50, 51, 60, 73]. PCL films were surface modified as described in 2.2.4-5. 10 ng/mL and 100 pg/mL GDNF treated PCL films were analysed *via* ELISA to investigate the protein release mechanism from surface modified films. GDNF immobilised films incubated at 37 °C indicated a burst release mechanism within 24 hours followed by sustained release for at least 6 days. ELISA analysis of 10 ng/mL and 100 pg/mL immobilised GDNF incubated at 4 °C indicated GDNF remained bound to PCL surfaces for at least 7 days as no GDNF was detected at each time point assessed. These results indicate that polymer scaffolds modified using air plasma and N3S linkage retain bioactive factors whilst stored at 4 °C. Furthermore, upon implantation to the injury site bioactive factors are released for at least 7 days. However, conclusions drawn from the data obtained is limited due to the short time period assessed *i.e*. 7 days and the use of PBS as incubation media.

2.4.2 Fabrication of highly aligned PCL microfibre scaffolds

The use of electrospun fibre scaffolds as intraluminal guidance structures within NGCs is an attempt to mimic the extracellular matrix (ECM) architecture. Studies have shown that providing contact guidance *via* aligned electrospun fibre scaffolds can significantly improve neurite growth *in vitro* and *in vivo*[165, 182, 183, 185, 197]. Collector speeds of 500, 600 and 800 rpm were assessed for achieving fibre diameters of 5 or 8 µm using constant parameters as described in 2.2.2. The average fibre diameter of 5 µm was chosen for *in vitro* studies and 8 µm was chosen for *ex vivo* studies based on previous reports[156, 191, 194, 195]. The fibre diameter post surface functionalisation was not investigated. Sandoval-Castellanos *et al.* evaluated fibre diameter post modification and found no significant differences between unmodified, air and allylamine plasma modified PCL microfibres[198]. SEM image analysis revealed a correlation between the collector speed during electrospinning and alignment of PCL fibres. Increasing fibre alignment was measured as collector speeds increased from 500 to 800 rpm. 77 % of fibres showed 0-2° angular difference between fibres using 800 rpm collector speed compared to 48 % of fibres showing 0-2° angular difference using 500 rpm collector speed (figure 34b). Surface topography is a property of nano- and micro-fibre scaffolds that can affect cell morphology, phenotype and adhesion[204-206]. SEM images of PCL electrospun microfibres with average diameters of 6 and 5 µm showed surface topographies of elliptic shape along elongated grooves in the fibre direction (figure 33) in correlation with our research groups previous analysis by Daud *et al*[191].

2.5 Conclusions

In this chapter, the efficacy of patented technology[272] using allylamine plasma deposition to electrostatically bind heparin and growth factors was analysed using XPS. The higher sensitivity of XPS allowed detection of low concentrations of 50 µg/mL heparin and 100 ng/mL GDNF

incubated on allylamine plasma modified PCL films. Silicon contamination and oxygen contamination was detected from survey and high resolution scans of allylamine plasma modified, heparin and GDNF treated PCL films (figure 8). Allylamine plasma treated TCP samples were analysed *via* XPS to investigate the oxygen contamination and efficacy of the allylamine plasma modification method. An increase in the oxygen-to-carbon ratio for allylamine plasma treated TCP compared to TCP indicated oxygen contamination (table 9). An extra peak position at ~406 eV, assigned to nitrate, on the N 1s spectra for allylamine plasma treated TCP provided additional evidence of oxygen contamination (figure 16). Contamination could be a result of technical equipment failure *e.g.* a leak allowing inlet of air into the reaction chamber, water vapour contamination in the reaction chamber, or reactive species on the surfaces of samples reacting with air upon removal from the reaction chamber.

An alternative surface modification was successfully developed for the immobilisation of heparin and GDNF using air plasma and long chain aminosilane. PCL films treated with air or argon plasma at different discharge powers of 10 and 50 W were analysed by XPS in order to elucidate which gas and discharge power resulted in exposure of the highest concentration of hydroxyl groups for binding *N*[1]-(3-trimethoxysilylpropyl)diethylenetriamine (N3S) or 11-aminoundecyltriethoxy-silane. High resolution scans of the C 1s region of treated PCL films indicated that air or argon plasma at 10 W exposed the highest concentration of hydroxyl groups of the PCL chain (table 15). A Ninhydrin assay was utilized to confirm the optimum gas and discharge power for binding 11-aminoundecyltriethoxysilane or *N*[1]-(3-trimethoxysilylpropyl)diethylenetriamine. For both aminosilanes assessed, highest concentrations were measured on PCL films modified with air plasma at 10 W (figure 21 and 22). Due to the low concentrations of sulfur detected on PCL surfaces treated with 50 µg/mL heparin sulfate, 100 µg/mL concentration was used in the characterisation

of air plasma and N3S surface functionalisation. XPS and ATR-FTIR analysis of N3S, heparin sulfate and GDNF (100 ng/mL) treated PCL films confirmed successful and reproducible immobilisation of all three compounds (see section 2.3.5-6). SEM-EDX was utilised to investigate the distribution of N3S, heparin sulfate and GDNF on the surface of PCL microfibres. Silicone was detected uniformly on PCL microfibres treated with N3S (figure 35a). Silicone and sulfur was detected uniformly on heparin and GDNF treated PCL microfibres (figure 35b and c).

Key findings:

1. Absence of the sulfur peak position ~169 eV and low sulfur concentration (0.1 - 0.2 %) from survey scans of heparin and GDNF treated PCL films indicated low deposition of the proteins when using allylamine plasma surface modification.

2. Carbon-to-oxygen ratios of unmodified PCL (3.0) versus heparin treated PCL films (2.9) indicated a thin or non-homogenous deposition of heparin when using allylamine plasma surface modification.

3. Oxygen-to-carbon ratios of unmodified PCL (0.28) versus allylamine plasma modified PCL films (0.39) indicated oxygen contamination of samples.

4. Extra peak positions of 400 eV and ~169 eV on XPS survey scans assigned to nitrogen and sulfur, respectively, confirmed the presence of N3S, heparin and GDNF on surface modified PCL films.

5. Higher concentrations of sulfur (0.7 %) were detected on PCL samples treated with heparin and GDNF when using chemical linkage of N3S compared to samples modified with allylamine plasma (0.1-0.2 %).

6. Successful fabrication of highly aligned electrospun PCL microfibres with 5, 6 or 8 µm average fibre diameters determined using SEM imaging.

7. Water contact angle analysis demonstrated increasing hydrophilic surface properties after each subsequent step of surface functionalisation using air plasma treatment and N3S linkage.

8. 10 ng/mL and 100 pg/mL GDNF immobilised PCL films showed a burst release mechanism within 24 hours followed by sustained release up to 6 days.

9. No release of GDNF was detected from 10 ng/mL and 100 pg/mL GDNF immobilised PCL films incubated at 4 °C over a 7 day period.

Chapter 3. *In vitro* analysis of GDNF immobilised PCL films

3.1 Introduction and chapter aims

In this chapter, the effect of five concentrations of GDNF immobilised to PCL films on NG108-15 neuronal cell differentiation is assessed compared to controls: TCP, NH_2^+ monolayer PCL, heparin-bound PCL and corresponding GDNF concentrations exogenously delivered *via* growth medium. The concentrations of GDNF assessed were as follows: 100, 10 and 1 ng/mL and 100 and 1 pg/mL. Concentrations were chosen based on previous research by Sandoval-Castellanos *et al.* [198, 288] in which they assessed neurotrophic factors, nerve growth factor (NGF) and brain-derived neurotrophic factor (BDNF) on neuronal cell differentiation of the PC12 cell line and chick dorsal root ganglia (DRG). The aforementioned concentrations were immobilised using the patented method[272] described in 2.2.3 and 2.2.6-7 As this method of immobilisation was found to have low-reproducibility due to technical faults the efficacy of the surface modification method developed using air plasma and (N3S) (described in 2.2.4-7) on NG108-15 neuronal cell differentiation was

subsequently investigated. The cytotoxicity of functionalized PCL surfaces at each step of both surface modification methods was assessed by measuring cell viability on day 7 *via* the Resazurin assay. The chapter aims are as follows:

- To compare the effects of controls TCP, NH2+ monolayer PCL, heparin-bound PCL and exogenous GDNF delivery to immobilised GDNF concentrations ranging from 100 ng/mL to 1pg/mL on average and maximum neurite length of NG108-15 neuronal cells.

- To compare the effects of controls TCP, NH2+ monolayer PCL, heparin-bound PCL and exogenous GDNF delivery to immobilised GDNF concentrations ranging from 100 ng/mL to 1pg/mL on NG108-15 neuronal cell viability.

- To identify a concentration of GDNF that promotes longest average and maximum neurite length *in vitro* for assessment in 3D nerve injury models (Chapter 4).

- To compare the effects of functionalized surfaces air plasma treated PCL, N3S-, heparin sulfate- and 100 ng/mL GDNF-bound PCL to TCP on average, maximum neurite length and viability of NG108-15 neuronal cells in order to assess the surface modification method efficacy.

3.2 Materials and methods

3.2.1 *In vitro* culture of NG108-15 neuronal cells on tissue culture plastic (TCP)

NG108-15 neuroblastoma x glioma rat/mouse hybrid neuronal cells (ECACC, Salisbury, U.K) were maintained in treated T75 flasks using 14 mL Dulbecco's modified eagle medium (DMEM, Sigma-Aldrich) supplemented with 10% (v/v) foetal calf serum (FCS), 100 units/mL penicillin (SLS) and 100 µg/mL streptomycin (SLS), 0.25 µg/mL antimycotic (amphotericin B) solution (Merck), and

2mM L- glutamine (Fisher-Scientific). Cells were passaged after reaching approximately 70-80% confluency. Trypsin (Merck) was used to detach cells from the flask surface. 10% (v/v) FCS DMEM was used to inhibit Trypsin and the cell suspension was pipetted into a universal tube to be centrifuged at 1000 rpm for 5 minutes. The supernatant was discarded, and the cell pellet was re-suspended in warm 10% FCS DMEM. Cell numbers were counted using a haematocytometer before seeding.

3.2.2 *In vitro* culture of NG108-15 neuronal cells on PCL films functionalized using allylamine plasma polymerisation

Neuronal cells were used experimentally within ten passages. Neuronal cells were seeded onto the following film conditions in triplicate: unmodified PCL, NH_2^+ coated PCL, heparin-bound PCL and GDNF-immobilised PCL, over three independent experiments. Cells were also seeded onto TCP as a control. A volume containing approximately 1 x 10^3 cells were seeded onto 10 mm diameter films in a 48 well plate in 10% (v/v) FCS DMEM. Cells were cultured in a humidified atmosphere incubator at 37 °C, 5% CO_2 for 48 h. At 48 h, 10% FCS DMEM was discarded from all conditions. To stimulate neurite extension DMEM supplemented with 100 units/mL penicillin and 100 µg/mL streptomycin, 0.25 µg/mL antimycotic (amphotericin B) solution, and 2mM L-glutamine (serum-free DMEM) was added to cells cultured on TCP, PCL, amine coated PCL, heparin-immobilised PCL and GDNF-immobilised PCL. In addition, 100 ng/mL, 10 ng/mL, 1 ng/mL, 100 pg/mL and 1 pg/mL GDNF in serum-free DMEM was added to cells cultured on unmodified PCL films as a control. Cells were cultured in an incubator at 37 °C, 5% CO_2 for 120 h. At 120 h, culture medium was discarded from the wells and cells were fixed to be immunolabelled.

3.2.3 *In vitro* culture of NG108-15 neuronal cells on PCL films functionalized using air plasma and silinization

NG108-15 neuronal cells were used experimentally within ten passages. Neuronal cells were seeded onto the following film conditions in triplicate: TCP, air plasma treated, N3S-, heparin sulfate- and 100 µg/mL GDNF-bound PCL, over three independent experiments. A volume containing approximately 1.5 x 10^4 cells were seeded onto 22 mm diameter films in a 12 well plate in 10% (v/v) FCS DMEM. Cells were cultured in a humidified atmosphere incubator at 37 °C, 5% CO_2 for 48 h. At 48 h, 10% FCS DMEM was discarded from all conditions. To stimulate neurite extension DMEM supplemented with 100 units/mL penicillin and 100 µg/mL streptomycin and 2mM L-glutamine (serum-free DMEM) was added to cells cultured on TCP, air plasma treated-, N3S-, heparin sulfate- and 100 µg/mL GDNF-bound PCL. Cells were cultured in an incubator at 37 °C, 5% CO_2 for 120 h. At 120 h, culture medium was discarded from the wells and cells were fixed to be immunolabelled.

3.2.4 Resazurin assay

A fluorometric resazurin reduction assay was used to indirectly measure metabolic activity rates of NG108 neuronal cells. For assessing the metabolic activity of neuronal cells cultured on allylamine plasma modified surfaces, 1 mM resazurin stock was prepared by adding 0.025 g resazurin sodium salt (Sigma-Aldrich) to 100 ml sterile phosphate buffered saline (PBS, Merck) in a class II biosafety cabinet. A 1 mM resazurin stock solution of resazurin salt in PBS was diluted to a working solution of 100 µM in assay-dependent culture medium. For assessing the metabolic activity of NG108-15 neuronal cells cultured on air plasma and N3S-bound surfaces a lower working concentration of 12.5 µg/mL was used. At day 7, PCL films were transferred to a fresh sterile well plate to ensure readings corresponded solely to cells attached to the film and warm resazurin working solution was added in an assay-dependent volume. Cells cultured on modified surfaces using allylamine plasma polymerisation, were incubated for 4 hours at 37 °C, 5% CO_2

covered in aluminium foil. Cells cultured on modified surfaces using air plasma and N3S, were incubated for 1 hour at 37 °C, 5% CO_2 covered in aluminium foil. The reduced formazan product was transferred in triplicate of 200 µl to a 96 well plate and the fluorescence read in a fluorescence plate reader at 540/635 nm. In order to determine background fluorescence from the culture medium, a control with no cells present on a PCL film and just the resazurin working solution was used. Background fluorescence readings were subtracted from all other fluorescence values. In addition to a blank control, a negative control was used to demonstrate cell death. For the negative control (sham control) cells were incubated in 0.1% (v/v) Triton for 20 minutes at room temperature to kill cells, the solution was discarded and resazurin working solution was added.

3.2.5 Immunolabelling NG108-15 neuronal cells

Cultured cells were fixed using 3.7% formaldehyde (Merck) and incubated for 30 minutes at room temperature. The formaldehyde was discarded, and the wells were washed thrice with PBS. Cells cultured on control and experimental PCL films were incubated in 0.1% (v/v) Triton for 45 minutes at room temperature. The triton was discarded, and each well was washed twice with PBS. Cells were incubated in 3% Bovine serum albumin (BSA, Merck) in PBS at room temperature for 30 minutes to block binding sites. 3% BSA was discarded, and cells were washed once with PBS. Cells were incubated for 24 - 48 h with mouse anti-βIII tubulin antibody (marker for neurites, 1:2000, Promega, UK) diluted in 1% BSA at 4º C. Primary antibody solution was discarded and cells were washed once with PBS. Cells were incubated with 10 µL aliquot of DAPI plus horse anti-mouse IgG antibody conjugated with Texas Red (2BScientific, 1:500) diluted in 1% BSA at room temperature for 2 – 3 h covered with aluminium foil. Secondary antibody solution was discarded, and cells were washed three times with PBS. Samples were stored in PBS covered with parafilm and aluminium foil at 4 °C.

3.2.6 Fluorescence microscopy of NG108-15 neuronal cells

Images were acquired *via* fluorescent microscopy (Zeiss Axioplan2 Imaging microscope with QImaging QI Click camera) using Image Pro-Plus software. Neuronal cells fixed on 2D PCL film samples were placed on a microscope slide with Vectashield® and imaged using a 10× objective lens. For imaging Texas Red labelled samples incident and excitation wavelengths λ_{ex} = 543 nm/ λ_{em} = 576 nm were used. DAPI labelled nuclei were visualised using incident and excitation wavelengths λ_{ex} = 750 nm/ λ_{em} = 480 nm. Images were captured as raw data files.

3.2.7 Image analysis

ImageJ (NIH, USA) post-processing software was used for minimal image processing, this included adjusting brightness/contrast and image exposure in order to improve neurite clarity. Neurites were measured using the segmented line and measure tool of ImageJ. A random area of the images was selected for analysis and the neurites of cell bodies that fell into a gridded area of 6 mm^2 were measured. Total number of cells, number of cells bearing neurites, maximum number of neurites per cell and average, maximum and minimum neurite length was measured.

3.2.8 Statistical analysis

Statistical comparisons between groups were made using GraphPad Prism (version 9.0 for Windows; GraphPad Software, San Diego, CA). Significance analysed by Kruskal-Wallis Dunn's multiple comparisons test for non-gaussian data or One-way ANOVA Tukey's multiple comparisons test for normally distributed data. Data was considered significantly different if $p < 0.05$.

3.3 Results

3.3.1 Effect of allylamine plasma surface functionalized PCL films on metabolic activity of NG108 neuronal cells

NG108-15 neuronal cells were seeded at a density of 1 x 10^3 cells per well onto TCP, PCL with GDNF supplemented serum-free DMEM, NH_2^+, heparin sulfate and GDNF functionalized PCL films in triplicate over three independent experiments. Neuronal cells were grown for 48 hours in 10% FCS DMEM to permit adhesion and proliferation and then in serum-free DMEM for 5 days to promote differentiation.

To assess the biocompatibility of GDNF functionalized PCL using allylamine plasma modification, a fluorometric resazurin reduction assay was used to indirectly measure the metabolic activity of NG108-15 neuronal cells cultured on heparin- and GDNF-functionalized films on day 7. The metabolic activity of neuronal cells cultured on heparin and GDNF functionalized PCL films was compared to those cultured on controls of TCP, allylamine plasma modified PCL and unmodified PCL plus serum-free media supplemented with GDNF concentrations corresponding to the immobilised concentrations. Figure 39 shows the relative fluorescence values from NG108-15 neuronal cells cultured on unmodified PCL and surface functionalized PCL. Pure PCL is not included as a control group as the cells did not attach to this material in each independent experiment. The relative fluorescence gives an indirect measurement of metabolic activity as the concentration of formazan product (fluorescent product) from the reduction of resazurin salt is directly proportional to the metabolic rate of the neuronal cells. As the data was non-gaussian nor log-normal, the median relative fluorescence value is given for each group. A Kruskall-Wallis Dunn's multiple comparisons test revealed no significant differences between groups. In general, the metabolic activity of neuronal cells cultured on PCL films surface functionalized with GDNF was higher compared to the corresponding GDNF concentration added to the serum-free medium

apart from the 1 ng/mL concentration. The metabolic rate was higher on amine-functionalized surfaces compared to heparin indicating decreased growth rates on heparin surfaces. Highest fluorescence measured was from neuronal cell cultures on 100 ng/mL GDNF-immobilised PCL films, followed by 100 pg/mL GDNF-immobilised PCL. Fluorescence measured for all PCL conditions were not significantly different from TCP indicating the material conditions were not cytotoxic to the NG108 neuronal cells. However, as the main objective of the functionalized PCL was to increase neurite growth, metabolic activity can infer the differentiation state of the neuronal cells because proliferating cells typically have higher metabolic rates compared to non-proliferating cells (*e.g.* differentiating or quiescent cells)[298].

3.3.2 Effect of allylamine plasma surface functionalized PCL films on NG108 neuronal cell differentiation

To examine the effect of surface functionalized PCL on neuronal cell differentiation, the neurite growth from NG108 neuronal cells was measured using fluorescence microscope images of the cells cultured on TCP, allylamine plasma-, heparin-, GDNF- functionalized PCL films and unmodified PCL films plus serum-free medium supplemented with corresponding immobilised GDNF concentrations assayed. Figure 40 shows the median neurite length of NG108 neuronal cells cultured on TCP and allylamine plasma surface functionalized PCL films. A Kruskal-Wallis Dunn's multiple comparisons test revealed significant differences between the average neurite growth of neuronal cells cultured on TCP compared to PCL functionalized with 100 ng/mL, 10 ng/mL and 100 pg/mL GDNF. Moreover, a similar trend to the metabolic activity was observed where the median neurite length measured was higher on PCL film surfaces functionalized with GDNF compared to unmodified PCL films plus differentiation medium supplemented with the corresponding GDNF concentrations. This trend can be visualised in figure 43c-l which shows

representative fluorescence micrographs of NG108-15 neuronal cells cultured GDNF-functionalized PCL and unmodified PCL with exogenous GDNF delivery of corresponding immobilised concentrations. In contrast to the metabolic activity, the neurite length increases on PCL surface functionalized with heparin (50 µg/mL) compared to allylamine plasma modified PCL. The highest median neurite length measured was on PCL films surface functionalized with 100 pg/mL GDNF followed by 100 ng/mL GDNF whereas the lowest median neurite length was measured on TCP.

Figure 41 shows the maximum neurite length measured on all surfaces assessed. The highest maximum neurite length was measured on PCL films surface functionalized with 100 pg/mL GDNF followed by 10 ng/mL. A non-parametric Kruskal-Wallis Dunn's multiple comparisons test revealed no significant differences between groups. A similar trend to the median neurite length was observed where the maximum neurite length measured was higher on PCL films surface functionalized with GDNF compared to unmodified PCL films plus medium supplemented with the corresponding GDNF concentration. In contrast to the median neurite length, the maximum length was higher on allylamine plasma modified PCL films compared to PCL surface functionalized with heparin.

The percentage of the neuronal cell population expressing neurites was calculated to further assess the neurotrophic effect of the different GDNF concentrations. The highest percentage of neuronal cells expressing neurites was seen on PCL films surface functionalized with 10 ng/mL GDNF followed by TCP. In correlation with the maximum neurite length, the percentage of neuronal cells expressing neurites was higher on allylamine plasma modified PCL films compared to PCL functionalized with heparin. The range for each material except TCP and PCL surface functionalized with 100 ng/mL, was high suggesting that neuronal cell differentiation response

within each condition was quite varied. This may be due to the surface modification method having low reproducibility due to technical faults as the XPS analysis suggests (see section 2.3.1). The percentage of neuronal cells expressing neurites is not an entirely reliable measure of neuronal cell differentiation as it relies on a total number of cells in the fluorescent image. For example, there may be 20 cells imaged on TCP and 10 of these cells are expressing short neurites whereas there may be 200 cells imaged on PCL films surface functionalized with GDNF and 60 cells are expressing long neurites giving percentages of 50% expression compared to 30%.

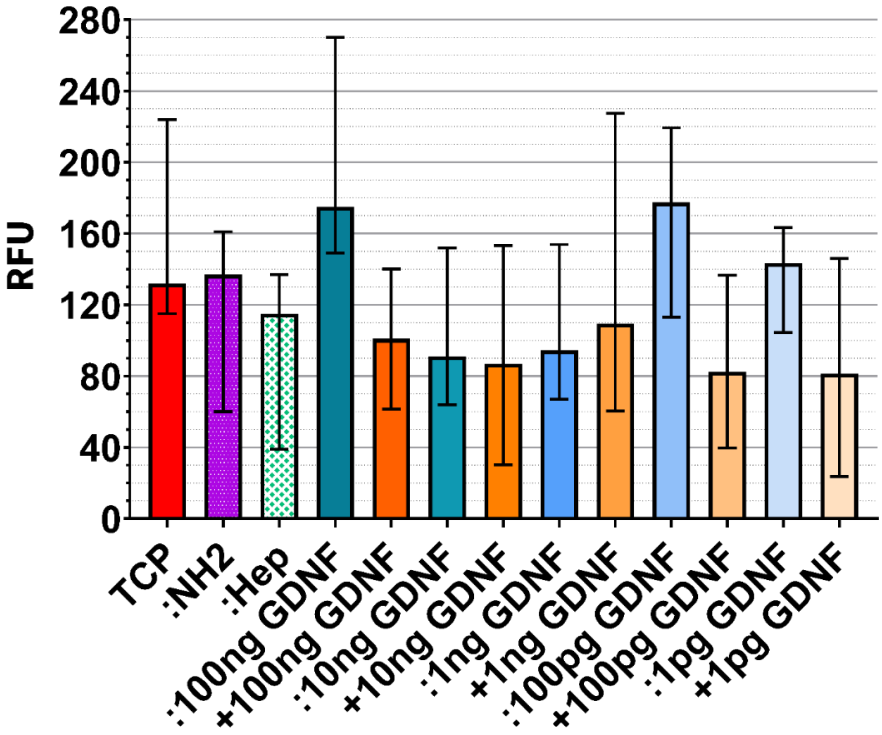

Figure 39. Resazurin assay relative fluorescence values of culture media day 7 from NG108 neuronal cell cultures grown under different conditions, TCP, unmodified PCL and surface modified PCL films. The colon prior to conditions represents films that have been functionalized via allylamine plasma. The plus represents unmodified PCL films where the GDNF concentration has been added to the differentiation culture media on day 5. The column graph displays the median measured from three independent experiments with triplicate used within experiments. Significance analysed by Kruskal-Wallis Dunn's multiple comparisons test revealed no significant differences between groups. Error bars = interquartile range.

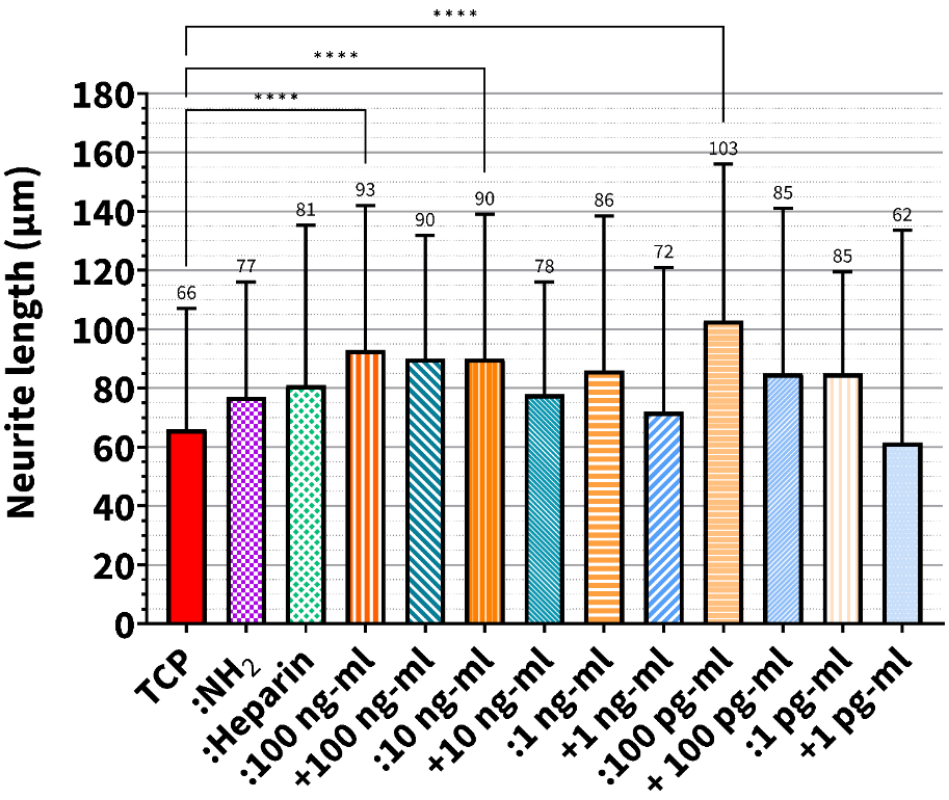

Figure 40. Median neurite length of NG108 cells cultured on TCP, unmodified PCL and surface modified PCL day 7. The column graph displays measurements from three independent experiments with triplicate used within experiments. Significance analysed by Kruskal-Wallis Dunn's multiple comparisons test and is displayed as **** p< 0.0001. The median is displayed above the error bars which show the 75th percentile.

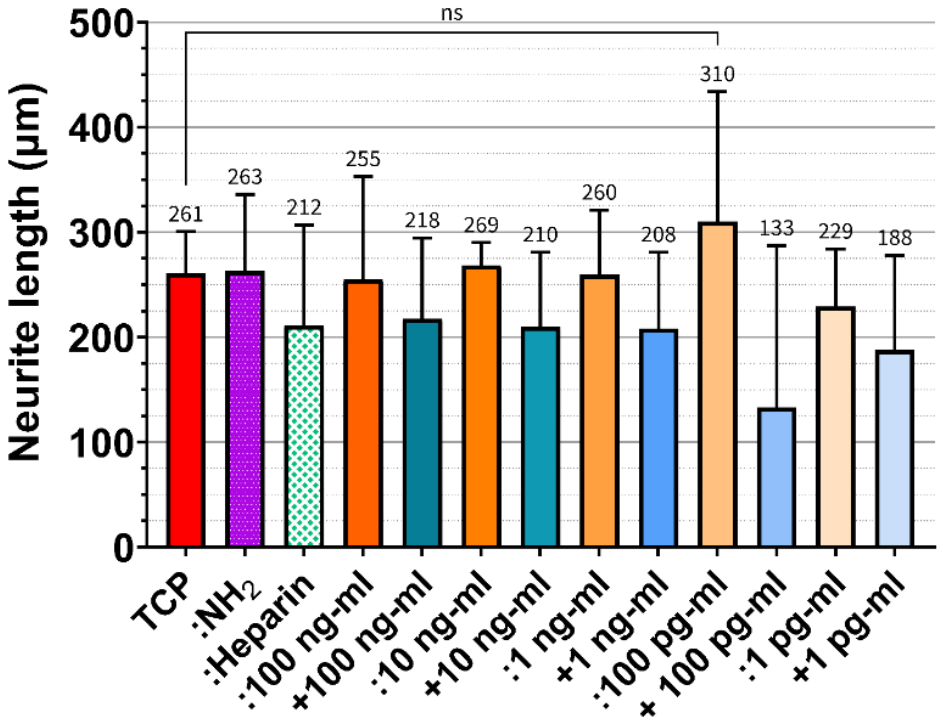

Figure 41. Maximum neurite length of NG108 cells cultured on TCP, unmodified PCL and surface modified PCL day 7. The column graph displays data from three independent experiments with triplicates used within experiments. Significance analysed by Kruskal-Wallis Dunn's multiple comparisons test revealed no significant differences between all groups and is displayed as ns p> 0.05. The median is displayed above the error bars which show the 75th percentile.

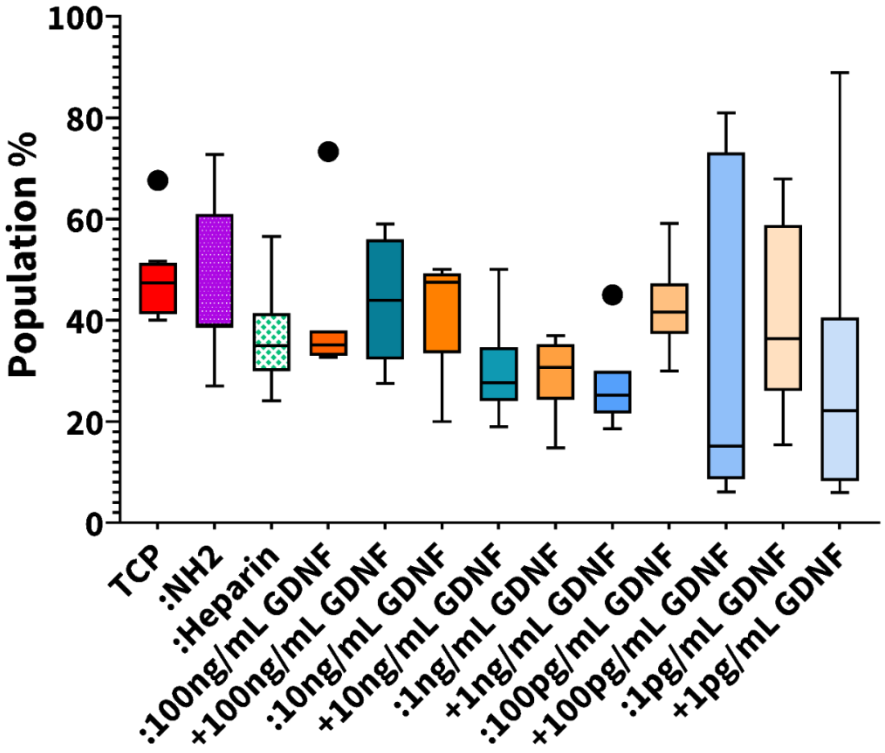

Figure 42.Percentage of NG108 neuronal cells expressing neurites cultured on TCP, unmodified PCL and surface modified PCL day 7. The box plot displays data from three independent experiments with triplicates used within experiments. Solid circles represent outliers and error bars = 25th and 75th percentiles.

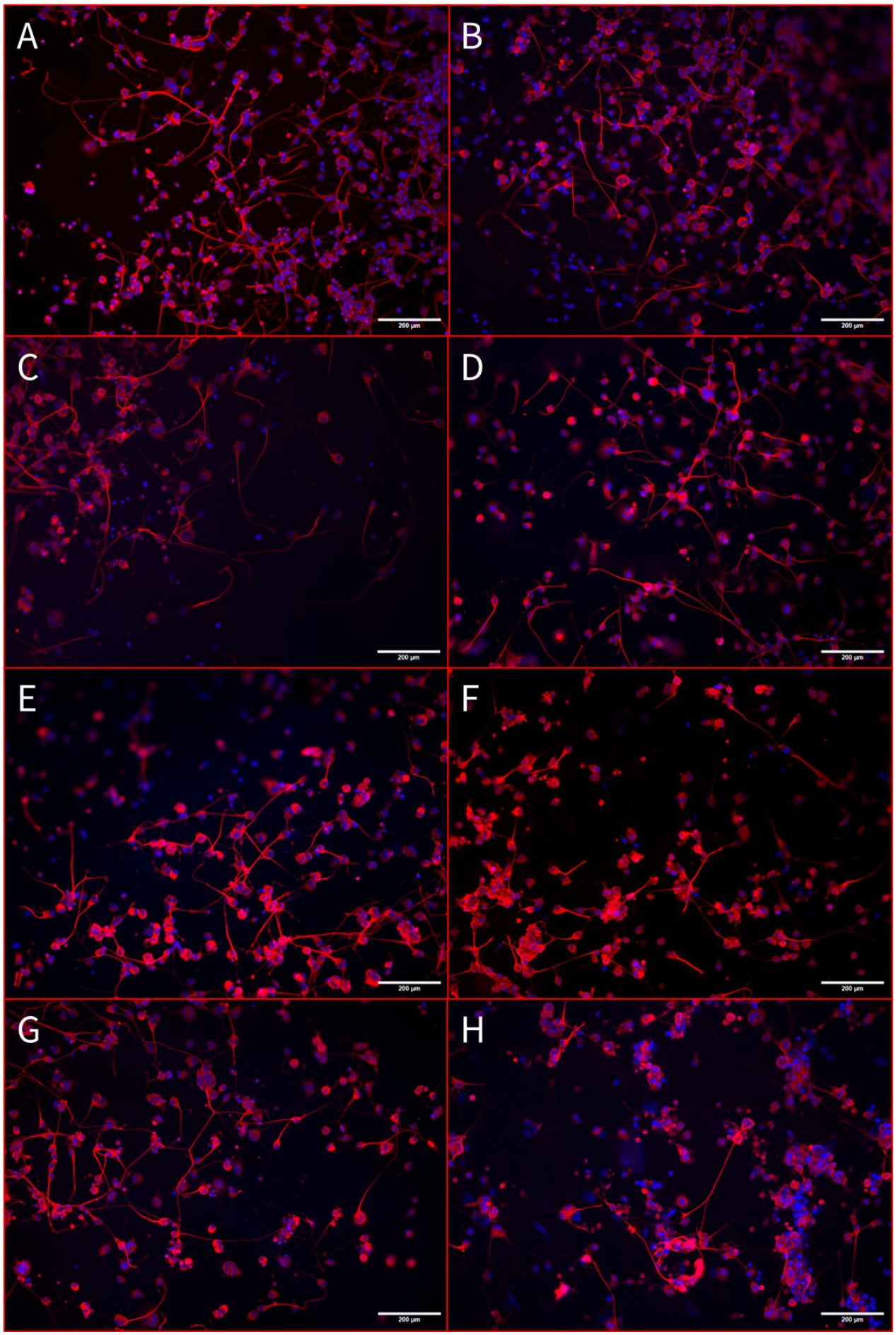
A
B
C
D
E
F
G
H
200 µm

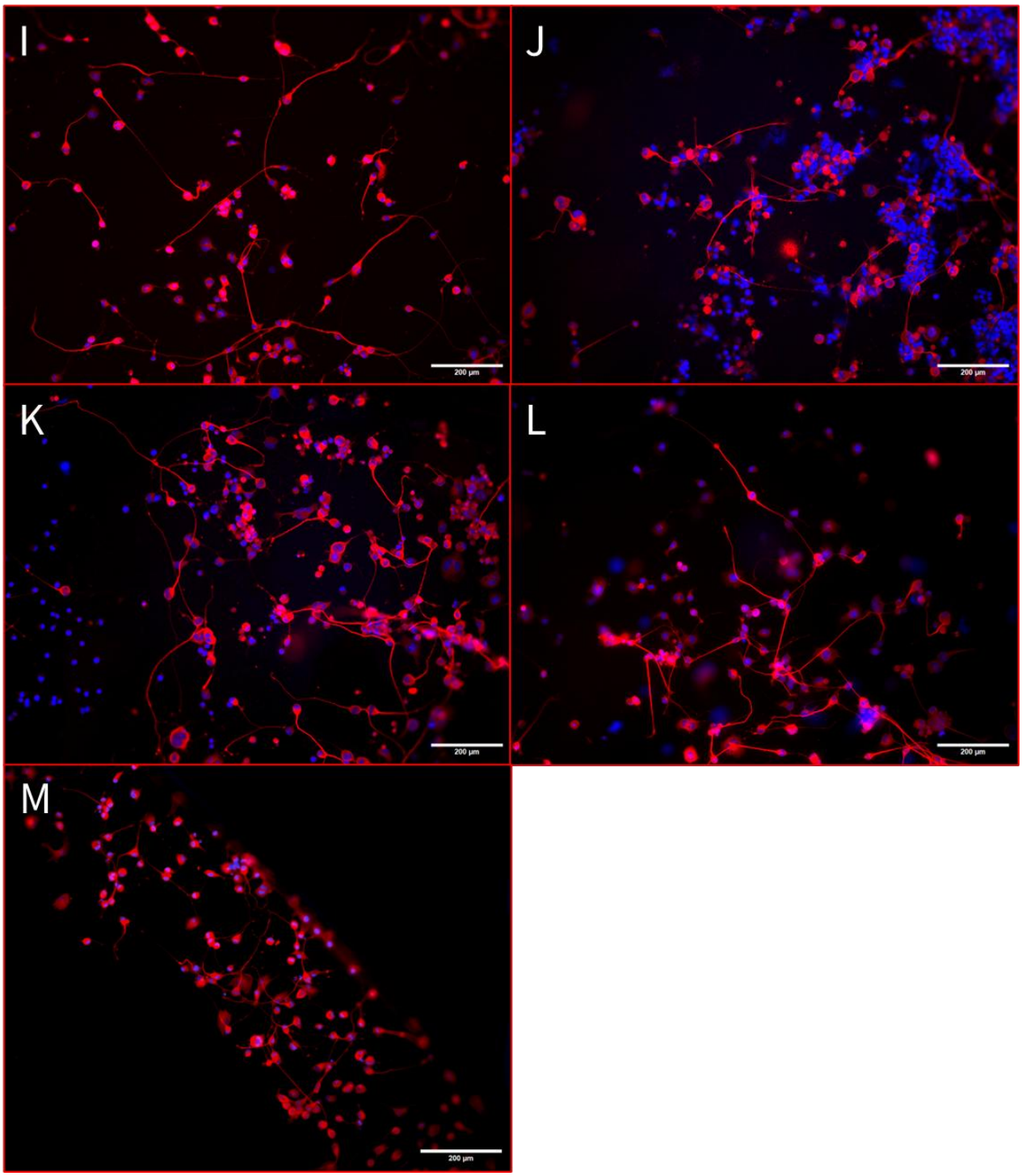

Figure 43. Representative epifluorescence micrographs of day 7 NG108-15 neuronal cells grown on surface functionalized PCL and PCL with exogenous GDNF delivery. A) NH_2^+ coated PCL; B) heparin-PCL; C) 100 ng/mL GDNF-immobilised PCL; D) 100 ng/mL GDNF-in solution PCL; E) 10 ng/mL GDNF-immobilised PCL; F) 10 ng/mL GDNF-in solution PCL; G) 1 ng/mL GDNF-immobilised PCL; H) 1 ng/mL GDNF-in solution PCL; I) 100 pg/mL GDNF-immobilised PCL; J) 100 pg/mL GDNF-in solution PCL; K) 1 pg/mL GDNF-immobilised PCL; L) 1 pg/mL GDNF-in solution PCL and M) TCP. Cell nuclei were directly labelled with 40,6-diamidino-2-phenylindole dihydrochloride (DAPI, blue) and neurites were immunolabelled against β-tubulin III (red). Seeding density = 1 x 10^3 cells, scale bar = 200 µm.

3.3.3 The effect of silane surface functionalized PCL films on metabolic activity of NG108 neuronal cells

NG108-15 neuronal cells were seeded at a density of 1.5 x 10^4 cells per well onto TCP, air plasma, *N*[1]-(3-trimethoxysilylpropyl)diethylenetriamine (N3S), heparin and 100 ng/mL GDNF functionalized PCL films in triplicate over three independent experiments. Neuronal cells were grown for 48 hours in 10% FCS DMEM to permit adhesion and proliferation and then in serum-free DMEM for 5 days to promote differentiation.

To assess the biocompatibility of PCL films surface modified using air plasma and covalently bonded N3S, a fluorometric resazurin reduction assay was used to indirectly measure the metabolic activity of NG108-15 neuronal cells cultured on TCP, air plasma treated PCL, N3S, heparin sulfate and 100 ng/mL GDNF surface functionalized PCL films on day 7. Figure 44a shows the representative metabolic activity (in relative fluorescence units) of neuronal cells cultured on TCP compared to functionalized PCL films. A One-way ANOVA Tukey's multiple comparisons test revealed a significant difference between TCP and all surface functionalized PCL groups with the highest metabolic activity measured on TCP. Each consecutive step of the surface functionalisation results in an increase in the relative fluorescence indicating somewhat increased biocompatibility of heparin sulfate- and GDNF-coated PCL compared to air plasma treated and N3S functionalized PCL.

3.3.4 The effect of silane surface functionalized PCL on NG108 neuronal cell differentiation

To assess the effect of the air plasma and N3S surface functionalized PCL films on neuronal cell differentiation, percentage population of cells expressing neurites, neurite length and maximum neurite length was measured from fluorescent images.

The highest percentage of neuronal cells expressing neurites was measured on TCP followed by GDNF surface functionalized PCL films (figure 44b). A decrease in the percentage of neuronal cells expressing neurites was measured on air plasma treated PCL compared to TCP and the lowest percentage measured was on N3S-bound films. However, the percentage of neuronal cells expressing neurites was seen to increase on heparin-bound films and increasing further on 100 ng/mL GDNF-bound PCL films.

Figure 45a shows the median neurite length measured from NG108 neuronal cells cultured on TCP compared to air plasma and N3S-surface functionalized PCL groups. A non-parametric Kruskal-Wallis Dunn's multiple comparisons test revealed a significant difference between the average neurite length measured on TCP compared to all surface functionalized PCL conditions except air plasma treated PCL. Each consecutive step of the surface functionalisation method up to heparin immobilisation resulted in an increase in median neurite length with the highest neurite length measured on heparin-bound PCL films. Unexpectedly, the median neurite length decreases slightly on 100 ng/mL GDNF immobilised PCL films. This trend can be visualised in figure 46 which shows representative fluorescent images of NG108-15 neuronal cells grown on all four surface functionalized PCL groups on day 7.

A similar trend was observed for the maximum neurite length measured on TCP versus surface functionalized PCL films. Figure 45b shows the maximum neurite length of NG108 neuronal cells cultured on TCP, air plasma and N3S surface functionalized PCL groups. A non-parametric Kruskal-Wallis Dunn's multiple comparisons test revealed no significant differences between the

maximum neurite length measured on TCP compared to the surface functionalized PCL groups. The highest maximum neurite length was measured on 100 ng/mL GDNF surface functionalized PCL dissimilar to the median neurite length. The lowest maximum length was measured on air plasma treated PCL films.

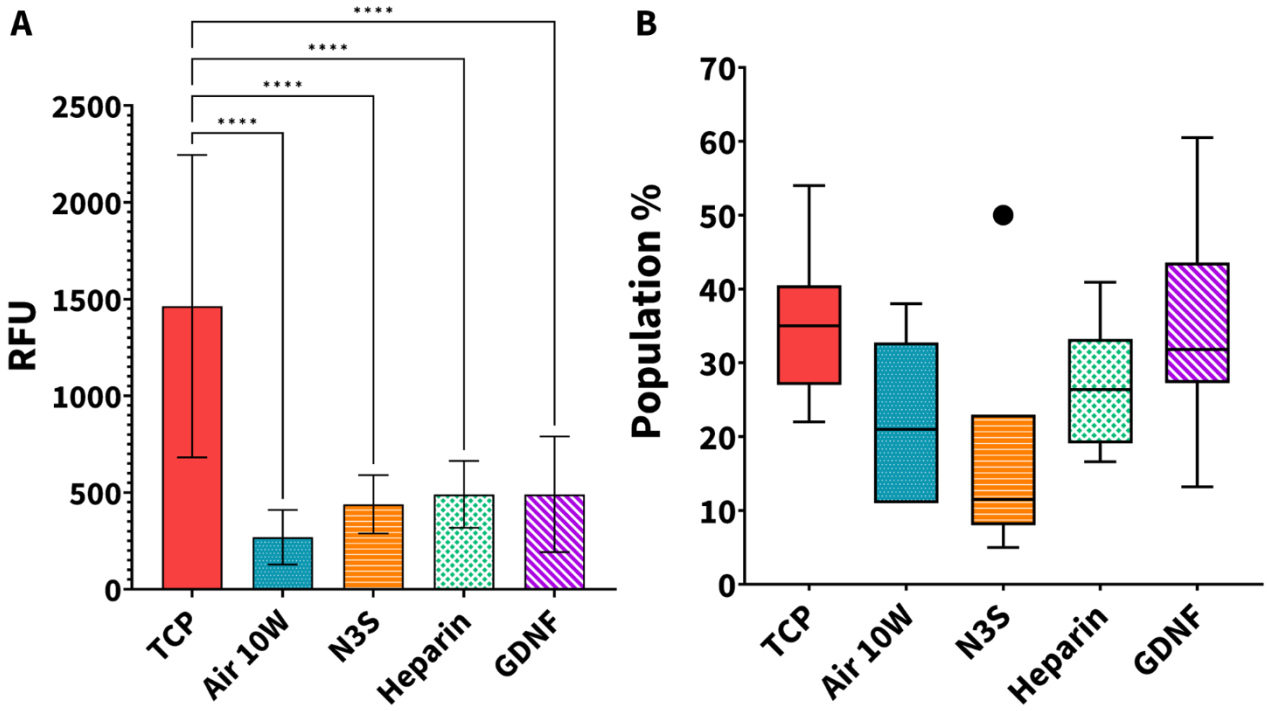

Figure 44. Resazurin assay was performed on day 7 for NG108 neuronal cells cultured on TCP and air plasma surface functionalized PCL (a). Percentage of NG108 neuronal cells expressing neurites on day 7 grown under different conditions, TCP and surface modified PCL films (b). PCL films modified as described in 2.2.4-7. The column graph and box plot display measurements from three independent experiments with triplicate used within experiments. Significance analysed by One-way ANOVA Tukey's multiple comparisons test and displayed as **** $p<0.0001$ (a). Error bars = standard deviation. Solid circles represent outliers and error bars = 25th and 75th percentiles (b).

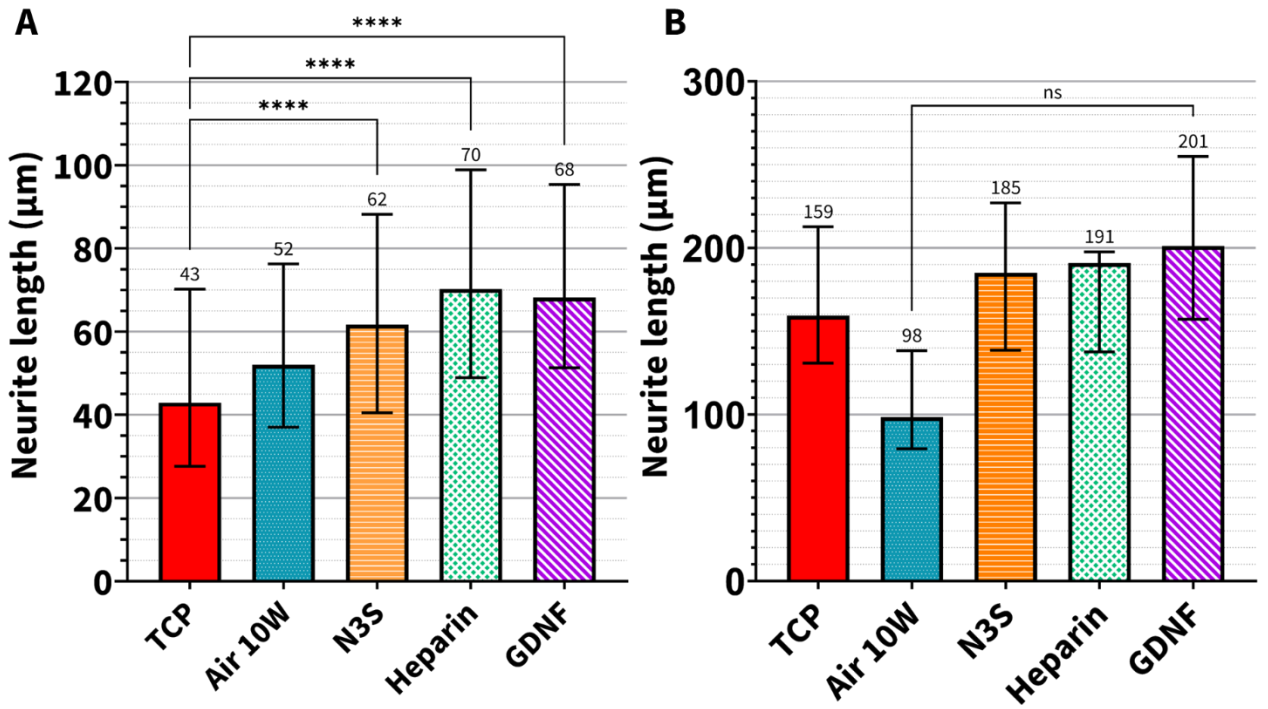

Figure 45. Median neurite length (a) and maximum neurite length of NG108 cells cultured on TCP and surface modified PCL films (b), day 7. The column graph displays measurements from three independent experiments with triplicate used within experiments. Significance analysed by Kruskal-Wallis Dunn's multiple comparisons test and displayed as ns $p > 0.05$, **** $p < 0.0001$ for. Error bars = interquartile range.

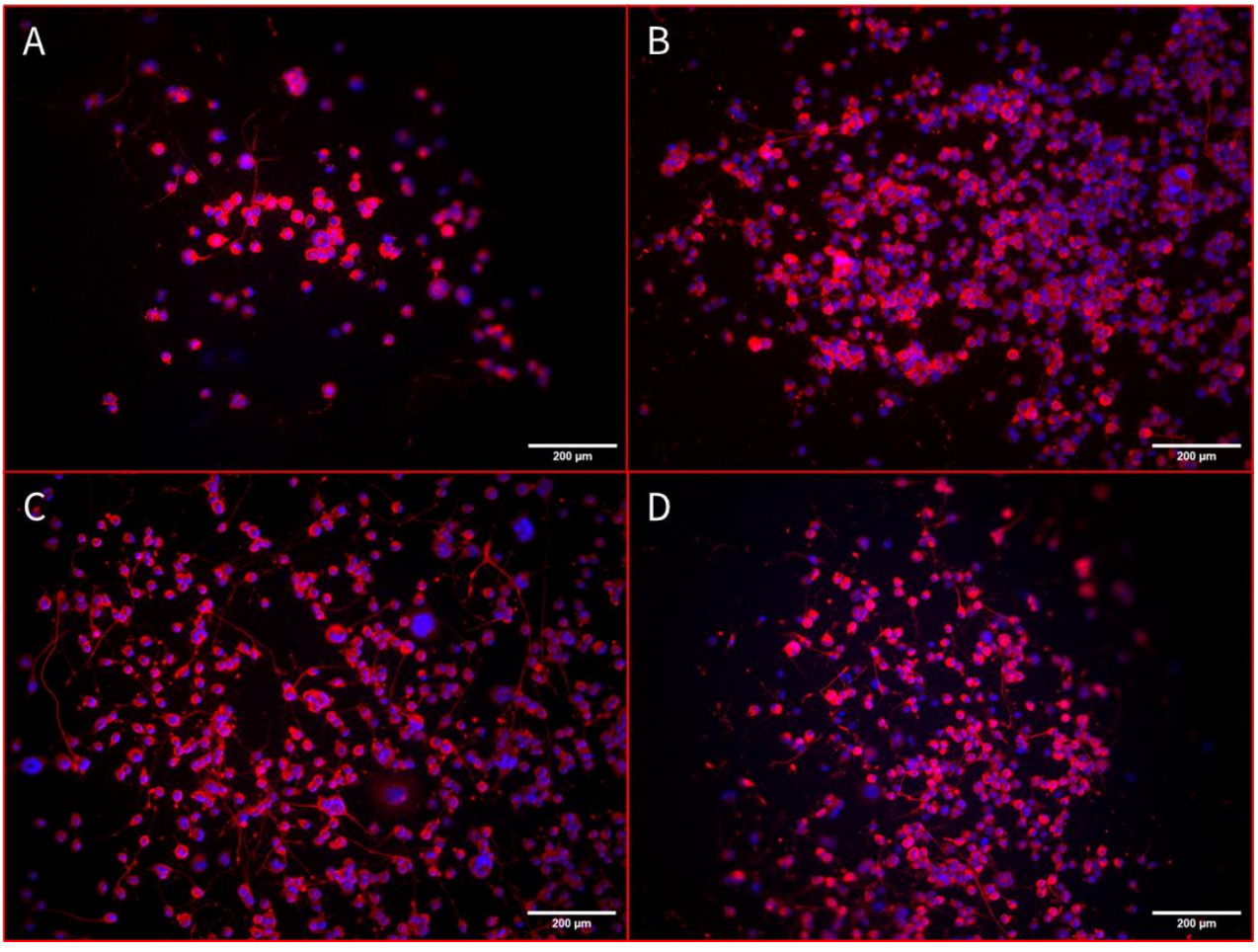

Figure 46. Representative epifluorescence micrographs of day 7 NG108-15 neuronal cells grown on surface functionalized PCL. Air plasma treated PCL (a), N3S bound-PCL (b), heparin bound-PCL (c) and 100 ng/mL GDNF-bound PCL (d). Representative fluorescence images of TCP can be found in figure 43m. Cell nuclei were directly labelled with 40,6-diamidino-2-phenylindole dihydrochloride (DAPI, blue) and neurites were immunolabelled against β-tubulin III (red). Seeding density = 1.5 x 104 cells, scale bar = 200 µm.

3.4 Discussion

One of the main objectives of this research was to investigate the neurotrophic effects of glial cell-derived neurotrophic factor (GDNF) on neurite outgrowth. GDNF has been shown to promote the survival of motor neurons *in vitro* and *in vivo*, preventing muscular atrophy and improving functional recovery[189, 236, 241, 258]. The focus of many studies on neurotrophic factor delivery is NGF because it plays a prominent role in sensory neuron regeneration[78, 79], however, there have been reports of greater neurotrophic effects of GDNF on sensory neurons when compared to NGF[258, 262].

GDNF concentrations ranging from 100 ng/mL to 1 pg/mL were immobilised using allylamine plasma surface modification as described in 2.2.3 and 2.2.6-7. TCP, -NH_2 monolayer, heparin sulphate immobilised and unmodified PCL films with GDNF supplemented medium were used as controls. A general trend was observed for median and maximum neurite lengths measured on immobilised GDNF compared to supplemented GDNF PCL films. All concentrations of immobilised GDNF assessed promoted higher neurite lengths compared to the corresponding concentration supplemented into growth medium as shown in figure 40. For example, 10 ng/mL immobilised GDNF promoted a maximum neurite length of 269 µm whereas 10 ng/mL GDNF supplement promoted a maximum neurite length of 210 µm. This is in agreement with the literature, Hu *et al.* 2016 observed greater neurite extension from PC12 neuronal cells when NGF was delivered locally from scaffold structures opposed to supplementation in growth medium[257]. No neurite length data were obtained for unmodified PCL film controls due to low attachment of the NG108-15 cell line.

However, Daud *et al.* 2012 reported a maximum neurite length of 109 ± 15 µm from NG108-15 neuronal cells on unmodified PCL films[191]. This value is 65% lower than the highest maximum neurite length measured in the present study on 100 pg/mL immobilised GDNF PCL films (310 µm). As shown in figure 41, a Kruskal-Wallis Dunn's multiple comparisons test revealed no significant difference between the highest maximum neurite length measured on 100 pg/mL immobilised GDNF PCL films compared to TCP (261 µm). The maximum neurite length of NG108-15 neuronal cells cultured on TCP is higher than reported in the literature. Daud *et al*. 2012 reported a maximum neurite length of 84 ± 22 µm from NG108-15 cell populations cultured on TCP. This is potentially due to differences in seeding densities compared to the present study.

As shown in figure 39, a resazurin assay on day 7 revealed no significant differences between NG108-15 neuronal cell metabolic activity on TCP compared to PCL films coated with heparin and GDNF using allylamine plasma deposition indicating that surface modifications were not cytotoxic. However, the metabolic activity of NG108-15 neuronal cell cultures on TCP were significantly higher compared to PCL films modified using air plasma and N3S immobilisation (figure 44a). This may infer the differentiation state of the neuronal cells because proliferating cells typically have higher metabolic rates compared to non-proliferating cells (*e.g.* differentiating or quiescent)[298]. As shown in figure 45a, median neurite length increased with each step of surface functionalisation from air plasma modified PCL films to heparin immobilised films. Neurite lengths measured on N3S, heparin sulfate and 100 ng/mL GDNF immobilised PCL films were significantly higher than on TCP, steadily increasing from 43 µm (TCP) to 70 µm (heparin-PCL). Median neurite lengths were slightly lower on 100 ng/mL GDNF immobilised films at 68 µm compared to heparin immobilised PCL. In contrast, maximum neurite lengths were lowest on air plasma modified PCL at 98 µm and highest on 100 ng/mL GDNF immobilised PCL films at 201 µm.

Interestingly, comparison of median and maximum neurite lengths measured on -NH_2 monolayer surfaces, heparin and 100 ng/mL GDNF immobilised surfaces obtained using each surface functionalisation method revealed neurite lengths were higher on allylamine plasma modified surface conditions. For example, the median and maximum neurite lengths measured on -NH_2 monolayer PCL modified *via* allylamine plasma were 77 µm and 212 µm, respectively (figure 40 and 41). Comparison to -NH_2 monolayers obtained *via* air plasma and N3S immobilisation, median and maximum neurite lengths were lower at 62 µm and 185 µm, respectively (figure 45). Median and maximum neurite lengths of heparin immobilised PCL surfaces *via* allylamine plasma modification were 81 µm and 212 µm, respectively, compared to 70 µm and 191 µm for heparin immobilised *via* air plasma and N3S linkage. Data analysis of neuronal cell differentiation on air plasma and N3S immobilised PCL films is limited due to fewer controls as compared to the allylamine plasma modification study. Further investigation is required using control groups of unmodified PCL with GDNF supplemented medium and immobilised concentrations of 10 ng/mL and 100 pg/mL GDNF.

Comparison of the percentage of NG108-15 neuronal cell population expressing neurites on both surface modification methods revealed all conditions using both methods showed lower percentages of neuronal cells expressing neurites compared to TCP excluding 10 ng/mL GDNF immobilised using allylamine plasma plus heparin adsorption (figure 42 and 44b). This outcome is possibly due to differences in factors such as surface topography, substrate stiffness and surface chemistry between TCP and surface modified PCL films. For example, TCP is typically modified using air or oxygen plasma and has a smooth rigid surface providing focal adhesion points for cell attachment[299]. PCL films unmodified or surface modified are likely to have different surface roughness or structural characteristics compared to TCP impacting cell attachment and

differentiation[299]. PCL films are less rigid potentially affecting neuronal cell response *via* signalling pathways and gene expression[300]. In addition, as discussed in 2.3.1-2, non-uniform or low efficiency in surface modification can lead to poor binding efficiency of heparin sulfate or GDNF potentially limiting cellular response to GDNF signalling.

3.5 Conclusions

This chapter identified allylamine plasma surface functionalized PCL films including bound heparin sulfate (50 µg/mL) and GDNF surfaces supported the attachment and growth of NG108-15 cells as no significant differences were revealed by a Kruskal-Wallis Dunn's multiple comparisons test when comparing cell viability on TCP to the modified surfaces. In addition, GDNF-bound PCL was shown to improve the extent of NG108-15 neuronal cell differentiation compared to TCP as the median neurite length was higher in all GDNF-bound groups compared to TCP. Furthermore, NG108-15 neuronal cells were shown to successfully attach and grow on the second method of surface modification using air plasma treatment and *N*[1]-(3-trimethoxysilylpropyl)diethylenetriamine to bind heparin sulfate (100 µg/mL) and GDNF (100 ng/mL). However, in contrast to the primary surface medication using allylamine plasma, A One-way-ANOVA Tukey's multiple comparisons test identified a significant difference between the cell metabolic activity on TCP verses all surface functionalized PCL films using air plasma and N3S. This may infer the differentiation state of the neuronal cells because proliferating cells typically have higher metabolic rates compared to non-proliferating cells (*e.g.* differentiating or quiescent)[298]. GDNF surface functionalized PCL supported greatest neuronal cell differentiation compared to TCP and each subsequent step of the air plasma surface modification method.

Key findings

1. 100 ng/mL and 100 pg/mL bound GDNF resulted in highest median and maximum neurite length of NG108-15 neuronal cells.

2. Immobilisation of GDNF onto the PCL surface resulted in higher average and maximum neurite length compared to the corresponding concentration of exogenously supplied GDNF in growth medium.

3. Surface functionalisation of PCL using air and N3S aminosilane resulted in lower metabolic activity rates in NG108-15 neuronal cells compared to TCP.

4. Maximum neurite length was highest on 100 ng/mL bound GDNF compared to TCP, air plasma treated, N3S and heparin bound PCL surfaces.

Chapter 4. In vitro analysis of surface functionalized PCL scaffolds

4.1 Introduction and chapter aims

This chapter explores the effect of providing contact guidance in combination with local delivery of glial cell-derived neurotrophic factor (GDNF) on neuronal cell differentiation and Primary Schwann cell morphology. One of the main objectives of this research was to understand the effect of different concentrations of GDNF on neurite growth and to determine if the neurotrophic factor has potential use in nerve guidance conduits for peripheral nerve repair. Based on the median and maximum neurite length data presented in 3.3.2, GDNF concentrations 10 ng/mL and 100 pg/mL were chosen to assess the effect of GDNF on neurite growth of NG108-15 neuronal cell line and embryonic chick dorsal root ganglia (cDRG) explant nerve injury models. Heparin sulfate immobilised PCL films showed increased neurite length compared to TCP controls thus was chosen as a control group for comparison of aligned PCL microfibres. Heparin sulfate (100 µg/mL) and GDNF was immobilised to PCL microfibres using the method described in 2.2.4-7 using air plasma and 0.1 M *N*[1]-(3-trimethoxysilylpropyl)diethylenetriamine (N3S). Schwann cells are known to play an important role in peripheral nerve regeneration, degrading myelin and degenerating axons, providing axon guidance *via* the bands of Büngner and releasing neurotrophic factors to provide hepatotactic cues. As such, it's important to develop intraluminal guidance structures that support the proliferation and growth of Schwann cells as well as promoting axon growth. The ability of functionalized PCL microfibres to support Schwann cell growth and differentiation was assessed *via* the analysis of primary Schwann cell morphology. Schwann cells were isolated from the trigeminal ganglia (TG) of thy-1-YFP-H transgenic mice strain. Finally, heparin and 10 ng/mL GDNF immobilised aligned PCL microfibres were combined with microporous poly(glycerol sebacate) (PGS) conduits fabricated by PhD candidate, Louis Johnson and to be tested *in vivo*

using the thy-1-YFP-H mice strain. Surface functionalized aligned PCL microfibre scaffolds of average diameter 8 µm were fabricated by PhD candidate, Rebecca Lomax and were inserted into microporous PGS conduits at a 5 % fibre density for evaluation in a 5 mm sciatic nerve injury gap model to be performed by Louis Johnson. The chapter aims are as follows:

- Examining the effects of GDNF immobilised-PCL microfibre scaffolds: 10 ng/mL and 100 pg/mL on NG108-15 neuronal cell differentiation.
- Examining the effects of aligned PCL microfibre scaffolds versus TCP surfaces on primary Schwann cell morphology isolated from thy-1-YFP-H transgenic mice strain.
- Examining the effects of GDNF immobilised-PCL aligned microfibres on embryonic chick dorsal root ganglion explant neurite outgrowth compared to 2D TCP surfaces and heparin-immobilised PCL microfibres.

4.2 Materials and methods

4.2.1 PCL microfibre scaffold preparation

4.2.1.1 PCL microfibre scaffold fabrication

PCL microfibres were fabricated as described in section 2.2.2. A summary of the parameters used to generate 5, 6 and 8 µm PCL fibres are shown in table 3. Fibre scaffolds with an average of 5 µm were used for the culture of primary neurons and Schwann cells dissociated from the trigeminal ganglia of thy-1-YFP-H transgenic mice. Fiber scaffolds with an average of 6 µm were used for the culture of NG108-15 neuronal cell line. Fibre scaffolds with an average of 8 µm were used for the culture of embryonic chick DRGs and *in vivo* analysis.

4.2.1.2 Combining microporous PGS nerve conduits and aligned microfibres

Microporous PGS nerve conduits were created by Louis Johnson for combination with heparin and GDNF functionalized PCL microfibre scaffolds for *in vivo* assessment in thy-1-YFP-H transgenic mice nerve injury models. In order to fill 5 mm long conduits with a 5 % fibre density, electrospun fibres were cut into 10 mm x 150 mm strips and removed to be weighed. Fibre density was calculated using a method based on fibre weight. Using average conduit lumen diameter of 1.1 mm and fibre length of 150 mm, the lumen volume was calculated (Equation 1).

Equation 1

$$V_{tube} = (\pi r^2)\, x\, l$$

r = radius of the internal diameter l = length of the fibre bundle

The fibre scaffold volume ($V_{fibre\ scaffold}$) that was required to the fill the conduit with a specific percentage of fibres was calculated as follows:

Equation 2

$$\boldsymbol{V_{fibre\ scaffold}\ (mm^3) = \frac{\%\ fibre\ density\ \cdot\ V_{tube}\ (mm^3)}{100}}$$

Using the fibre scaffold volume ($V_{fibre\ scaffold}$), the required weight of the PCL scaffold ($m_{fibre\ scaffold}$) was calculated using the following equation:

Equation 3

$$\boldsymbol{m_{fibre\ scaffold}\ (g) = V_{fibre\ scaffold}\ (cm^3)\ \cdot\ \rho_{PCL}}$$

ρ_{PCL} = PCL density = 1.145 g/cm^3

The fibre scaffolds of desired mass were then surface modified using methods described in 2.2.4-7 for *in vitro* and *in vivo* assessment. 4 mm length heparin (100 µg/mL) and GDNF (10 ng/mL) functionalized fibre scaffolds of 5 % density were threaded into 5 mm length microporous PGS conduits and kept in sterile sodium chloride 0.9 % (w/v) solution before surgery.

4.2.1.3 Air plasma treatment of PCL microfibre scaffolds

PCL microfibres were exposed to low-pressure air in a Diener Electronic Zepto plasma cleaner at 40 kHz, 10 W and 0.3 mbar for 120 seconds.

4.2.1.4 Silane modification of PCL microfibre scaffolds

Air treated PCL scaffolds were incubated in 0.1 M *N*[1]-(3-trimethoxysilylpropyl)diethylenetriamine (N3S; Sigma, UK) in 95% (v/v) propan-2-ol (Fisher Scientific, UK) in deionised water for 2 h. The supernatant was discarded and PCL fibre samples were washed in sterile PBS thrice.

4.2.1.5 Coating in heparin

N3S covalently bound PCL microfibres were incubated in an assay dependent volume of 100 µg/mL heparin sodium (Merck, UK) in PBS in a class II biosafety cabinet for 18 hours at room temperature. The supernatant was removed and samples were rinsed three times in sterile PBS before incubation in GDNF or left to dry in a class II biosafety cabinet overnight before culture.

4.2.1.6 Coating in GDNF

Heparin-immobilised PCL microfibre samples were incubated in 10 ng/mL or 100 pg/mL mouse GDNF (Antibodies.com Ltd, UK) in PBS. Samples were incubated in a class II biosafety cabinet for 5 hours at room temperature. The supernatant was discarded and the samples were rinsed three times in sterile PBS. Samples were then left to dry overnight in a class II biosafety cabinet before culture.

4.2.2 NG108-15 culture on PCL microfibre scaffolds

4.2.2.1 *In vitro* culture of NG108-15 neuronal cells on functionalized PCL microfibres

NG108-15 neuronal cells were used experimentally within ten passages. Neuronal cells were seeded onto the following conditions in triplicate over three independent experiments: TCP, heparin sulfate- and 10 ng/mL and 100 pg/mL GDNF-bound PCL microfibre scaffolds with average fibre diameter 6 µm and density of 5%. A volume containing approximately 2.0 x 10^3 cells were seeded onto 0.5 x 0.5 mm scaffolds in a 96 well plate in 10% (v/v) FCS DMEM. Cells were cultured in a humidified atmosphere incubator at 37 °C, 5% CO2 for 72 h. At 72 h, 10% FCS DMEM was discarded from all conditions. To stimulate neurite extension DMEM supplemented with 100 units/mL penicillin and 100 µg/mL streptomycin and 2mM L-glutamine (serum-free DMEM) was added to cells cultured on TCP, heparin and GDNF functionalized PCL microfibres. Cells were cultured in an incubator at 37 °C, 5% CO2 for 120 h. At 120 h, culture medium was discarded from the wells and cells were fixed to be immunolabelled.

4.2.2.2 Immunocytochemistry labelling of NG108-15 neuronal cells

Cells were pre-fixed by removing half the volume of the culture medium and replacing with 3.7 % (v/v) paraformaldehyde (PFA; Thermo Fisher Scientific, UK) in PBS for 10 minutes at room temperature. The PFA solution was discarded and samples washed twice in PBS. 3.7 % (v/v) PFA in PBS was then added to microfibre culture samples for a further 10 minutes at room temperature. To permeabilise and block non-specific protein binding sites, samples were incubated in 0.5 % (v/v) Triton X-100 in PBS and 10 %wt Normal Donkey Serum (NDS) in PBS for 1 hour at room temperature. Samples were incubated in mouse anti-βIII Tubulin (1:300, BioLegend, UK) in 1% (v/v) NDS:PBS at room temperature for 60 minutes. The supernatant was discarded and samples were washed thrice in PBS for 5 minutes. Samples were then incubated in donkey anti-

mouse-FITC (1:200, Jackson ImmunoResearch) in 1% (v/v) NDS:PBS for 60 minutes in the dark at room temperature. The supernatant was discarded and samples washed thrice in PBS for 5 minutes each in the dark. Well plates were stored in PBS at 4 °C, wrapped in parafilm and aluminium foil. Scaffolds were mounted onto glass slides with Vectashield® and 1.5 mm thick coverslips then sealed using clear nail polish.

4.2.3 Primary trigeminal ganglia neuronal and glial cell culture

4.2.3.1 Animals and animal housing

All animal procedures were carried out in accordance with the Animals (Scientific Procedures) Act 1986, under valid UK Home Office project licence (PPL P34A34A7, licence holder: Prof F. Boissonade) and personal licence (PIL I13817520, licence holder: R. Lomax). Experiments were carried out with the thy-1-YFP-H transgenic mice strain.

4.2.3.2 Animal preparation and trigeminal ganglia isolation

Mice were sacrificed by cervical dislocation and confirmed *via* permanent cessation of the circulation. The trigeminal ganglia (TG) were surgically removed immediately after sacrifice. The ganglia are located at the base of the skull as shown in figure 47. Isolated ganglia were kept in ice-cold, calcium- and magnesium- free Hanks' balanced salt solution (HBSS; Thermo Fisher Scientific, UK) with 1% (v/v) penicillin-streptomycin prior to digestion.

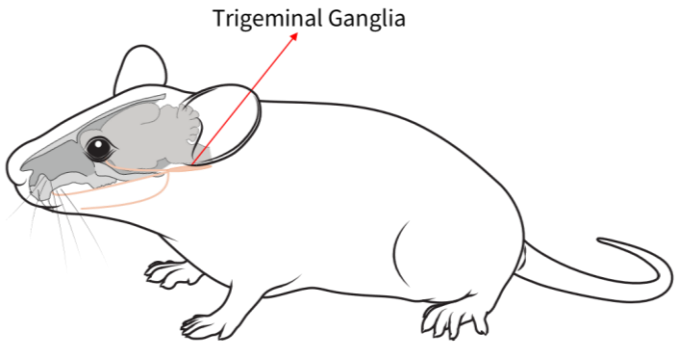

Figure 47.Surgical location of the trigeminal ganglia at the base of the skull.

4.2.3.3 Mouse trigeminal ganglia dissociation and culture

Isolated trigeminal ganglia were digested with warm 12.5 mg/mL Type IV collagenase (Sigma Aldrich) in Bottenstein and Sato medium[301] comprising of 1:1 DMEM: Ham's F12 supplemented with 10 % (v/v) FCS, 1 % (v/v) L-glutamine and 1 % (v/v) penicillin-streptomycin plus 40 units DNAse (2 units/µl) and 5 mM magnesium chloride for 60 minutes at 37 °C in a water bath. The TG solution was aspirated every 15 minutes to aid digestion. The solution was then centrifuged at 200 x g for 5 minutes. The digestion process was repeated with fresh, warm Type IV collagenase, DNAse and magnesium chloride in 1:1 10% FCS DMEM: Ham's F12. TG cells were homogenised by aspirating and centrifuged at 200 x g for 5 minutes. The cell pellet was resuspended in 10 % FCS Bottenstein and Sato medium and counted using Trypan blue (1:2) and a haemocytometer. 3 x 10^5 cells were seeded onto TCP or functionalized PCL microfibres in a 24-well plate. After 48 h the culture medium was replaced with 1:1 DMEM: Ham's F12 supplemented with 1 % (v/v) N2 supplement (Thermo Fisher Scientific, UK), 1 % (v/v) L-glutamate and 1 % (v/v) penicillin-streptomycin to promote neuronal cell survival and differentiation. Cells were cultured for a total of ten days at 37 °C, 5% CO_2. The culture medium was changed every 72h and cells were fixed on day 10.

4.2.3.4 Fixation of primary TG cultures

Cells were pre-fixed by removing half the volume of the culture medium and replacing with 3.7 % (v/v) paraformaldehyde (PFA; Thermo Fisher Scientific, UK) in PBS for 10 minutes at room temperature. The PFA solution was discarded and samples washed twice in PBS. TG cells were then fixed solely in 3.7 % (v/v) PFA in PBS for a further 10 minutes at room temperature. Samples were stored in PBS at 4 °C and sealed with parafilm.

4.2.3.5 Immunocytochemistry labelling of primary TG neuronal and glial cells

To permeabilise and block non-specific protein binding sites, samples were incubated in 0.5 % (v/v) Triton X-100 in PBS and 10 %wt Normal Donkey Serum (NDS) in PBS for 1 hour at room temperature. Samples were incubated in diluted primary antibodies, mouse anti-βIII Tubulin (1:300, BioLegend, UK) and rabbit anti-S100β (1:250, Proteintech, UK) in 1% (v/v) NDS:PBS at room temperature for 60 minutes. The supernatant was discarded and sampled were washed thrice in PBS for 5 minutes. Samples were then incubated in secondary antibodies, donkey anti-mouse-FITC (1:200, Jackson ImmunoResearch) and donkey anti-rabbit-Cy3 (1:200, Jackson ImmunoResearch) in 1% (v/v) NDS:PBS for 60 minutes in the dark at room temperature. The supernatant was discarded and samples washed thrice in PBS for 5 minutes each in the dark. Well plates were stored in PBS at 4 °C, wrapped in parafilm and aluminium foil. Scaffolds were mounted onto glass slides with Vectashield® and 1.5 mm thick coverslips then sealed using clear nail polish.

4.2.4 Embryonic chick dorsal root ganglia isolation and culture

4.2.4.1 Chick DRG isolation

Fertilised brown leghorn chicken eggs (*Gallus gallus domesticus*, Henry Stewart Co. Ltd., UK) were cleaned of pathogens using 20% industrial methylated spirit in deionised water (Fisher Scientific) and incubated at 37.5 °C in a humidified Rcom Suro 20 incubator with a 45° rotation each way every hour for 3 days. On day 3 the eggs were transferred to a 37.5 °C incubator (no CO_2) without rotation. The care of chick embryos was guided by the Home Office (UK) guidelines, where chick embryos were sacrificed before or on the latest embryo development day (EDD) 14. For experimental work, embryos were used on EDD 13. Eggs were cracked into a sterile Petri dish in a class II biosafety cabinet. Embryos were sacrificed *via* decapitation and the body transferred to a sterile petri dish. The body was placed ventral side up and internal organs were removed with forceps. The body was rinsed and kept hydrated with sterile PBS. Using no. 5 forceps, DRGs were

removed and placed in warm 10 % (v/v) FCS DMEM supplemented with 100 units/mL penicillin and 100 µg/mL streptomycin and 2mM L- glutamine. If the nerve root was attached, they were trimmed close to the DRG body using a scalpel. Throughout the dissection procedure, a wild M3Z Heerbrugg Switzerland dissection microscope was used.

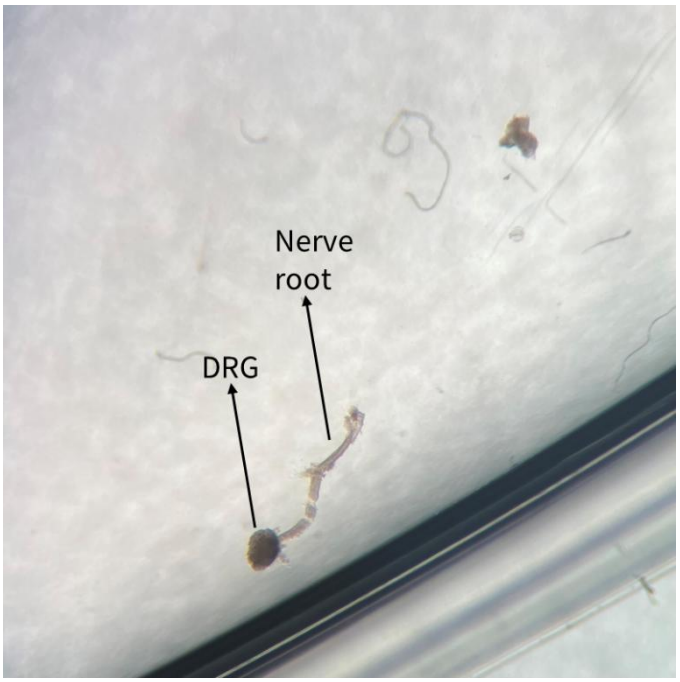

Figure 48. Optical microscope image of a dorsal root ganglion (DRG) dissected from a EDD 13 chick embryo submerged in sterile PBS.

4.2.4.2 Embryonic chick DRG explant culture

Using a P20 pipette a single DRG was placed onto 0.5 mm^2 functionalized PCL microfibre scaffolds with a fibre density of 5 % calculated based on fibre weight (see 4.2.1.2, equations 1-3). DRGs were left to attach in 50 µl of 10 % (v/v) FCS DMEM for 1h at 37 °C, 5 % CO_2. A further 150 µl of 10 % FCS DMEM was added and DRGs were cultured for 7 days at 37 °C, 5% CO_2 with media topped up every 72h. After 7 days DRGs were fixed and immunolabelled.

4.2.4.3 Immunocytochemistry labelling of chick DRGs

Cells were pre-fixed by removing half the volume of the culture medium and replacing with 3.7 % (v/v) paraformaldehyde (PFA; Thermo Fisher Scientific, UK) in PBS for 10 minutes at room temperature. The PFA solution was discarded and samples washed twice in PBS. 3.7 % (v/v) PFA in PBS was then added to microfibre culture samples for a further 10 minutes at room temperature. To permeabilise and block non-specific protein binding sites, samples were incubated in 0.5 % (v/v) Triton X-100 in PBS and 10 %wt Normal Donkey Serum (NDS) in PBS for 1 hour at room temperature. Samples were incubated in mouse anti-βIII Tubulin (1:500, BioLegend, UK) in 1% (v/v) NDS:PBS at room temperature for 24 hours. The supernatant was discarded and samples were washed thrice in PBS for 5 minutes. Samples were then incubated in donkey anti-mouse-Cy3 (1:200, Jackson ImmunoResearch) in 1% (v/v) NDS:PBS for 120 minutes in the dark at room temperature. The supernatant was discarded and samples washed thrice in PBS for 5 minutes each in the dark. Well plates were stored in PBS at 4 °C, wrapped in parafilm and aluminium foil. Scaffolds were mounted onto glass slides with Vectashield® and 1.5 mm thick coverslips then sealed using clear nail polish.

4.2.5 Fluorescence microscopy

Images of NG108-15 neuronal cells and primary Schwann cells cultured on aligned PCL microfibres were acquired *via* the Zeiss LSM880 AiryScan Confocal microscope. Images of chick DRGs cultured on aligned PCL microfibres and TCP samples were acquired *via* the Leica THUNDER Imager Live Cell microscope. All aligned PCL microfibre samples were mounted on a microscope slide with Vectashield® covered by a 22 x 22 mm coverslip sealed with clear nail polish for imaging using either a 5x or 10x objective lens. Incident and excitation wavelengths λ_{ex} = 554 nm/λ_{em} = 558 nm were used for imaging Cy3 immunolabelled samples. Incident and excitation wavelengths λ_{ex} = 489 nm/λ_{em} = 517 nm were used for imaging FITC immunolabelled samples. DAPI labelled nuclei

were visualised using incident and excitation wavelengths λ_{ex} = 350 nm/ λ_{em} = 452 nm. Images were captured as raw data files.

4.2.6 Fluorescence microscopy image analysis

ImageJ (NIH, USA) post-processing software was used for minimal image processing, this included adjusting brightness/contrast and image exposure in order to improve clarity. Neurites and primary Schwann cells were measured using the segmented line and measure tool of ImageJ. A random area of each image was selected for analysis and the neurites of cell bodies that fell into a gridded area of 950 μm^2 were measured. For measuring the aspect ratio of Schwann cells, the width and length of cells were measured within a random gridded area of 950 μm^2 of the image. For neurite extension analysis of embryonic chick DRGs, the longest neurite extension was measured from the edge of the cell body mass.

4.2.7 Statistical analysis

Statistical comparisons between groups were made using GraphPad Prism (version 10.2.3 for Windows; GraphPad Software, San Diego, CA). Significance was analysed by Kruskal-Wallis Dunn's multiple comparisons test for non-gaussian data or One-way ANOVA Tukey's multiple comparisons test for normally distributed data. Data was considered significantly different if $P < 0.05$.

4.3 Results

4.3.1 NG108-15 neuronal cell differentiation on GDNF-immobilised PCL microfibre scaffolds

NG108-15 neuronal cells were seeded at a density of 2 x 10^3 cells onto TCP, heparin-immobilised aligned PCL microfibres, 10 ng/mL and 100 pg/mL GDNF-immobilised aligned PCL microfibres in

triplicate over three independent experiments. Neuronal cells were grown for 72 hours in 10 % (v/v) FCS DMEM to permit adhesion and proliferation. At 72 hours the media was replaced with serum-free DMEM and neuronal cells were cultured for 5 days to promote differentiation. Aligned electrospun PCL fibres with an average fibre diameter of 6 µm were used and cut to dimensions of 5 mm^2. PCL electrospun microfibres were surface modified using the method described in 2.2.4-5 using air plasma and 0.1 M *N*[1]-(3-trimethoxysilylpropyl)diethylenetriamine (N3S). Heparin immobilised PCL microfibres were used as a control as heparin was shown to promote greater neuronal cell differentiation on PCL films compared to TCP (figure 45). 10 ng/mL GDNF and 100 pg/mL GDNF were chosen to be assessed as median and maximum neurite lengths measured on functionalized PCL films indicated these concentrations promoted greatest NG108 neuronal cell differentiation (see figures 40 and 41). The neurite length of NG108-15 cells was measured using fluorescence micrographs to assess the effect of the bioactive PCL microfibres on neuronal cell differentiation. Neurites were immunolabelled against β-Tubulin III and can be visualised in green. Figure 49a shows the median neurite length measured on TCP compared to heparin and GDNF immobilised PCL microfibres. The median neurite length was used as the data was found to be neither normally distributed nor log-normal. A Kruskal-Wallis Dunn's multiple comparisons test revealed no significant differences between groups however, the greatest median neurite length was measured on heparin and 10 ng/mL GDNF surfaces. Figure 49b displays the maximum neurite length measured on TCP compared to surface functionalized PCL microfibres where no significant differences were found upon analysis using a Kruskal-Wallis Dunn's multiple comparisons test. The median neurite length measured on 100 pg/mL GDNF microfibres was the second lowest yet the highest maximum neurite length measured. The median and maximum neurite length indicates that heparin and 10 ng/mL GDNF immobilised PCL microfibres are potential intraluminal scaffolds to be investigated *in vivo* nerve injury models.

In order to investigate the question; 'do aligned microfibres promote greater neurite growth compared to 2D culture surfaces?', the neurite lengths measured on surface functionalized PCL aligned microfibres were compared to PCL films and are shown in figure 50. A general trend can be observed when comparing median neurite length measured on heparin and GDNF immobilised PCL films and aligned microfibres. Median neurite length was greater on heparin and 10 ng/mL GDNF immobilised PCL microfibres compared to corresponding PCL films. Moreover, a significant difference was revealed between median length measured on heparin immobilised PCL films and immobilised aligned microfibres *via* Kruskal-Wallis Dunn's multiple comparisons test. Of particular note is the 2-fold increase in maximum neurite length measured on heparin immobilised aligned PCL scaffolds compared to heparin immobilised films. The maximum neurite length displays a much clearer trend as neurite lengths were higher on bioactive aligned microfibres for all groups analysed, however, no significant differences were found.

As one of the objectives of nerve guidance conduits is to provide contact guidance to migrating cells and growing axons, the orientation of NG108-15 neuronal cells was investigated using fluorescent micrographs. Figure 51 displays representative images of neuronal cells cultured on TCP, heparin, 10 ng/mL and 100 pg/mL GDNF immobilised aligned PCL microfibres on day 8. NG108-15 neuronal cells were observed to be orientated in the direction of fibre alignment indicating that the PCL microfibres provided a suitable substrate to orient neuronal cell growth (figure 51b-c). In contrast, NG108-15 cells cultured on TCP were observed to be randomly orientated (figure 51a).

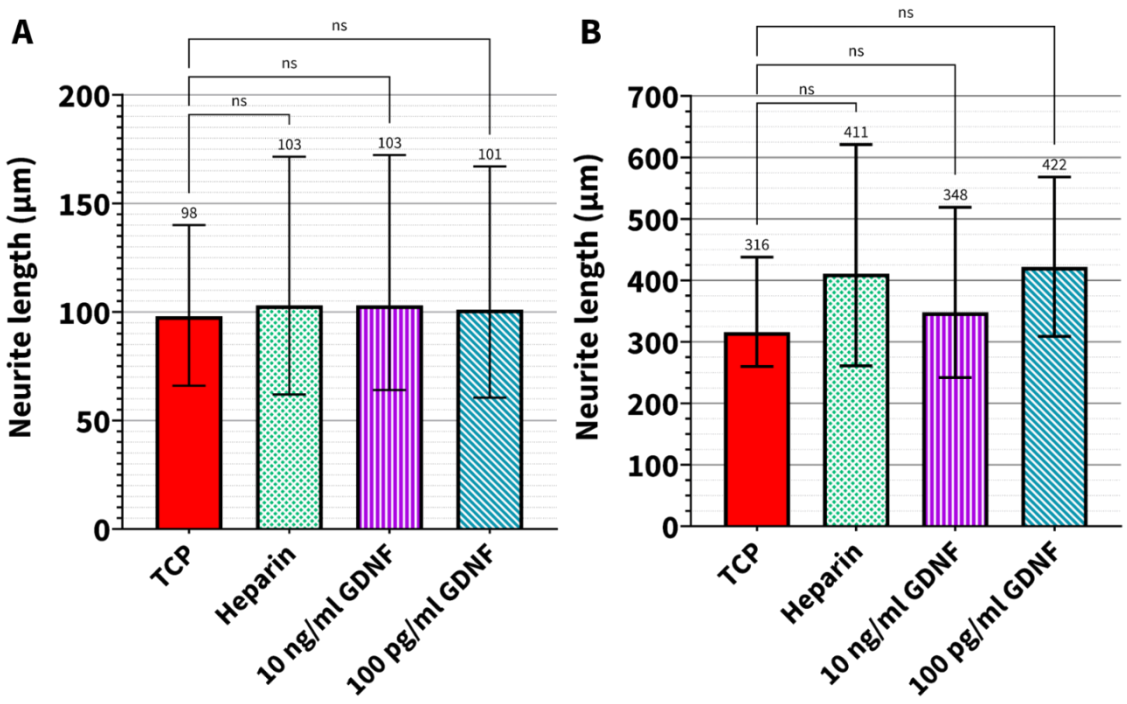

Figure 49. Median neurite length (a) and Maximum neurite length (b) of NG108-15 cells cultured on TCP versus surface functionalized PCL microfibre scaffolds day 8. The column graph displays measurements from three independent experiments with triplicate used within experiments. Significance analysed by Kruskal-Wallis Dunn's multiple comparisons test revealed no significant differences between groups and is displayed as ns $p > 0.05$ (ns). The median neurite length is displayed above the error bars which show the interquartile range.

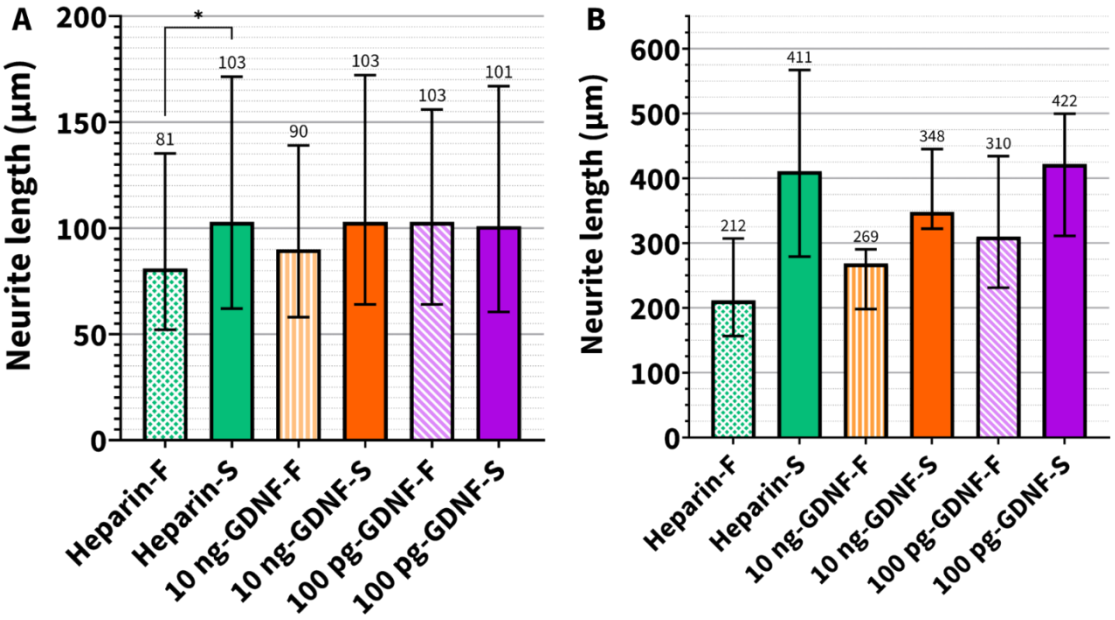

Figure 50. Median neurite length (a) and maximum neurite length (b) of NG108-15 cells cultured on surface functionalized PCL films (denoted by -F) versus surface functionalized PCL microfibre scaffolds (denoted by -S) day 8. The column graph displays measurements from three independent experiments with

triplicate used within experiments. Significance analysed by Kruskal-Wallis Dunn's multiple comparisons test and is displayed as * $p \leq 0.05$, error bars = interquartile range.

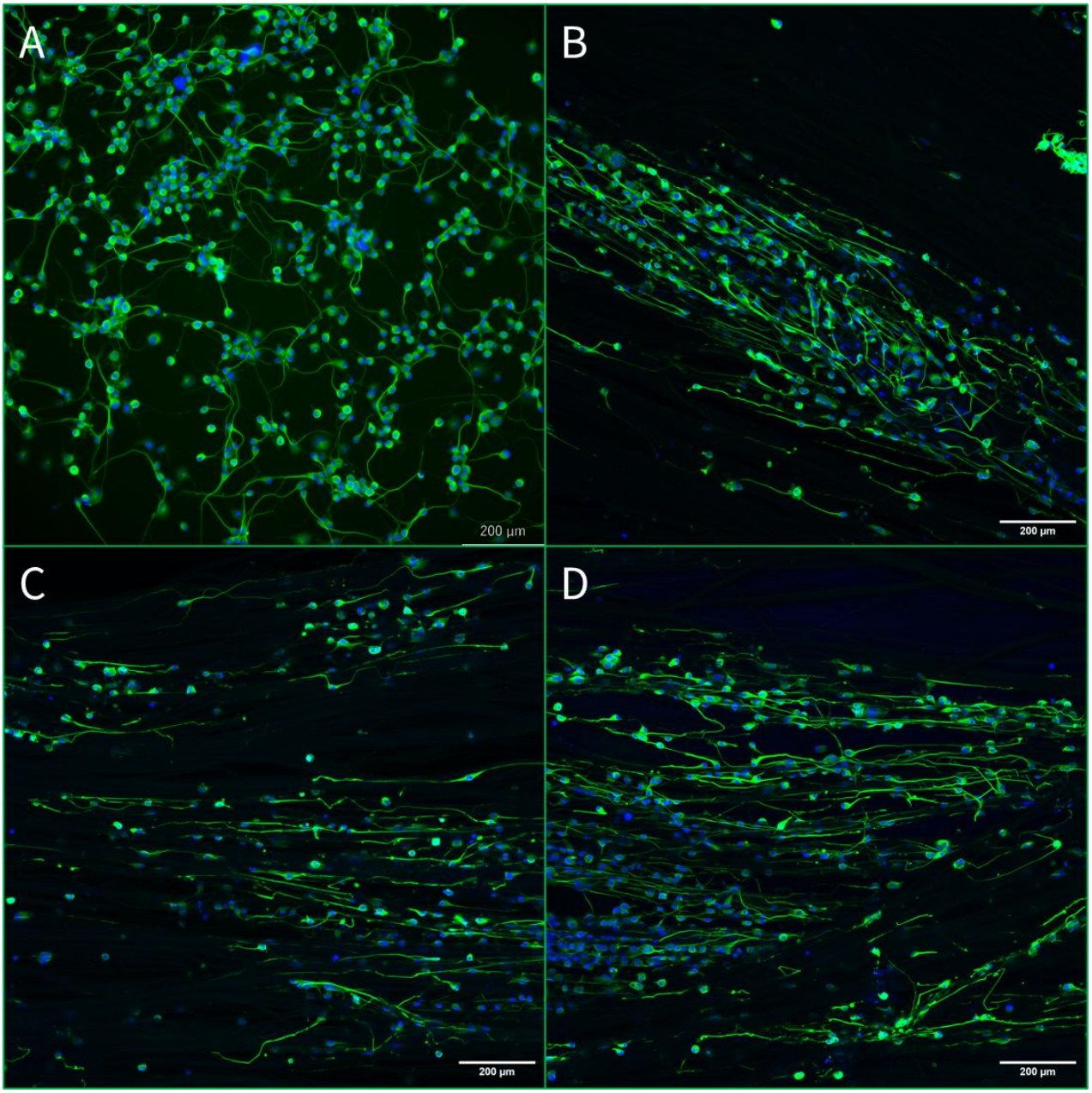

Figure 51. Representative fluorescent images of NG108-15 neuronal cells cultured on TCP versus surface functionalized PCL microfibre scaffolds day 8. TCP (a), Heparin sulfate bound PCL microfibres (b), 10 ng/mL GDNF bound PCL microfibres (c) and 100 pg/mL GDNF bound PCL microfibres (d). Cell nuclei were directly labelled with 40,6-diamidino-2-phenylindole dihydrochloride (DAPI, blue) and neurites were immunolabelled against β-tubulin III (green). Seeding density = 2.0 x 103 cells, scale bar = 200 µm.

4.3.2 Trigeminal ganglia Schwann cell morphology on surface functionalized PCL microfibre scaffolds

Schwann cells play an important role in peripheral nerve degeneration and regeneration post-injury, degrading myelin and axons, forming Bands of Büngner and releasing neurotrophic factors to guide regenerating axons. A key aspect to consider when developing intraluminal guidance scaffolds is providing cell recognition sites and trophic ques to migrating Schwann cells to support their function and promote their survival. Primary Schwann cells and neurones isolated from trigeminal ganglia (TG) of thy-1-YFP-H mice strains were cultured on 5 µm average diameter PCL aligned microfibres immobilised with heparin sulfate, 10 ng/mL and 100 pg/mL GDNF to assess the effect of aligned microfibres on Schwann cell morphology. Schwann cell morphology is indicative of the cell phenotype *i.e.* myelinating versus non-myelinating. Trigeminal ganglia cell cultures were seeded onto 10 x 20 mm scaffolds and cultured for 48 hours in 10 % (v/v) FCS 1:1 DMEM/Ham's F12 to promote attachment. The culture medium was replaced after 48 hours with 1 % (v/v) N2 supplemented 1:1 DMEM/Ham's F12 to promote neuronal cell differentiation. TG cells were cultured for 10 days before fixing and immunolabelling. Neurites were immunolabelled against β-Tubulin III (green) and Schwann cells were immunolabelled against S100β (red). The aspect ratio of primary Schwann cells cultured on TCP was measured and compared to functionalized aligned PCL microfibres. Figure 52a shows a representative fluorescence image of TG cells cultured on TCP. TCP supported growth of Schwann cells and neurons however, Schwann cell morphology was mixed on TCP surfaces. Schwann cells exhibited the characteristic bipolar spindle shape morphology but a high number of Schwann cells also exhibited a flattened circumferential morphology as well as tripolar-like morphology (highlighted area of figure 52a). Aligned PCL microfibres were observed to promote bipolar spindle shape morphology of TG Schwann cells illustrated by the significantly lower aspect ratio measured on all surface

functionalized PCL microfibre groups compared to TCP (figure 53a). This effect on Schwann cell morphology can be visualised in figures 52b and 53b-d.

Moreover, neuron morphology also differed between substrates. On TCP neurons were observed to have radial axonal outgrowth (figure 52a) whereas on aligned functionalized PCL scaffolds axons can be observed growing along the direction of fibre alignment (figure 52b, 53d). Few neurons were found on aligned PCL scaffolds and were observed only on heparin immobilised and 100 pg/mL GDNF immobilised aligned microfibres.

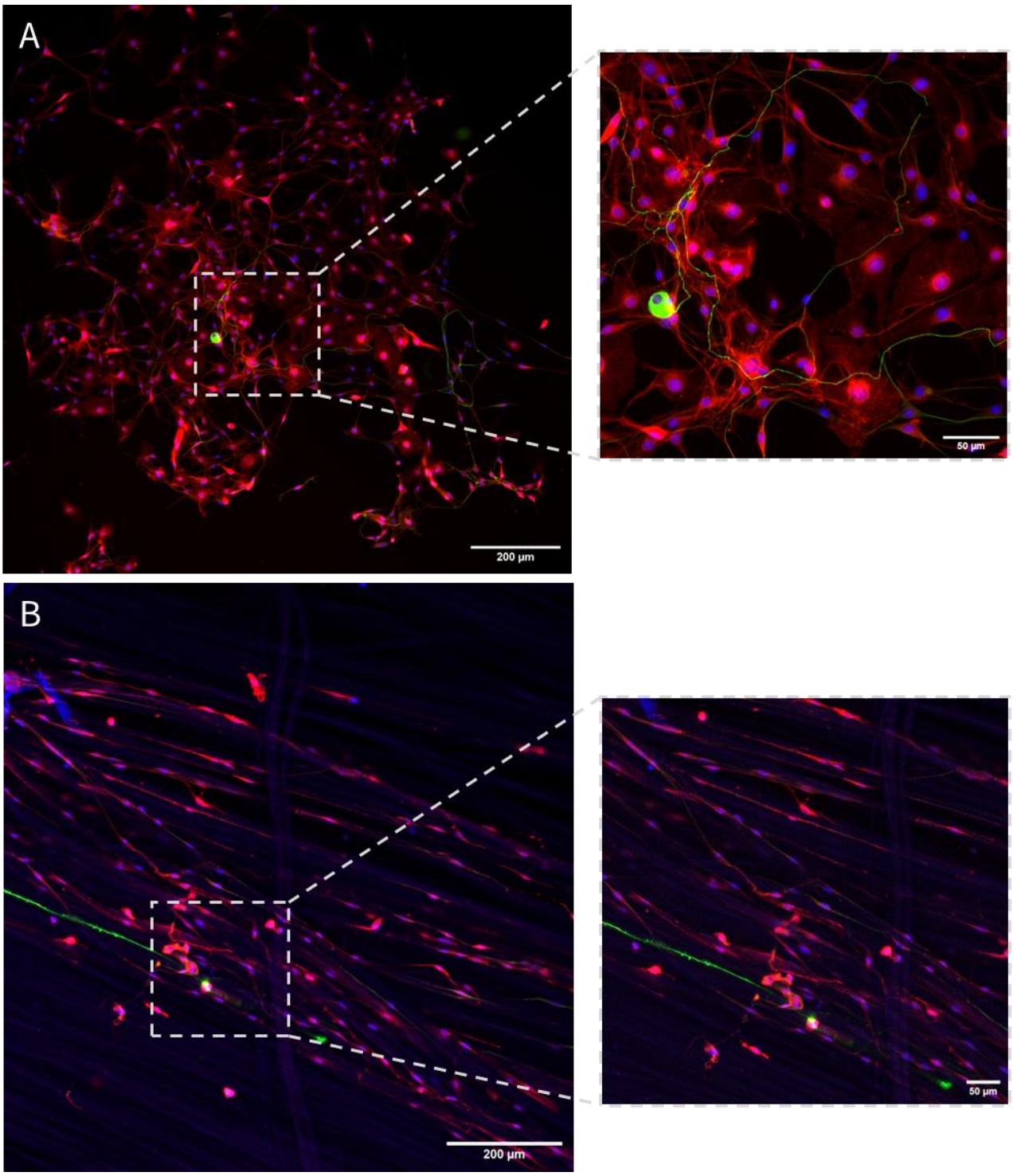

Figure 52. Representative fluorescent images of primary Schwann cells isolated from thy-1-YFP-H mice trigeminal ganglia cultured on TCP (a) and heparin immobilised PCL microfibres (b).

Cell nuclei were directly labelled with 40,6-diamidino-2-phenylindole dihydrochloride (DAPI, blue), neurites were immunolabelled against β-tubulin III (green) and Schwann cells were labelled against S100β (red). Neuronal and Schwann cell morphology is highlighted in the right hand side images. Left hand side scalebar = 200 µm, right hand side scale bar = 50 µm.

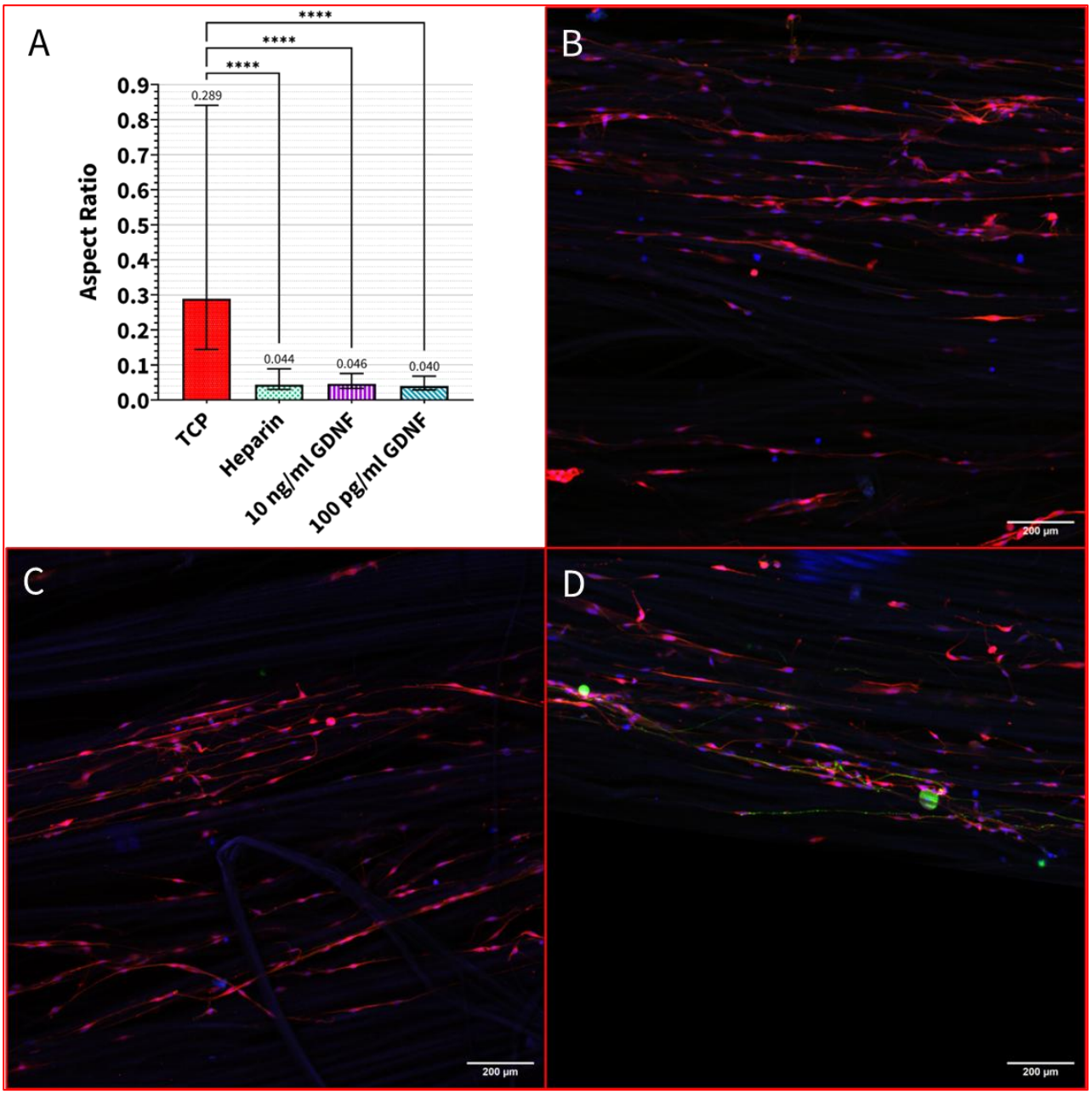

Figure 53. Aspect ratio of Primary Schwann cells isolated from thy-1-YFP-H mice trigeminal ganglia cultured on TCP, 10 ng/mL and 100 pg/mL GDNF immobilised PCL microfibres (a). Representative fluorescent images of primary Schwann cells cultured on 10 ng/mL GDNF immobilised PCL (b) and 100 pg/mL GDNF (c,d). Cell nuclei were directly labelled with 40,6-diamidino-2-phenylindole dihydrochloride (DAPI, blue), neurites were immunolabelled against β-tubulin III (green) and Schwann cells were labelled against S100β (red). Significance analysed by Kruskal-Wallis Dunn's multiple comparisons and are displayed as *** $p \leq 0.001$. Median aspect ratio is shown in the bar graph taken from triplicates over three independent experiments. Error bars = interquartile range and scale bar = 200 µm.

4.3.3 Embryonic chick dorsal root ganglion explant nerve injury model on GDNF-immobilised PCL microfibre scaffolds

The assessment of heparin, 10 ng/mL and 100 pg/mL GDNF immobilised PCL aligned microfibres gave varied results on the ability of the functionalized surfaces to promote NG108-15 neuronal cell differentiation. As such, the effects of heparin and GDNF immobilised PCL fibres were evaluated using an embryonic chick dorsal root ganglion nerve injury model as it provides more physiologically relevant conditions for comparison. Dorsal root ganglia (DRG) were isolated from chick embryos sacrificed on EDD 13 and were cultured on TCP, heparin sulfate (100 µg/mL), 10 ng/mL and 100 pg/mL GDNF immobilised PCL aligned microfibres in triplicate over three independent experiments. Aligned PCL microfibres with 8 µm average fibre diameter were cut to dimensions of 5 mm^2 and used at a fibre density of 5 % in order to mimic the dimensions and density used in thy-1-YFP-H mice *in vivo* assessments in collaboration with Louis Johnson. DRG were cultured in 10 % (v/v) FCS DMEM for 24 hours to promote attachment. After 24 hours media was replaced with serum-free DMEM and DRG were cultured for 6 days to allow neurite growth. Figure 54 displays a column graph of neurite extension from chick DRG cultured on TCP versus heparin and GDNF immobilised PCL microfibres. A Kruskal-Wallis Dunn's multiple comparisons test reveal a significant difference between neurite extension length on GDNF immobilised PCL microfibres compared to TCP. The longest neurite length was measured on 10 ng/mL GDNF immobilised PCL scaffolds which was significantly higher than TCP and heparin sulfate immobilised PCL scaffolds. Figure 55 shows representative fluorescence images of DRG cultured on all groups and highlights the effect of 10 ng/mL GDNF immobilised PCL scaffolds on neurite length compared to TCP. Neurites were immunolabelled against β-Tubulin III and can be visualised in red. A difference in morphology was observed with DRG cultured on PCL scaffolds exhibiting flattened morphologies (figure 55b and d) and circular morphologies (figure 55c). All

DRG cultured on TCP had circular morphologies (figure 55a) and often had no neurite extension after 7 days with some extending small neurites. This effect seen on TCP highlights the importance of intraluminal guidance structures for providing contact guidance and the addition of neurotrophic cues for increasing axonal growth in peripheral nerve regeneration.

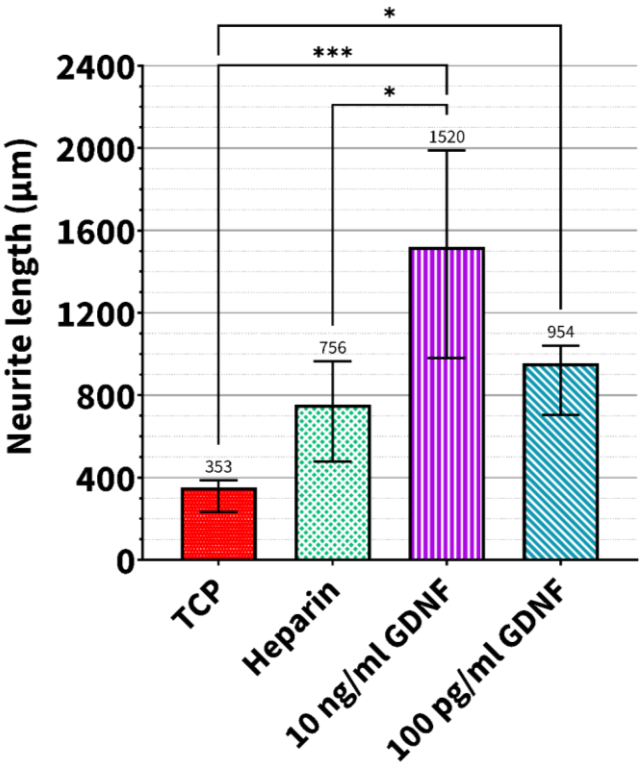

Figure 54. Neurite length extension from the cell body mass of chick DRGs cultured on heparin or GDNF immobilised PCL microfibre scaffolds versus TCP. Significance analysed by Kruskal-Wallis Dunn's multiple comparisons test and is displayed as * $p \leq 0.05$, *** $p \leq 0.001$. Chick embryos were sacrificed on EDD 13. The median neurite length is displayed above the error bars, error bars = interquartile range.

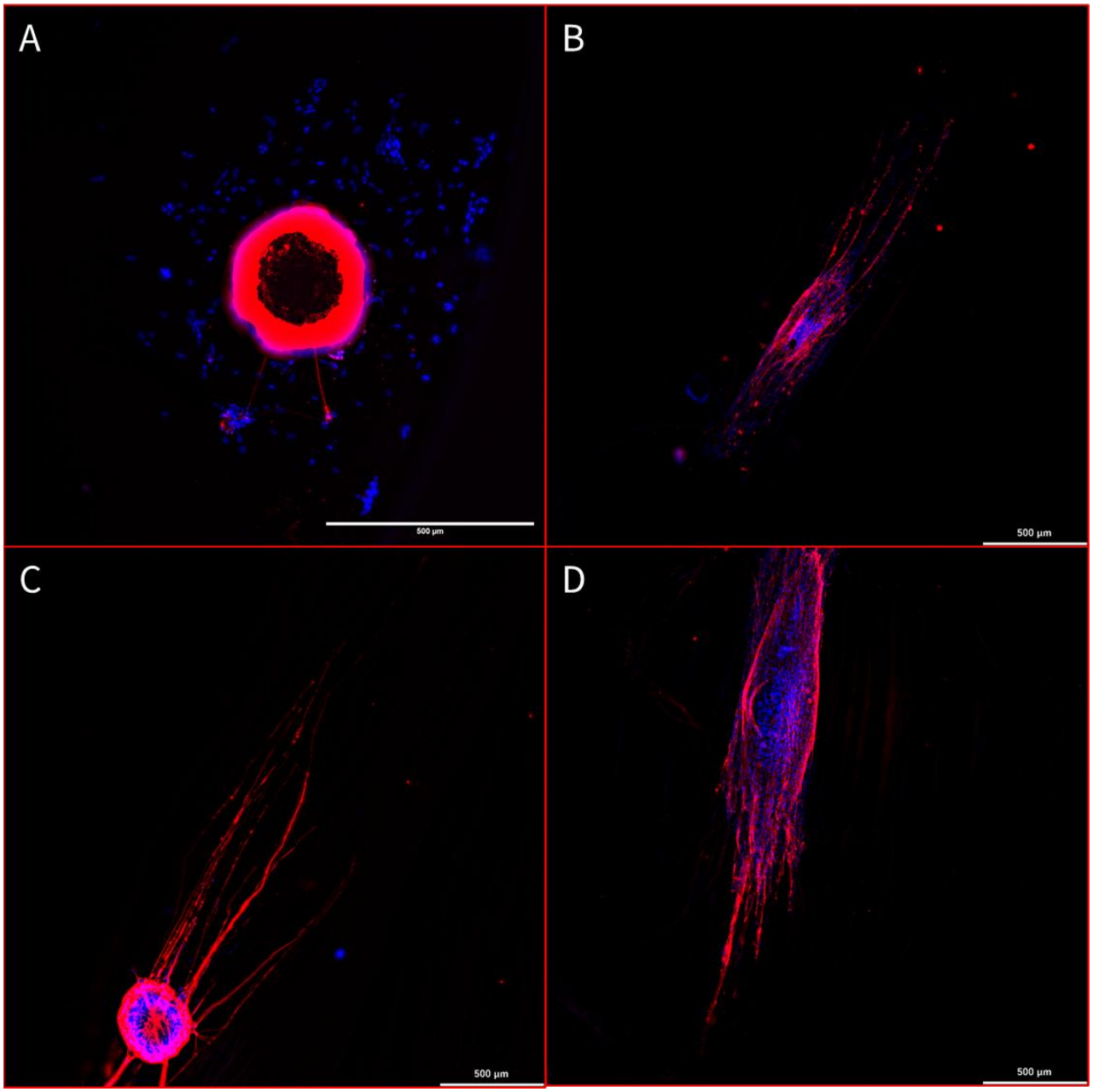

Figure 55. Representative fluorescence images of embryonic chick DRGs cultured on TCP versus heparin and GDNF immobilised PCL microfibre scaffolds. TCP (a), 100 µg/mL heparin immobilised PCL microfibres (b), 10 ng/mL GDNF immobilised PCL microfibres (c) and 100 pg/mL GDNF immobilised PCL microfibres (d). Cell nuclei were directly labelled with 40,6-diamidino-2-phenylindole dihydrochloride (DAPI, blue) and neurites were immunolabelled against β-tubulin III (red). Scale bar = 500 µm.

4.4 Discussion

4.4.1 Primary Schwann cell attachment and growth on bioactive PCL fibres

Numerous studies focus on the effect of nano- and microfibre properties such as fibre diameter, density and alignment on neuronal cell differentiation and morphology, however research indicates that considering optimum properties for Schwann cell adhesion and migration may be of more importance for improving peripheral nerve regeneration outcomes. Schwann cells have been shown to play numerous roles post nerve injury, providing contact guidance for regenerating axons through the bands of Büngner[61, 62, 84], degradation of axons and myelin distal to the injury site[56, 57], release of growth factors[77, 79] and cytokines[67, 68] and cell-to-cell interaction with immune cells[64-66]. Primary neurons and Schwann cells were isolated from the trigeminal ganglia of thy-1-YFP-H transgenic mice and cultured on heparin and GDNF immobilised PCL microfibres with an average fibre diameter of 5 µm. TCP was used as a control opposed to laminin and poly-L-lysine coated wells due to funding constraints. At the time of thesis submission an *in vivo* study in collaboration with PhD candidate Louis Johnson was on going using the thy-1-YFP-H transgenic mice as they express a subpopulation of sensory neurons conjugated with yellow fluorescent protein (YFP) allowing individual axons to be visualised and traced across the injury gap for in-depth analysis[302, 303]. The average fibre diameter was chosen based on previous reports which showed highest neurite length of neuronal and Schwann cell co-cultures on 5 µm average PCL fibre diameters[156, 191, 194]. The effect of heparin and GDNF immobilised PCL scaffolds on neurite length of TG neuronal cells was not assessed due to poor yield of neurons. However, neurons aligned to the fibre direction were observed on confocal images of heparin and 100 pg/mL GDNF PCL microfibres (figure 52b and 53d) indicating that primary sensory neurons were able to attach

and grow on functionalized scaffolds. The density of PCL scaffolds may have made it difficult to image the few neurons that attached.

To assess the effect of heparin and GDNF immobilised PCL fibres on primary Schwann cell morphology, the aspect ratio was measured compared to 2D TCP surfaces. Schwann cell morphology can be indicative of the cell phenotype *i.e.* myelinating versus non-myelinating[190, 203, 212]. Using fluorescent imaging, the aspect ratio of Schwann cells was found to be significantly higher on TCP surfaces than on PCL microfibres. Schwann cells exhibited the characteristic bipolar spindle shape morphology but a high proportion of Schwann cells also exhibited a flattened circumferential morphology as well as tripolar-like morphology on TCP (highlighted area of figure 52a). Schwann cells with flattened circumferential morphology as well as tripolar-like morphology on 2D surfaces has been reported by other studies[215, 219, 304]. For example this effect was observed by Koroleva *et al.* on methacrylated poly lactic acid (PLA) films[304]. Primary TG Schwann cells exhibited solely bipolar spindle shape morphologies with highly extended processes on heparin and GDNF PCL microfibres supporting the utilization of aligned surface topography for promoting non-myelinating Schwann cell phenotype which is associated with the formation of the bands of Büngner[190, 203].

4.4.2 The neurotrophic ability of GDNF on neurite growth of sensory neurons *in vitro* and *ex vivo*

Our research group has previously investigated the neurotrophic ability of nerve growth factor (NGF) and brain-derived neurotrophic factor (BDNF) on neurite extension of neuronal cell lines and *ex vivo* dorsal root ganglia (DRG) nerve injury models. Using allylamine plasma polymerisation and physical adsorption of heparin sulfate to immobilise NGF and BDNF *via* electrostatic interactions, Sandoval-Castellanos *et al.* demonstrated that delivery of neurotrophic

factors significantly increased neurite growth of embryonic chick DRG compared to unmodified PCL microfibres[198].

Using the highest maximum neurite lengths measured shown in figure 41 as a starting point, concentrations of 10 ng/mL and 100 pg/mL were immobilised onto N3S-linked aligned PCL fibres with average fibre diameters of 6 µm. There were no significant differences found between median neurite length or maximum neurite length of NG108-15 neuronal cells cultured on TCP compared to heparin and GDNF immobilised PCL microfibres in contrast to results using PCL films (figures 49a and b). Nonetheless, median and maximum neurite length were higher on all surface functionalized PCL microfibres compared to TCP supporting the theory that topographic cues combined with haptotactic cues promote greater neurite growth *in vitro*. Comparison between NG108-15 neuronal cell differentiation on heparin and neurotrophic factor immobilised PCL microfibres and PCL films provided further evidence to support this theory. Higher median neurite lengths on aligned PCL scaffolds were observed when compared to functionalized PCL films, except on 100 pg/ml immobilised GDNF samples. Median neurite length was higher at 103 µm for 100 pg/ml GDNF immobilised PCL films compared to 101 µm on immobilised PCL scaffolds. Median neurite length was significantly higher on heparin immobilised PCL scaffolds compared to heparin immobilised PCL films measuring 103 µm and 81 µm, respectively. In contrast, maximum neurite lengths were higher on all functionalized PCL scaffolds compared to films. The longest neurite length measured was 422 µm on 100 pg/ml GDNF immobilised scaffolds followed by heparin immobilised scaffolds at 411 µm. Comparison of NG108-15 neurite lengths measured on functionalized PCL films and scaffolds suggests that heparin alone is a potential candidate for *in vivo* analysis which is beneficial for translation to clinic as functionalisation with solely heparin is more cost-effective compared to neurotrophic factors.

Furthermore, 10 ng/ml and 100 pg/ml GDNF were used as starting concentrations for assessing the combined effect of topographical and trophic ques on neurite growth *in vitro* based on results shown in figure 41. The inferred optimum concentrations observed on PCL films may not directly apply to PCL microfibres due to key differences between the two substrates. The optimum concentration on both substrates is primarily affected by surface area and morphology. Films typically have a smooth flat surface which may allow for uniform modification of the surface thus homogenous attachment of bioactive factors. However, polymer films have a lower surface area to volume ratio compared to electrospun microfibres. In theory, there are a higher number of potential binding sites on electrospun microfibres compared to polymer films, thus a higher amount of a concentration of heparin or neurotrophic factor may bind compared to a polymer film. Furthermore, a second factor which should be considered is the modification depth of plasma functionalisation. Plasma treatment modifies 1 – 3 nm of the sample surface meaning fibres at the centre of a 3D structure are left potentially unmodified. For example, fibres between layers are most likely overlapping and are in contact with one another, these points of contact are unlikely modified by plasma treatment. Thus, immobilisation of bioactive factors may occur solely on the surface of the outermost fibres of a 3D electrospun scaffold potentially affecting cell ingress and migration *in vivo* leading to poor axon regeneration.

In vitro analysis of neurite length in response to GDNF delivery provides proof-of-concept but as the physiological conditions do not mimic those *in vivo*, using *ex vivo* models can provide physiological conditions closer to *in vivo* conditions. Embryonic chick DRG were isolated on EDD 13 and cultured for 7 days on TCP versus heparin, 10 ng/mL and 100 pg/mL GDNF immobilised PCL microfibre scaffolds with average fibre diameter of 8 µm. An average fibre diameter of 8 µm was chosen based on studies by our research group[191, 194, 195]. Neurite length was significantly

higher on 10 ng/mL and 100 pg/mL GDNF immobilised PCL aligned microfibres compared to TCP (figure 54). The longest median neurite length measured from chick DRG explants was 1520 µm on 10 ng/mL GDNF immobilised PCL microfibres. The shortest neurite length measured was 353 µm on TCP. Surprisingly, neurite extension from chick DRG explants on 10 ng/mL GDNF immobilised PCL scaffolds was significantly higher than on heparin immobilised PCL scaffolds. This is in contrast to *in vitro* results as maximum neurite length of NG108-15 neuronal cells was higher on heparin and 100 pg/mL GDNF scaffolds compared to 10 ng/mL GDNF scaffolds. This may be due to the difference in physiological conditions or the use of different fibre diameters for neuronal cell lines compared to DRG explants. This outcome highlights the limitations of assessing the effects of neurotrophic delivery on neurite growth when using neuronal cell lines *in vitro* compared to primary cells *ex vivo.*

Literature reports longer neurite extension on unmodified PCL microfibres to the data presented herein this study. Daud *et al*. 2012 observed neurite lengths of up to 2.5 mm from adult rat DRG explants after 10 days on 1 µm diameter PCL fibres[191]. This is in agreement with a study by Behbehani *et al*. 2017 which reported a maximum neurite extension of 2.1 ± 0.33 mm from rat DRG explants after 21 days of culture on 5 µm diameter PCL fibres in PEG conduits[156]. The variation in measurements are likely due to differences in culture time and fibre diameters assessed between studies. The effect of fibre diameter is highlighted in a study by Jin *et al.* 2023, who report much lower neurite extension from rat DRG explants on unmodified PCL nanofibres (589 ± 70 µm) after 5 days[305]. Notedly, although the longest neurite length measured herein is lower compared to studies by Duad *et al.* 2012 and Behbehani *et al.* 2017 on unmodified PCL fibres, the species, development stage of the animal studied, fibre diameter and culture times differ between the

aforementioned studies and the present study which is likely to affect the extent of neurite growth thus somewhat limits comparison.

However, literature supports the hypothesis that incorporation of neurotrophic factors to aligned polymer scaffolds promotes greater neurite growth compared to topographic ques alone. Sandoval-Castellanos *et al*. 2021 assessed the effects of local delivery of 1 pg/mL to 1 µg/mL NGF and/or BDNF from surface modified PCL microfibres on embryonic chick DRG explant neurite growth[198]. 8 µm fibre diameter PCL scaffolds were functionalized *via* allylamine plasma and subsequent heparin sulfate and NGF/BDNF adsorption. The group reported a longest average neurite length of 3041 ± 843 µm on 1 ng/mL NGF immobilised PCL scaffolds. For immobilised BDNF conditions, 1 ng/mL BDNF promoted longest outgrowth (1,536 ± 762 µm) although, approximately half that of 1 ng/mL immobilised NGF. Dual delivery of both growth factors did not seem to have a synergistic effect on neurite growth, measuring lower at 1,107 ± 456 µm for 1 ng/mL immobilised NGF plus BDNF[198]. This is in contrast to a study by Madduri *et al*. 2010 wherein they fabricated 40 ng GDNF plus NGF loaded silk fibroin (SF) membranes functionalized topographically with aligned or randomly aligned SF nanofibres[306]. They reported axonal growth of approximately 11 and 10 mm from embryonic chick DRG and spinal cord explants on NGF plus GDNF loaded aligned nanofibre membranes, respectively, after 5 days of culture. Comparison to the literature highlights the requirement of further optimisation of the herein developed surface modification method before *in vivo* evaluation can take place.

4.5 Conclusions

In this chapter the effects of local delivery of GDNF and topographic cues provided by aligned PCL microfibres were assessed on neurite growth *in vitro* and *ex vivo* models. Furthermore, the effects of highly aligned functionalized PCL scaffolds versus flat 2D surfaces on primary Schwann cell

attachment and morphology were investigated. GDNF concentrations of 10 ng/mL and 100 pg/mL were chosen to be evaluated based on the greatest maximum and median neurite length promoted from NG108-15 neuronal cells (see 3.3.2). Comparison between heparin and GDNF functionalized PCL films and aligned microfibres revealed that aligned 3D surfaces promoted higher median and maximum neurite growth than PCL films *in vitro* (figure 50). Mixed outcomes were observed on neurite growth from NG108-15 neuronal cells compared to embryonic chick DRG models. As chick DRG explant models are closer to physiological conditions *in vivo*, 10 ng/mL GDNF was chosen as a concentration to be assessed in thy-1-YFP-H mice 5 mm sciatic nerve gap injury models conducted in collaboration with Louis Johnson.

Key findings

1. Heparin and 10 ng/mL GDNF immobilised PCL microfibres promoted greatest median neurite length from NG108-15 neuronal cells however the neurite length was not significantly higher compared to TCP (figure 49a).

2. 100 ng/mL GDNF, followed by heparin immobilised PCL microfibres promoted greatest maximum neurite length from NG108-15 neuronal cells but the length was not significantly higher than TCP (figure 49b).

3. Significantly lower aspect ratios of primary Schwann cells isolated from mice trigeminal ganglia were observed on surface functionalized PCL microfibres compared to TCP (figure 53a).

4. Primary Schwann cells cultured on functionalized PCL microfibres exhibited bipolar spindle shape morphology whereas a high proportion on TCP exhibited flattened circumferential and tripolar like morphology indicative of a myelinating phenotype (figure 52).

5. Successful attachment and growth of trigeminal ganglia neurons on heparin and 100 pg/mL GDNF immobilised PCL microfibres (figure 52b and 53d).

6. 10 ng/mL GDNF immobilised aligned PCL microfibres promoted significantly greater neurite extension from chick DRG explants compared to heparin immobilised PCL microfibres and TCP (figure 54).

Chapter 5. Conclusions and Future Research

In conclusion, a method for modifying the PCL surface was successfully developed allowing the immobilisation of GAG mimetic, heparin sulfate and neurotrophic factor, GDNF characterised *via* XPS, ATR-FTIR and SEM-EDX analysis. *In vitro* NG108-15 neuronal cell differentiation assays reported in 4.3.1, demonstrated the stimulatory effect of providing topographic cues *via* aligned fibre scaffolds on neurite growth supporting the view of current literature. Moreover, surface functionalisation of hydrophobic polymer surfaces using a combination of plasma modification and covalent bonding of long chain aminosilane N^1-(3-trimethoxysilylpropyl)diethylenetriamine, was shown to increase surface hydrophilicity for promoting cell attachment. However, further characterisation of modified PCL is required to elucidate the full extent of the modification method effects on biomechanical, surface and bulk properties of PCL, for example, analysis of the effects of heparin and GDNF immobilisation on fibre diameter.

The varied outcomes of different GDNF concentrations on neurite length *in vitro* and *ex vivo* nerve injury models highlighted the limitations of using neuronal cell lines on 2D surfaces for studying delivery systems intended for peripheral nerve repair applications. Nevertheless, 10 ng/mL GDNF immobilised PCL microfibres were shown to promote significantly higher neurite extension from chick DRG explants compared to heparin sulfate immobilised PCL microfibres and TCP.

Furthermore, primary Schwann cells from mice trigeminal ganglia were shown to successfully attach and differentiate on surface functionalized aligned PCL scaffolds demonstrated by significantly lower aspect ratios compared to on TCP. High numbers of primary Schwann cells were observed on functionalized PCL scaffolds, exhibiting characteristic bipolar spindle shape morphology in contrast to the high proportion of Schwann cells exhibiting flattened circumferential morphologies cultured on TCP. The neurotrophic effect of GDNF on chick DRG neurite extension and successful attachment and differentiation of primary Schwann cells on surface functionalized PCL scaffolds indicates the delivery system developed herein this study may be a potential candidate for *in vivo* nerve injury studies. Nonetheless, further optimisation of the system is required through investigation into the effects of multi-delivery of neurotrophic factors and fibre density of polymer microfibres on neuronal and glial cell growth.

5.1 Future research

Improvements on the current research include evaluation of the surface modified PCL microfibres biomechanical properties. The Young's modulus (E) of native nerve has been reported to be approximately 38.5 MPa[26, 307] which is lower than the E of PCL which is ~400 MPa[143]. Analysis of the Young's modulus and elongation at break would provide a better understanding of the biocompatibility of modified PCL scaffolds for application in peripheral nerve repair. In addition, degradation rate and the degradation mechanism is an important material property to consider for biomedical engineering applications. Degradation products have the potential to cause immune reactions, oedema and fibrotic tissue formation at the site of injury. PCL degrades *in vivo via* hydrolysis of ester linkages and evidence supports the theory that low molecular weight PCL is degraded by macrophages and giant cells[144]. However, future *in vivo* analysis focusing on extent

of fibrotic tissue formation and immune reaction markers would provide valuable insight into the feasibility of PCL scaffolds in peripheral nerve repair.

Noted in section 4.4.2, high density electrospun fibre mats with numerous layers are likely to be modified by air plasma solely on the outermost fibres. A method to improve surface modification of fibres throughout the 3D scaffold is as follows; decreasing spinning time to obtain one fibre thick mats followed by plasma modification of both sides of the mat and subsequent adsorption of bioactive factors. Finally the mat at a desired density is rolled into a thread prior to conduit insertion which should allow in theory a 3D scaffold which is modified through it's depth opposed to only the surface fibres.

The effect of heparin and GDNF immobilised PCL scaffolds on neurite length of TG neuronal cells was not assessed due to poor yield of TG neurons. To improve cell yield the isolation protocol needs to be developed further, gradient extraction could be used in future research to achieve purer sensory neuron cultures[308]. Furthermore, the density of PCL scaffolds may have made it difficult to observe any TG neurons that attached. Future work investigating different fibre densities on neuronal cell and Schwann cell attachment and response would be beneficial for elucidating optimum properties for intraluminal guidance structures. For example, studies by Xie *et al.* and Nisbet *et al*. challenged the view that neurites will extend parallel to aligned fibres[200, 201]. Over certain fibres densities, neurites from chick DRGs grew perpendicular rather than parallel to the PCL fibre direction. However, when high density fibre scaffolds were coated with laminin, the neurites extended once again parallel to fibre orientation.

Additional research to develop the study herein includes comparison of mono and dual delivery of different concentrations of immobilised NGF, BDNF and GDNF on chick DRG neurite outgrowth. Liu *et al.* reported a synergistic effect of GDNF and NGF encapsulated bicomponent PCL and PLGA

scaffolds leading to longer neurite growth when compared to solo delivery of either NGF or GDNF[248].

Developing on the above future research, the effects of mono and dual density gradients on neurite length would provide useful insights for the development of nerve guide conduits. Studies have shown that providing haptotactic cues lead to significant increase in neurite extension toward increasing neurotrophic factor densities *in vitro* and *ex vivo*[250, 305, 309]. Of particular interest is a study by Xue *et al*. who fabricated electrospun nanofibres with a bi-directional gradient of collagen-fibronectin. The bi-directional gradient of collagen and fibronectin promoted Schwann cell migration to the centre of the scaffold from both directions, a modification that could potentially increase the rate of nerve regeneration by promoting faster Schwann cell migration from proximal and distal ends to form the migrating substrate for axon growth.

Finally, future investigation to improve the scope of this research includes expression profiling of neuronal and glial cells grown on flat and aligned PCL surfaces. Expression profiles can give deeper insight into the cell state indicating if the conditions provided by the bioactive scaffolds are optimum for stimulating desired effects such as growth factor/myelin production markers in Schwann cells[190], precursor neural markers such as Nestin and mature neural markers such as β-tubulin and Map2[211].

References

1. Williams, L.R. Exogenous fibrin matrix precursors stimulate the temporal progress of nerve regeneration within a silicone chamber. *Neurochem Research* **12**, 851-860 (1987).
2. Schröder, J.M., May, R. & Weis, J. Perineurial cells are the first to traverse gaps of peripheral nerves in silicone tubes. *Clinical neurology and neurosurgery* **95**, 78-83 (1993).
3. Saladin, K.S. Human Anatomy, Edn. Fifth. (McGraw-Hill, New York; 2017).
4. Thomas, P.K. The connective tissue of peripheral nerve: an electron microscope study. *Journal of Anatomy* **97**, 35-44 (1963).
5. Gamble, H.J. & Eames, R.A. An electron microscope study of the connective tissues of human peripheral nerve. *Journal of Anatomy* **98**, 655-663 (1964).
6. Röhlich, P. & Weiss, M. Studies on the histology and permeability of the peripheral nervous barrier. *Acta Morphol Acad Sci Hung* **5**, 335-347 (1955).
7. Shanthaveerappa, T.R. & Bourne, G.H. The 'perineural epithelium', a metabolically active, continuous, protoplasmic cell barrier surrounding peripheral nerve fasciculi. *Journal of Anatomy* **96**, 527-537 (1962).
8. Sunderland, S.S. The anatomy and physiology of nerve injury. *Muscle & Nerve* **13**, 771-784 (1990).
9. Topp, K.S. & Boyd, B.S. Structure and Biomechanics of Peripheral Nerves: Nerve Responses to Physical Stresses and Implications for Physical Therapist Practice. *Physical therapy* **86**, 92-109 (2006).
10. Sunderland, S. The connective tissue of peripheral nerve. *Brain* **88**, 841-854 (1965).
11. Uzman, B.G. & Villegas, G.M. A comparison of nodes of Ranvier in sciatic nerves with node-like structures in optic nerves of the mouse. *Journal of biophysical and biochemical cytology* **7**, 761-762 (1960).
12. Uzman, B.G. & Nogueira-Graf, G. Electron microscope studies of the formation of Nodes of Ranvier in mouse sciatic nerves. *Journal of biophysical and biochemical cytology* **3**, 589-598 (1957).
13. Morell, P. & Quarles, R.H. Basic Neurochemistry: Molecular, Celluar and Medical Aspects, Edn. 6th. (Lippincott-Raven, Philadelphia; 1999).
14. Spencer, P.S. & Lieberman, A.R. Scanning electron microscopy of isolated peripheral nerve fibres. *Zeitschrift für Zellforschung und Mikroskopische Anatomie* **119**, 534-551 (1971).
15. Hubert, R.J. & VanMeter, K. Gould's Pathophysiology for the Health Professions. (Elsevier, 2018).
16. Chiras, D.D. Human biology, Edn. 8. (Jones & Bartlett Learning, Burlington; 2015).
17. Pavelka, M. & Roth, J. Functional Ultrastructure: Atlas of Tissue Biology and Pathology, Edn. 3. (Springer, 2015).
18. Seddon, H.J. A Classification of Nerve Injuries. *British Medical Journal* **2**, 4260-4260 (1942).
19. Sunderland, S. A Classification of Peripheral Nerve Injuries Producing Loss of Function. *Brain* **74**, 491-516 (1951).
20. Kouyoumdjian, J., Graç, C. & Ferreira, V.M. Peripheral nerve injuries: A retrospective survey of 1124 cases. *Neurology India* **65**, 551-555 (2017).
21. Kouyoumdjian, J.A. Peripheral nerve injuries: A retrospective survey of 456 cases. *Muscle & Nerve* **34**, 785-788 (2006).

22. Noble, J., Munro, C.A., Prasad, V.S.S.V. & Midha, R. Analysis of Upper and Lower Extremity Peripheral Nerve Injuries in a Population of Patients with Multiple Injuries. *The Journal of Trauma: Injury, Infection, and Critical Care* **45**, 116-122 (1998).
23. Ragel, B.T., Park, G.C. & Brevard, S. Median Nerve Repair with Autologous Sciatic Nerve Graft: A Case Report. *ISRN Surgery* (2011).
24. Jones, P.E. et al. Combat Injury of the Sciatic Nerve - An Institutional Experience. *Military Medicine* **183** (2018).
25. Haftek, J. STRETCH INJURY OF PERIPHERAL NERVE. *The Journal of Bone & Joint Surgery British Volume* **52-B**, 354-365 (1970).
26. Rydevik, B.L. et al. An in vitro mechanical and histological study of acute stretching on rabbit tibial nerve. *Journal of Orthopaedic Research* **8**, 694-701 (1990).
27. Health, U., Vol. 2024 (
28. Olney, R.K. Carpal tunnel syndrome: Complex issues with a "simple" condition. *Neurology* **56**, 1431-1432 (2001).
29. LeBlanc, K.E. & Cestia, W. Carpal tunnel syndrome. *American Family Physician* **83**, 952-958 (2011).
30. Padua, L.P. et al. Carpal tunnel syndrome: clinical features, diagnosis, and management. *Lancet neurology* **15**, 1273-1284 (2016).
31. Perţea, M. et al. Value of ultrasonography in the diagnosis of carpal tunnel syndrome - a new ultrasonographic index in carpal tunnel syndrome diagnosis: A clinical study. *Medicine* **99** (2020).
32. Services, U.D.o.H.a.H. Carpal tunnel syndrome. (U.S. Department of Health and Human Services, Public Health Service, National Institutes of Health, Bethesda, Maryland; 2012).
33. Kline, D.G., Kim, D., Midha, R., Harsh, C. & Tiel, R. Management and results of sciatic nerve injuries: a 24-year experience. *Journal of Neurosurgery* **89**, 13-23 (1998).
34. Topuz, K. et al. Early surgical treatment protocol for sciatic nerve injury due to injection – a retrospective study. *British Journal of Neurosurgery* **25**, 509-515 (2011).
35. Gentili, F., Hudson, A.R., Kline, D. & Hunter, D. Early changes following injection injury of peripheral nerves. *Canadian journal of surgery* **23**, 177-182 (1980).
36. Rice, A.S.C. & McMahon, S.B. Peripheral nerve injury caused by injection needles used in regional anaesthesia: influence of bevel configuration studied in a rat model. *British Journal of Anaesthesia* **69**, 433-438 (1992).
37. Farber, S.J. et al. Peripheral nerve injury after local anesthetic injection. *Anesthesia and analgesia* **117**, 731-739 (2013).
38. van Haren, F.G.A.M., Steegers, M.A.H., Vissers, K.C.P. & van den Heuvel, S.A.S. A qualitative evaluation of the oncologists', neurologists', and pain specialists' views on the management and care of chemotherapy-induced peripheral neuropathy in The Netherlands. *Supportive Care in Cancer* **32**, 301 (2024).
39. Staff, N.P., Grisold, A., Grisold, W. & Windebank, A.J. Chemotherapy-induced peripheral neuropathy: A current review. *Annals of Neurology* **81**, 772-781 (2017).
40. Pike, C.T., Birnbaum, H.G., Muehlenbein, C.E., Pohl, G.M. & Natale, R.B. Healthcare Costs and Workloss Burden of Patients with Chemotherapy-Associated Peripheral Neuropathy in Breast, Ovarian, Head and Neck, and Nonsmall Cell Lung Cancer. *Chemotherapy Research and Practice* **2012**, 913848 (2012).
41. Quasthoff, S. & Hartung, H.P. Chemotherapy-induced peripheral neuropathy. *Journal of Neurology* **249**, 9-17 (2002).

42. Verstappen, C.C.P., Heimans, J.J., Hoekman, K. & Postma, T.J. Neurotoxic Complications of Chemotherapy in Patients with Cancer. *Drugs* **63**, 1549-1563 (2003).
43. Windebank, A.J. & Grisold, W. Chemotherapy-induced neuropathy. *Journal of the Peripheral Nervous System* **13**, 27-46 (2008).
44. Eid, S.A. et al. Transcriptomic profiling of sciatic nerves and dorsal root ganglia reveals site-specific effects of prediabetic neuropathy. *Translational Research* **270**, 24-41 (2024).
45. Chiles, N.S. et al. Diabetes, peripheral neuropathy, and lower-extremity function. *Journal of Diabetes and its Complications* **28**, 91-95 (2014).
46. Willison, H.J.P., Jacobs, B.C.P. & van Doorn, P.A.P. Guillain-Barré syndrome. *The Lancet* **388**, 717-727 (2016).
47. Suzuki, C. et al. Loss of intraepidermal nerve fibers in Guillan-Barre syndrome. *Journal of the Neurological Sciences* **381**, 854 (2017).
48. Florian, I.A., Lupan, I., Sur, L., Samasca, G. & Timiş, T.L. To be, or not to be...Guillain-Barré Syndrome. *Autoimmunity Reviews* **20**, 102983 (2021).
49. Waller, A.V. Experiments on the section of the glossopharyngeal and hypoglossal nerves of the frog, and observations of the alterations produced thereby in the structure of their primitive fibres. *Philosophical Transactions of the Royal Society of London* **140**, 423-429 (1850).
50. Chaudhry, V. & Cornblath, D.R. Wallerian degeneration in human nerves: Serial electrophysiological studies. *Muscle & Nerve* **15**, 687-693 (1992).
51. Gilliatt, R.W. & Hjorth, R.J. Nerve conduction during Wallerian degeneration in the baboon. *Journal of Neurology, Neurosurgery, Psychiatry* **35**, 335-341 (1972).
52. Touma, E., Kato, S., Fukui, K. & Koike, T. Calpain-mediated cleavage of collapsin response mediator protein (CRMP)-2 during neurite degeneration in mice. *European Journal of Neuroscience* **26**, 3368-3381 (2007).
53. Wang, M.S. et al. Calpain inhibition protects against Taxol-induced sensory neuropathy. *Brain* **127**, 671-679 (2004).
54. Stirling, D.P. & Stys, P.K. Mechanisms of axonal injury: internodal nanocomplexes and calcium deregulation. *Trends in Molecular Medicine* **16**, 160-170 (2010).
55. Nikolaeva, M.A., Mukherjee, B. & Stys, P.K. Na+-dependent sources of intra-axonal Ca2+ release in rat optic nerve during in vitro chemical ischemia. *Journal of Neuroscience* **25**, 9960-9967 (2005).
56. Martini, R., Fischer, S., López-Vales, R. & David, S. Interactions between Schwann cells and macrophages in injury and inherited demyelinating disease. *Glia* **56**, 1566-1577 (2008).
57. De, S., Avilés Trigueros, M., Kalyvas, A. & David, S. Phospholipase A 2 plays an important role in myelin breakdown and phagocytosis during Wallerian degeneration. *Molecular and Cellular Neuroscience* **24**, 753-765 (2003).
58. Lee, H.K. et al. Proteasome inhibition suppresses Schwann cell dedifferentiation in vitro and in vivo. *Glia* **57**, 1825-1834 (2009).
59. Trapp, B.D., Hauer, P. & Lemke, G. Axonal regulation of myelin protein mRNA levels in actively myelinating Schwann cells. *Journal of Neuroscience* **8**, 3515-3521 (1988).
60. Liu, H.M., Yang, L.H. & Yang, Y.J. Schwann cell properties: 3. C-fos expression, bFGF production, phagocytosis and proliferation during Wallerian degeneration. *Journal of Neuropathology and Experimental Neurology* **54**, 496-496 (1995).
61. García-Mateo, N. et al. Schwann cell-derived Apolipoprotein D controls the dynamics of post-injury myelin recognition and degradation. *Frontiers in Cellular Neuroscience* **8**, 374-374 (2014).

62. Ohmi, S. Electron microscopy of peripheral nerve regeneration. *Zeitschrift für Zellforschung und Mikroskopische Anatomie* **56**, 625-631 (1962).
63. Beuche, W. & Friede, R.L. The role of non-resident cells in Wallerian degeneration. *Journal of Neurocytology* **13**, 767-796 (1984).
64. Goethals, S., Ydens, E., Timmerman, V. & Janssens, S. Toll-like receptor expression in the peripheral nerve. *Glia* **58**, 1701-1709 (2010).
65. Lee, H. et al. Necrotic neuronal cells induce inflammatory Schwann cell activation via TLR2 and TLR3: Implication in Wallerian degeneration. *Biochemical and Biophysical Research Communications* **350**, 742-747 (2006).
66. Karikó, K., Ni, H., Capodici, J., Lamphier, M. & Weissman, D. mRNA is an endogenous ligand for Toll-like Receptor 3. *Journal of Biological Chemistry* **279**, 12542-12550 (2004).
67. Shamash, S., Reichert, F. & Rotshenker, S. The cytokine network of wallerian degeneration: Tumor necrosis factor-α, interleukin-1α, and interleukin-1β. *Journal of Neuroscience* **22**, 3052-3060 (2002).
68. Tofaris, G.K., Patterson, P.H., Jessen, K.R. & Mirsky, R. Denervated Schwann cells attract macrophages by secretion of leukemia inhibitory factor (LIF) and monocyte chemoattractant protein-1 in a process regulated by interleukin-6 and LIF. *Journal of Neuroscience* **22**, 6696-6703 (2002).
69. Nathan, C. Neutrophils and immunity: challenges and opportunities. *Nature Reviews Immunology* **6**, 173-182 (2006).
70. Boivin, A. et al. Toll-like receptor signaling is critical for Wallerian degeneration and functional recovery after peripheral nerve injury. *Journal of Neuroscience* **27**, 12565-12576 (2007).
71. Meyer Zu Hörste, G., Hu, W., Hartung, H.-P., Lehmann, H.C. & Kieseier, B.C. The immunocompetence of Schwann cells. *Muscle & Nerve* **37**, 3-13 (2008).
72. Holtzman, E. & Novikoff, A.B. Lysosomes in the rat sciatic nerve following crush. *The Journal of Cell Biology* **27**, 651-669 (1965).
73. Sulaiman, O.A.R. & Gordon, T. Effects of short- and long-term Schwann cell denervation on peripheral nerve regeneration, myelination, and size. *Glia* **32**, 234-246 (2000).
74. Mueller, M. et al. Macrophage response to peripheral nerve injury: The quantitative contribution of resident and hematogenous macrophages. *Laboratory Investigation* **83**, 175-185 (2003).
75. Perry, V.H., Brown, M.C. & Gordon, S. The macrophage response to central and peripheral nerve injury: A possible role for macrophages in regeneration. *Journal of Experimental Medicine* **165**, 1218-1223 (1987).
76. Mueller, M. et al. Rapid response of identified resident endoneurial macrophages to nerve injury. *American Journal of Pathology* **159**, 2187-2197 (2001).
77. Lindholm, D., Heumann, R., Meyer, M. & Thoenen, H. Interleukin-1 regulates synthesis of nerve growth factor in non-neuronal cells of rat sciatic nerve. *Nature* **330**, 658-659 (1987).
78. Hikawa, N. & Takenaka, T. Myelin-stimulated macrophages release neurotrophic factors for adult dorsal root ganglion neurons in culture. *Cellular and Molecular Neurobiology* **16**, 517-528 (1996).
79. Heumann, R., Korsching, S., Bandtlow, C. & Thoenen, H. Changes of Nerve Growth Factor Synthesis in Nonneuronal Cells in Response to Sciatic Nerve Transection. *The Journal of Cell Biology* **104**, 1623-1631 (1987).
80. La Fleur, M., Underwood, J.L., Rappolee, D.A. & Werb, Z. Basement membrane and repair of injury to peripheral nerve: Defining a potential role for macrophages, matrix

metalloproteinases, and tissue inhibitor of metalloproteinases-1. *Journal of Experimental Medicine* **184**, 2311-2326 (1996).
81. Gaudet, A.D., Popovich, P.G. & Ramer, M.S. Wallerian degeneration: Gaining perspective on inflammatory events after peripheral nerve injury. *Journal of Neuroinflammation* **8**, 1-13 (2011).
82. Moalem, G., Xu, K. & Yu, L. T lymphocytes play a role in neuropathic pain following peripheral nerve injury in rats. *Neuroscience* **129**, 767-777 (2004).
83. Austin, P.J., Kim, C.F., Perera, C.J. & Moalem-Taylor, G. Regulatory T cells attenuate neuropathic pain following peripheral nerve injury and experimental autoimmune neuritis. *Pain* **153**, 1916-1931 (2012).
84. Chen, B., Chen, Q., Parkinson, D.B. & Dun, X.P. Analysis of Schwann cell migration and axon regeneration following nerve injury in the sciatic nerve bridge. *Frontiers in Molecular Neuroscience* **12**, 308-308 (2019).
85. Cattin, A.-L. et al. Macrophage-Induced Blood Vessels Guide Schwann Cell-Mediated Regeneration of Peripheral Nerves. *Cell* **162**, 1127-1139 (2015).
86. Atkins, S. et al. Scarring impedes regeneration at sites of peripheral nerve repair. *NeuroReport* **17**, 1245-1249 (2006).
87. Sunderland, S. & Bradley, K.C. Endoneurial tube shrinkage in the distal segment of a severed nerve. *Journal of Comparative Neurology* **93**, 411-420 (1950).
88. Deumens, R. et al. Repairing injured peripheral nerves: Bridging the gap. *Progress in Neurobiology* **92**, 245-276 (2010).
89. Hayashida, K., Hiroto, S., Morooka, S., Kuwabara, K. & Fujioka, M. The vascularized sural nerve graft based on a peroneal artery perforator for reconstruction of the inferior alveolar nerve defect. *Microsurgery* **35**, 244-248 (2015).
90. Plate, J.F., Ely, L.K., Pulley, B.R., Smith, B.P. & Li, Z. Combined proximal nerve graft and distal nerve transfer for a posterior cord brachial injury. *Journal of Neurosurgery* **118**, 155-159 (2013).
91. Magdi Sherif, M. & Amr, A.H. Intrinsic Hand Muscle Reinnervation by Median-Ulnar End-to-Side Bridge Nerve Graft: Case Report. *Journal of Hand Surgery* **35**, 446-450 (2010).
92. Spyriounis, P.K. & Vourtsis, S.A. Spinal accessory nerve iatrogenic trauma following cervical lymph node biopsy. Treatment by anterior medial antebrachial cutaneous nerve graft: A case report. *European Journal of Plastic Surgery* **38**, 319-322 (2015).
93. Walaszek, I. & Zyluk, A. Reconstruction of the median and musculocutaneous nerves with a nerve graft combined with end-to-side neurorrhaphy: A case report. *Journal of Hand Surgery* **40**, 643-645 (2015).
94. Sallam, A.A., El-Deeb, M.S. & Imam, M.A. Nerve Transfer Versus Nerve Graft for Reconstruction of High Ulnar Nerve Injuries. *Journal of Hand Surgery* **42**, 265-273 (2017).
95. Ousterout, D.G. et al. Reading frame correction by targeted genome editing restores dystrophin expression in cells from Duchenne muscular dystrophy patients. *Molecular therapy : the journal of the American Society of Gene Therapy* **21**, 1718-1726 (2013).
96. Lundborg, G., Rosén, B., Abrahamson, S.O., Dahlin, L. & Danielsen, N. Tubular repair of the median nerve in the human forearm. Preliminary findings. *Journal of Hand Surgery: British & European Volume* **19**, 276-276 (1994).
97. Merle, M., Lee Dellon, A., Campbell, J.N. & Chang, P.S. Complications from silicon-polymer intubulation of nerves. *Microsurgery* **10**, 130-133 (1989).
98. Shin, R.H., Friedrich, P.F., Crum, B.A., Bishop, A.T. & Shin, A.Y. Treatment of a segmental nerve defect in the rat with use of bioabsorbable synthetic nerve conduits: A comparison

of commercially available conduits. *Journal of Bone and Joint Surgery* **91**, 2194-2204 (2009).
99. Waitayawinyu, T. et al. A Comparison of Polyglycolic Acid Versus Type 1 Collagen Bioabsorbable Nerve Conduits in a Rat Model: An Alternative to Autografting. *The Journal of Hand Surgery* **32A**, 1521-1529 (2007).
100. Bertleff, M.J.O.E., Meek, M.F. & Nicolai, J.P.A. A prospective clinical evaluation of biodegradable Neurolac nerve guides for sensory nerve repair in the hand. *Journal of Hand Surgery* **30**, 513-518 (2005).
101. Costa Serrão de Araújo, G., Couto Neto, B., Harley Santos Botelho, R. & Carpi Malta, M. Clinical evaluation after peripheral nerve repair with caprolactone Neurotube. *Hand* **12**, 168-174 (2017).
102. Chiriac, S., Facca, S., Diaconu, M., Gouzou, S. & Liverneaux, P. Experience of using the bioresorbable copolyester poly(DL-lactide-ε-caprolactone) nerve conduit guide Neurolac™ for nerve repair in peripheral nerve defects: Report on a series of 28 lesions. *Journal of Hand Surgery (European Volume)* **37**, 342-349 (2012).
103. Meek, M.F. & Jansen, K. Two years after in vivo implantation of poly(DL-lactide-ε-caprolactone) nerve guides: Has the material finally resorbed? *Journal of Biomedical Materials Research Part A* **89A**, 734-738 (2009).
104. Ekholm, M. et al. Histological study of tissue reactions to ε-caprolactone-lactide copolymer in paste form. *Biomaterials* **20**, 1257-1262 (1999).
105. Hernández-Cortés, P., Garrido, J., Camara, M. & Ravassa, F.O.v. Failed digital nerve reconstruction by foreign body reaction to Neurolac® nerve conduit. *Microsurgery* **30**, 414-416 (2010).
106. Bell, J.H.A. & Haycock, J.W. Next generation nerve guides: Materials, fabrication, growth factors, and cell delivery. *Tissue Engineering: Part B* **18**, 116-128 (2012).
107. Mackinnon, S.E. & Dellon, A.L. Clinical nerve reconstruction with a bioabsorbable polyglycolic acid tube. *Plastic and Reconstructive Surgery* **85**, 419-424 (1990).
108. Weber, R.A., Breidenbach, W.C., Brown, R.E., Jabaley, M.E. & Mass, D.P. A randomized prospective study of polyglycolic acid conduits for digital nerve reconstruction in humans. *Plastic and Reconstructive Surgery* **106**, 1036-1045 (2000).
109. Donoghoe, N., Rosson, G.D. & Dellon, A.L. Reconstruction of the human median nerve in the forearm with the Neurotube™. *Microsurgery* **27**, 595-600 (2007).
110. Rosson, G.D., Williams, E.H. & Dellon, A.L. Motor nerve regeneration across a conduit. *Microsurgery* **29**, 107-114 (2009).
111. Reichardt, L.F. & Tomaselli, K.J. Extracellular matrix molecules and their receptors: functions in neural development. *Annual Review of Neuroscience* **14**, 531-570 (1991).
112. Archibald, S.J., Krarup, C., Shefner, J., Li, S.-T. & Madison, R.D. A collagen-based nerve guide conduit for peripheral nerve repair: An electrophysiological study of nerve regeneration in rodents and nonhuman primates. *The Journal of Comparative Neurology* **306**, 685-696 (1991).
113. Archibald, S.J., Shefner, J., Krarup, C. & Madison, R.D. Monkey median nerve repaired by nerve graft or collagen nerve guide tube. *The Journal of Neuroscience* **15**, 4109-4123 (1995).
114. Tong, X.j. et al. Sciatic nerve regeneration navigated by laminin-fibronectin double coated biodegradable collagen grafts in rats. *Brain Research* **663**, 155-162 (1994).
115. Yoshii, S. & Oka, M. Peripheral nerve regeneration along collagen filaments. *Brain Research* **888**, 158-162 (2001).

116. Itoh, S. et al. Evaluation of cross-linking procedures of collagen tubes used in peripheral nerve repair. *Biomaterials* **23**, 4475-4481 (2002).
117. Taras, J.S., Nanavati, V. & Steelman, P. Nerve conduits. *Journal of Hand Therapy* **18**, 191-197 (2005).
118. Bushnell, B.D., McWilliams, A.D., Whitener, G.B. & Messer, T.M. Early Clinical Experience With Collagen Nerve Tubes in Digital Nerve Repair. *Journal of Hand Surgery* **33**, 1081-1087 (2008).
119. Meyer, R.A. & Bagheri, S.C. A bioabsorbable collagen nerve cuff (NeuraGen) for repair of lingual and inferior alveolar nerve injuries: A case series. *Journal of Oral and Maxillofacial Surgery* **67**, 2550-2551 (2009).
120. Wangensteen, K.J. & Kalliainen, L.K. Collagen tube conduits in peripheral nerve repair: A retrospective analysis. *Hand* **5**, 273-277 (2010).
121. Yoshii, S., Oka, M., Shima, M., Taniguchi, A. & Akagi, M. 30 mm regeneration of rat sciatic nerve along collagen filaments. *Brain Research* **949**, 202-208 (2002).
122. Kim, Y., Nowzari, H. & Rich, S.K. Risk of prion disease transmission through bovine-derived bone substitutes: A systematic review. *Clinical Implant Dentistry and Related Research* **15**, 645-653 (2013).
123. Prusiner, S.B. Novel proteinaceous infectious particles cause Scrapie. *Science* **216**, 136-144 (1982).
124. Dobie, K. & Barron, R. Dissociation between Transmissible Spongiform Encephalopathy (TSE) infectivity and proteinase K-resistant PrPSc levels in peripheral tissue from a murine transgenic model of TSE disease. *Journal of Virology* **87**, 5895-5903 (2013).
125. Dai, J., Bell, E. & Russakovsky, V. (2008).
126. Yuan, Y., Zhang, P., Yang, Y., Wang, X. & Gu, X. The interaction of Schwann cells with chitosan membranes and fibers in vitro. *Biomaterials* **25**, 4273-4278 (2004).
127. Freier, T., Montenegro, R., Koh, H.S. & Shoichet, M.S. Chitin-based tubes for tissue engineering in the nervous system. *Biomaterials* **26**, 4624-4632 (2005).
128. Freier, T., Koh, H.S., Kazazian, K. & Shoichet, M.S. Controlling cell adhesion and degradation of chitosan films by N-acetylation. *Biomaterials* **26**, 5872-5878 (2005).
129. Haastert-Talini, K. et al. Chitosan tubes of varying degrees of acetylation for bridging peripheral nerve defects. *Biomaterials* **34**, 9886-9904 (2014).
130. Madihally, S.V. & Matthew, H.W.T. Porous chitosan scaffolds for tissue engineering. *Biomaterials* **20**, 1133-1142 (1999).
131. Kasoju, N. & Bora, U. Silk fibroin in tissue engineering. *Advanced Healthcare Materials* **1**, 393-412 (2012).
132. Badylak, S.F. in Tissue Engineering 179-189 (Birkhäuser Boston, 1993).
133. Andrée, B., Bä, A., Haverich, A. & Hilfiker, A. Small intestinal submucosa segments as matrix for tissue engineering: review. *Tissue Engineering: Part B* **19**, 279-291 (2013).
134. Arnold, G.A., Mathews, K.G., Roe, S., Mente, P. & Seaboch, T. Biomechanical comparison of four soft tissue replacement materials: An in vitro evaluation of single and multilaminate porcine small intestinal submucosa, canine fascia lata, and polypropylene mesh. *Veterinary Surgery* **38**, 834-844 (2009).
135. Tottey, S. et al. The effect of source animal age upon extracellular matrix scaffold properties. *Biomaterials* **32**, 128-136 (2011).
136. Grimes, M., Pembroke, J.T. & McGloughlin The effect of choice of sterilisation method on the biocompatibility and biodegradability of SIS (small intestinal submucosa). *Biomedical Materials and Engineering* **15**, 65-71 (2005).

137. Voytik-Harbin, S.L., Brightman, A.O., Kraine, M.R., Waisner, B. & Badylak, S.F. Identification of extractable growth factors from small intestinal submucosa. *Journal of Cellular Biochemistry* **67**, 478-491 (1997).
138. Hodde, J.P., Record, R.D., Liang, H.A. & Badylak, S.F. Vascular endothelial growth factor in porcine-derived extracellular matrix. *Endothelium* **8**, 11-24 (2001).
139. Azzarello, J., Ihnat, M.A., Kropp, B.P., Warnke, L.A. & Lin, H.-K. Assessment of angiogenic properties of biomaterials using the chicken embryo chorioallantoic membrane assay. *Biomedical Materials* **2**, 61-61 (2007).
140. Yang, B. et al. In vitro evaluation of the bioactive factors preserved in porcine small intestinal submucosa through cellular biological approaches. *Journal of Biomedical Materials Research Part A* **93**, 1100-1109 (2009).
141. Badylak, S.F. & Gilbert, T.W. Immune response to biologic scaffold materials. *Seminars in Immunology* **20**, 109-116 (2008).
142. Sandor, M. et al. Host response to implanted porcine-derived biologic materials in a primate model of abdominal wall repair. *Tissue Engineering. Part A* **14**, 2021-2031 (2008).
143. Engelberg, I. & Kohn, J. Physico-mechanical properties of degradable polymers used in medical applications: A comparative study. *Biomaterials* **12**, 292-304 (1991).
144. Woodward, S.C., Brewer, P.S., Moatamed, F., Schindler, A. & Pitt, C.G. The intracellular degradation of poly(e-caprolactone). *Journal of Biomedical Materials Research* **19**, 437-444 (1985).
145. Sun, M. & Downes, S. Physicochemical characterisation of novel ultra-thin biodegradable scaffolds for peripheral nerve repair. *Journal of Materials Science: Materials in Medicine* **20**, 1181-1192 (2009).
146. Bittner, G.D., Ballinger, M.L. & Raymond, M.A. Reconnection of severed nerve axons with polyethylene glycol. *Brain Research* **367**, 351-355 (1986).
147. Krause, T.L. & Bittner, G.D. Rapid morphological fusion of severed myelinated axons by polyethylene glycol. *Proceedings of the National Academy of Sciences of the United States of America* **87**, 1471-1475 (1990).
148. Spaeth, C.S., Robison, T., Fan, J.D. & Bittner, G.D. Cellular mechanisms of plasmalemmal sealing and axonal repair by polyethylene glycol and methylene blue. *Journal of Neuroscience Research* **90**, 955-966 (2012).
149. Mikesh, M. et al. Polyethylene glycol solutions rapidly restore and maintain axonal continuity, neuromuscular structures, and behaviors lost after sciatic nerve transections in female rats. *Journal of Neuroscience Research* **96**, 1223-1242 (2018).
150. Abdou, S.A. & Henderson, P.W. Fusogens: chemical agents that can rapidly restore function after nerve injury. *Journal of Surgical Research* **233**, 36-40 (2019).
151. Bittner, G.D., Sengelaub, D.R. & Ghergherehchi, C.L. Conundrums and confusions regarding how polyethylene glycol-fusion produces excellent behavioral recovery after peripheral nerve injuries. *Neural Regeneration Research* **13**, 53-57 (2018).
152. Paskal, A.M., Paskal, W., Pietruski, P. & Wlodarski, P.K. Polyethylene glycol: The future of posttraumatic nerve repair? systemic review. *International Journal of Molecular Sciences* **20**, 1-10 (2019).
153. Arcaute, K., Mann, B.K. & Wicker, R.B. Fabrication of off-the-shelf multilumen poly(ethylene glycol) nerve guidance conduits using stereolithography. *Tissue Engineering. Part C, Methods* **17**, 27-38 (2011).

154. Evangelista, M.S. et al. Single-lumen and multi-lumen poly(ethylene glycol) nerve conduits fabricated by stereolithography for peripheral nerve regeneration in vivo. *Journal of Reconstructive Microsurgery* **31**, 327-335 (2015).
155. Pateman, C.J. et al. Nerve guides manufactured from photocurable polymers to aid peripheral nerve repair. *Biomaterials* **49**, 77-89 (2015).
156. Behbehani, M. et al. Pre-clinical evaluation of advanced nerve guide conduits using a novel 3D in vitro testing model. *International Journal of Bioprinting* **4** (2017).
157. Rai, R., Tallawi, M., Grigore, A. & Boccaccini, A.R. Synthesis, properties and biomedical applications of poly(glycerol sebacate) (PGS): A review. *Progress in polymer science* **37**, 1051-1078 (2012).
158. Langer, R., Wang, Y., Ameer, G.A. & Sheppard, B.J. A tough biodegradable elastomer. *Nature biotechnology* **20**, 602-606 (2002).
159. Jaafar, I.H., Ammar, M.M., Jedlicka, S.S., Pearson, R.A. & Coulter, J.P. Spectroscopic evaluation, thermal, and thermomechanical characterization of poly(glycerol-sebacate) with variations in curing temperatures and durations. *Journal of Materials Science* **45**, 2525-2529 (2010).
160. Sundback, C.A. et al. Biocompatibility analysis of poly(glycerol sebacate) as a nerve guide material. *Biomaterials* **26**, 5454-5464 (2005).
161. Chen, Q.-Z. et al. Characterisation of a soft elastomer poly(glycerol sebacate) designed to match the mechanical properties of myocardial tissue. *Biomaterials* **29**, 47-57 (2008).
162. Jeffries, E.M., Allen, R.A., Gao, J., Pesce, M. & Wang, Y. Highly elastic and suturable electrospun poly(glycerol sebacate) fibrous scaffolds. *Acta Biomaterialia* **18**, 30-39 (2015).
163. Weiss, P. Erzwingung elementarer Strukturverschiedenheiten am in vitro wachsenden Gewebe - Die Wirkung mechanischer Spannung auf Richtung und Intensität des Gewebewachstums und ihre Analyse. *Wilhelm Roux' Archiv für Entwicklungsmechanik der Organismen* **116**, 438-554 (1929).
164. Weiss, P. In vitro experiments on the factors determining the course of the outgrowing nerve fiber. *Journal of Experimental Zoology* **68**, 393-448 (1934).
165. Ebendal, T. The relative roles of contact inhibition and contact guidance in orientation of axons extending on aligned collagen fibrils in vitro. *Experimental Cell Research* **98**, 159-169 (1976).
166. Dunn, G.A. Mutual contact inhibition of extension of chick sensory nerve fibres in vitro. *The Journal of Comparative Neurology* **143**, 491-507 (1971).
167. Gilbert, W., Mottelay, P.F. & Wright, E. William Gilbert of Colchester, Physician of London: On the Loadstone and Magnetic Bodies and on the Great Magnet the Earth. A New Physiology Demonstrated with Many Arguments and Experiments. (J. Wiley & Sons, 1893).
168. Rayleigh, F.R.S.L. XX. On the equilibrium of liquid conducting masses charged with electricity. *The London, Edinburgh, and Dublin Philosophical Magazine* **14**, 184-186 (1882).
169. Boys, C.V. On the Production, Properties, and some suggested Uses of the Finest Threads. *Proceedings of the Physical Society of London* **9**, 8-19 (1887).
170. Cooley, J.F. (U.S. Patent, 1902).
171. Anton, F. (U.S Patent, 1934).
172. Simons, H.L. (U.S. Patent, 1966).
173. Bornat, A. (U.S Patent 1982).
174. How, T.V. (U.S. Patent, 1985).
175. Bornat, A. (U.S. Patent, 1987).
176. Berry, J.P. (U.S. Patents, 1991).

177. Taylor, G.I. Disintegration of water drops in an electric field. *Proceedings of the Royal Society of London. Series A, Mathematical and physical sciences* **280**, 383-397 (1964).
178. Reneker, D.H. & Chun, I. Nanometre diameter fibres of polymer, produced by electrospinning. *Nanotechnology* **7**, 216-223 (1996).
179. Doshi, J. & Reneker, D.H. Electrospinning process and applications of electrospun fibers. *Journal of Electrostatics* **35**, 151-160 (1995).
180. Cloupeau, M. & Prunet-Foch, B. Electrostatic spraying of liquids in cone-jet mode. *Journal of Electrostatics* **22**, 135-159 (1989).
181. Shin, Y.M., Hohman, M.M., Brenner, M.P. & Rutledge, G.C. Experimental characterization of electrospinning: the electrically forced jet and instabilities. *Polymer* **42**, 09955-09967 (2001).
182. Bini, T.B., Gao, S., Wang, S. & Ramakrishna, S. Poly(l-lactide-co-glycolide) biodegradable microfibers and electrospun nanofibers for nerve tissue engineering: An in vitro study. *Journal of Materials Science* **41**, 6453-6459 (2006).
183. Corey, J.M. et al. Aligned electrospun nanofibers specify the direction of dorsal root ganglia neurite growth. *Journal of Biomedical Materials Research. Part A* **83A**, 636-645 (2007).
184. Schnell, E. et al. Guidance of glial cell migration and axonal growth on electrospun nanofibers of poly-ε-caprolactone and a collagen/poly-ε-caprolactone blend. *Biomaterials* **28**, 3012-3025 (2007).
185. Ghasemi-Mobarakeh, L., Prabhakaran, M.P., Morshed, M., Nasr-Esfahani, M.-H. & Ramakrishna, S. Electrospun poly(ε-caprolactone)/gelatin nanofibrous scaffolds for nerve tissue engineering. *Biomaterials* **29**, 4532-4539 (2008).
186. Xie, J. et al. The differentiation of embryonic stem cells seeded on electrospun nanofibers into neural lineages. *Biomaterials* **30**, 354-362 (2009).
187. Wang, H.B., Mullins, M.E., Cregg, J.M., McCarthy, C.W. & Gilbert, R.J. Varying the diameter of aligned electrospun fibers alters neurite outgrowth and Schwann cell migration. *Acta Biomaterialia* **6**, 2970-2978 (2010).
188. Gnavi, S. et al. The influence of electrospun fibre size on Schwann cell behaviour and axonal outgrowth. *Materials Science & Engineering C* **48**, 620-631 (2015).
189. Chew, S.Y., Mi, R., Hoke, A. & Leong, K.W. Aligned Protein-Polymer Composite Fibers Enhance Nerve Regeneration: A Potential Tissue-Engineering Platform. *Advanced Functional Materials* **17**, 1288-1296 (2007).
190. Chew, S.Y., Mi, R., Hoke, A. & Leong, K.W. The effect of the alignment of electrospun fibrous scaffolds on Schwann cell maturation. *Biomaterials* **29**, 653-661 (2008).
191. Daud, M.F.B., Pawar, K.C., Claeyssens, F., Ryan, A.J. & Haycock, J.W. An aligned 3D neuronal-glial co-culture model for peripheral nerve studies. *Biomaterials* **33**, 5901-5913 (2012).
192. Behbehani, M. et al. Pre-clinical evaluation of advanced nerve guide conduits using a novel 3D in vitro testing model. *International Journal of Bioprinting* **4**, 123 (2018).
193. Sandoval-Castellanos, A.M., Claeyssens, F. & Haycock, J.W. Bioactive 3D Scaffolds for the Delivery of NGF and BDNF to Improve Nerve Regeneration. *Frontiers in materials* **8**, 734683 (2021).
194. Taylor, C.S. et al. Aligned Polyhydroxyalkanoate Blend Electrospun Fibers as Intraluminal Guidance Scaffolds for Peripheral Nerve Repair. *ACS Biomaterials Science & Engineering* **9**, 1472-1485 (2023).
195. Behbehani, M. in Materials Science and Engineering (University of Sheffield, 2019).

196. Cirillo, V., Guarino, V., Alvarez-Perez, M.A., Marrese, M. & Ambrosio, L. Optimization of fully aligned bioactive electrospun fibers for in vitro nerve guidance. *Journal of Materials Science* **25**, 2323-2332 (2014).
197. Kriebel, A. et al. Three-dimensional configuration of orientated fibers as guidance structures for cell migration and axonal growth. *Journal of Biomedical Materials Research Part B: Applied Biomaterials* **102**, 356-365 (2014).
198. Sandoval-Castellanos, A.M., Claeyssens, F. & Haycock, J.W. Bioactive 3D Scaffolds for the Delivery of NGF and BDNF to Improve Nerve Regeneration. *Frontiers in Materials* **8**, 734683-734683 (2021).
199. Wang, H.B. et al. Creation of highly aligned electrospun poly-L-lactic acid fibers for nerve regeneration applications. *Journal of Neural Engineering* **6**, 016001 (2009).
200. Nisbet, D.R., Rodda, A.E., Horne, M.K., Forsythe, J.S. & Finkelstein, D.I. Neurite infiltration and cellular response to electrospun polycaprolactone scaffolds implanted into the brain. *Biomaterials* **30**, 4573-4580 (2009).
201. Xie, J., Liu, W., MacEwan, M.R., Bridgman, P.C. & Xia, Y. Neurite Outgrowth on Electrospun Nanofibers with Uniaxial Alignment: The Effects of Fiber Density, Surface Coating, and Supporting Substrate. *ACS Nano* **8**, 1878-1885 (2014).
202. Yang, K. et al. Nanotopographical Manipulation of Focal Adhesion Formation for Enhanced Differentiation of Human Neural Stem Cells. *ACS Applied Materials & Interfaces* **5**, 10529-10540 (2013).
203. Pires, L.R., Rocha, D.N., Ambrosio, L. & Pêgo, A.P. The role of the surface on microglia function: implications for central nervous system tissue engineering. *Journal of the Royal Society Interface* **12**, 20141224 (2015).
204. D'Amato, A.R. et al. Exploring the effects of electrospun fiber surface nanotopography on neurite outgrowth and branching in neuron cultures. *PloS one* **14**, e0211731 (2019).
205. Wu, T., Xue, J. & Xia, Y. Engraving the Surface of Electrospun Microfibers with Nanoscale Grooves Promotes the Outgrowth of Neurites and the Migration of Schwann Cells. *Angewandte Chemie (International Edition)* **59**, 15626-15632 (2020).
206. Nelson, D.W., Puhl, D.L., Funnell, J.L., Kruger, U. & Gilbert, R.J. Multivariate analysis reveals topography dependent relationships amongst neurite morphological features from dorsal root ganglia neurons. *Journal of Neural Engineering* **19** (2022).
207. Koh, H.S., Yong, T., Chan, C.K. & Ramakrishna, S. Enhancement of neurite outgrowth using nano-structured scaffolds coupled with laminin. *Biomaterials* **29**, 3574-3582 (2008).
208. Zander, N.E., Orlicki, J.A., Rawlett, A.M. & Beebe, T.P. Quantification of Protein Incorporated into Electrospun Polycaprolactone Tissue Engineering Scaffolds. *ACS Applied Materials & Interfaces* **4**, 2074-2081 (2012).
209. Abbasi, N., Soudi, S., Hayati-Roodbari, N., Dodel, M. & Soleimani, M. The effects of plasma treated electrospun nanofibrous poly (ε-caprolactone) Scaffolds with different orientations on mouse embryonic stem cell proliferation. *Cell Journal (Yakhteh)* **16**, 245-254 (2014).
210. Schaub, N.J. et al. The effect of surface modification of aligned poly-l-lactic acid electrospun fibers on fiber degradation and neurite extension. *PloS one* **10**, e0136780-e0136780 (2015).
211. Abbasi, N. et al. Influence of oriented nanofibrous PCL scaffolds on quantitative gene expression during neural differentiation of mouse embryonic stem cells. *Journal of Biomedical Materials Research. Part A* **104**, 155-164 (2016).

212. Wang, J., Chen, N., Ramakrishna, S., Tian, L. & Mo, X. The effect of plasma treated PLGA/MWCNTs-COOH composite nanofibers on nerve cell behavior. *Polymers* **9**, 713 (2017).
213. Ghobeira, R. et al. Multifaceted polymeric nerve guidance conduits with distinctive double-layered architecture and plasma-induced inner chemistry gradient for the repair of critical-sized defects. *Biomaterials Advances* **143**, 213183 (2022).
214. Namhongsa, M. et al. Plasma surface modification of two-component composite scaffolds consisting of 3D-printed and electrospun fiber components from biodegradable PLGA and PLCL. *European Polymer Journal* **194**, 112135 (2023).
215. Taylor, C.S. et al. Aminosilane Functionalized Aligned Fiber PCL Scaffolds for Peripheral Nerve Repair. *Macromolecular Bioscience* **23**, e2300226 (2023).
216. Aliakbarshirazi, S. et al. Advanced Hollow Cathode Discharge Plasma Treatment of Unique Bilayered Fibrous Nerve Guidance Conduits for Enhanced/Oriented Neurite Outgrowth. *Biomacromolecules* **25**, 1448-1467 (2024).
217. France, R.M. & Short, R.D. Plasma treatment of polymers: effects of energy transfer from an argon plasma and post-plasma storage on the surface chemistry of polystyrene. *Polymer Degradation and Stability* **45**, 339-346 (1994).
218. France, R.M. & Short, R.D. Plasma treatment of polymers effects of energy transfer from an argon plasma on the surface chemistry of poly(styrene), low density poly(ethylene), poly(propylene) and poly(ethylene terephthalate). *Journal of the Chemical Society - Faraday Transactions* **93**, 3173-3178 (1997).
219. Taylor, C.S. et al. Cost effective optimised synthetic surface modification strategies for enhanced control of neuronal cell differentiation and supporting neuronal and Schwann cell viability. *Journal of Biomedical Materials Research Part B: Applied Biomaterials* **109**, 1713-1723 (2021).
220. DiStefano, P.S. et al. The neurotrophins BDNF, NT-3, and NGF display distinct patterns of retrograde axonal transport in peripheral and central neurons. *Neuron* **8**, 983-993 (1992).
221. Curtis, R. et al. Retrograde axonal transport of ciliary neurotrophic factor is increased by peripheral nerve injury. *Nature* **365**, 253-255 (1993).
222. Thompson, S.W.N., Vernallis, A.B., Heath, J.K. & Priestley, J.V. Leukaemia inhibitory factor is retrogradely transported by a distinct population of adult rat sensory neurons: Co-localization with trkA and other neurochemical markers. *European Journal of Neuroscience* **9**, 1244-1251 (1997).
223. Arvidsson, J., Ygge, J. & Grant, G. Cell loss in lumbar dorsal root ganglia and transganglionic degeneration after sciatic nerve resection in the rat. *Brain Research* **373**, 15-21 (1986).
224. Schmalbruch, H. Loss of sensory neurons after sciatic nerve section in the rat. *The Anatomical Record* **219**, 323-329 (1987).
225. Himes, B.T. & Tessler, A. Death of some dorsal root ganglion neurons and plasticity of others following sciatic nerve section in adult and neonatal rats. *Journal of Comparative Neurology* **284**, 215-230 (1989).
226. Liss, A.G., af Ekenstam, F.W. & Wiberg, M. Cell loss in sensory ganglia after peripheral nerve injury: An anatomical tracer study using lectin-coupled horseradish peroxidase in cats. *Scandinavian Journal of Plastic and Reconstructive Surgery and Hand Surgery* **28**, 177-188 (1994).
227. Reynolds, M.L. & Woolf, C.J. Reciprocal Schwann cell-axon interactions. *Current Opinion in Neurobiology* **3**, 683-693 (1993).

228. Dong, Z. et al. Neu differentiation factor is a neuron-glia signal and regulates survival, proliferation, and maturation of rat schwann cell precursors. *Neuron* **15**, 585-596 (1995).
229. Trachtenberg, J.T. & Thompson, W.J. Schwann cell apoptosis at developing neuromuscular junctions is regulated by glial growth factor. *Nature* **379**, 174-177 (1996).
230. Mahanthappa, N.K., Anton, E.S. & Matthew, W.D. Glial growth factor 2, a soluble neuregulin, directly increases Schwann cell motility and indirectly promotes neurite outgrowth. *Journal of Neuroscience* **16**, 4673-4683 (1996).
231. Li, H., Terenghi, G. & Hall, S.M. Effects of delayed re-innervation on the expression of c-erbB receptors by chronically denervated rat Schwann cells in vivo. *Glia* **20**, 333-347 (1997).
232. Terenghi, G., Calder, J.S., Birch, R. & Hall, S.M. A morphological study of Schwann cells and axonal regeneration in chronically transected human peripheral nerves. *Journal of Hand Surgery: European Volume* **23**, 583-587 (1998).
233. Terenghi, G. Peripheral nerve regeneration and neurotrophic factors. *Journal of Anatomy* **194**, 1-14 (1999).
234. Boyd, J.G. & Gordon, T. Neurotrophic factors and their receptors in axonal regeneration and functional recovery after peripheral nerve injury. *Molecular Neurobiology* **27**, 277-324 (2003).
235. Lin, L.F., Doherty, D.H., Lile, J.D., Bektesh, S. & Collins, F. GDNF: A glial cell line-derived neurotrophic factor for midbrain dopaminergic neurons. *Science* **260**, 1130-1132 (1993).
236. Henderson, C.E. et al. GDNF: A potent survival factor for motoneurons present in peripheral nerve and muscle. *Science* **266**, 1062-1064 (1994).
237. Oppenheim, R.W. et al. Developing motor neurons rescued from programmed and axotomy-induced cell death by GDNF. *Nature* **373**, 344-346 (1995).
238. Durbec, P. et al. GDNF signalling through the Ret receptor tyrosine kinase. *Nature* **381**, 789-793 (1996).
239. Jing, S. et al. GDNF–induced activation of the Ret protein tyrosine kinase is mediated by GDNFR-α, a novel receptor for GDNF. *Cell* **85**, 1113-1124 (1996).
240. Treanor, J.J.S. et al. Characterization of a multicomponent receptor for GDNF. *Nature* **382**, 80-83 (1996).
241. Naveilhan, P., ElShamy, W.M. & Ernfors, P. Differential regulation of mRNAs for GDNF and its receptors Ret and GDNFRα after sciatic nerve lesion in the mouse. *European Journal of Neuroscience* **9**, 1450-1460 (1997).
242. Hammarberg, H. et al. GDNF mRNA in Schwann cells and DRG satellite cells after chronic sciatic nerve injury. *Neuroreport* **7**, 857-860 (1996).
243. Yan, Q., Matheson, C. & Lopez, O.T. In vivo neurotrophic effects of GDNF on neonatal and adult facial motor neurons. *Nature* **373**, 341-344 (1995).
244. Trupp, M. et al. Peripheral expression and biological activities of GDNF, a new neurotrophic factor for avian and mammalian peripheral neurons. *The Journal of Cell Biology* **130**, 137-148 (1995).
245. Munson, J.B. & McMahon, S.B. Effects of GDNF on axotomized sensory and motor neurons in adult rats. *European Journal of Neuroscience* **9**, 1126-1129 (1997).
246. Xu, X. et al. Polyphosphoester microspheres for sustained release of biologically active nerve growth factor. *Biomaterials* **23**, 3765-3772 (2002).
247. Xu, X. et al. Ultrafine medicated fibers electrospun from W/O emulsions. *Journal of Controlled Release* **108**, 33-42 (2005).

248. Liu, C. et al. Nanofibrous bicomponent scaffolds for the dual delivery of NGF and GDNF: controlled release of growth factors and their biological effects. *Journal of Materials Science: Materials in Medicine* **32**, 9 (2021).
249. Yan, S., Xiaoqiang, L., Lianjiang, T., Chen, H. & Xiumei, M. Poly(l-lactide-co-ε-caprolactone) electrospun nanofibers for encapsulating and sustained releasing proteins. *Polymer* **50**, 4212-4219 (2009).
250. Handarmin et al. Nanofibrous scaffold with incorporated protein gradient for directing neurite outgrowth. *Drug Delivery and Translational Research* **1**, 147-160 (2011).
251. Whitehead, T.J., Avila, C.O.C. & Sundararaghavan, H.G. Combining growth factor releasing microspheres within aligned nanofibers enhances neurite outgrowth. *Journal of Biomedical Materials Research: Part A* **106**, 17-25 (2018).
252. Valmikinathan, C.M., Defroda, S. & Yu, X. Polycaprolactone and Bovine Serum Albumin Based Nanofibers for Controlled Release of Nerve Growth Factor. *Biomacromolecules* **10**, 1084-1089 (2009).
253. Xue, J., Wu, T., Li, J., Zhu, C. & Xia, Y. Promoting the Outgrowth of Neurites on Electrospun Microfibers by Functionalization with Electrosprayed Microparticles of Fatty Acids. *Angewandte Chemie* **58**, 3948-3951 (2019).
254. Xue, J., Zhu, C., Li, J., Li, H. & Xia, Y. Integration of Phase-Change Materials with Electrospun Fibers for Promoting Neurite Outgrowth under Controlled Release. *Advanced Functional Materials* **28**, 1705563 (2018).
255. Zuidema, J.M. et al. Porous Silicon Nanoparticles Embedded in Poly(lactic-co-glycolic acid) Nanofiber Scaffolds Deliver Neurotrophic Payloads to Enhance Neuronal Growth. *Advanced Functional Materials* **30**, 2002560 (2020).
256. Li, X. et al. Encapsulation of proteins in poly(l-lactide-co-caprolactone) fibers by emulsion electrospinning. *Colloids and surfaces, B, Biointerfaces* **75**, 418-424 (2010).
257. Hu, J., Tian, L., Prabhakaran, M.P., Ding, X. & Ramakrishna, S. Fabrication of nerve growth factor encapsulated aligned poly(ε-caprolactone) nanofibers and their assessment as a potential neural tissue engineering scaffold. *Polymers* **8**, 54 (2016).
258. Liu, C. et al. Incorporation and release of dual growth factors for nerve tissue engineering using nanofibrous bicomponent scaffolds. *Biomedical Materials* **13**, 044107 (2018).
259. Liu, C. et al. Spatio-temporal release of NGF and GDNF from multi-layered nanofibrous bicomponent electrospun scaffolds. *Journal of Materials Science: Materials in medicine* **29**, 102-113 (2018).
260. Wang, C.-Y. et al. The Effect of Aligned Core-Shell Nanofibres Delivering NGF on the Promotion of Sciatic Nerve Regeneration. *Journal of Biomaterials Science. Polymer edition.* **23**, 167-184 (2012).
261. Cho, Y.I., Choi, J.S., Jeong, S.Y. & Yoo, H.S. Nerve growth factor (NGF)-conjugated electrospun nanostructures with topographical cues for neuronal differentiation of mesenchymal stem cells. *Acta Biomaterialia* **6**, 4725-4733 (2010).
262. Fine, E.G., Decosterd, I., Papaloïzos, M., Zurn, A.D. & Aebischer, P. GDNF and NGF released by synthetic guidance channels support sciatic nerve regeneration across a long gap. *The European Journal of Neuroscience* **15**, 589-601 (2002).
263. Mahoney, D.J. et al. A method for the non-covalent immobilization of heparin to surfaces. *Analytical Biochemistry* **330**, 123-129 (2004).
264. Robinson, D.E. et al. Plasma polymer and biomolecule modification of 3D scaffolds for tissue engineering. *Plasma Processes and Polymers* **13**, 678-689 (2016).

265. Verna, J.-M., Fichard, A. & Saxod, R. Influence of glycosaminoglycans on neurite morphology and outgrowth patterns in vitro. *International Journal of Developmental Neuroscience* **7**, 389-399 (1989).
266. Menezes, R. et al. Investigation of glycosaminoglycan mimetic scaffolds for neurite growth. *Acta Biomaterialia* **90**, 169-178 (2019).
267. Idini, M. et al. Glycosaminoglycan functionalization of electrospun scaffolds enhances Schwann cell activity. *Acta Biomaterialia* **96**, 188-202 (2019).
268. Ikegami, Y. & Ijima, H. Development of heparin-conjugated nanofibers and a novel biological signal by immobilized growth factors for peripheral nerve regeneration. *Journal of Bioscience and Bioengineering* **129**, 354-362 (2020).
269. Lundborg, G., Dahlin, L.B. & Danielsen, N. Ulnar Nerve Repair by the Silicone Chamber Technique. *Scandinavian Journal of Plastic and Reconstructive Surgery and Hand Surgery* **25**, 79-82 (1991).
270. Doolabh, V.B., Hertl, M.C. & Mackinnon, S.E. The Role of Conduits in Nerve Repair: A Review. *Reviews in the Neurosciences* **7**, 47-84 (1996).
271. Singh, D. et al. Additive manufactured biodegradable poly(glycerol sebacate methacrylate) nerve guidance conduits. *Acta Biomaterialia* **78**, 48-63 (2018).
272. Aileen Crawford-Corrie, David John Buttle & Haycock, J.W. (University of Sheffield, United States; 2020).
273. Kristensen, E.M.E. et al. Heparin coating durability on artificial heart valves studied by XPS and antithrombin binding capacity. *Colloids and Surfaces B: Biointerfaces* **49**, 1-7 (2006).
274. Hawker, M.J., Pegalajar-Jurado, A., Hicks, K.I., Shearer, J.C. & Fisher, E.R. Allylamine and Allyl Alcohol Plasma Copolymerization: Synthesis of Customizable Biologically-Reactive Three-Dimensional Scaffolds. *Plasma Processes and Polymers* **12**, 1435-1450 (2015).
275. Cheng, L. et al. Comparative study of different nitrogen-containing plasma modifications applied on 3D porous PCL scaffolds and 2D PCL films. *Applied Surface Science* **516**, 146067-146067 (2020).
276. Das, S.K., Dickinson, C., Lafir, F., Brougham, D.F. & Marsili, E. Synthesis, characterization and catalytic activity of gold nanoparticles biosynthesized with Rhizopus oryzae protein extract. *Green Chemistry* **14**, 1322-1334 (2012).
277. Hellgren, N., Haasch, R.T., Schmidt, S., Hultman, L. & Petrov, I. Interpretation of X-ray photoelectron spectra of carbon-nitride thin films: New insights from in situ XPS. *Carbon* **108**, 242-252 (2016).
278. Girardeaux, C. & Pireaux, J.-J. Analysis of Polystyrene (PS) by XPS. *Surface Science Spectra* **4**, 130-133 (1996).
279. Battiston, K.G., McBane, J.E., Labow, R.S. & Santerre, J.P. Differences in protein binding and cytokine release from monocytes on commercially sourced tissue culture polystyrene. *Acta Biomaterialia* **8**, 89-98 (2012).
280. Jacobs, T. et al. Plasma treatment of polycaprolactone at medium pressure. *Surface and Coatings Technology* **205**, 543-547 (2011).
281. Sivan, M. et al. Plasma treatment effects on bulk properties of polycaprolactone nanofibrous mats fabricated by uncommon AC electrospinning: A comparative study. *Surface and Coatings Technology* **399**, 126203-126203 (2020).
282. Can-Herrera, L.A. et al. Surface modification of electrospun polycaprolactone microfibers by air plasma treatment: Effect of plasma power and treatment time. *European Polymer Journal* **84**, 502-513 (2016).

283. Jacobs, T. et al. Improved cell adhesion to flat and porous plasma-treated poly-ε-caprolactone samples. *Surface and Coatings Technology* **232**, 447-455 (2013).
284. Yi, S.Y. et al. Substrate-independent adsorption of nanoparticles as anti-biofilm coatings. *Biomaterials Science* **10**, 410-422 (2022).
285. Chowdhury, A.K.M.S., Cameron, D.C. & Hashmi, M.S.J. Bonding structure in carbon nitride films: variation with nitrogen content and annealing temperature. *Surface & Coatings Technology* **112**, 133-139 (1999).
286. Gouzman, I., Brener, R. & Hoffman, A. Nitridation of diamond and graphite surfaces by low energy N+2 ion irradiation. **331-333**, 283-288 (1995).
287. Littlejohn, D. & Chang, S.-G. An XPS study of nitrogen-sulfur compounds. *Journal of Electron Spectroscopy and Related Phenomena* **71**, 47-50 (1995).
288. Sandoval-Castellanos, A.M., Claeyssens, F. & Haycock, J.W. Biomimetic surface delivery of NGF and BDNF to enhance neurite outgrowth. *Biotechnology and Bioengineering* **117**, 3124-3135 (2020).
289. Edlund, U., Dånmark, S. & Albertsson, A.C. A strategy for the covalent functionalization of resorbable polymers with heparin and osteoinductive growth factor. *Biomacromolecules* **9**, 901-905 (2008).
290. Wan, X. et al. Poly(ε-caprolactone)/keratin/heparin/VEGF biocomposite mats for vascular tissue engineering. *Journal of Biomedical Materials Research Part A* **108**, 292-300 (2020).
291. Elzein, T., Nasser-Eddine, M., Delaite, C., Bistac, S. & Dumas, P. FTIR study of polycaprolactone chain organization at interfaces. *Journal of Colloid and Interface Science* **273**, 381-387 (2004).
292. Mello, B.L. et al. Grafting 3-trimethoxysilylpropyl)diethylenetriamine on microcrystalline cellulose for the adsorption of dyes: Experimental and modeling studies. *Reactive and Functional Polymers* **196**, 105836-105836 (2024).
293. Viard, J., Beche, E., Perarnau, D., Berjoan, R. & Durand, J. XPS and FTIR study of silicon oxynitride thin films. *Journal of the European Ceramic Society* **17**, 2025-2028 (1997).
294. Harada, N.S. et al. Quantifying adsorption of heparin on a PVC substrate using ATR-FTIR. *Polymer International* **54**, 209-214 (2005).
295. Jeong, J.O. et al. Development and characterization of heparin-immobilized polycaprolactone nanofibrous scaffolds for tissue engineering using gamma-irradiation. *Royal Society of Chemistry Advances* **7**, 8963-8972 (2017).
296. Cao, L. et al. 2-*N*, 6-*O*-sulfated chitosan-assisted BMP-2 immobilization of PCL scaffolds for enhanced osteoinduction. *Materials Science and Engineering: C* **74**, 298-306 (2017).
297. Hanuman, S., Pande, G. & Nune, M. Aminolysis of Polycaprolactone Nanofibers for Applications in Uterine Tissue Engineering. *Trends in Biomaterials & Artificial Organs* **35** (2021).
298. Coller, H.A. The paradox of metabolism in quiescent stem cells. *Federation of European Biochemical Societies Letters* **593**, 2817-2839 (2019).
299. Lo, C.-M., Wang, H.-B., Dembo, M. & Wang, Y.-l. Cell movement is guided by the rigidity of the substrate. *Biophysical Journal* **79**, 144-152 (2000).
300. Discher, D.E., Janmey, P. & Wang, Y.-l. Tissue cells feel and respond to the stiffness of their substrate. *Science* **310**, 1139-1143 (2005).
301. Bottenstein, J.E. & Sato, G.H. Growth of a Rat Neuroblastoma Cell Line in Serum-Free Supplemented Medium. *Proceedings of the National Academy of Sciences* **76**, 514-517 (1979).

302. Yu, C.Q. & Rosenblatt, M.I. Transgenic Corneal Neurofluorescence in Mice: A New Model for In Vivo Investigation of Nerve Structure and Regeneration. *Investigative Ophthalmology & Visual Science* **48**, 1535-1542 (2007).
303. Feng, G. et al. Imaging neuronal subsets in transgenic mice expressing multiple spectral variants of GFP. *Neuron* **28**, 41-51 (2000).
304. Koroleva, A. et al. Two-photon polymerization-generated and micromolding-replicated 3D scaffolds for peripheral neural tissue engineering applications. *Biofabrication* **4**, 025005-025005 (2012).
305. Jin, B. et al. Combining a Density Gradient of Biomacromolecular Nanoparticles with Biological Effectors in an Electrospun Fiber-Based Nerve Guidance Conduit to Promote Peripheral Nerve Repair. *Advanced Science* **10**, e2203296 (2023).
306. Madduri, S., Papaloïzos, M. & Gander, B. Trophically and topographically functionalized silk fibroin nerve conduits for guided peripheral nerve regeneration. *Biomaterials* **31**, 2323-2334 (2010).
307. Yan, L. et al. An experimental and numerical study of the microstructural and biomechanical properties of human peripheral nerve endoneurium for the design of tissue scaffolds. *Frontiers in Bioengineering and Biotechnology* **10**, 1029416-1029416 (2022).
308. Katzenell, S., Cabrera, J.R., North, B.J. & Leib, D.A. in Innate Antiviral Immunity: Methods and Protocols. (ed. K. Mossman) 229-251 (2017).
309. Dinis, T.M. et al. Method to Form a Fiber/Growth Factor Dual-Gradient along Electrospun Silk for Nerve Regeneration. *ACS Applied Materials & Interfaces* **6**, 16817-16826 (2014).